SETTING CONSTRAINTS ON THE LUNAR EXOSPHERE: A COMPREHENSIVE ANALYSIS OF VELOCITY RESOLVED SODIUM AND POTASSIUM LINE PROFILE MEASUREMENTS

BY

DONA CHATHUNI P. KURUPPUARATCHI

A Dissertation

Submitted to the Department of Physical Sciences

and the Committee on Graduate Studies

In partial fulfillment of the requirements

for the degree of

Doctor of Philosophy in Engineering Physics

12/2020

Embry-Riddle Aeronautical University

Daytona Beach, Florida

SETTING CONSTRAINTS ON THE LUNAR EXOSPHERE: A COMPREHENSIVE ANALYSIS OF VELOCITY RESOLVED SODIUM AND POTASSIUM LINE PROFILE MEASUREMENTS

by

Dona Chathuni P. Kuruppuaratchi

This dissertation was prepared under the direction of the candidate's Dissertation Committee Chair, Dr. Edwin J. Mierkiewicz, Thesis Committee members Dr. Ronald J. Oliversen (external), Dr. Menelaos Sarantos (external), Dr. Ahsley Kehoe, and Dr. Jason Aufdenberg. It was submitted to the Department of Physical Sciences in partial fulfillment of the requirements for the degree

of

Doctor of Philosophy in Engineering Physics

DISSERTATION COMMITTEE

DISSERTATION COMMITTEE

Edwin Mierkiewicz
Digitally signed by Edwin Mierkiewicz
DN: cn=Edwin Mierkiewicz, o, ou, email=mierkiee@erau.edu, c=US
Date: 2020.12.15 22:17:23 -06'00'

Dr. Edwin J. Mierkiewicz,
Committee Chair

Dr. Jason Aufdenberg,
Committee Member

Dr. Ashley Kehoe,
Committee Member

Ronald J Oliversen
Digitally signed by Ronald J Oliversen
Date: 2020.12.15 07:33:00 -05'00'

Dr. Ronald J. Oliversen,
External Committee Member
NASA/GSFC

Dr. Menelaos Sarantos
External Committee Member
NASA/GSFC

Edwin Mierkiewicz
Digitally signed by Edwin Mierkiewicz
DN: cn=Edwin Mierkiewicz, o, ou, email=mierkiee@erau.edu, c=US
Date: 2020.12.15 22:17:54 -06'00'

Dr. Edwin J.Mierkiewicz
Graduate Program Chair
Engineering Physics

Dr. Terry Oswalt,
Department Chair,
Physical Sciences

Christopher Grant
Digitally signed by Christopher Grant
Date: 2020.12.17 13:37:44 -05'00'

Dr. Karen Gaines, Dean, College
of Arts and Sciences

Dr. Christopher Grant,
Vice Chancellor

ABSTRACT

This dissertation outlines and presents the most comprehensive set of velocity-resolved measurements of sodium D2 (5889.9509 Å) lines taken over multiple lunations spanning seven years (2011 – 2017). These data are used to study the morphology and dynamics of the lunar exosphere. Additionally, potassium D1 (7698.9646 Å) is used as a complement to sodium. The two species approach, with sodium being the main attraction, provides constraints on the critical drivers of the lunar exosphere. Observations were made at the National Solar Observatory McMath – Pierce Telescope, Kitt Peak, Arizona where I personally collected both sodium and potassium data over about a dozen observing runs. This work builds on the initial velocity resolved measurement analysis of sodium by Mierkiewicz et al. (2014) and includes the sodium analysis of Kuruppuaratchi et al. (2018), and potassium analysis of Rosborough et al. (2019). This work is divided into an analysis of exospheric responses as a function of phase angle (temporal) and an analysis of exospheric responses as a function of latitude and altitude (spatial). Sodium results suggest that photon stimulated desorption (PSD) is the major source mechanism for the lunar sodium exosphere near subsolar points while contributions from charged particle sputtering and micrometeoroid impact vaporization are more important near the dawn and dusk terminators. For potassium, the exosphere exhibits dawn-dusk asymmetry because of impact vaporization and a connection to the surface abundance of potassium. A two species study investigating the response of the exosphere to micrometeoroid impacts shows that sodium appears to have a smooth, gradual response to meteor activity, while potassium appears to have a short-term but significant response. Potassium is found to track closely

with surface abundance tied to the regions on the Moon where there are known abundances of potassium (KREEP regions). The spatial study is performed keeping in mind prior works that speculated the possible contribution of plasma sheet ions in the response of the exosphere during magnetotail passage. A large part of this work is focused on the analysis of sodium and potassium based on the near lunar plasma environment: (i.e., solar wind, magnetosheath, and magnetotail) as a function of latitude. Sodium exospheric temperatures and relative intensities indicate that the relative importance of source processes vary depending on the near lunar plasma environment. Potassium, on the other hand, hints at being modulated by micrometeorite impact vaporization throughout all plasma regions. Potassium also shows enhancements in brightness around latitudes where KREEP regions are. Sodium shows some indication of surface enhancement since relative intensity data tend to peak at low-mid latitudes in both North and South regions. Sodium temperatures also show an increase from low to high latitudes. A closer look at the amount of time the Moon spent interacting with the plasma sheet revealed that sodium temperatures showed a positive correlation with time spent in the plasma sheet. Sodium intensities however did not seem to respond as well. The radial dependence of the sodium exosphere indicated that linewidths narrow as a function of altitude. Analysis of these velocity resolved observations from this unique dataset, taken over multiple lunations and years as a function of latitude, altitude, and phase, has helped define baseline and variable conditions of the lunar exosphere - thereby making important contributions towards the study of the near space environment of the Moon which is not only important for testing theoretical models of Surface Bounded Exospheres (SBEs) but also for understanding the atmosphere – surface interactions that will affect human exploration.

ACKNOWLEDGEMENTS

After 5 long years, countless hours of hard work, long nights, stress, personal turmoil, and things that I cannot sometimes put into words – I have completed my dissertation. While it is a task by itself to write into words what one feels after completing such an important milestone, you must know that this is the product of not only my hard work but the combined effort of some very important people. This work would not have been possible without their constant guidance and support, and a simple acknowledgement in here probably does not do them justice, but for now, I will try.

I would first like to thank Ron who has always given his 100% to not only my dissertation work but his role as a mentor, despite anything that goes on in his life. Whenever I had a problem, could not handle the stress, or just felt burnt out, it was Ron who encouraged me to keep my head up. Ron believed in me even during the times I did not believe in myself. Words cannot thank you enough for all the help and effort you have put into my growth as a graduate student and as a person – but here it is, big thank you Ron! I am forever thankful for everything you have taught me and will continue to teach me. I miss the observing days at the telescope, listening to Fleetwood Mac, talking about work, life, and very random things. It has been an honor working beside you and I look forward to working with you in the future and having you as my mentor during my postdoc. Cheers to a new adventure (ft. Fleetwood Mac)!

Next thank you goes to Ed. Thank you, Ed, for taking me on as a graduate student, and for always believing in me. I have always felt I was not the best type of student, and I work in strange ways, but you have always encouraged me and were not disappointed in me despite any mistakes I made (which was probably a lot of times). You are a wonderful advisor and

always willing to listen to any issue with compassion and offer valuable insight. I also always appreciate your upbeat personality, despite doing a million things, it is always a pleasure to see someone so jolly. It has been a long journey, and I have learnt a lot from you too so big thank you to you, Ed! Look forward to working with you in the future and writing more papers!

I would also like to thank Menelaos who has really helped push this lunar project even further by offering extremely valuable insight through the use of his models. I know I have not known you for as long as Ed or Ron, but you have also offered me guidance and support. You always have lots of fun ideas and interesting ways of looking at things, I have truly learnt a lot from you. Thank you! I look forward to working with you too.

Thank you to the rest of the committee members for checking my work and providing their input – the discussions have been very interesting!

Thank you to Nick Derr for his huge help with some very important data processing and prepping steps, including his work on the logbooks and the automation of potassium data reduction. Without your help, it would have taken this work much longer to come into completion. Thank you to Sarena Robertsen for her help in reducing potassium data and building on Nick's work for streamlining the potassium data reductions. Thank you to Sara Rosborough and Grace Butcher for their help in reducing sodium data.

This work would also not have been possible without the actual data itself, so thank you to the following people for helping with observing: Nick Derr (U Wisconsin/Harvard), Maggie Gallant (ERAU), Chad Freer (ERAU), Sara Rosborough (ERAU/ U Maryland), Sarena Robertsen (ERAU/US Navy), Andrea Hughes (ERAU), Maurice Wilson (ERAU), Will Fanning (ERAU) , Ed Mierkiewicz (ERAU), Christina McFarland (ERAU), Bert

Kalio (ERAU), Derek Gardner (U Wisconsin), Cassie Hatcher (U Oregon), Jesus Hinonjosa (U Texas – Brownsville), Mike Line (Caltech), Sean McKillop (U Maryland), Lori Spalsbury (U Maine/Adnet), Nick Walter (U Wisconsin), Lauren Wooten (U Maryland), Nuri Emrahoglu (Cukurova University, Turkey), George Hilton (Newton Engineering/GSFC), Christa Krosner (GSFC), Pat Lawton (GSFC), Ron Oliversen (GSFC), Olivia Lupie (GSFC), Mike Myslinski (GSFC), Eric Galayda (NSO/MDM), Eric Palmer (Raytheon), Chuck Rasbach (Lockheed Martin), Jean Rasbach (Douglas County School, CO), Fred Roesler (U Wisconsin), Jen Sun (Adnet/GSFC), and last but not least, myself.

A heartfelt thank you to my family and friends for their constant support, encouragement, and words of wisdom. Thank you to my parents for their undying love and support, and for always believing in me, no matter what. It is an honor to be your daughter. I am grateful to my wonderful friends, who are always there for me. Thank you for making life more bearable during times when work was so overwhelming.

I would like to thank the National Solar Observatory for use of their fine telescope and especially the assistance of Detrick Branston and Matt Penn. The lunar team will always be appreciative of the advice from Dr. Fred Roesler, University of Wisconsin and Jody Wilson, University of New Hampshire. Finally, this work was supported by NASA grants NNX11AE38G and NNX13AL30G and by the Solar System Exploration Research Virtual Institute (SSERVI) .

Table of Contents

TABLE OF TABLES

TABLE OF FIGURES

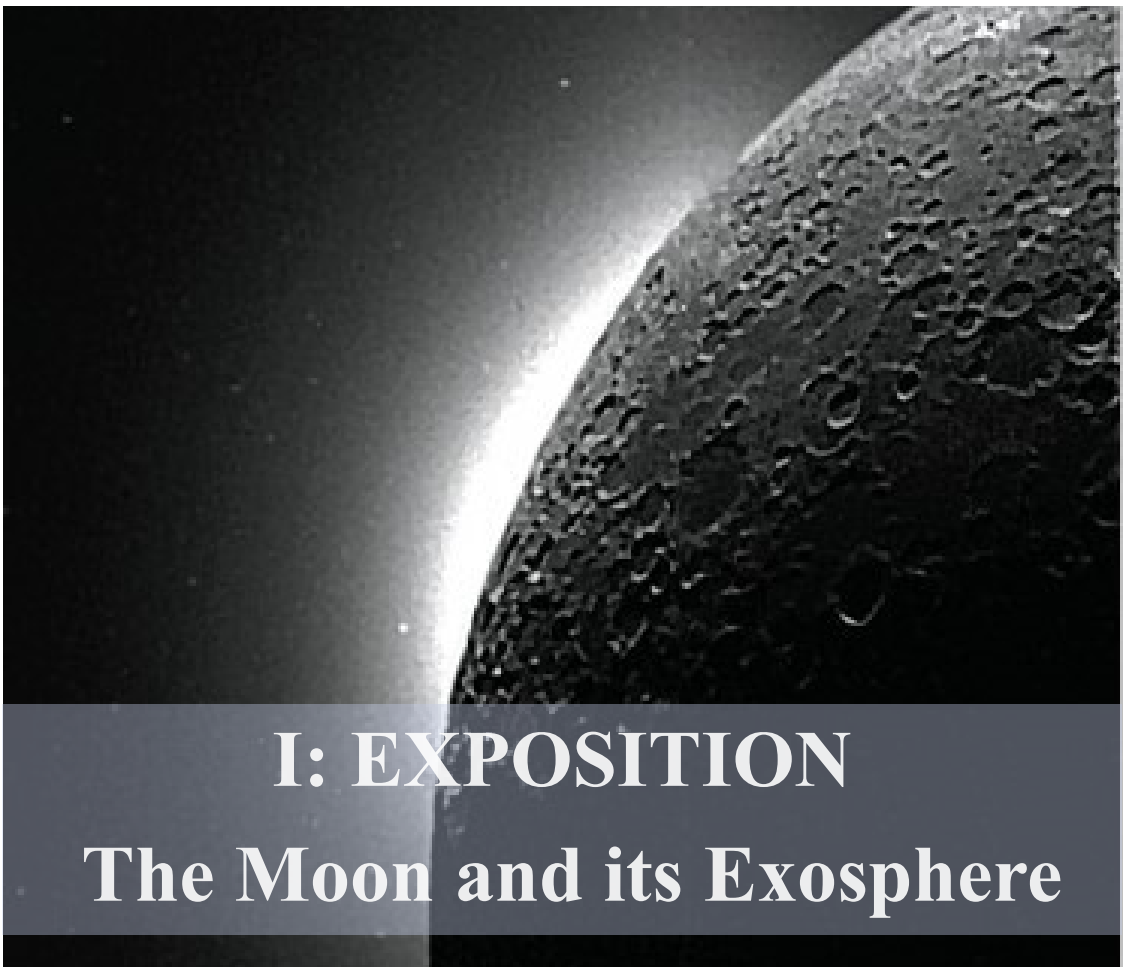

I: EXPOSITION
The Moon and its Exosphere

Photo Credit: Clementine Mission

CHAPTER 1. INTRODUCTION

1.1. A Brief History of the Moon and its Importance

Our Moon, a familiar object in the sky, is a key player in the role of understanding our Solar System. Not only is the Moon the brightest and one of the most familiar objects in our night sky, but it is also Earth's closest companion and only natural satellite. Since the Moon today does not have plate tectonics like Earth and does not have an atmosphere capable of weathering its surface, it has preserved the early history of the inner Solar System like a time capsule – giving it great scientific importance in the understanding of Earth and other terrestrial planets in our Solar System. The ways the Moon can be used to understand the evolution of our planet and inner Solar System as highlighted by the National Research Council (NRC, 2007) are briefly summarized below:

1) *Early Earth-Moon System*: The leading hypothesis is that the Moon was formed from the debris of a collision of a Mars-sized protoplanet, named Theia, 4.5 billion (Ga) years ago (Herwartz et al., 2014). As such, the composition and thermal histories of the Moon and Earth were intricately linked before they started to evolve separately. Studying the structure and composition of the lunar surface provides clues as to how and when the Earth and Moon separated, why they separated, and how they influence one another (NRC, 2007).
2) *Terrestrial Planet Differentiation and Evolution*: The Moon has undergone differentiation into a crust, mantle, and core within a few hundred million years after formation – a process that is defined by the magma ocean hypothesis. Studying the diversity of lunar rocks (chemical makeup and mineralogy) can reveal

information about the fractional differentiation of an initial ocean of magma (Hiesinger and Jaumann, 2014). Studying the differentiation process on the Moon can help us fFigure out how to apply the lunar model to understand other rocky bodies (NRC, 2007).

3) *Solar System Impact Record*: Since its formation 4.5 Ga years ago, the Moon has experienced both early and late bombardment from Solar System debris. Studying the heavily cratered surface of the Moon provides clues to the early bombardment history of the inner Solar System. The terminal cataclysm hypothesis claims that about 4 Ga years ago a burst of large impacts occurred in the inner Solar System (including the Moon). If this hypothesis is confirmed through the study of lunar impact craters, then this provides important constraints on the evolution of terrestrial planets and the origin and evolution of life on Earth (NRC, 2007).
4) *Lunar Environment*: The lunar atmosphere belongs to a class of tenuous atmospheres known as Surface Bounded Exospheres (SBE) (Elphic et al., 2015), and is the most common type of satellite atmosphere in the Solar System. The Moon's surface is a testament to products produced over long (over billions of years) and short (years, months, days) timescales by exposure to solar and galactic radiation (solar wind particles and cosmic rays), space plasmas (e.g., Earth's magnetospheric plasma) and solar ultraviolet radiation. Additionally, the lunar surface contains volatiles that may provide clues to the sources of volatiles in the younger days of the Solar System (NRC, 2007).

The Moon's proximity to Earth and its almost pristine nature, allows it to be used as a home base for studying the fundamental processes that drive planetary formation and

evolution – allowing us to peek back into geological times for which evidence on Earth has already been erased (Hiesinger and Jaumann, 2014).

Following the collision between Theia and Earth the early Moon was formed about 20,000 km from Earth. Today the Earth-Moon tidal interaction has slowed the Earth's rotation and slowly increased the Earth-Moon distance to its current mean location of 384,400 km. The combined information from all missions, starting with the Apollo and Surveyor era missions of the early space age, has provided us with a rich data set for studies in geology, geochemistry, mineralogy, petrology, chronology, and internal structure that is unequaled for any planetary body other than the Earth (Hiesinger and Jaumann, 2014).

While there is a wealth of information on the Moon, the most relevant scientific context to this dissertation from the four overarching themes listed above is *the lunar environment*. The purpose of this dissertation is to provide new insights into lunar atmospheric dynamics in terms of how the atmosphere varies spatially and temporally, how atoms are released from the regolith through surface interactions with the near-Earth space environment, and how atoms behave once released from the regolith into the atmosphere.

Throughout the Solar System, SBEs are a common occurrence and in addition to the Moon, other planetary bodies that host SBEs include: Mercury (Potter and Morgan 1985; 1986; Killen and Ip, 1999), large asteroids (Hurley, 2009), and the Galilean satellites – e.g., Io, Europa, Ganymede (NRC 2007). The surfaces of these planetary bodies are constantly bombarded with high-energy particles such as solar wind ions, coronal mass ejections (CME), micrometeorites, solar photons, magnetospheric plasma ions and galactic cosmic rays. The resulting surface and atmospheric changes caused by the continuous surface bombardment of these energetic particles and solar irradiation are known as space

weathering. While space weathering is also prevalent on planetary bodies hosting similar tenuous environments throughout the Solar System, the way their SBEs interact with their external environments may differ depending on the specific conditions of the host body. For example, the SBE on an icy satellite has different surface-atmosphere dynamics compared to the surface-atmosphere dynamics on surfaces with silicates such as the Moon and Mercury (Hurley, 2009). Also, depending on the magnetic environment surrounding each body, their SBEs are exposed to varying types and amounts of space plasmas. For instance, unlike the Moon, Mercury has a global magnetic field and magnetosphere which means the SBE is exposed to the Hermean magnetospheric plasma more than solar wind plasma. Similarly, the Jovian satellites interact with an internal plasma source in the Jovian magnetosphere which is different from the plasma environment of Mercury and Earth's magnetosphere. On the other hand, the Moon does not have an appreciable, intrinsic magnetic field, and is exposed to the solar wind plasma directly - except when the Moon spends approximately five to six days in the Earth's magnetosphere every lunation. To add to the complexity, the Moon also has localized "crustal" magnetic fields in regions known as lunar magnetic anomalies. When the solar wind interacts with these magnetic anomalies, "mini magnetospheres" are formed (Bhardwaj et al., 2015) and so these regions are then shielded from plasma particles. While lunar magnetic anomalies are interesting regions, this topic is beyond the scope of this dissertation. Ideally, SBEs on various planetary bodies should be studied as a group for us to understand why certain processes affect one entity more than the other. However, due to the proximity and ease of access to the Moon, it acts as the Rosetta Stone for predicting or modeling outcomes for the interactions between other SBEs and their external environments.

1.2. The Moon's Exotic Atmosphere

Starting with Galileo's telescopic observations of the Moon (Galilei, 1610) in the 17th Century, and through the beginning of the Apollo missions, there was a wrongly held belief that the Moon had no atmosphere. This misconception was due to no observable clouds or hazes around the Moon and the lack of refraction for stellar occultations, both of which could indicate the presence of an atmosphere. The Moon has an exotic, tenuous atmosphere, like that of a cometary coma (Stern, 1999). It was not until the Apollo program, that the presence of this tenuous atmosphere of the Moon was confirmed through direct in-situ observations. The Apollo 17 mission's Lunar Atmospheric Composition Experiment (LACE) instrument detected small amounts of atoms/molecules including helium (He), argon (Ar), possibly neon (Ne), ammonia (NH_3), methane (CH_4), and carbon dioxide (CO_2) (Dunbar, 2014).

In an SBE, atoms and molecules released from the surface travel in parabolic trajectories with a minuscule probability of colliding with each other, before escaping into space or returning to the lunar surface. The lunar SBE is so thin, that it is considered a good vacuum on Earth with a density ~100 times less than that at the International Space Station's altitude. The Earth also has an exosphere above ~ 500 km where atoms and molecules travel in parabolic arcs until they escape into space or return to lower altitudes in the atmosphere. The key difference for the Moon is the entire atmosphere is the exosphere.

The lunar exosphere is made up of neutral gases, plasma, and ejected dust particles that are generated by surface interactions with the near-space environment (Hiesinger and Jaumann, 2014). These constituents are of scientific interest but also important from an

engineering perspective, due to their effect on space exploration (both human and robotic) on the lunar surface (Hiesinger and Jaumann, 2014). From the analysis of lunar rocks brought back by the Apollo missions, compared to the Earth, the bulk Moon is significantly depleted in volatile elements, including water, and this has been interpreted to be a direct consequence of the violent impact origin of the Moon (Hiesinger and Jaumann, 2014); the origin of this volatile depletion is still not well understood (Righter, 2019). Known volatile constituents include but are not limited to: He, Ar , Na (sodium), K (potassium), and Rn (radon) that are captured from the solar wind, originate from the Moon by radioactive decay, space weathering by solar wind particles, or micrometeorite impacts (Stern, 1995; Hiesinger and Jaumann, 2014). The relevant species to this dissertation are sodium and potassium. While sodium and potassium are minor constituents of this exosphere, they have strong resonant scattering signals (Catherine et al., 2016), allowing them to be observed with ground-based telescopes. As such, a large portion of the lunar exospheric research conducted focuses on sodium and potassium, with more observations made of sodium since its intensity is several times brighter. This dissertation focuses on the lunar sodium exosphere with a complementary discussion on the lunar potassium exosphere.

Understanding the fragile environment that is the lunar exosphere, before future missions disturb its current state, is critical. Once missions, both manned and unmanned, return regularly to the Moon, the fragile lunar atmosphere will be contaminated by exhaust gases and disturbed dust. Understanding the chemical makeup of the Moon along with how atoms move once they are released from the surface has important implications for future explorations. For instance, understanding how some volatiles move once released from the regolith can have implications for understanding the transport of other volatiles, such as

water, which is important for future explorations. Constraining the abundance of volatiles in the lunar regolith also helps in understanding how exactly the Earth-Moon system was formed. While there is much to be discussed about various elements discovered on the Moon, here on I focus on the two alkali volatiles, sodium (Section 1.2.1.) and potassium (Section 1.2.2.).

1.2.1. Observational Evidence of the Moon's Sodium Exosphere

Following a hiatus after the Apollo program, sodium and potassium were sought after and discovered in the Moon's exosphere (Potter and Morgan, 1988; Tyler et al., 1988) – a move that was motivated by the discovery of these two species in Mercury's exosphere (Hunten et al., 1988). Sodium in the rarified lunar exosphere has a large spatial distribution about the surface – extending out further than a couple of lunar radii (Killen, 2019; Mendillo et al., 1991). A Field of View (FOV) offset technique by Mendillo et al. (1991) and a coronograph imaging by Mendillo and Flynn (1993) detected the extended sodium emission out to almost four lunar radii and up to 15-20 lunar radii on the nightside (Figures 1.1, 1.2).

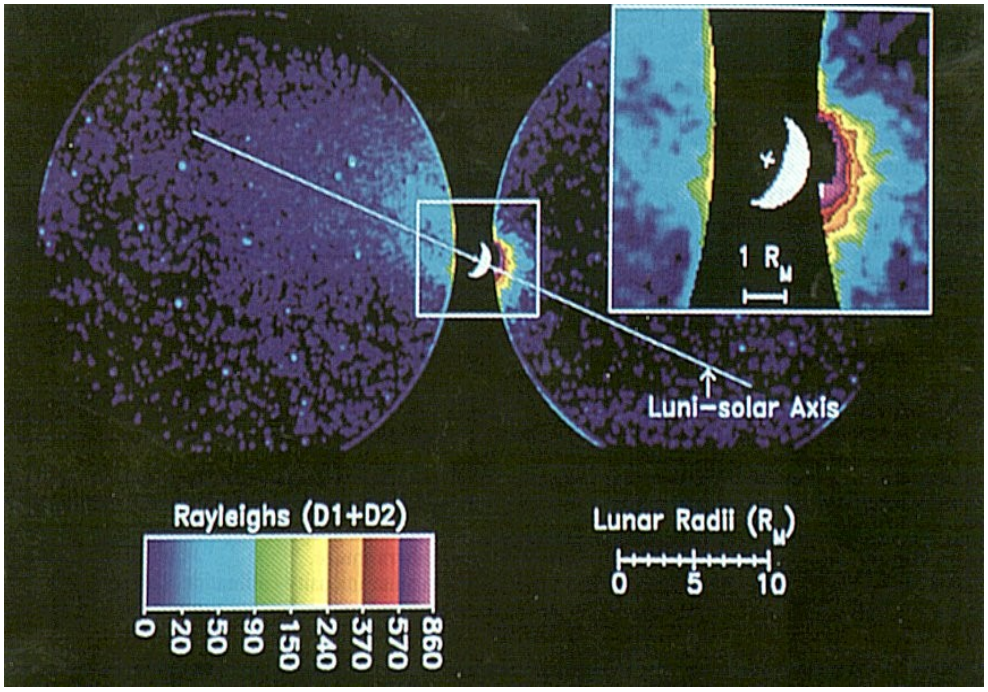

Figure 1.1: Image of the lunar sodium atmosphere five days after new Moon obtained from an FOV offset technique (Mendillo et al., 1991).

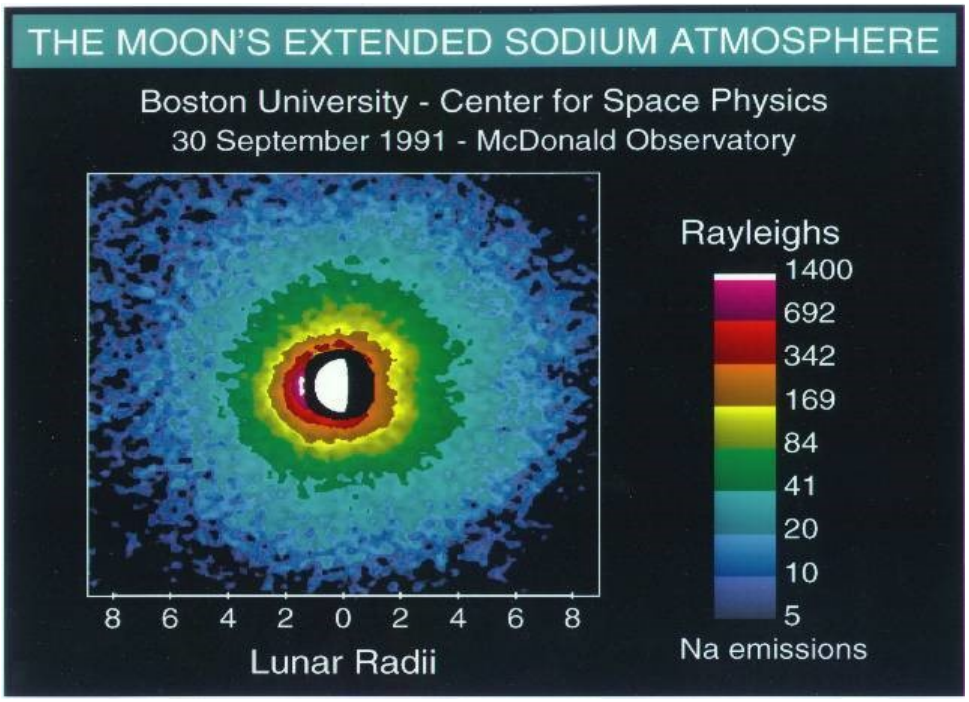

Figure 1.2: The lunar extended sodium atmosphere at third quarter obtained from a coronograph imaging method (Mendillo and Flynn 1993).

The lunar SBE is a result of a delicate balance between source, sink, and escape mechanisms. Source mechanisms that generate the lunar sodium exosphere are attributed to photon-stimulated desorption (PSD) (by direct photon energy transfer), charged particle sputtering (solar wind ions, transient ion events such as coronal mass ejections and plasma crossings in Earth's magnetosphere), impact vaporization (micrometeoroids: showers and sporadic sources), thermal desorption (evaporation of material from the regolith), and radioactive outgassing (Figure 1.3). Each of these processes has its energy spectrum and spatial distribution, making observations made along a single line of sight (LOS) inadequate in disentangling them (Killen et al., 2019). Note that while thermal desorption is mentioned here, it is not a major contributor to the lunar sodium and potassium exosphere – given that the bulk of our temperatures are representative of a higher energy process (Section 4.1). Additionally, radioactive decay also plays a role in generating the lunar exosphere but is more relevant for potassium as a decay product of thorium. Figure 1.3 shows the elements that are released through radiogenic outgassing. The source processes described here are also applicable to potassium (Section 1.2.2).

The main characteristics of the source processes are:

1) *PSD*: non-thermal and has a characteristic temperature of ~1200 K (Yakshinisky and Madey, 1999, 2004; Sarantos et al., 2010) with a cosine dependence on solar zenith angle (SZA). Threshold energy of ~4 eV is required for PSD to occur from SiO_2 silicates (Dukes and Johnson, 2017). For potassium, PSD has a characteristic temperature of ~ 800 K (Yakshinisky and Madey, 1999).
2) *Charged particle sputtering*: characterized by a hot, non-thermal velocity distribution and having a form of cosine dependence on the angle of the surface

element to the solar wind normal and a possible temperature dependence (Killen et al., 2019). Charged particle sputtering is not limited to sputtering by solar wind ions but also includes ions encountered during transit of the Earth's plasma sheet. This process is best described by a Sigmund-Thompson distribution (Sigmund, 1969) and can be approximated with a Maxwellian distribution with a characteristic temperature of ~ 10, 000 K (Poppe et al., 2013).

3) *Impact vaporization*: characterized by a temperature distribution of around 3000 – 5000 K (Sarantos et al., 2012; Dukes and Johnson, 2017; Kuruppuaratchi et al., 2018; Killen et al., 2019). The ejected vapor cloud contains three types of photoemission: blackbody radiation due to heat released on impact, molecular bands, and atomic line emission (Dukes and Johnson, 2017). The intensity of line emissions for atoms and molecules, including sodium, to the blackbody continuum of 3000 – 4000 K is largest right after impact, followed by a Boltzmann distribution for vapor temperatures of 4000 – 6000 K (Dukes and Johnson, 2017). The impactor temperature is correlated with the velocity component normal to the target surface (Sugita et al., (1998). The temperature is expected to be maximum at planetary ram direction and is dependent on the type of meteor source: sporadic or shower (Killen et al., 2019).
4) *Thermal Desorption*: characterized by a distribution reflecting the lunar surface temperature. The temperature of the lunar surface cycles between ~25 K (on Permanently Shadowed Regions (PSR), 100 K - 400 K on the lunar nighttime (Dukes and Johnson, 2017). For adsorbed alkali atoms such as sodium and

potassium, thermal desorption has a characteristic temperature that is less than 1000 K (Dukes and Johnson, 2017).

The morphology and composition of SBEs are not only affected by the source processes but also bear evidence of the fate of the returning atoms and molecules to the regolith (Johnson, 1990; Cassidy et al., 2008). Once released, gases in the lunar atmosphere can be pulled back to the regolith by gravity (sink), or escape through gravitational escape, get pushed away by solar radiation pressure, or become photoionized and lost to the solar wind (Yakshinskiy and Madey, 1999; Kuruppuaratchi et al., 2019) (Figure 1.4).

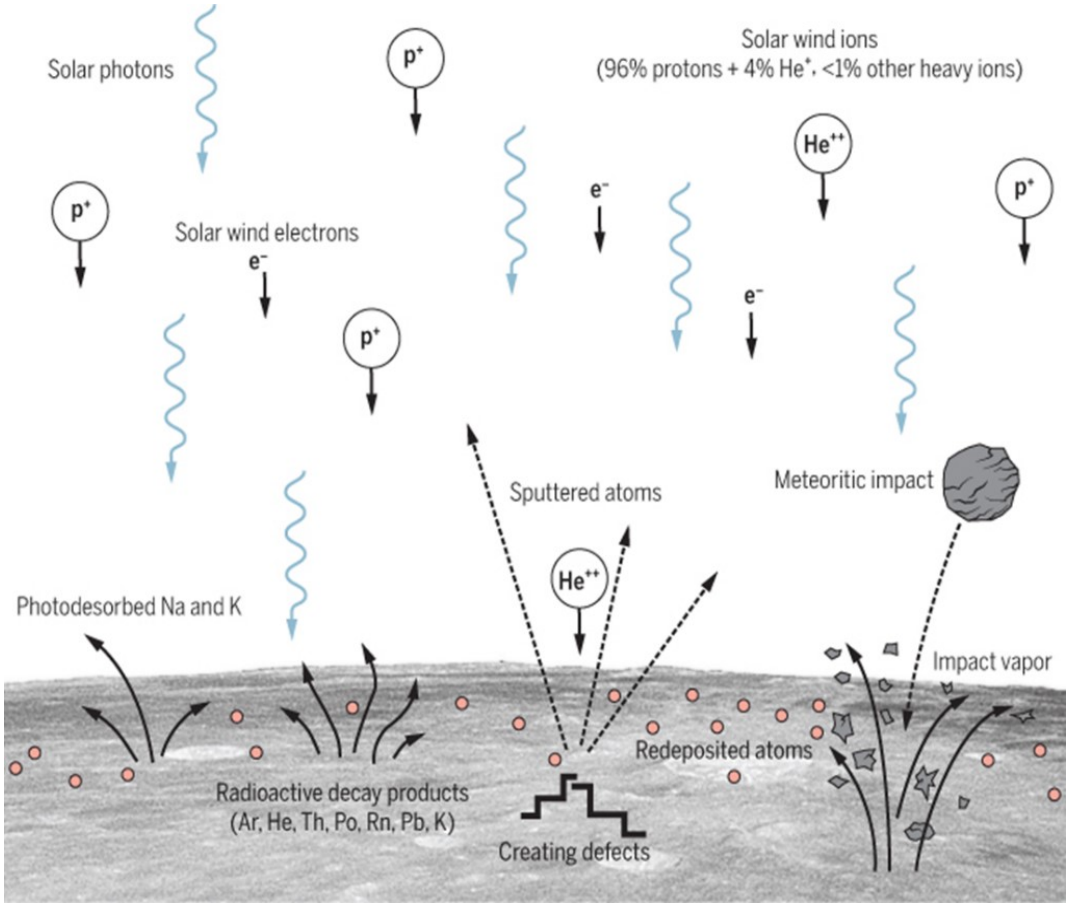

Figure 1.3: Schematic depicting major and minor source mechanisms (PSD, charged particle sputtering, impact vaporization) of the lunar SBE (Catherine et al., 2016).

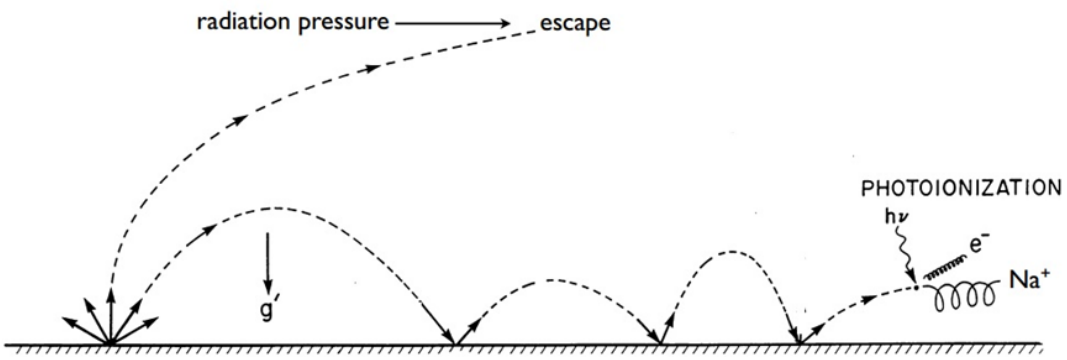

Figure 1.4: Schematic depicting the dynamics of transport in the lunar sodium exosphere. As adapted from Smyth and Marconi (1995) and reproduced in Stern (1999).

The exact recipe for the generation of the lunar SBE is yet to be determined, however, ground-based and spacecraft observations are being used to disentangle the relative contributions from these various source processes. One indicator of the source nature is exospheric altitude variations in intensity. Starting with early lunar exospheric studies, observed altitude distributions (scale heights) showed that the sodium exosphere had a hot (suprathermal) and cold (thermal) component (Potter and Morgan, 1988b, 1991; Sprague et al., 1992; Morgan and Shemansky, 1991; Ip, 1991; Stern, 1999). Potter and Morgan (1988b) obtained scale heights for sodium ranging from approximately 44 km to 510 km (191 K to 1736 K), indicative of a two-component exosphere. The hot component is presumed to be a population of recently released sodium atoms from impact vaporization, PSD, and/or charged particle sputtering; the cooler population is a result of thermal desorption and/or collisional thermalization of the primary (hot) population via interactions with the lunar surface (Ip, 1991; Morgan and Shemansky, 1991; Potter and Morgan, 1988b, 1991; Sprague et al., 1992; Stern, 1999).

A second indicator of the source nature is the dependence of the exospheric column density with the angle from the subsolar point. PSD and charged particle sputtering are expected to be the main source processes if their density varies as the cosine of the latitude since the fluxes of the solar photons and solar wind ions per unit lunar surface follows a similar law (Yokota et al., 2014). Imaging (Mendillo et al., 1993; Potter and Morgan, 1998) and spectroscopic (Sprague et al., 1992, 2012) observations indicate that the distribution of atmospheric sodium along the limb visible from Earth appears to peak at the subsolar point and that the variation in the emission changes more rapidly with SZA than a cosine function (i.e., than a pure photodesorption source). Mendillo et al. (1997) suggested that dayside source functions with cosine squared dependence with SZA best explained observations in sodium limb brightness. Potter and Morgan (1998) suggested that solar photons can stimulate desorption of sodium trapped below the surface and that the temperature dependence for sputtering of sodium atoms from the surface was best explained by a cosine cubed dependence on latitude (a function of SZA). On the contrary, Killen et al. (2019) reported line-of-sight intensities that do not follow any power of cosine model as a function of the lunar phase or latitude with corresponding scale heights in the range of 500 to 1500 km. Furthermore, Killen et al. (2019) report North-South asymmetries in their intensity profiles, which is consistent with the findings of Potter and Morgan (1991). Sprague et al. (1992) suggested that thermal desorption dominates near the subsolar point and PSD dominates at high SZAs. Note that thermal desorption of alkalis is only possible close to the subsolar point since it is temperature-dependent and is also expected to be less efficient on the Moon compared to Mercury (Madey et al., 1998).

Previous studies (e.g., Sprague et al., 1992; Madey et al., 1998; Yakshinsky et al., 1999; Mendillo et al., 1999; Sarantos et al., 2010; Tenishev et al., 2013; Kuruppuaratchi et al., 2018) argued that PSD is the major source mechanism for the lunar sodium exosphere, however, its efficiency varies temporally and spatially due to the variability of the ion influx to the lunar surface (Sarantos et al*.,* 2010). As the Moon moves from a pure solar wind environment and spends approximately five to six days per month inside the Earth's magnetosphere, it comes into contact with various plasma environments (e.g., lobes, plasma sheet) – each with their population of ions of variable energies and fluxes (Mendillo et al.,1997; Sarantos et al., 2008, 2010). Potter and Morgan (1994) and Potter et al. (2000) observations before, during, and after lunar passage through the Earth's magnetotail indicated that impacts by the solar wind may be a significant source of sodium in the lunar atmosphere since the sodium density before magnetotail passage was found to be higher than the density post magnetotail passage. On the contrary, Mendillo et al. (1997) suggested that while solar wind sources are likely candidates for source processes, it is unlikely that solar wind sputtering is a dominant source mechanism since they witnessed an extended lunar atmosphere during times when the Moon was shielded from the solar wind (i.e., full Moon period). Wilson et al. (2006) demonstrated that the difference in sodium brightness observed in five separate eclipses was correlated to the augmentation of the lunar sodium exosphere through ion sputtering when the Moon moved from residing in the cooler plasma in the lobes to the hotter denser plasma in the plasma sheet. Sarantos et al. (2008) showed that in the magnetosheath and solar wind, solar wind ions enhance PSD efficiency by bringing atoms to the surface (ion enhanced diffusion) to release in a process known as ion-enhanced PSD. In the magnetosphere, however, the Moon is out of contact

with direct solar wind particles (Potter and Morgan, 1994) and thus roles of impact vaporization and plasma sheet ions are emphasized (Sarantos et al., 2008; 2010).

In addition to ion-enhanced diffusion by solar wind particles, Potter et al. (2000) and Sarantos et al. (2010) suggested the energetic particles found in the plasma sheet also allows for ion-enhanced PSD. Modeling by Sarantos et al. (2010) assumes that the PSD efficiency is variable over a month (e.g., higher when the Moon is exposed to the solar wind) to explain the rate of brightening of the lunar exosphere from full to quarter Moon as seen by an Earth observer. Similarly, Tenishev et al. (2013) concluded that PSD is the dominating source process that exceeds the rate of meteoritic impact vaporization by a factor of about eight to nine. Sprague et al. (2012) used a summary of observations found in Sarantos et al. (2010) to find that the lunar sodium was statistically brighter when exiting the full Moon phase than entering it. Likewise, the continuous sequence of observations of Potter et al. (2000) was interpreted to mean that Earth's plasma sheet ions effectively enrich the sodium reservoir. Additionally, Kuruppuaratchi et al. (2018) saw relative intensities that increased from full Moon toward quarter phases with large variations when the Moon was inside the magnetosphere region. This, along with previously mentioned studies (i.e., Potter and Morgan 2000; Wilson et al., 2006; Sarantos et al., 2008, 2010), suggests that the type of plasma environment the Moon interacts with (solar wind, magnetotail lobes, magnetosheath, and plasma sheet) influences the lunar sodium exosphere.

Alongside the effects of PSD by a variable ion influx rate, other driving mechanisms contribute to the lunar sodium exosphere as well. The mechanisms include impacts by meteor sources and spatial non-uniformity of the exosphere due to the compositional variation of sodium on the surface. The effect of impact vaporization was

investigated by previous ground-based studies that observed an increase in exospheric sodium abundances through the Leonids (Smith et al., 1999) and the Taurids (Verani et al., 1998).

Two robotic missions have made space-based observations of the lunar sodium exosphere over multiple lunations. The first of these observations were made by the Japanese Kaguya, formerly known as SELonographic and ENgineering Explorer (SELENE), spacecraft's Telescope for Visible Light (TVIS) instrument from December 2008 to June 2009 (Kagitani et al., 2010). Observations by Kaguya indicated that the ionized sodium (Na^+) and potassium (K^+) atmosphere showed a dawn-dusk asymmetry (Yokota el., 2014). The second of these observations were made by the Lunar Atmosphere and Dust Environment Explorer (LADEE) Ultraviolet and Visible Spectrometer (UVS) from November 2013 to April 2014. Observations by LADEE UVS (Colaprete et al., 2016; Szalay et al., 2016) showed that micrometeoroid bombardment is not a dominant source mechanism of the exosphere but is sporadic. For example, while there was a strong enhancement in the lunar exosphere following the Geminids shower (Colaprete et al., 2016), no strong correlation was noted between sporadic meteoritic influx measurements made by the LADEE Lunar Dust Experiment and neutral exospheric density as measured by LADEE Ultraviolet-Visible Spectrometer (UVS) (Szalay et al., 2016).

As meteorites hit the lunar surface, the material becomes molten and species that are ejected have a similar composition to the regolith mineralogy. Stubbs et al. (2014) suggested that the response of the lunar environment to meteoroid streams could be relatively localized. For example, potassium was found to be enhanced over KREEP (potassium rare earth elements and phosphorus) regions, indicating a dependence on lunar

surface composition (Colaprete et al., 2016; Rosborough et al., 2019). Sodium, on the other hand, is more evenly distributed on the lunar surface and so its surface-exosphere relationship is less constrained. Nevertheless, LADEE UVS results suggested a possible correlation between sodium and surface albedo (highlands vs. mare) (Colaprete et al., 2016), which could be a result of large sodium enhancements on the nearside surface as revealed by the Chandrayaan-1 X-ray Spectrometer (Athiray et al., 2014). LADEE and Kaguya results both confirmed the presence of an annual cycle for the sodium exosphere and is most likely due to the cumulative response of sodium to meteoroid streams (Colaprete et al., 2016). Additionally, some of the daily trends seen by Kaguya could be explained if there were sodium surface enhancements around ± 90^{o} Selenographic longitudes, which could be interpreted as different PSD rates between the near-side and far-side regolith (Kagitani et al., 2010; Colaprete et al., 2015). To add to this complexity, micrometeoroids can also add some fraction of their volatiles to the site of impact upon vaporization (Hurley et al., 2009). There are Na-enhanced and Na-rich meteoroids with sodium being part of the "glue" that holds together grains that make-up meteoroids or are part of the composition of the grains (Matlovic et al., 2020), respectively. The same meteoroids help make up the terrestrial sodium layer in Earth's atmosphere. The fraction of the lunar environment that is made-up from regolith released volatiles or micrometeoroid introduced volatiles is not known.

1.2.2. Observational Evidence of the Moon's Potassium Exosphere

Since potassium is a complementary study to the lunar sodium exosphere in this dissertation, a brief history of its observations is included here. Out of these two alkali species, potassium emission is harder to observe as it is several times fainter than sodium

(Potter and Morgan, 1988a). Additionally, potassium is a heavier element, and its scale height (~90 km) is lower than that of sodium (~120 km) (Potter and Morgan, 1988a), thus potassium is only observed closer to the lunar surface. Recall sodium can be seen many lunar radii from the lunar limb, especially on the lunar nightside, indicating that lunar sodium has a tail – an effect of solar radiation pressure on its large scattering cross-Section. Depending on the radial component of the heliocentric velocity, neutral sodium atoms can be accelerated in the anti-solar direction by solar radiation pressure, allowing some atoms to escape the lunar gravity and populate the sodium tail (Wilson et al., 2003; Mierkiewicz et al., 2006; Line et al., 2012; Tenishev et al., 2013). Conversely, potassium has a smaller scattering cross-Section than sodium and is heavier than sodium, leading it to be less affected by solar radiation pressure and thus having no tail.

As discussed earlier for sodium, the D2 fine structure emission for potassium (7664.8991 Å) is also brighter than the potassium D1 emission. However, due to the presence of a strong terrestrial O_2 emission line that drowns out the potassium D2 emission, the D1 emission (7698.9646 Å) is observed (Bleeker and Huber, 2012). In addition to the original discovery of lunar potassium two other ground-based studies have obtained potassium measurements (Kozlowski et al., 1990; Sprague et al., 1992). Kozlowski et al. (1990) observed temperatures of 396 and 2500 K (corresponding to scale heights of 52 and 329 km) on one night, indicating a two-component exosphere. Sprague et al. (1992) made observations of two nights and reported a scale height ranging from 85 to 185 km, once again indicating the presence of a hotter and colder population.

As with sodium, the LADEE mission observed potassium over multiple lunations. Colaprete et al. (2016) observed a systematic factor of two difference in potassium

intensities over a lunation, a trend that was more regular over time than intensity variation in sodium. Additionally, potassium was found to respond to meteor showers much more than sodium, with the response to the Geminids meteor shower being most notable. Whether this may be indicative of the composition of micrometeoroids itself is unclear. The potassium exosphere was also found to be closely related to the surface enrichment of potassium found in KREEP soils shown in Figure 1.5. Potassium is produced through radioactive decay of Thorium (Th) in these regions. Colaprete at al. (2016) also reported that any variation in solar wind was dwarfed by this strong variation in surface potassium.

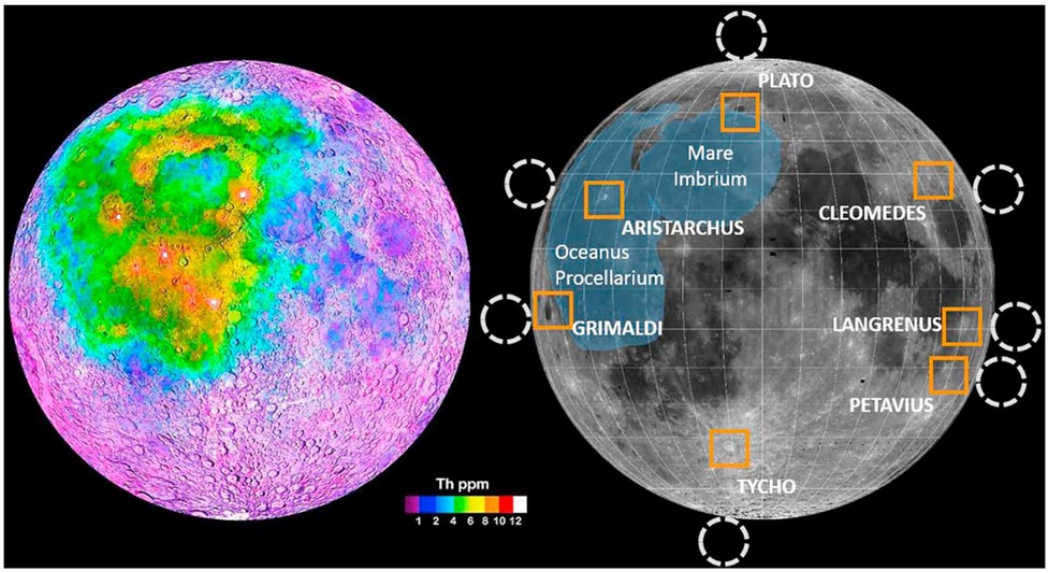

Figure 1.5: Overview of KREEP regions and the location of our FOV (white dotted circles) as shown in Rosborough et al. (2019). The colored map on the left was made using Lunar Prospector gamma-ray data (Prettyman et al., 2006) showing thorium parts per million and the peak locations of potassium according to Colaprete et al. (2016) is shown in by the shaded blue region on the right image.

1.2.3. Temperature of the Exosphere

The effective temperature of the lunar sodium exosphere, which is only an approximation to a Maxwellian temperature, can be attributed to a collisionless

combination of source processes discussed earlier in Section 1.2.1. Although intensity distributions of the lunar sodium exosphere have been measured on several occasions, exospheric temperatures have mainly been inferred from model fits to the observed altitude distributions (e.g., Sprague et al., 1992, 2012; Potter et al., 2000; Kagitani et al., 2010, Killen et al., 2019). A different method of inferring exospheric temperatures is the direct linewidth observations of Mierkiewicz et al. (2014), Kuruppuaratchi et al. (2018), and Rosborough et al. (2019). Linewidth measurements differ from observed altitude (scale height) distributions by offering a direct probe of the bulk radial kinematics (velocities) of the observed exospheric column at specific altitudes. The effective temperature (derived from linewidths) of the exosphere and its altitude variation can also be used as an indicator of source processes as it provides a unique and different method of investigating the source processes. A more detailed discussion of the difference in scale height derived temperatures and linewidth derived temperatures for an exosphere can be found in Section 4.1.3.

1.3. Scientific Relevance and Significance of Study

From previous ground-based observations (scale height and linewidth derived) and space-based observations of the lunar exosphere, the main contributors to the lunar exosphere are known – PSD, charged particle sputtering, impact vaporizations, with PSD being the major contributor. In addition to the relative importance of source processes, other processes such as loss rates through sticking and residence times of atoms of a species, remain debated. Each source process for the lunar exosphere will eject material from the surface that is characterized by a certain temperature, spatial distribution, and temporal variability (Killen et al., 2019).

To disentangle the various source and loss processes and determine how critical each of these processes are, it is important to monitor the lunar exosphere at various altitudes including the extended corona, spanning multiple lunations, and good latitudinal coverage. Monitoring the health of the lunar exosphere in such a way will help determine the importance of transient or episodic events, including meteoroids, varying solar wind conditions, plasma sheet crossings, and transient ion events such as CMEs (Killen et al., 2019). Such a task is addressed by a long-baseline dataset with both good latitudinal and temporal coverage, which is a highlight of the analysis presented in this work.

The focus of this dissertation is the investigation of the lunar exosphere, using direct velocity-resolved measurements of sodium D2 (5889.9509 Å) and a smaller companion investigation of potassium D1 (7698.9646 Å) velocity-resolved measurements taken over multiple years– providing a unique and complementary way of investigating the morphology and dynamics of the lunar SBE.*

The total amount of sodium data collected spans over nine years, shown in Figure 1.6, represents the most comprehensive coverage of lunar exospheric observations taken to-date. These observations were made at the National Solar Observatory (NSO) McMath-Pierce (MMP) Solar Telescope by using high-resolution Fabry-Perot spectroscopy. While our observing campaign in 2009 began with sodium observations only, starting 2014 we observed both sodium and potassium. Our potassium dataset is also the most comprehensive dataset taken to date, only second to our sodium dataset. Figure 1.7 shows the amount of potassium coverage we have.

* wavelengths are measured in air

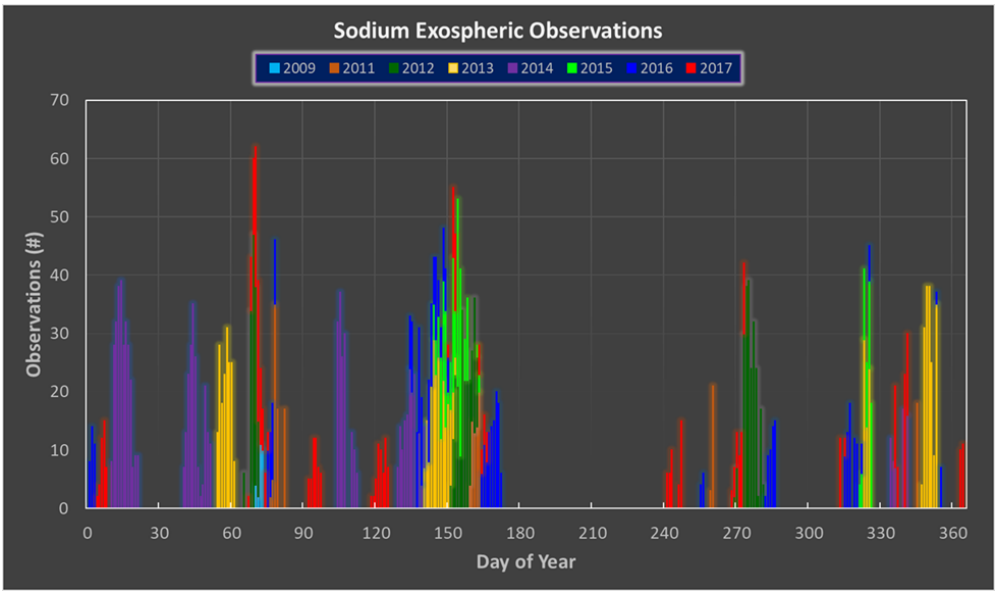

Figure 1.6: Number of sodium observations per night for 2009 – 2017. The gap in data seen from 170 to 240 Day of Year is due to the monsoon season in Southern Arizona.

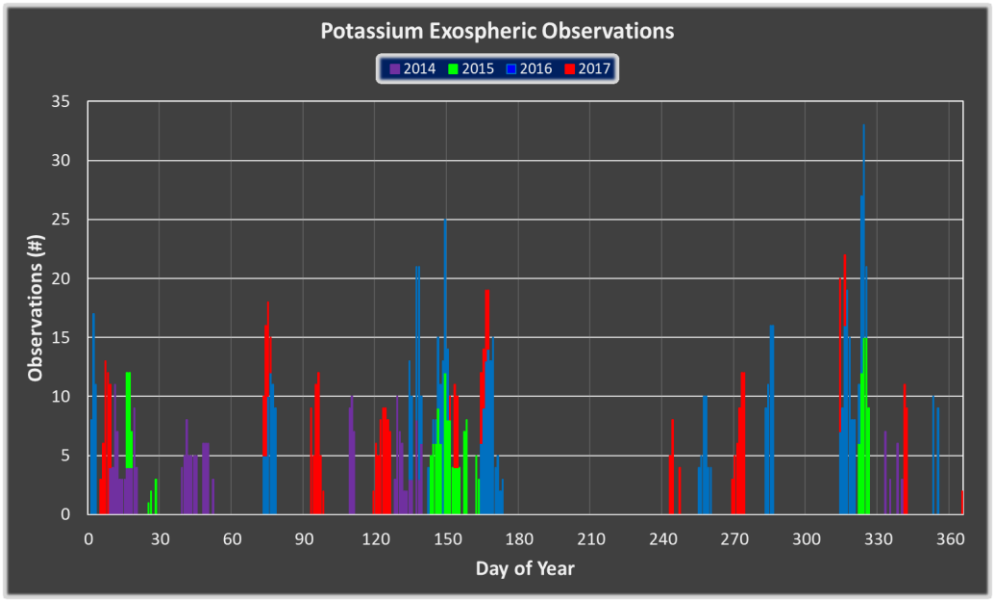

Figure 1.7: Total number of potassium observations by day of the year 2014 -2017.

This unique long-baseline dataset, along with models, will help fill in gaps in the current understanding of the lunar exosphere by determining its temporal and spatial variability. This work is a continuation of the direct lunar sodium emission line profile observation analysis done by Mierkiewicz et al. (2014), Kuruppuaratchi et al. (2018), and Rosborough et al. (2019). Note that data presented in the proceeding Chapters range from 2013 – 2017, but our full dataset includes data from 2011 and 2012 that are not shown in this dissertation as they need be reduced. In Part II of this dissertation, I discuss the instrumentation and observational strategy used to collect lunar sodium and potassium observations, followed by the data processing and analysis strategy. In Part III, I discuss our earlier published sodium and potassium results and compare them to extended datasets in the same analysis style. In Part IV, I discuss the new analysis (by plasma region, latitude, and altitude) of sodium and potassium data together with their implications.

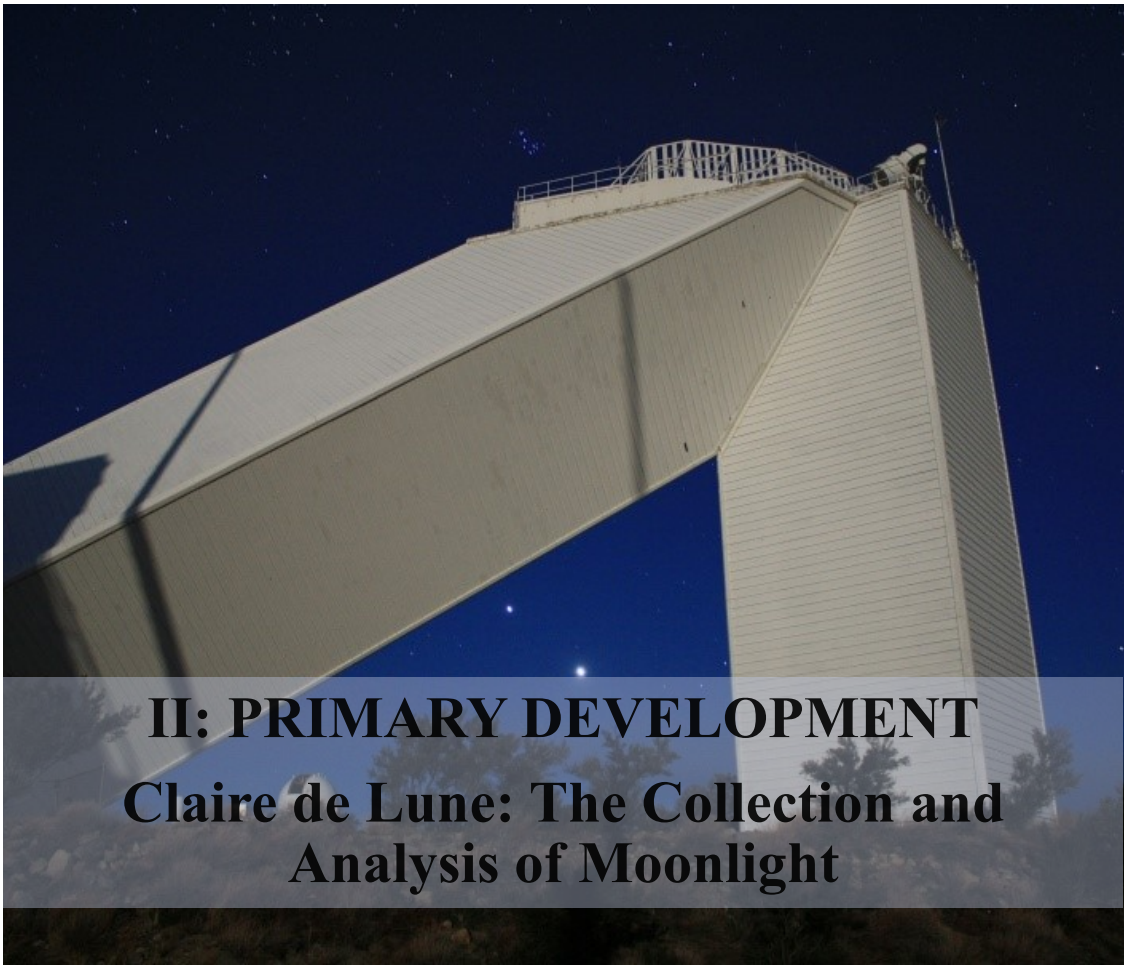

II: PRIMARY DEVELOPMENT

Claire de Lune: The Collection and Analysis of Moonlight

Photo Credit: APOD

CHAPTER 2. TELESCOPE, INSTRUMENTATION, AND OBSERVATIONS

2.1. Telescope Facility

In this Chapter, I describe the telescope facility used for the lunar program, the Fabry-Perot instrument, and our data collection strategy. Additional details are found in Kuruppuaratchi (2015). All observations were made from the National Solar Observatory (NSO) McMath-Pierce Solar Telescope (MMP), Kitt Peak, Arizona. Our observations were made with the Main telescope, one of the three telescopes the NSO MMP facility houses, by feeding a Fabry-Perot Spectrometer (FPS) located at the telescope's North Port. Figures 2.1 shows the McMath-Pierce Solar Telescope and the path of the incident and reflected light beam.

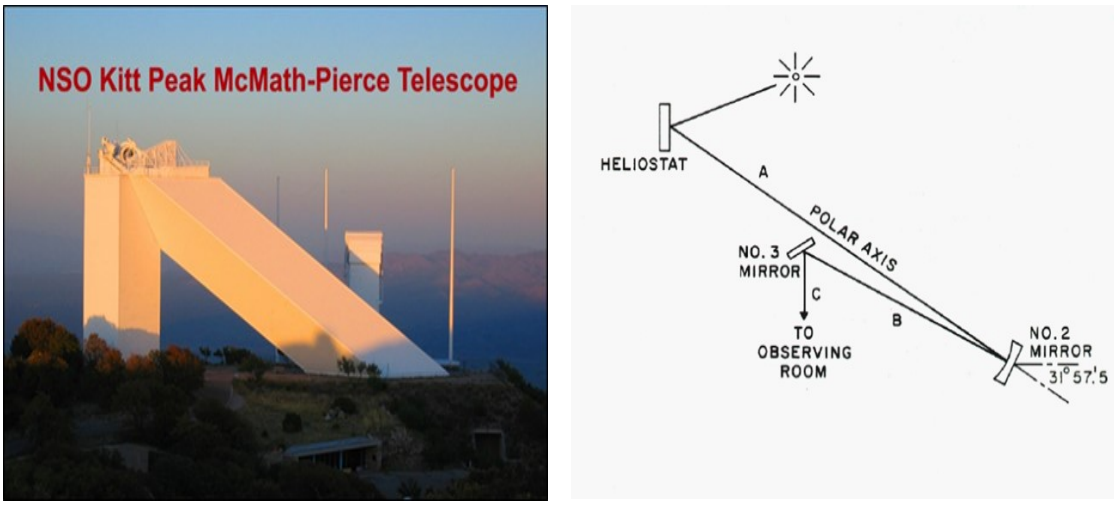

Figure 2.1 (left): MMP structure with the 2 m heliostat situated on top of the solar tower at an elevation of 2096 m; **(right)**: The path of the incident and reflected light where the 1.6 m #2 mirror produces an f/54 beam (NOAO/AURA/NSF).

2.2 High-Resolution Fabry-Perot Spectroscopy of Lunar Exospheric Emissions

To make high spectral resolution observations of the diffuse lunar exospheric emissions requires an instrument with high resolution, high signal-to-noise capabilities, efficient scattered light rejection, and a well-defined instrumental profile (IP) – all possible with the use of the Fabry-Perot spectrometer (Roesler, 1974; Hernandez, 1986; Tufte, 1997).

2.2.1. UW/GSFC FPS: Optical Layout

The UW/GSFC dual etalon FPS was built at the University of Wisconsin (UW), Madison to observe the neutral oxygen and carbon emissions of comet Hale-Bopp from the MMP North Port (Oliversen et al., 2002). The FPS consists of two etalons arranged in series, a combination that results in high spectral purity and contrast by extending the free spectral range (FSR) and suppressing the broad Lorentzian wings of a single etalons transmission function (Roesler, 1974). The second etalon sharpens the common transmission peak of the two-etalon system (Roesler, 1974). All these aspects of a dual etalon FPS help meet the challenge of accounting for hyperfine structures (~1 km/s separation) associated with deconvolving the observed line profiles (Section 3.2). Similarly, the FPS is well suited for measuring thermal widths (~1 - 2 km/s), non-thermal features (~1 - 3 km/s) (Section 4.1), and terrestrial airglow emissions (e.g. sodium airglow emissions) (Mierkiewicz et al., 2014).

The FPS is stationed below the Main #3 mirror at the North Port with a white foam core board at the top of the instrument where the telescope focal plane lies. A guide camera is placed in the tunnel, 3.2 m above the instrument, looking down at the focal plane where the Moon is imaged. Light passes through a 3 arcmin entrance aperture, although this field

of view (FOV) was decreased to 2 arcmin in diameter (occasionally 1 arcmin) in observing runs later than 2014. The data presented in this dissertation for 2 and 3 arcmin FOV will not contain a large percentage of the cold component sodium population. However, the FOV reduction from 3 arcmin to 2 arcmin was done to compare sodium observations with potassium observations, with the latter having a smaller scale height and thus more suited to be observed from a FOV closer to the lunar surface. While the focus of this dissertation is on sodium, later in Chapters 5 and 6, potassium data and its comparison to sodium will be introduced and discussed as a companion study.

The FPS optical layout and ray-tracing diagram are shown in Figure 2.2. The entrance lens (L1) images the #2 mirror (and the #1 mirror) at the iris above the field lens (L2). Together, L2 and the Fabry-Perot collimating lens (L3) image the sky between the Fabry-Perot etalons. The iris on top of L2 is a pupil stop that is used in rejecting stray light and assists the alignment of the telescope and the instrument. The FPS collimating lens (L3) directs parallel light through a narrowband filter and the FP chambers. The camera lens (L4) focuses the parallel beam onto the CCD (charged coupled device) detector. The lens specifications are found in Table 2.1. It is important to note that the sky is not imaged onto the detector; instead, the image of the #2 mirror is conjugate with the FP ring pattern at the detector. Figure 2.3 shows a picture of the entire FPS with the front covers removed and a close-up picture of the FP chambers.

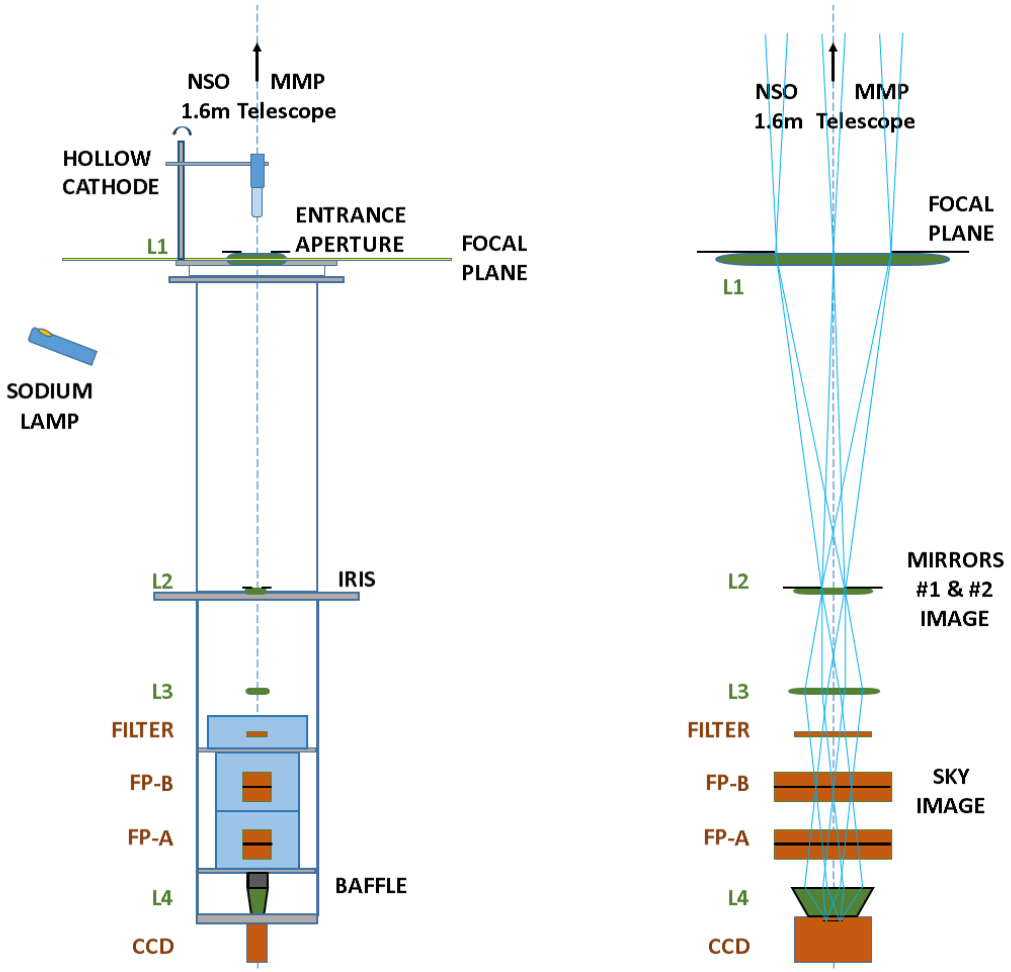

Figure 2.2: (left) Schematic of the FPS showing individual components and the optical axis. (right) Ray tracing diagram with the horizontal axis expanded by a factor of 4.

Table 2.1: *FPS lens parameters*

Lens	Focal Length (mm)	Diameter (mm)
L1 (entrance lens)	762	152.4
L2 (field lens)	750	58
L3 (FP collimating lens)	308	59
L4 (camera lens/ ring imaging lens)	200	50

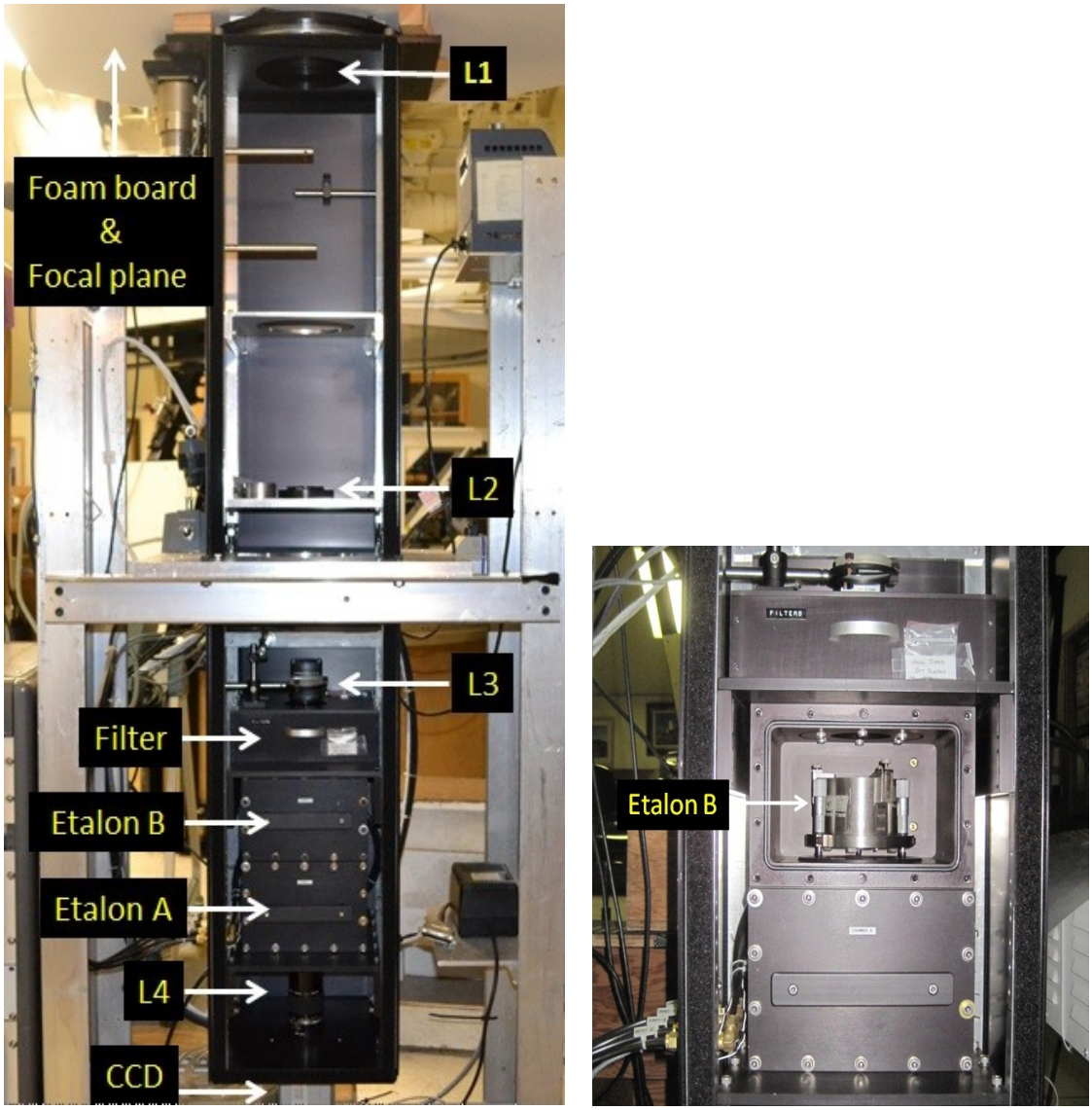

Figure 2.3: The UW/GSFC 50 mm dual etalon FPS situated at the MMP North Port (left). The FPS etalon is shown with the front covers taken off (right).

2.2.2. UW/GSFC dual etalon Fabry-Perot: Working Description

The FPS was modified to observe the lunar sodium and potassium exosphere by changing etalon spacing and coupling optics. The Fabry-Perot etalon specifications for both sodium and potassium are listed in Table 2.2. The FPS operates in the annular summing mode which allows for the entire 0.08 nm (Na) and 0.1 nm (K) spectral range of

interest to be simultaneously imaged onto a CCD camera (Coakley et al., 1996). Table 2.3 summarizes the CCD specifications.

The FP dual etalon spectrometer consists of two etalons made from fused silica with highly reflective (91 ± 1 % near Balmer α 6563 Å), broadband (~4800 – 9500 Å) multi-layer dielectric coatings on their interior faces (Mierkiewicz et al., 2014). The higher resolution etalon is A while the lower resolution etalon is B. A narrowband blocking, 2-cavity filter is used to isolate the sodium D2 and potassium D1 emission lines and minimize the number of adjacent orders being transmitted to decrease the continuum source contributions.

It is important to note, unwanted light will still appear in each FPS image in the form of ghosts, reflected ring features, along with parasitic and stray light. Ghosts are the suppressed orders getting through and appearing in an image. The orders passed are etalon dependent (FSR is inversely proportional to the etalon spacing). Table 2.4 shows the number of orders encompassed by the sodium and potassium narrowband filters for the high-resolution etalon A. The high-resolution etalon transmits more orders than the low-resolution etalon by the ratio of the etalon spacing, 4/1.76. In addition to ghosts, sources of unwanted light arise due to reflections between multiple surfaces within the FP such as reflections off the back part of the etalons, reflection between the etalons, reflections off the narrowband filter surface, etc. These unwanted light sources are symmetric about the optical axis and can be mitigated by making the outside surfaces (uncoated) of the etalons to be slightly wedged to move the unwanted light away from the optical axis to make off-axis reflections.

Table 2.2: *Table of parameters for the 50 mm dual etalon Fabry-Perot Spectrometer.*

FPS parameter		Na	K
Wavelength (Å)		5889.9506 Å	7698.9646 Å
Resolving Power/ Resolution		180,000 (1.7 km/s)	180,000 (1.7 km/s)
Wavelength Coverage (Å)		0.8	1.0
d (cm)	Etalon A Etalon B	0.4 0.176	0.4 0.176
Wavenumber FSR (cm^{-1})	Etalon A Etalon B	1.25 2.84	1.25 2.84
Wavelength FSR (Å)	Etalon A Etalon B	0.43 0.98	0.74 1.68
Field of View (FOV)		2 and 3 arcmin *	2 and 3 arcmin *
Spectral Bin Size		0.3097 km/s/bin	0.3097 km/s/bin

Table 2.3: *Table of parameters for CCD detector*

CCD Parameter	Specification
Detector	Andor 912BV
Array size	512 x 512
Pixel Size	24 μm
Shift Speed	44.975 μs
Read Rate	50 kHz
Temperature (Camera)	-80° C (Water-cooled), -70° C (air-cooled)
File Format	FITS unsigned 16-bit image

** 3 arcmin and 2 arcmin FOV, at a mean lunar distance of 384,400 km, is approximately 336 km and 224 km, respectively (variable by ± 7%).*

Table 2.4: *Table of parameters for narrowband filters*

Filter Name	Center Wavelength (Å)	Bandpass FWHM (Å)	Orders passed (Etalon A)
Na D2 (ANDV11321)	5890	4	9
K D1 (ANDV13173)	7699	5.5	7

2.3. Focus, Collimation, and Pressure Tuning

Since this is a solar telescope, the solar observer uses the #3 mirror over a different port and different instrument during the day, at night we move it back to the North port. On a typical observing run, observers first adjust the focus of the telescope by moving the #2 and #3 mirrors about 5 m up the tunnel followed by adjusting the tip/tilt (collimation) of the #2 and #3 mirrors to align the telescope axis with the FP optical axis. The focus is adjusted on the Sun, using sunspots, or on the surface features of the Moon.

Once focus and collimations are done, it is time to pressure tune the etalons. Pressure tuning correctly aligns the transmission peaks of the two etalons at a specific wavelength. The etalons are housed in individual chambers, filled with dry nitrogen. By adjusting the pressure in the FP chamber, the wavelength transmitted by the etalon at a particular angle can be altered. This procedure is called tuning. Each FP etalon is 'tuned' using standard emission line calibration sources listed in Table 2.5. For a given wavelength, etalon A is set at a pressure that determines the correct ring radius (angle), i.e., we place the wavelength of interest in the middle of the spectral window. The pressure in the chamber with etalon B is adjusted to match the radius (angle) of etalon A. The pressure difference between the chambers for etalon A and etalon B is actively maintained by the

pressure controller with a -0 +2 torr dead-band. The potassium observations were made starting in 2014 after the correct CCD camera lens (wavelength-dependent since K D1 is outside the visual specification of the lens) focus for potassium observations was determined.

Table 2.5: *Table of sodium and potassium calibration lamps with their respective wavelengths.*

Calibration Source Lines	Wavelength (Å)
Na D2	5889.9509
Th I (Na)	5891.4510
K D1	7698.9646
Th I (K)	7647.3800

2.3.1. Wavelength Calibration

The calibration process is described in terms of sodium with brief references to potassium. Note that apart from the types of calibration lamps used, the process of wavelength calibration itself follows the same procedure for both sodium and potassium. Sodium wavelength calibration is determined using the sodium "Gates lamp" and Th I hollow cathode lamp. Both these lamps are shown in Figure 2.4 situated at the focal plane of our instrument. A ring image of the sodium calibration lamp, which defines the rest wavelength of sodium, is shown in Figure 2.5. As seen in Figure 2.5, the sodium lamp produces what looks like two bright rings - this is not to be confused with the hyperfine doublet seen in the lunar sodium emission. The two bright rings belong to the same D2 emission line but with a self-absorption feature (dark ring in between the bright rings). The self-absorption feature is a result of the sodium atoms in the center of the lamp being hotter than their surrounding atoms. The hotter atoms in the center are absorbed and remitted by

surrounding cooler atoms, preventing some of the light from the center atoms from ever reaching the edge of the tube – resulting in the center of the emission ring to appear darker. Once the sodium calibration spectrum is fit, the self-reversal centroid position combined with the shift due to Earth-Moon Doppler motion is used to calculate the velocity of sodium atoms in the lunar reference frame. A discussion based on the velocity of sodium atoms in the lunar frame of reference can be found in Chapter 4.

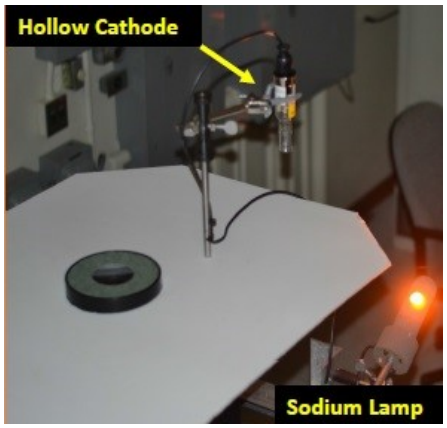

Figure 2.4: Calibration setup showing white foam board at the focal plane. The sodium "Gates" lamp (orange lamp at the bottom) reflects light off a card covering the ceiling port for wavelength calibration. The hollow cathode (HC) lamp is placed over the aperture, covered with a diffuser, for instrumental profile and stability measurements. Note that in this image, the HC lamp is off to the side of the instrument aperture, and when in use, we need to swing the HC lamp so that it is situated right a few inches above the entrance aperture.

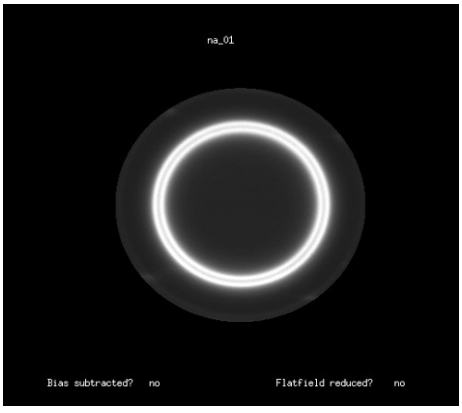

Figure 2.5: A raw FPS ring image of the sodium calibration lamp. The dark ring is the self-absorption feature. Filename: na_01.fits; Integration time: 10 seconds; Date: February 19, 2014. Time: 4:03 UT.

2.4. Clair de Lune: Observing the Moon

Using the telescope and instrument described in the preceding Sections, we collect the light of the Moon or "Clair de Lune" using the observational strategy described in this Section. To adequately monitor the health of the lunar exosphere, observations need to have good spatial and temporal coverage – a strength found in this extensive dataset which includes measurements made over a multitude of latitudes and radial distances away from the limb.

While our observational campaign initially contained more data going radially outwards from select locations off the limb of the Moon, this was later adjusted to include a multitude of latitudes. Lunar sodium observations were made from 2009 – 2017. The observing runs, from which the data presented in this thesis are taken, are summarized in Appendix A.

2.4.1. Moonlighting at the MMP: Observational Setup

On a typical observing night, we first check and adjust the telescope focus and collimation, then do the appropriate FPS tuning and wavelength calibrations. We locate the Moon in the sky by either slewing the main telescope to the Moon manually or using the telescope preset command. As simple as this sounds, it is sometimes surprisingly hard to find the Moon using the MMP as its pointing accuracy is about ½ degree. As a result, we sometimes had to make the final acquisition by looking up the tunnel along the telescope axis and move the Moon to the North port. Figure 2.6 shows the image of the Moon as it is projected onto the white foam board at the instrument focal plane.

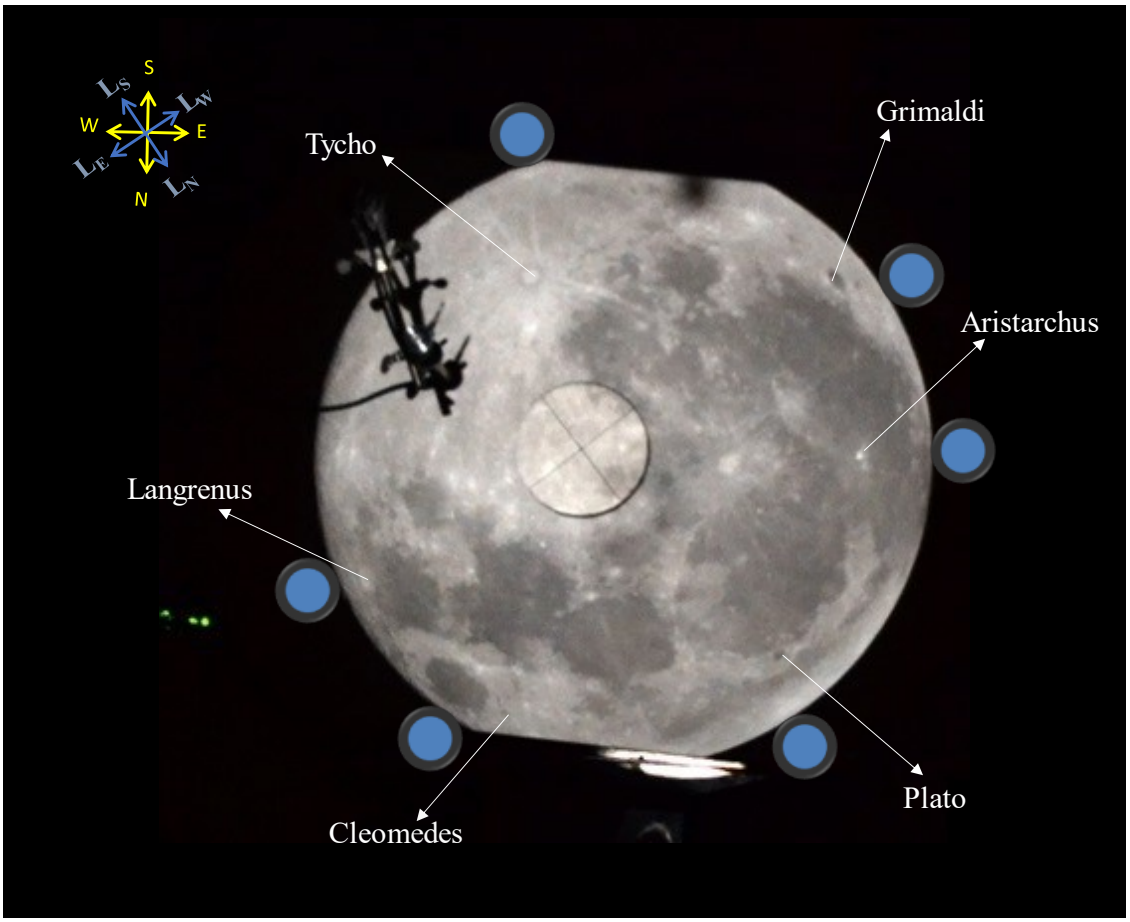

Figure 2.6: An image of the Moon as seen on our instrument focal plane (white foam board). Most major craters are marked although we have made observations off the limb of craters not shown here. The approximate location of our 3 arcmin FOV is shown adjacent to the craters (blue dot is the 2 arcmin FOV). In this setup, the calibration lamp clamp is seen on the upper left corner. This lamp is pushed out of the way when taking images. The small black dot on the top of the Moon is the shadow of the guide camera. The Moon appears flat on the top and bottom because the image of the Moon is off the white foam core. In the N-S dimension, the full Moon can be up to 34 inches in diameter, while the foam core is 30" x 40" inches. Our FP entrance aperture is underneath the crosshairs cover.

An image of the Moon and the approximate size of our 2 arcmin FOV (blue circle) for some of the various locations off the limb are shown in Figure 2.6. The crater locations are marked but note that we use the crater as a reference and move to the limb in a cardinal

direction from the crater, i.e., for an observation off the limb of Aristarchus we call it FOV at limb and record origin as Aristarchus. Observations are made off the limb from the craters shown in Figure 2.6 with a 3 arcmin FOV, which was reduced to a 2 arcmin FOV after 2014.

2.4.2. Moonlighting at the MMP: Observational Sequence, Limb Offset, Drift, and Sky Background

Observations are usually made off the sunlit side of the Moon, but occasionally we have taken data off the terminator near full Moon (phase < 10°). Note that the East/West references made are according to telescope coordinates and in Selenographic coordinates, the West limb as observed from Earth is the Moon's East longitude and vice versa.

Our observational strategy involves slewing to a reference crater, centering on the crosshairs of the centering disk shown in Figure 2.6, then moving the telescope in a cardinal direction to specific limb offsets. Once a crater is chosen, the telescope is moved manually or by using the computer-controlled 'preset' command. The telescope 'preset' command has adequate precision when moving short distances (< few degrees). The non-sidereal motion of the Moon is accounted for by adjusting the thumbwheel tracking rates in both right ascension (RA) and declination (δ). A list of the craters and directions of telescope motion from which we move from the limb is shown in Appendix B. Offsets were made up to 1 lunar radius in the East/West direction and up to 15 arcmin in the North/South direction. Figure 2.7. shows an example of the FOV offset at the edge of the limb East of Aristarchus crater. Figure 2.8. depicts the fashion in which we offset from the limb; this example shows limb offsets out to 2 minutes in RA ($0.5 * \cos\delta$). For example, in Figure 2.8, we have centered on the Grimaldi crater, and offset the telescope in RA. We start by

offsetting to the limb and taking a 300-second exposure (occasionally this was 600 seconds). We then move out to the next offset (i.e., field lens edge and so on) and repeat the procedure. The telescope is centered back on the crater before each successive offset to ensure that the starting point is the same for each observation made for a given sequence off the limb. We need to center back on the crater to ensure the same starting point because there is a field rotation of the image at the focal plane. Note that the offsets in East/West direction are in seconds and minutes of times, while offsets in N/S direction are made in arcsec and arcmin offsets in declination. At the mean lunar distance, 384, 400 km, 1 arcmin FOV is ~112 km. Therefore, for a 3 arcmin FOV, our first 3 offsets for example, corresponded to: a)1.5 arcmin (168 km), b) 4.9 * cos(δ) arcmin (550 * cos(δ) km), and c) 8.5 * cos(δ) arcmin (950 * cos(δ) km) off the limb, where δ is the declination of the Moon. For more detail and conversion from units of time to arcsec and arcmin, refer to Section 3.2.1. in Kuruppuaratchi. (2015).

Figure 2.7: The 3 arcmin entrance aperture of the instrument is shown positioned at the limb East of the Aristarchus crater. The image is a nonlinear sketch that shows the aperture mask and Moon. The centering disk with the crosshairs is not shown here but during an observation taken off the Aristarchus crater, it would be positioned on Plato or Grimaldi, for example, for guiding. The hollow cathode assembly is seen in the upper left quadrant.

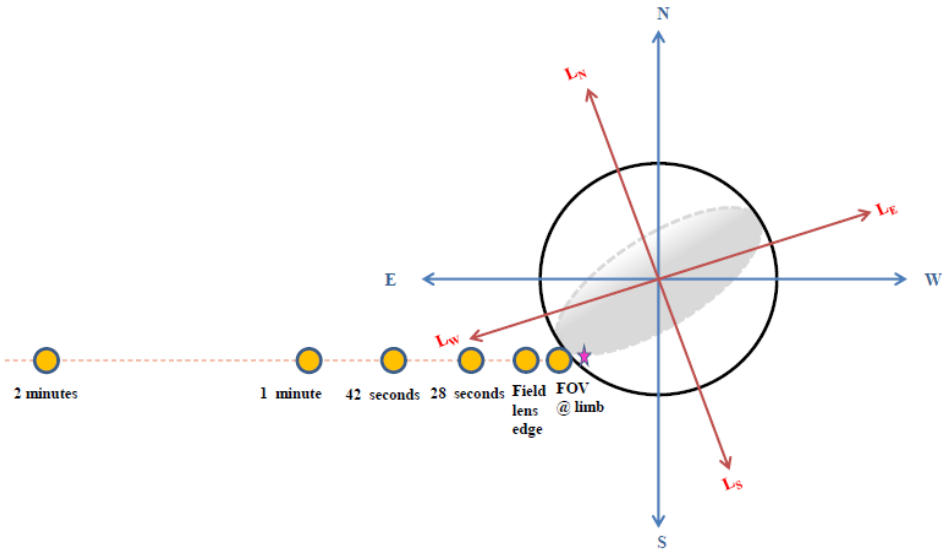

Figure 2.8: Schematic of observations, with different offsets, made off the Grimaldi limb (pink star denotes Grimaldi crater) on the Selenographic West limb of the Moon.

An important aspect of our data collection is that we do not make observations in the lunar frame of reference (Selenographic coordinates). We instead make observations in telescope (celestial) coordinates and this means that our FOV experiences latitudinal drift as we move away from the limb in various offsets. This latitudinal drift is introduced due to a combination of the 23° tilt between the celestial and ecliptic planes and, to a minor degree, the 5° tilt between the lunar and ecliptic planes. We usually choose craters near the limb to minimize the latitudinal drift during offsets. Secondly, the ~13°/day (~0.55 °/hr) Eastward motion of the Moon also introduces drift in our observations. This motion is compensated by adjusting the telescope tracking rates. Any remaining differential motion is accounted with manual guiding by using a 'guide' crater to make telescope adjustments. We do this by placing the crosshairs on the centering disk on a guiding crater, usually a bright spot or crater on the Moon once we have moved off the limb to the desired offset.

Terrestrial sodium is a potential source of contamination for any lunar sodium observations. The sodium nightglow layer peaks at an altitude of 90 ± 5 km and is a product of the ablation of tons of interplanetary dust that enters Earth's atmosphere daily (Slanger et al., 2005). Other sources are volcanic dust and particles from the oceans (Umberto, 2002). Figure 2.9 shows a series of sodium twilight observations taken on April 6, 2017, that show that the sky background rapidly falls off and is not a source of contamination for observations less than 1 lunar radii away. Nevertheless, we typically take nightly sky background image(s) with large offsets (typically 10 degrees away) from the Moon center. The intensity of the terrestrial sodium source is variable and can vary by up to a factor of 2 nightly and even seasonally (Alan Liu, private communication; Marsh et al., 2013; Gardner et al., 1986). Our lunar log summary, or our digital observer's log, can be found in Appendix C. Our ephemeris data is filled into the logbooks using JPL Horizons through the use of a Java code written by Nick Derr. Due to the volume of lunar logs, I have only shown a sample in Appendix C but our full dataset will be archived in the future for data retrieval.

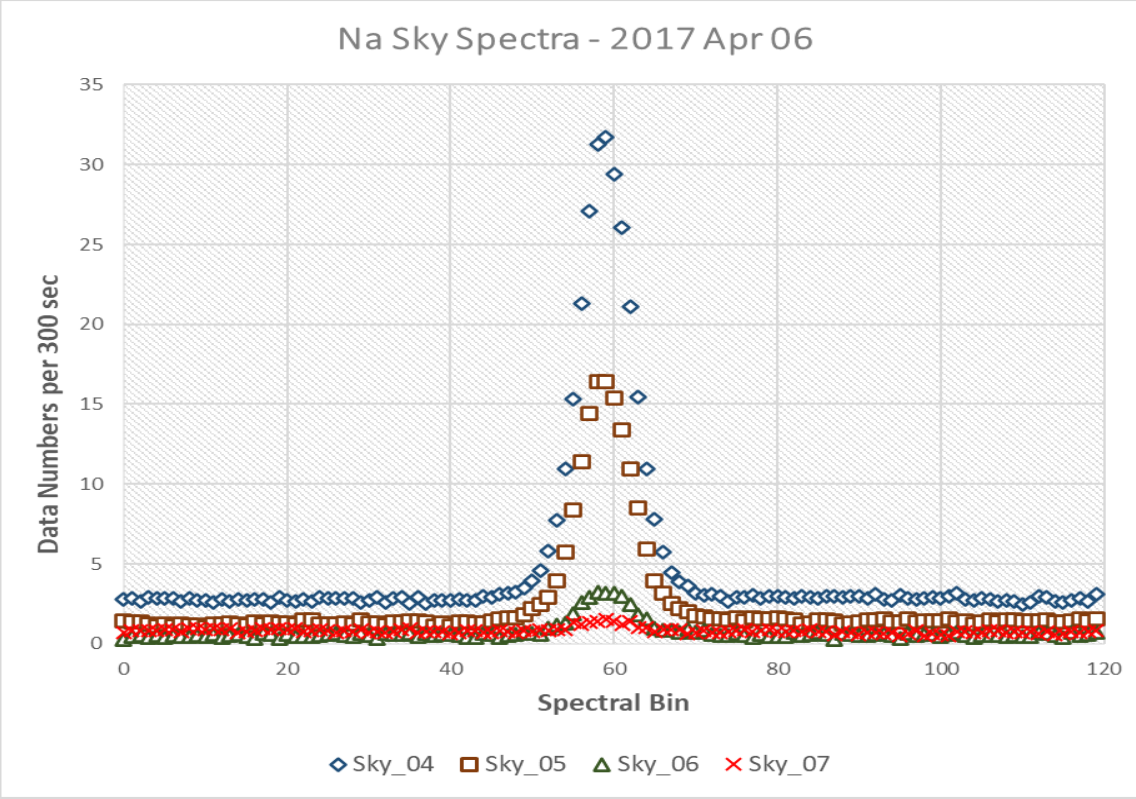

Figure 2.9: Sodium twilight spectra intensity as a function of time. Sky_04 (solar elevation = -6°) is the earliest time and sky_07 (solar elevation = -10°) is the last in the sequence. Observations were made at an Hour Angle (HA) = 0 at the Sun's declination – ensuring that there is no tracking and air mass is constant. As can be seen, the intensity falls off rapidly with time.

In the next Chapter, I discuss our data reduction and analysis procedure for both sodium and potassium, along with intensity calibrations, data quality control, and sources of light contamination.

Chapter 3: DATA REDUCTION AND ANALYSIS

In this Chapter, I build upon the material of Chapter 2 by discussing how we proceed once we have made our lunar observations or collected our "Clair de Lune". While our results are the main attraction of this study, the effort that goes into collecting, reducing, and processing data should also be appreciated. Here, I discuss the data reduction, processing, and analysis steps. For more details, refer to Chapter 4 in Kuruppuaratchi et al. (2015).

For data reduction and analysis of our lunar data, we use a variety of programming languages, including initial data processing in the Interactive Data Language (IDL) for finding FP ring centers and extracting line profile data from raw FPS images, Voigt Fit (VF) fitting package in UNIX for the least-squares fitting of Voigt profiles to spectra, and Matrix Lab (MATLAB) and Python for data analysis. Our usual data processing steps for sodium include (1) bias subtraction, (2) ring summing, (3) instrument profile (IP) creation, (4) data fitting, (5) data quality control (QC). Note that because the camera is cooled at very low temperatures, dark current is not an issue.

3.1. Data Reduction Procedures

Our Andor CCD camera operates in the "baseline" clamp mode, where the bias is automatically removed at the end of each exposure and a constant DC offset of 300 is added back to all our raw images. This DC offset is then removed during data reduction.

3.1.1. Fabry-Perot CCD Annular/Ring Summing Technique

An IDL ring summing code is used to convert FP ring images into 1-D spectra which are then fitted with an N-component model using the least-squares chi-minimization

fitting code, VoigtFit, of R.C. Woodward (private communication). The number of components, N, depends on the type of image (e.g., calibration, moon, sky).

Annular summing makes use of the property that equal area annuli in Fabry-Perot ring pattern correspond to equal spectral intervals. Annular summing is done by averaging the pixels in an annulus with a specific radius (or angle) from the center of the FP fringe (ring) pattern. By doing this, the raw FP ring image can be disassembled into many annuli (each annulus has the same area in pixels) and reassembled into a 1-D spectrum by assigning the average pixel count per annulus to a spectral bin – the final product is then the line profile. The ring summing code determines the radial distance of the center of each pixel from the FP image ring center (Coakley et al., 1996). The FP ring center is determined from a series of calibration rings (thorium HC lamp and sodium lamp) by finding the x and y coordinates of the ring image that produces the highest intensity and the narrowest full-width half -maximum (FWHM). Each of these pixels is sorted into the appropriate spectral bins and any slight differences in the number of pixels per annulus are adjusted by the total pixel count (intensity) average. Our ring summing code also performs a filtering routine which consists of removing any pixel with a count of 3-sigma away from the average pixel value of a given equal-area bin. The filtering is done four times after which the final count per equal-area bin is plotted as a function of spectral bin number to obtain the 1-D line profile. Figure 3.1. schematically depicts the location of the annuli from the center of the FP ring pattern on an Hα FP image and shows the increasing ring diameter going outwards from the center.

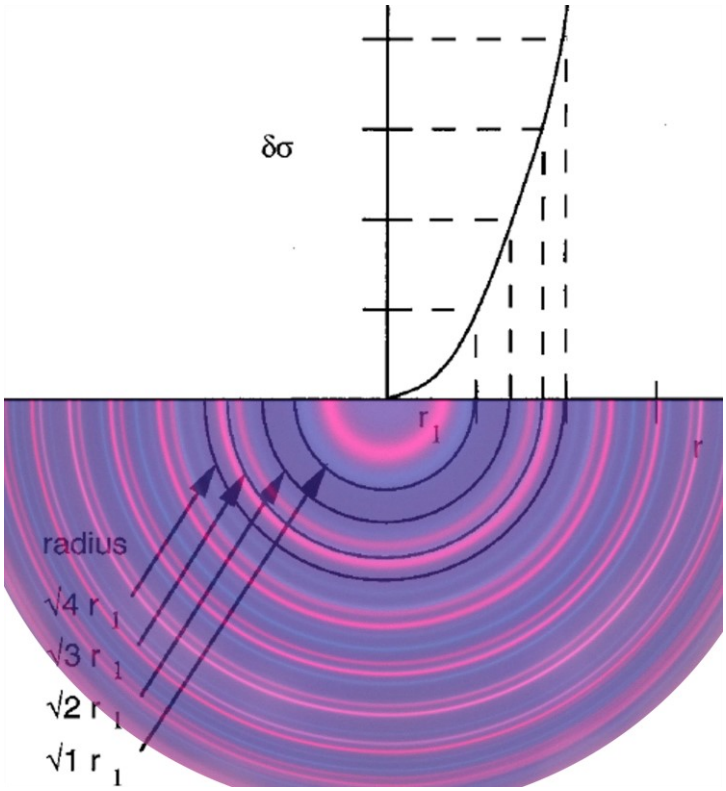

Figure 3.1: Cartoon depicting annular summing technique, parabolic dispersion, and expanding ring diameter going outwards from the center. Credit: Based on Coakley et al. 1996 and the FP Hα and Hβ image (NASA/GSFC).

Figure 3.2. shows a raw FP calibration ring image for a Th I scan. The Th I emission is the bright circle, and the ghosts are the fainter rings. In this case, the most probable other lines (ghosts) are an Ar I line at 5888.591 Å and a weaker Th I line at 5889.953 Å. The Ar I line is a result of the argon fill gas in the HC lamp becoming excited. Also, the Th I line is seen in other orders due to the proximity of the next order (only 0.43 Å away in Etalon A). Figure 3.3. shows its corresponding ring summed 1-D spectrum.

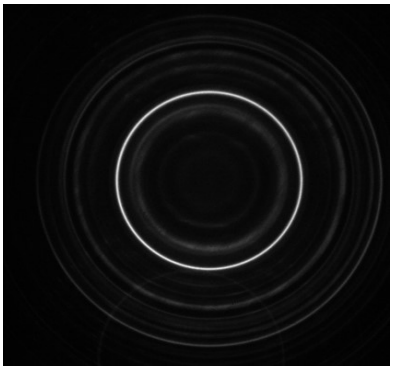

Figure 3.2: Thorium hollow cathode lamp fringe pattern with the bright central fringe representing the Th I line at 5891.451 Å. Filename: th_02.fits, Date: February 19, 2014, Time: 4:21 UT, Integration time: 30 seconds.

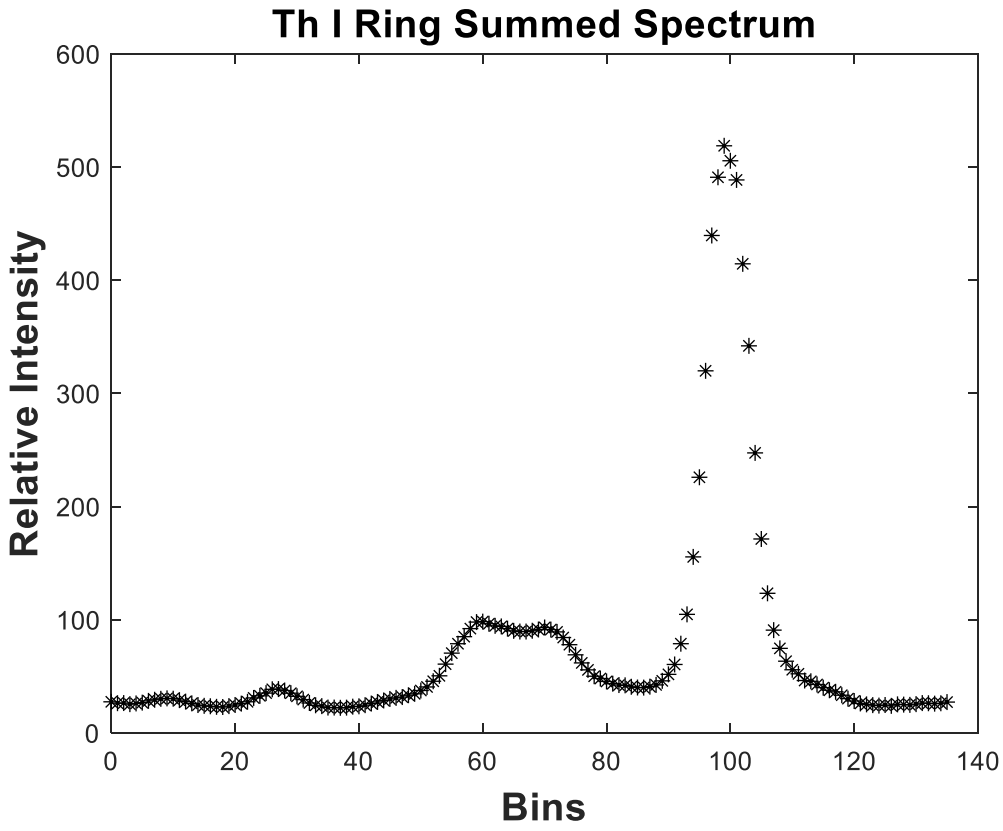

Figure 3.3: Ring-summed spectra of the ring image shown in Figure 3.2. The large peak is the strong Th I line at 5891.451 Å while the smaller, weaker peaks are the ghosts. The spectral interval per bin is 0.3097 km/s.

3.1.2. Dispersion

To take advantage of the FPS ability to measure a fraction of km/s, we need to measure the spectral dispersion. The spectral dispersion (spectral interval (or velocity) per

spectral bin) is constant in velocity space or wavenumber. The instrument dispersion is measured by having both the Th I 5891.451 Å and the Na 5889.9509 Å emissions in the same order. The spectral dispersion per bin is calculated by using the centroid (position in bins) of the thorium line and the sodium self-reversal feature.

We calculated the average dispersion from five measurements taken in March 2012, April 2014, and May 2014. The dispersion values calculated 2 years apart show that the dispersion was stable. A sample spectrum used to calculate the dispersion is shown in Figure 3.4. The average dispersion value is 0.3097 ± 0.0006 km/s/bin. Note that ghosts are visible in Figure 3.4 due to the blocking filters transmitting some adjacent orders. These ghosts had to be fit to properly fit the entire dispersion spectrum.

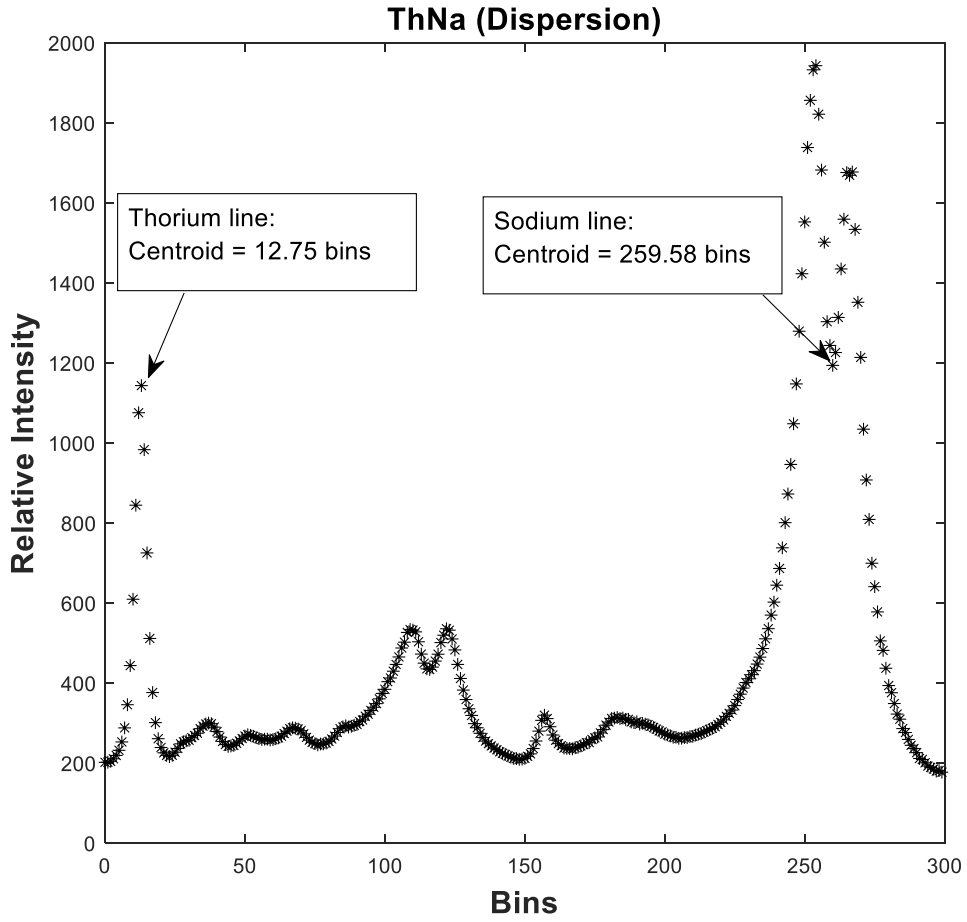

Figure 3.4: Th and Na spectrum obtained from having both lamps turned on together, (taken March 2012). This spectrum was used to determine the position of the Th I line and the Na self-reversal centroid to calculate the dispersion. The dispersion or spectral interval is 0.3097 km/s/bin.

3.1.3. Instrumental Profile (IP) Creation

A particularly important step in our data reduction procedure is the instrumental profile (IP) creation. Any spectrometer will mark observations with its distinct spectral signature known as the IP, $I(\lambda)$, through convolution of the IP and the source spectrum. The IP is a measure of the response of the instrument to a δ-function input spectrum. Practically, the function input is a narrow spectral line with an intrinsic width which is much narrower than the spectral resolution of the instrument. For our sodium observations,

a Th I line at 5891.451 Å obtained from a thorium HC lamp is used as an approximation of the δ-function input spectrum. Due to the excitation mechanism within the thorium HC lamp and the large atomic mass of thorium, thermal broadening effects are reduced. This results in an intrinsic linewidth for thorium which is much smaller than the instrument resolution – making thorium an ideal candidate for IP creation. It is, in theory, possible to deconvolve a well-known IP using Fourier Transforms but this method is very sensitive to noise. In VoigtFit, a convolution of the model and its derivatives with the IP is performed to fit the convolved model to the data (R. C. Woodward).

To make an IP, we use a Th I scan taken at the etalon A and B pressures at the sodium wavelength and then reduce these pressures to match the ring radius of the Th I image to the ring radius of the sodium "gates" lamp image – we call this the reduced ring Th I scan. Recall that the sodium lamp (rest wavelength of sodium) sets the ring radius for lunar sodium images and we collect our lunar images set at the rest wavelength etalon pressures since the Earth-Moon velocity shift is less than 0.4 km/s. Figure 3.5 shows an image of the reduced ring thorium and Figure 3.6. shows its corresponding fitted spectrum. From Figure 3.6 we can see the thorium emission and several FP ghosts. The entire spectrum is fit in VF using 8 components, we then isolate the thorium emission by removing the other 7 components. By doing so, we are left with the residuals of the fit containing the thorium emission and continuum only. We then use ± 20 bins from the centroid position of the thorium emission as our IP range. The thorium emission at bin numbers corresponding to the IP range is then exported to VF where the final IP is created. During this final IP creation, the continuum is removed by making the wings of the IP

'flat'. Note that this method is an empirical determination of an IP from the calibration data we collect.

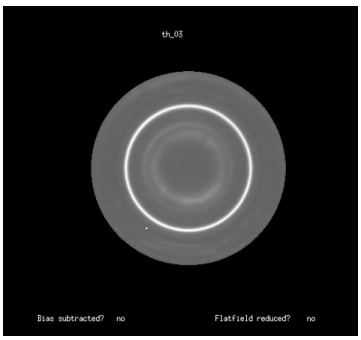

Figure 3.5.: Fabry-Perot ring image for a reduced ring thorium calibration scan. Filename: th_03.fits, date: April 19, 2014, time: 3:55 UT, integration time: 30 seconds.

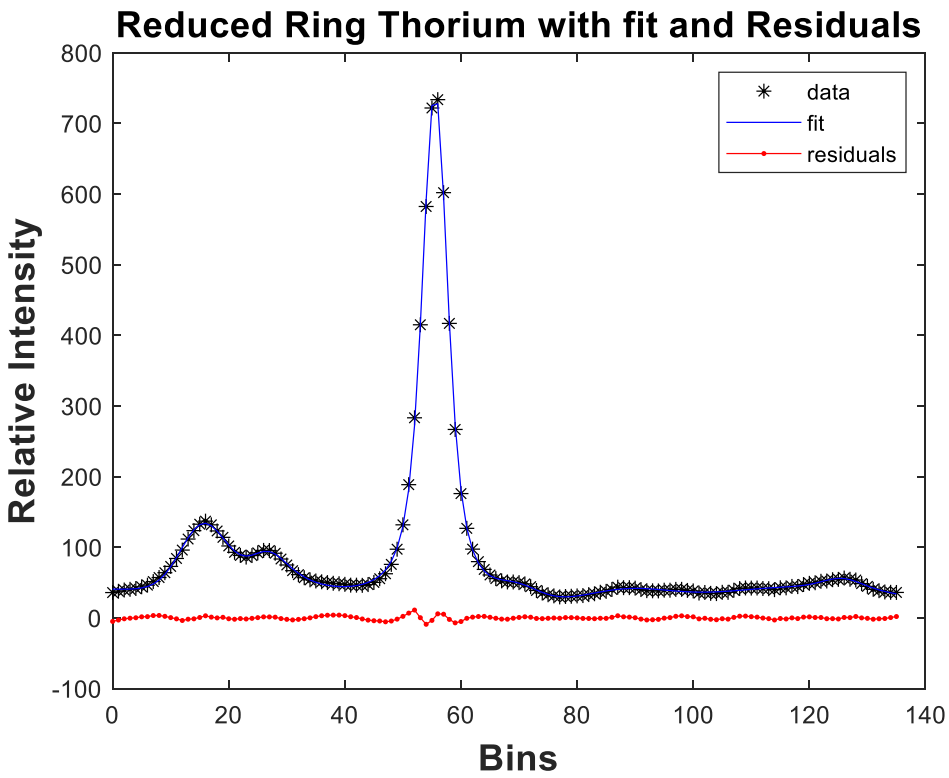

Figure 3.6.: Fitted spectrum of a reduced ring thorium image for the ring image shown in Figure 3.5. The large peak is the bright Th I emission at 5891.451 Å and the weaker emissions are ghosts from other orders and weak argon I line. The spectral interval per bin is 0.3097 km/s.

3.1.3. IP Stability and Master IP Creation

Thorium calibration lines were taken nightly to monitor both wavelength and instrumental stability. The FP tuning is sensitive to changes in temperature so monitoring the IPs throughout an observing run proves to be a good way to assess instrument stability. Figures 3.7 and 3.8. show the centroid position and the widths of the IPs taken over a run in April 2017. Both centroid position, which is reflective of temperature changes, and IP width vary very little throughout the run, and this behavior is consistent in all our observing runs. IP studies indicate an average full width at half maximum of 1.7 km/s, consistent with the earlier work of Mierkiewicz et al. (2014) and Kuruppuaratchi et al. (2018). Due to the stability of the IPs throughout an observing run, we switched to making a master IP per run. A master IP is created by aligning the emission peaks of the individual thorium I line in a run and adding the spectra together, before carrying out the rest of the steps involved in creating an IP.

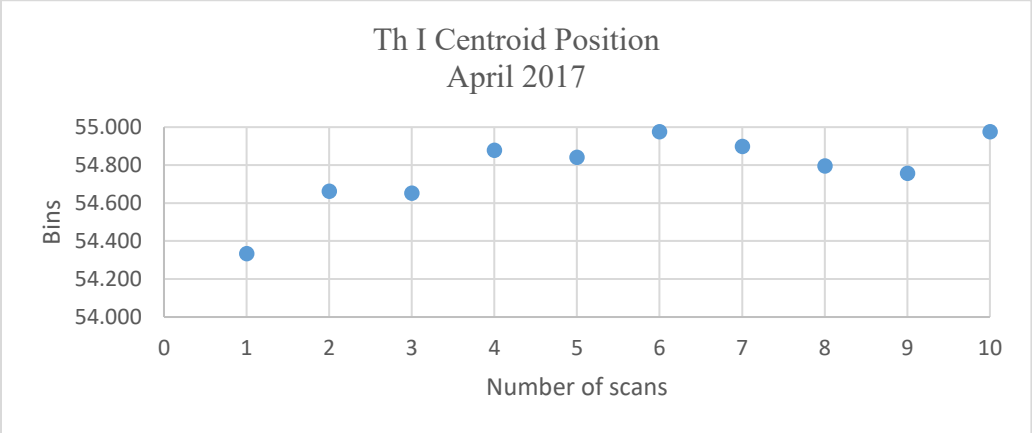

Figure 3.7: Th I centroid position over 10 nights in April 2017. The centroid position varies by less than 1 bin for the run and reflective of instrument temperature changes –the spectral interval is 0.3097 km/s/bin.

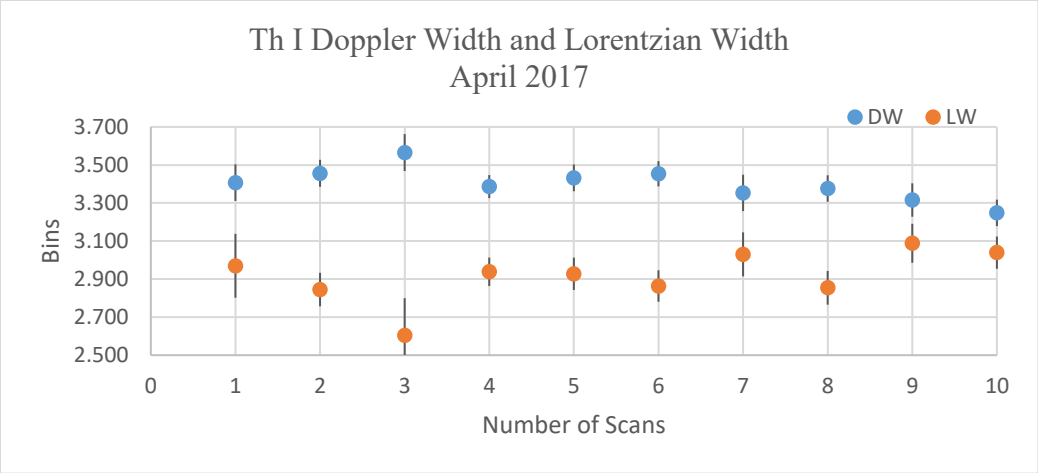

Figure 3.8: Th I Doppler and Lorentzian width (DW and LW, respectively) in bins for 10 nights in April 2017 showing consistency in FPS stability.

3.2. Fitting Model for Lunar Sodium and Potassium Spectra

An edited version of this Section was published by AGU in Kuruppuaratchi et al. (2018) (sodium) and Rosborough et al. (2019) (potassium). All lunar spectra are fit with a model consisting of N components and a sloping background convolved with an empirically determined IP using the VF code of R.C. Woodward (private communication, June 2014); with the number of components, N, varying with the type of the object (e.g., moon (Na, K), calibration (Na, Th), sky). Examples of sodium spectra, fit, and residuals are included in Figure 3.9. The spectrum in Figure 3.9 (top) was taken at phase angle 49.8° when the sodium emission is visible due to the lower continuum level. Figure 3.9 (bottom) was taken close to Full Moon (0°) and shows a raised continuum level with less prominent terrestrial water features and sodium emission. However, we do not see any systematic pattern in our residuals and are confident with our fitting methodology.

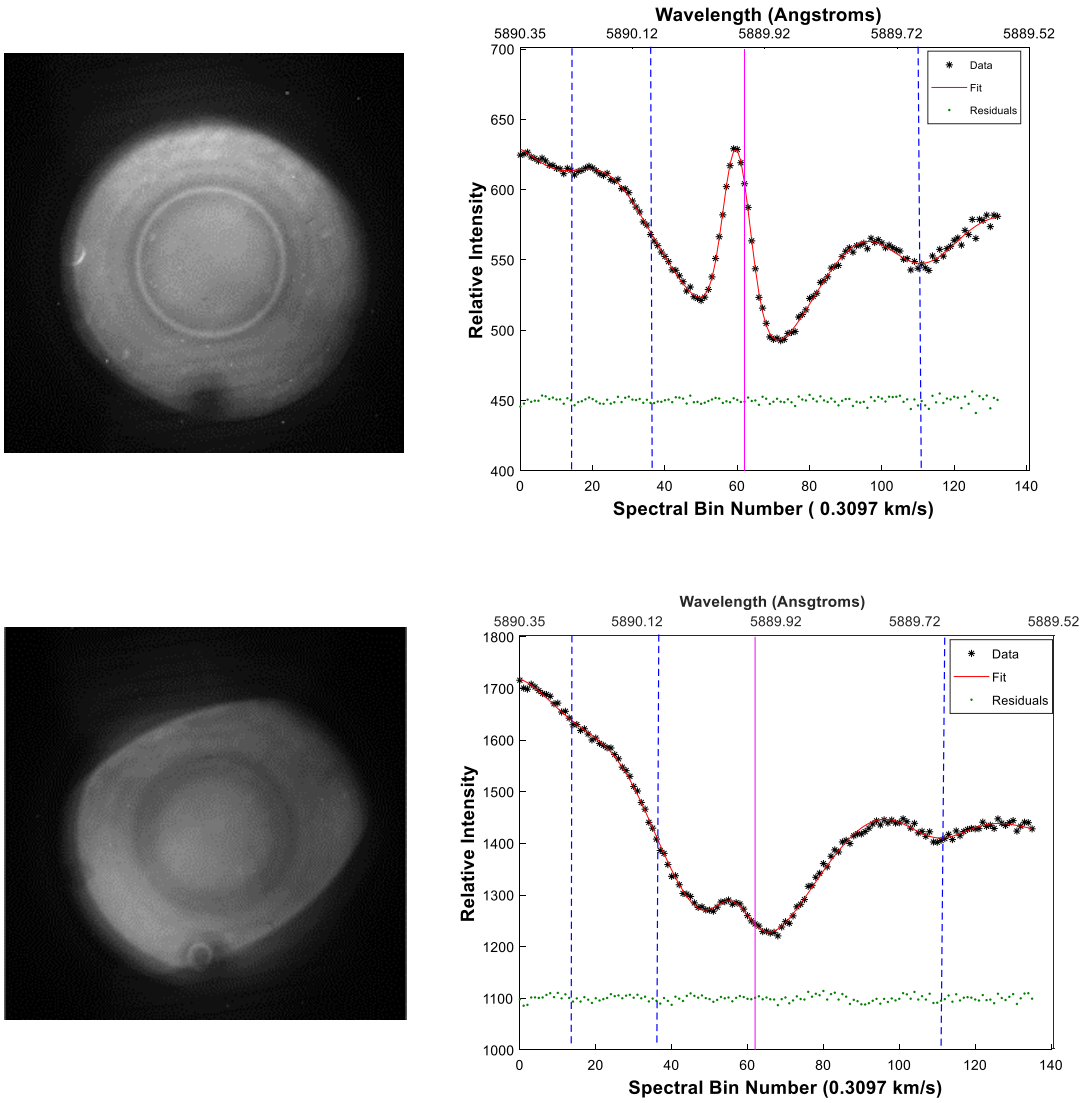

Figure 3.9: (top, left) Lunar sodium raw ring image and (top, right) its corresponding spectrum for an image taken on 19 February 2014, 8:37 UT at the limb off Grimaldi crater (49.85° waning phase) and (bottom, left) lunar sodium raw ring image and (bottom, right) its corresponding spectrum for an image taken on 14 February 2014, 9:06 UT off the limb off Aristarchus crater (8.72° waxing phase). Note that fit residuals have an offset of 1,100 and an offset of 450 for Figures 3.8 (top) and 3.8 (left), respectively.

The continuum is due to scattered moonlight within the Earth's atmosphere and off the telescope mirrors and superstructure. The sodium spectrum is fit with a six-component

model (See Figure 3.9 top and 3.9 bottom) that includes two Gaussians for the lunar sodium D2 s-resolved hyperfine structure emission components at 5889.9386 and 5889.9584 Å, a single Gaussian to fit the solar Fraunhofer absorption line at 5889.9509 Å, and three Gaussians for nearby terrestrial water absorption lines (marked by blue lines) at 5890.227, 5890.090, and 5889.637 Å (McNutt and Mack, 1963). A pink line marks the rest wavelength of sodium. The widths and areas of the Gaussians representing the terrestrial water lines at 5890.227 and 5890.090 Å are linked to the stronger water feature at 5889.637 Å in a 1:1 ratio and 0.67:1 ratio, respectively. The widths of the Gaussians representing the two sodium emissions components at 5889.9386 and 5889.9584 Å are linked in a 1:1 ratio, while their intensities are set in a 3:5 ratio. In Addition to the reflected solar spectra, terrestrial absorption lines, and the lunar emission, the ring images (top left and bottom left) include the black artifact (bottom) which is a chip in the number 2 mirror, smudges, dirt/glint from the #1 and #2 mirrors, cosmic ray hits, low contrast straight fringes toward the bottom of the ring image caused by reflections between the Fabry-Perot etalons, and scattered moonlight which causes the ring image to look asymmetric. Note that although in all the ring sum images shown here, the spectral bin numbers go up to 136, we have reduced this in our current fitting methodology to 120 bins. A Fabry-Perot fringe pattern has concentric annuli that grow closer when going further out from the central spot (radius squared relationship to wavelength). Since the outer rings are closer to each other, multiple rings can pass through a single pixel. However, a pixel will only be assigned to the closest bin. The consequence of this is digitalization results in increased noise due to sampling of fewer pixels and a decrease in spectral resolution at large ring radii (Kuruppuaratchi et al., 2015). Figures 3.9a and 3.9b both show evidence of digitization towards the blue end of

the spectrum. Limiting our spectrum to 120 bins helps us better model the spectrum and minimizes the effects of digitization. Note that this reduction in spectral range does not affect our fitting results, such as linewidth, and simply helps the model converge better.

Sodium (Figure 3.9) and potassium (Figure 3.10) line profile measurements include a fine structure component and hyperfine structure within this measurement. The fine structure is a result of interactions between the electron orbital angular momentum and electron spin state while the hyperfine structure is attributed to the interaction between nuclear spin and electron angular momentum (Britannica, 2015). For sodium, an alkali metal element, there are two components to the fine structure. These are known as the sodium doublet, D1 and D2, the wavelengths are shown in Table 3.1. For mesospheric terrestrial measurements, the sodium D2 line is brighter than the D1 line by a factor of 1.2 – 1.8 (Slanger et al., 2005) while in the local thermodynamic equilibrium the ratio is two. Therefore, the brighter sodium D2 line was chosen for studying the lunar exosphere. The high-spectral resolution of the FPS allows for the hyperfine line separation and relative intensities to be accounted for in the data reduction described in Chapter 2. The sodium D2 hyperfine structure wavelengths are shown in Table 3.2. Note that the D2 and D1 wavelengths are the weighted averages of the hyperfine wavelengths for sodium and potassium, respectively.

Table 3.1: *Wavelengths of the fine structure sodium and potassium emission lines (Juncar et al., 1981).*

Emission Line	D1 Wavelength (Å)	D2 Wavelength (Å)
Na	5895.9242	5889.9509
K	7698.9646	7664.8991

Table 3.2: *Wavelengths of the hyperfine structure in the sodium D2 and potassium D1 (Hanley et al., 2015) emission lines.*

S resolved state	Wavelength (Å)	Relative Intensities
$^2P_{3/2} - {}^2S_{1/2}$	5889.9386	3
$^2P_{3/2} - {}^2S_{1/2}$	5889.9584	5
$^4P_{1/2} - {}^2S_{1/2}$	7698.9586	3
$^4P_{1/2} - {}^2S_{1/2}$	7698.9681	5

Potassium observations and data analysis follows a similar procedure to sodium, apart from a few differences outlined here. While we image the entire 0.08 nm spectral range onto the CCD for sodium, we image 0.1 nm for potassium (both at a high spectral resolution of R ~ 180,000). As for data reduction, the steps are similar to sodium with the key difference being the modeling and fitting of the scattered light background including the fringing pattern seen in Figure 3.10. This water-like pattern is a result of internal fringing within the CCD at the potassium wavelength, something which cannot easily be corrected using flat fielding (Rosborough et al. 2019). Potassium is fit in a similar way to sodium, but with 3 components instead of 6 (Figure 3.10). The three components consist of the potassium Fraunhofer feature, and the potassium s-resolved emission doublet set in a 5:3 intensity ratio. The potassium spectrum does not contain terrestrial water absorption features seen in the sodium spectrum. For more details on data reduction and analysis, refer to Rosborough et al. (2019) and Derr (2015). IP creation for potassium is made from the nearest strong Th I (K) line at 7647.380 Å. For potassium lunar images, calibrations are done using a potassium lamp measured at 7698.9647 Å. The IP construction follows the same procedure as for sodium.

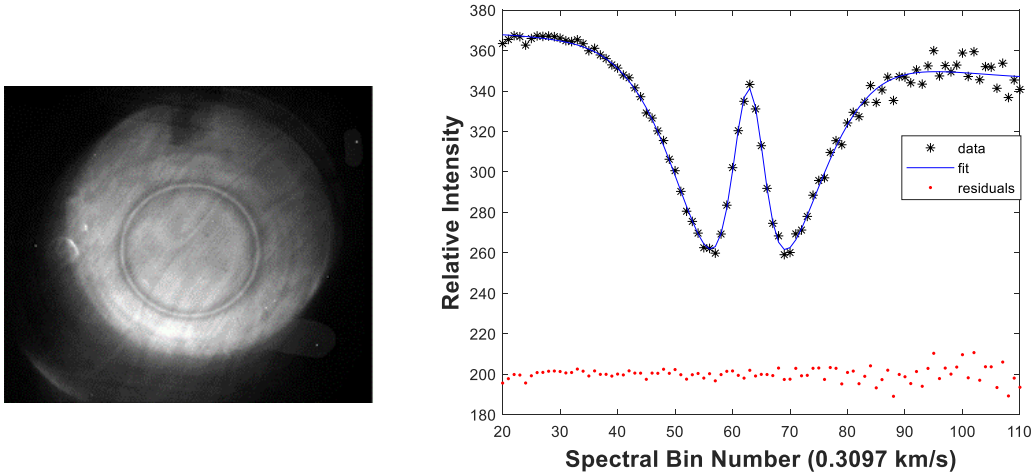

Figure 3.10: Raw FP image of potassium (left) taken on April 21, 2014 off the Grimaldi Limb. Corresponding ring summed image (right) along with the model fit and residuals show the potassium emission sitting in the Fraunhofer absorption feature. Note that there are no terrestrial absorption features at the potassium wavelength.

3.2.1. Line Profile Measurements

From the fit to our lunar sodium and potassium spectra we obtain three important pieces of information - linewidth derived effective temperature, relative intensity, and line of sight (LOS) velocities of atoms in the lunar reference frame. To obtain effective temperatures, we use the FWHM or the measured Doppler width of our emission line. The measured Doppler linewidth is related to effective temperature through the following relation where the $\Delta\lambda_{FWHM}$ is proportional to the square root of the temperature T of the emitting population as shown in Mierkiewicz et al. (2012),

$$\Delta\lambda_{FWHM} = 2\lambda_o\sqrt{\frac{2kTln(2)}{mc^2}} \qquad \text{Eq. 3.1}$$

Using Equation 3.1. we can then obtain Equation 3.2a, by using the mass of a neutral sodium atom,

$$T_{eff} = 4.51 \times 10^{13} \left(\frac{\Delta\lambda_{FWHM}}{\lambda_0}\right)^2 [\mathrm{K}] \qquad \text{Eq. 3.2a}$$

where T_{eff} is the effective temperature, m is the mass of the atom in kg, k is Boltzmann's constant, c is the speed of light, $\Delta\lambda_{FWHM}$ is the Doppler broadened wavelength, and λ_0 is the rest wavelength of the sodium emission.

If we use the atomic mass of potassium in Equation 3.1, we get the potassium equivalent of Equation 3.2b,

$$T_{eff} = 7.6 \times 10^{13} \left(\frac{\Delta\lambda_{FWHM}}{\lambda_0}\right)^2 [\mathrm{K}] \qquad \text{Eq. 3.2b}$$

where the variables are the same as for sodium but with λ_0 as the rest wavelength of potassium.

For non-relativistic limits, where v ≪ c, the wavelength shift is shown to be as follows:

$$\frac{\Delta\lambda}{\lambda_0} = \frac{v}{c}$$

Where v is the Doppler width in km/s. The measured Doppler widths are converted into units of km/s by multiplying the measured linewidth by the dispersion value of 0.3097 km/s/bin. Our lunar exospheric data are thus direct radial velocity measurements. Using the above relation, Equation 3.2 can be written as follows:

$$T_{eff} = C(m) \times v^2 \qquad \text{Eq. 3.3}$$

Where $C(m) = 501$ for sodium and $C(m)$ = 850 for potassium when the atomic mass of potassium is used in Equation. The measured Doppler widths and relative intensities along

with other fit parameters can be found in a condensed form in Appendix D2 for Sodium, and Appendix D1 for potassium.

We use the line center position of the emission to determine the velocity of the atoms in the lunar reference frame – this gives us the line of sight velocities of the atoms on the Moon. Sodium velocities will be presented and discussed later in Chapter 4.

To obtain the relative intensities in Analog Digital Units (ADU) of our emission line, we use the area under the line profile. Note it is difficult to obtain absolute calibration for our data through our observations because there are no diffuse calibrated emission sources of sodium or potassium in the sky. While stars are used for calibration, it is not adequate for calibration using the FPS as it is a point source. It is possible to use the Moon itself for calibration, however, due to the nature of the FP (especially parasitic light) (Section 3.2.2), it is not easy to estimate the number of photons entering our instrument. Luckily, for us, another lunar exosphere team made observations using a coronograph with some nights overlapping with ours. In the proceeding Section, I discuss how to use their coronograph data for calibrating our relative intensities.

3.2.1.1. Absolute Intensity Calibration

The calibration method used to obtain our data in absolute units is done using data taken from a different group and a different instrument known as a coronograph. The coronograph observations, taken from the team led by Rosemary Killen, were made from observing the occulted Moon at the same wavelength of sodium (Sodium D2).

Their lunar sodium Moon images are calibrated using the counts in the open Moon images and the Hapke bi-directional reflectance function (Hapke, 1984, 1986; Helfenstein

and Veverka, 1987; Mouawad et al., 2011). For detailed descriptions of the coronograph, data collection, and calibration refer to Killen et al. (2019). Note the occulting disk extends to about 200 km above the lunar limb, this means that our first offset (FOV at limb) for 2 arcmin which is ~ 240 km sits mostly inside the occulting disk. Therefore, I can only use offsets that are further out than FOV at the limb. In Figure 3.11 some offsets have double circles, this is because our FOV was slightly inside the occulting disk and so I have moved the center of the FOV circle by a few pixels. Note that the coronograph image of the Moon is not always centered on the occulting disk so sometimes even FOV at the field lens edge cuts into the occulting disk by a small amount.

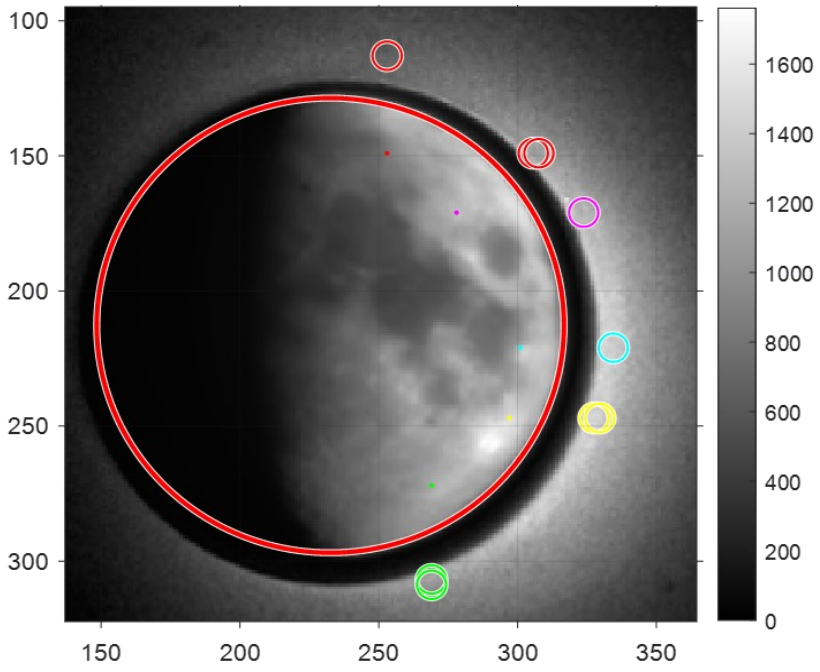

Figure 3.11: Coronograph image taken with a 1.5 Å wide narrow-band filter centered on the sodium D2 line (Courtesy of Rosemary Killen, private communication) calibrated in Rayleighs taken on April 5th, 2017 with 2 arcmin FOV superimposed. The various colors correspond to various offset reference craters. The colors represent a reference crater as follows: red (Atlas), pink (Cleomedes), cyan (Langrenus), yellow (Petavius), green (Janssen).

The first step in this procedure is to find the intersection coordinate (in pixels) between a point adjacent to the reference crater and the lunar limb. Utilizing the platescale of the CCD image (11.338 arcsec/pixel) and knowing our offset distance from the limb in arcseconds, I place the 2 arcmin FOV (5.25 pixels in radius) on the CCD image and find the mean pixel intensity value within the FOV circle using an imaging code written in MATLAB. For the night of April 5th, 2017, the values for our line profile derived relative intensity and the mean intensity value for each offset is shown in Table 3.3.

Table 3.3: *Table of results showing calibrated intensity within FOV, relative intensity from FPS line profile, and the ratio between calibrated intensity and relative intensity for April 5th, 2017.*

Crater	Intensity from FOV circle, R	Relative Intensity, ADU	Ratio, R/R_rel, (R/ADU)
Atlas (N) (Red)	664	257	2.58
Atlas (W) (Red)	1100	415	2.65
Cleomedes (Pink)	1241	434	2.86
Langrenus (Cyan)	1409	479	2.94
Petavius	1399	479	2.92
Average ratio			**2.79 ± 0.16**

From the results in Table 3.3, we can see that the ratio of the mean pixel intensity to the relative intensity is consistent for all offsets with an average ratio of 2.79 ± 0.16. Since the ratio is consistent, I can use it as a factor to multiply our relative intensities to get our calibrated intensity values. A similar example is shown in Figure 3.12, for the night of May 2nd, 2017. On this night the Moon is not centered on the occulting disk so I can only use offsets at 28 sec and 42 sec from the limb for two reference craters. Following the same

procedure as for April 5th, 2017 I place our 2 arcmin FOV off the limb of Langrenus and Cleomedes for 28 sec and 42 sec offsets. The results are summarized in Table 3.4 below.

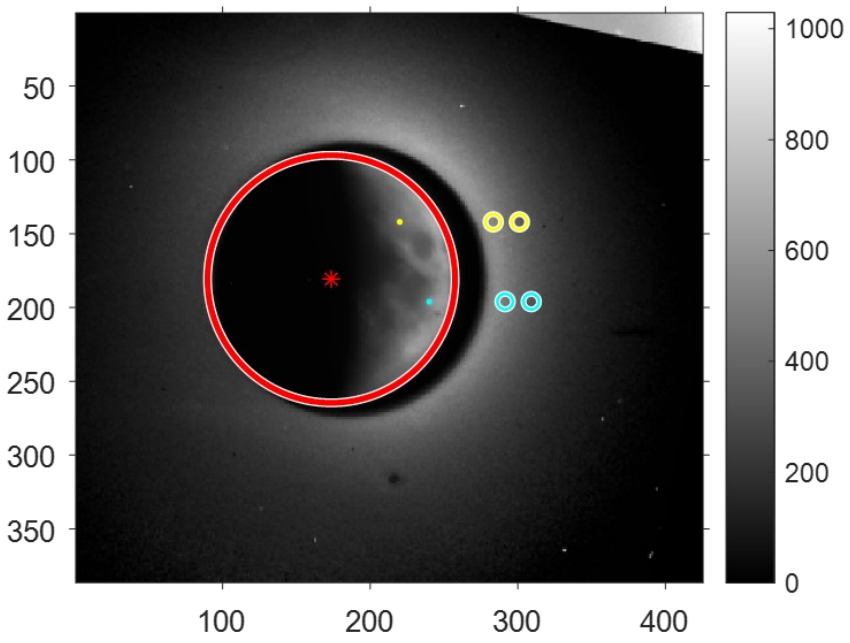

Figure 3.12: Coronograph image taken at the sodium D2 wavelength (courtesy of Rosemary Killen, private communication) taken on May 2nd, 2017, with 2 arcmin FOV superimposed. Yellow refers to Cleomedes and blue refers to Langrenus.

Table 3.4: *Table of results showing calibrated intensity within FOV, relative intensity from FPS line profile, and the ratio between calibrated intensity and relative intensity for May 2nd, 2017.*

Langrenus offset (blue)	**Intensity from FOV circle, R**	**Relative intensity (ADU)**	**Ratio of intensities (R/ADU)**
28 s	491	191	2.57
42 s	341	118	2.89
Cleomedes offset (yellow)			
28 s	539	188	2.82
42 s	377	132	2.86
Average ratio			**2.79 ± 0.14**

Results from May 2nd, 2017 also indicate that the ratio between the mean FOV circle intensity to the relative intensity is very consistent with an average ratio of 2.79 ± 0.15. For each night, I can use a conversion factor, or the ratio between derived and measured intensities, to convert our relative intensities to absolute intensity units. From the analysis of the two nights, the average ratio or conversion factor needed to multiply our relative intensities by is 2.79. Note that this intensity calibration assumes clear sky conditions at Kitt Peak and although we strive to only use the observations made under the best sky conditions (good transmission), there are some nights with light cirrus that can be problematic. Although the measured intensities are wrong when cirrus clouds affect the observations. In such cases, results are more variable, and an adjustment would have to be made or a confidence interval for our relative intensities can be calculated. Unfortunately, there is no coronograph data for potassium so this same exercise cannot be done for our potassium intensity calibration in the same way.

This is the method that is best suited for our intensity calibration for this dataset. The results in this dissertation will still be presented and discussed in terms of relative intensity units as it is the relative changes that important. In future publications, our relative intensities will be converted to absolute values using the methods as shown in Figure 3.11 and 3.12.

3.2.2. Sources of Light Contamination

Contamination sources exist in the form of parasitic light, Brillouin scattering (Potter et al. 1984), scattered light, and terrestrial sodium emission. The observed depth of the solar Fraunhofer D2 line is significantly filled in by scattered and parasitic light to approximately 70% of continuum compared to a known depth of 5% of the continuum at

line center; another much smaller contribution (~1–2%) is the filling of the Fraunhofer line due to Brillouin scattering (Potter et al., 1984). Parasitic light is a common affliction in FPS and is unwanted continuum light getting into the instrument through the transmission of light from unwanted orders. This parasitic light may include scattered light as well, but it is hard to delineate the two. As discussed in Chapter 2, the sodium background contamination is only a contributing factor at distances greater than one lunar radius from the lunar limb.

3.2.3. Quality Control

After following our data fitting procedure, we check all our fits to ensure that only the highest quality data make it into our data analysis. We check for various parameters in our data to determine fits that fall into three categories: good, fair, and bad. We first look at our fit residuals to see if there are any systematic patterns especially related to weather conditions. We check the consistency of each of our fit parameters and their errors for each Gaussian per observing run. We check to see if fits have any parameters that fall out of a nominal range and either refit them to fix the issue or remove them. We never delete any data, and any bad fits can be revisited later. A lot of times, especially when the continuum level is high, the water absorption features are not easy to fit and while the positions of the terrestrial water absorption features are known and can technically be fixed, we do not fix the centroid positions of these features. This is due to the following 2 reasons: 1) we are unable to establish a real continuum level because the wavelength coverage is insufficient, which is especially true for the broad wings of the sodium absorption line, 2) the scattered light affects the continuum level and shape. To deal with cases where the water features are not easy to fit, we use the fix and free method, where we will fix the centroid of a

feature, iterate till convergence is reached, then set the centroid free and refit the model. Doing this helps the model converge in cases where the continuum especially is high. We check the size of the error for each Gaussian parameter to see if the error is large compared to the actual fit parameter (signal-to-noise). Many of our fits fall into the 'good' category, while 'fair' fits are often refitted with good results. For each observing run, we conduct this rigorous quality control to ensure the health of our results.

A subset of our quality control passed data is shown in Part III, where I present and discuss the first comprehensive ground-based equatorial sodium observations by Kuruppuaratchi et al., (2018), and discuss their implications.

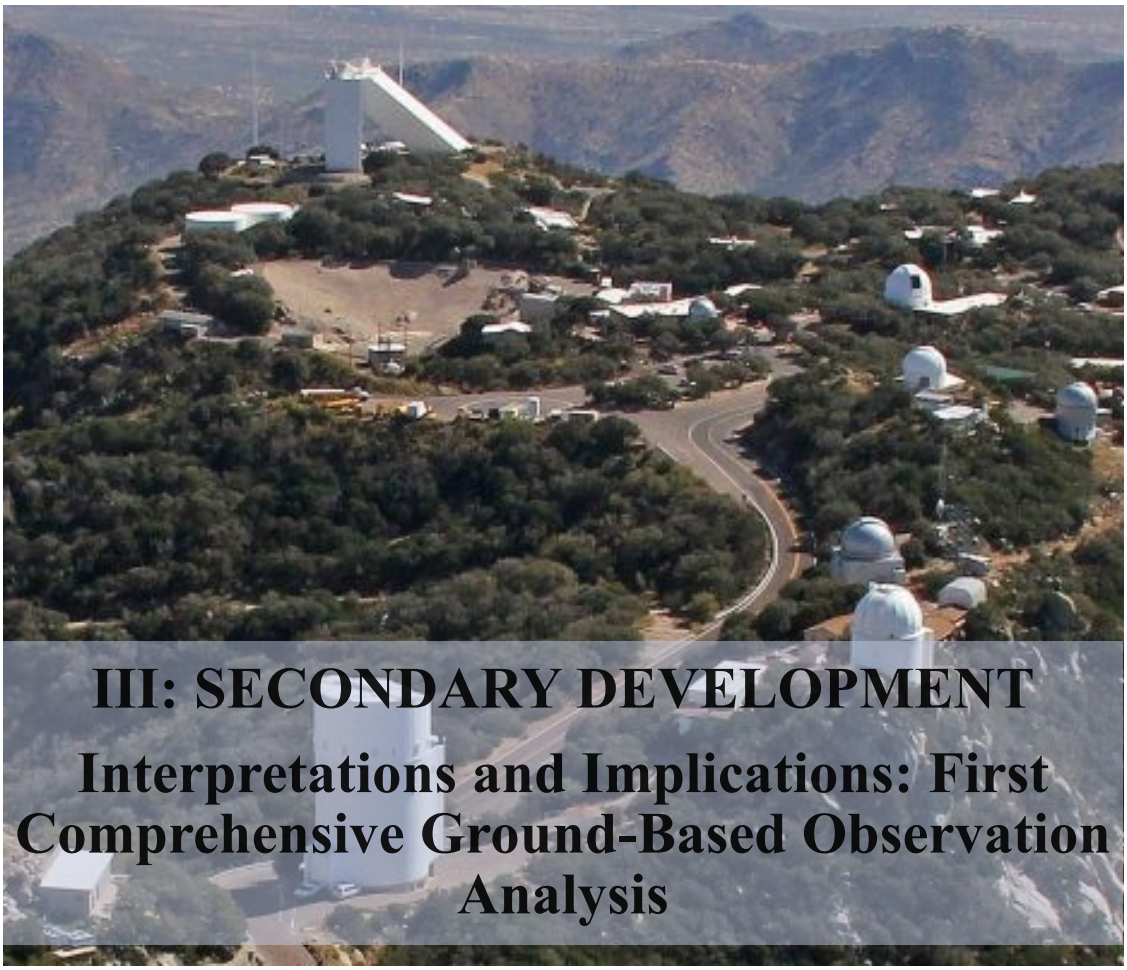

III: SECONDARY DEVELOPMENT

Interpretations and Implications: First Comprehensive Ground-Based Observation Analysis

Photo Credit: NOAO/AURA/NSF

CHAPTER 4. THE LUNAR SODIUM EXOSPHERE AT THE TIME OF THE LADEE MISSION

Key Points:

- First comprehensive sets of direct lunar sodium exospheric linewidth observations are presented as a function of lunar phase.
- Exospheric temperatures are highest near full Moon and decrease toward large phase angles.
- Photon stimulated desorption (PSD) dominates source mechanisms at subsolar points, with contributions by other processes near terminators.

In this Chapter, I discuss an edited version of the first comprehensive ground-based study of lunar sodium observations published in JGR Planets by Kuruppuaratchi et al. (2018) and concurrent with the LADEE mission. The LADEE mission made continuous equatorial sodium and potassium observations at noon local time and offers a complementary viewpoint to the ground-based dataset presented in this Chapter, which is comprised of observations made at various local times. The trends discussed in this Chapter are focused on the phase angle dependence of linewidths, linewidth derived effective temperatures, velocities (Section 4.1), relative intensities (Section 4.4), and what we can infer from these trends. The sodium data presented in this Chapter spans a period of 6 months (non-consecutive) from November 2013 to May 2014 encompassing the LADEE mission instrument testing and science phase and only includes 3 arcmin East and West equatorial data off the sunlit limb, limited to FOV at limb, edge, and 28 seconds offsets.

The effective temperature and relative intensity results are reported in terms of the Moon's location in and out of the magnetotail – that is, whether the observations are before full Moon, during full Moon, and after full Moon. A more accurate representation of the Moon's local plasma region is discussed later in Chapter 6.

4.1. Implications of Linewidth Measurements

The phase angle dependence of the exosphere is the focus of the Sections presented in this Chapter. I start off with the relationship of our sodium linewidths (Figure 4.1) and linewidth derived effective temperatures (Figure 4.2) as a function of lunar phase angle. To denote phase angles before full Moon, we define a modified phase angle where negative angles represent the waxing phase (unfilled symbols) and positive phase angles represent the waning phase (filled symbols). Linewidths are similar during the waxing and waning phase, with the largest linewidths (and corresponding effective temperatures) occurring near full Moon. A smoothing spline (piecewise polynomial) has been included in Figure 4.2 to highlight the overall trend of increasing temperatures towards full Moon.

The exosphere is hottest when the Moon is inside the Earth's magnetotail; typically, for phase angles <30° (approximately five-six days), the temperature range is 2500 – 9000 K, with an average temperature of 4330 ± 680 K. Away from magnetotail passage, data taken at phase angles greater than 40° on the waxing side have an average temperature of 1770 ± 190 K, consistent with data taken at phase angles greater than 40° on the waning side with an average temperature of 1700 ± 140 K. Refer to Table 4.1 for a list of average temperatures.

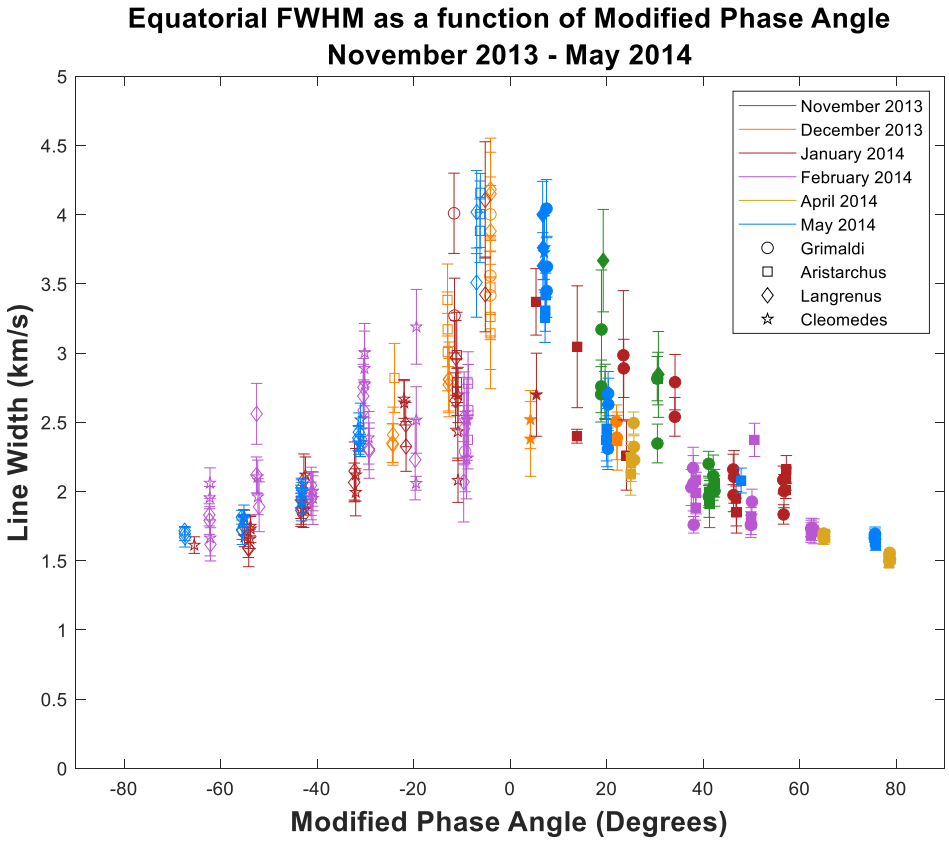

Figure 4.1: Linewidth as a function of modified phase angle (where modified phase angle denotes negative values for waxing phase angles and positive values for waning phase angles) for equatorial latitude regions (Kuruppuaratchi et al. 2018). Modified phase angles represent waxing phase data (open symbols) as negative and waning phase data (filled symbols) as positive. Pre– and post–full Moon linewidths are nearly symmetric about a phase angle of 0°, with the largest linewidths occurring near full Moon. FWHM = full width at half maximum.

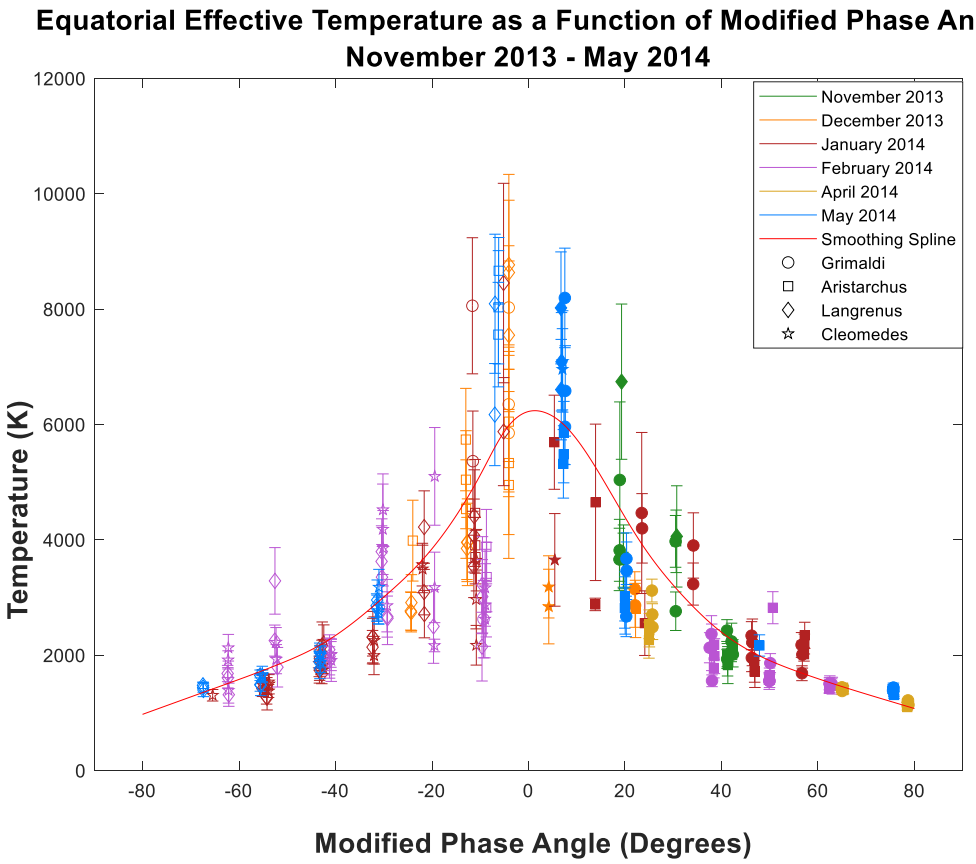

Figure 4.2: Temperature as a function of modified phase angle for equatorial latitude regions (Kuruppuaratchi et al. 2018). Pre– and post–full Moon linewidths are nearly symmetric about a phase angle of 0°, with the largest linewidth derived effective temperatures occurring near full Moon at the time when the Moon's orbit takes it through the Earth's magnetotail. A smoothing spline has been added to highlight the main trend of the data set.

Table 4.1: *Equatorial region linewidth derived effective temperature averaged according to the moon's approximate location relative to Earth's magnetotail (Kuruppuaratchi et al. 2018).*

Limb (Reference Crater)	Modified phase angle < -40° effective temperature (K)	Phase angle <30° effective temperature (K)	Modified phase angle > -40° effective temperature (K)
Aristarchus	N/A	4390 ± 660	1690 ± 130
Grimaldi	N/A	4560 ± 700	1710 ± 140
Langrenus	1750 ± 200	4740 ± 780	N/A
Cleomedes	1780 ± 180	3620 ± 580	N/A
Average	**1770 ± 190**	**4330 ± 680**	**1700 ± 140**

4.1.1. On the Issue of Possible Geometrical Effects

From previous Sections we know that our sodium effective temperatures increase from quarter phases towards full Moon and are largest during magnetotail passage. We also know that sodium has a tail that is the result of sodium atoms in the exosphere being pushed anti-sunward by solar radiation pressure. Some studies (Wilson et al. 2003) used observations during a lunar eclipse to provide constraints on the highest speeds in the lunar sodium exosphere. They concluded that since only ≤ 20 % of the escaping sodium atoms are ejected from the surface with speeds above 2.3 km/s (escape speed of the Moon), then solar radiation pressure must be responsible for most of the neutral sodium escape into the outer exosphere and sodium tail. Recall that around full Moon, our viewing geometry does imply that our FOV is pointing in the direction of the lunar tail and it is likely that we do

see some fraction of the sodium tail population. While we cannot give an exact proportion for the amount of sodium tail atoms our FOV intersects, we can (1) conclude from the shape of our line profiles that it cannot be a significant proportion, and (2) empirically determine how much of a linewidth increase would occur if we were to intersect progressively more red-shifted atoms in our FOV. Here, I discuss the implications of our high temperatures during magnetotail passage and also show, using an empirically determined model, that our high temperatures are not a result of our FOV seeing red-shifted atoms down the tail. The results from a sodium particle transport model discussed in Section 4.1.2. also reinforces the fact that the increase in linewidth towards full Moon is not primarily due to looking look down the lunar sodium tail.

Temperatures presented in Section 4.1 are higher than that expected for sodium atoms thermalized to the lunar surface, ~400 K at subsolar point (Stern, 1999), indicating that the source of these sodium atoms is dominated by an energetic, nonthermal process. Although our temperatures at large phase angles (greater than 40°) are close to that of a PSD source (~1700 K), PSD itself does not sufficiently account for most of our temperatures, specifically near the full Moon period. Note that even though PSD is a nonthermal source (Yakshinskiy and Madey, 1999, 2004; Schmidt, 2013), we see no evidence of a high-energy wing associated with non-Maxwellian profiles in our data. Alluding to (1) in the first paragraph of this Section, an ongoing speculation is that high temperatures during times when the FOV is pointed in the direction of the lunar sodium tail could be the result of seeing red-shifted atoms in the lunar tail. The proposed argument is that during full Moon sodium atoms with larger redshifts (as they move downwind of the Moon) will be observed, thereby widening the overall line profile and increasing the

effective temperature. Although this redshifted Doppler component is expected to distort the observed profile near the red wing of the line, no such asymmetry has been detected. However, the increase in continuum levels due to scattered moonlight near full Moon is rightfully acknowledged and does make the detection of a red wing problematic – especially if the effect due to geometry on linewidth is minimal. Nevertheless, careful inspection of our line profiles along with fits and residuals do not show asymmetry. This indicates that even though there can be some contribution from sodium tail atoms, it cannot be the bulk of atoms in our FOV.

As mentioned in (2) earlier, we can empirically determine the effect due to viewing geometry as the observational LOS intersects the extended lunar sodium tail during full Moon. To investigate this effect of geometry on our linewidths, we obtain the velocity of the sodium atoms in the lunar reference frame. Velocities in the lunar frame of reference are calculated using the shift in emission position from the rest wavelength and adjusting for the Earth-Moon motion. Sodium velocities calculated for FOV at Limb observations (an altitude of 168 km) are shown in Figure 4.3. Measured radial velocities at the limb show that waxing phase data are overall more redshifted than waning phase data and reach a maximum redshift right before full Moon.

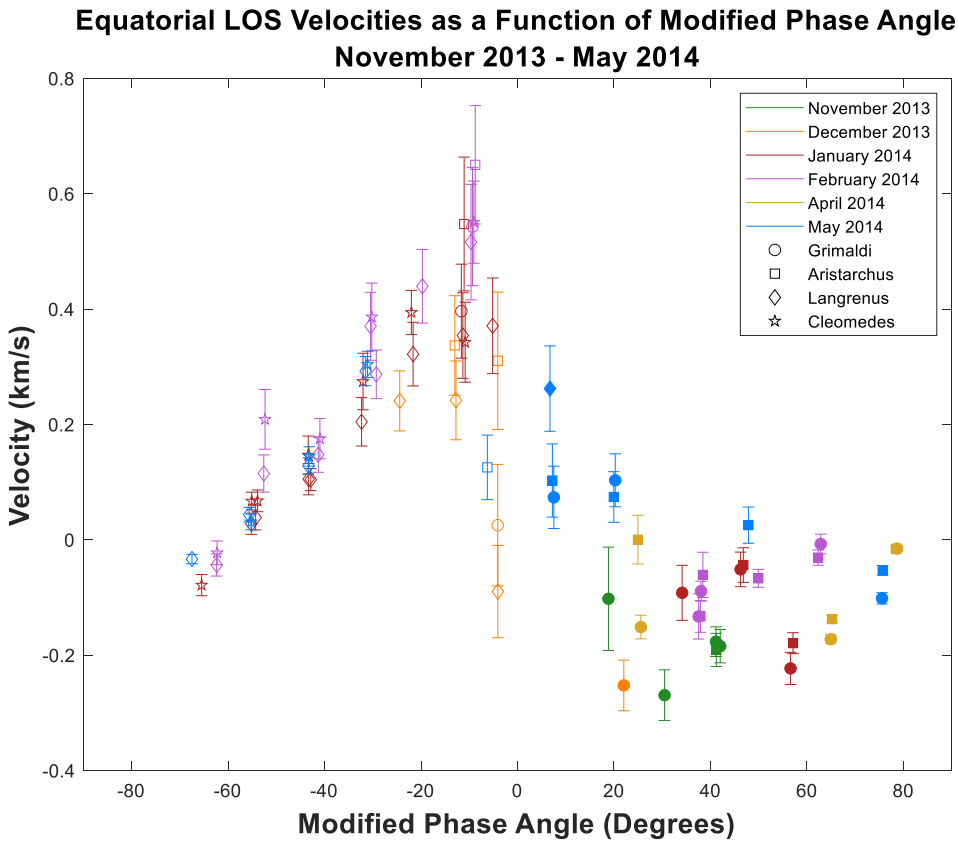

Figure 4.3: Sodium velocities in the lunar reference frame for data taken at the limb (Kuruppuaratchi et al. 2018). Line of sight (LOS) velocities were corrected by using the self-reversal feature in the sodium calibration lamp to determine the rest wavelength of sodium and then correcting for Earth-Moon motion. The maximum redshift of approximately 0.6 km/s occurs right before the full Moon. The general trend suggests that there is a linear increase in velocities for the waxing phase data toward full Moon and then rapidly decreasing after full Moon with more scatter in the waning phase data. Waning phase data show a larger scatter compared to waxing phase data.

To estimate the increase in linewidth due to viewing geometry/geometrical effects, a series of s-resolved sodium doublet synthetic emission spectra with equal intensities but shifted radial velocities (Figure 4.4) were coadded and fit. The s-resolved doublet is separated by 0.0198 Å (1.008 km/s) in a 3:5 intensity ratio (See Section 3.2). The width of each doublet component is 1.73 km/s corresponding to a temperature of 1500 K. The model spectra are a sum of Doppler-shifted spectra where each new sodium emission region is

shifted by 0.15 km/s (half a spectral bin). The final model spectrum has nine coadded spectra from 0 to 1.2 km/s to match the maximum velocity shift of 0.6 km/s as seen in our at-limb velocity data (refer to Figure 4.3). The model spectra are convolved with an IP and fit to determine the increase in linewidth due to the sum of different radial velocities. The results of these coadded synthetic spectra show an increase in linewidth of up to 0.3 km/s—an increase that does not adequately represent the increase in linewidth as we move toward smaller phase angles. While it is unrealistic to expect each contributing velocity component to have equal weight, we have made an important conclusion that the bulk of the measured increase seen at small phase angles is not due to geometrical effects of *looking down the tail* (e.g., Line et al., 2012); rather it represents a genuine increase in scale height owing to higher-velocity sodium atoms. Additionally, we see an increase in temperature going towards full Moon for potassium data as well (Section 5.2) and potassium, as we know, does not have a tail like the sodium exosphere as it is not affected by radiation pressure due to its heavier mass. Therefore, the increase in linewidth cannot be due to radiation pressure accelerating atoms as we move closer to the limb/terminator sides. Rather, the increase in temperatures represent a genuine physical process that is phase dependent and tied to the location of the source for each species.

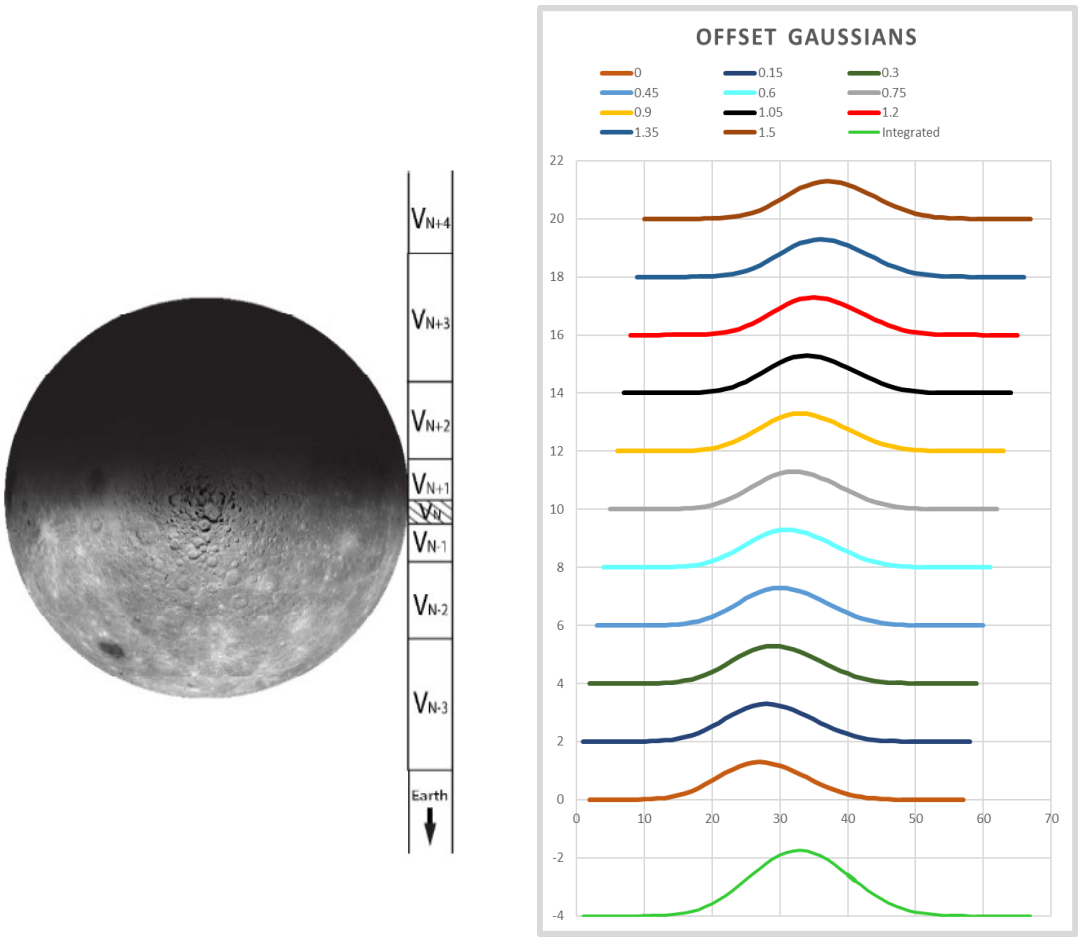

Figure 4.4: (left) A schematic view of the field of view, during full Moon, as viewed from above the lunar North pole (Kuruppuaratchi et al. 2018). For purposes of this model calculation the line of sight is divided into Sections of equal column density and temperature (i.e., equal contributions to the sodium emission line profile) but with different radial velocities. The line-of-sight length for each Section is arbitrary, but adjacent Sections have a velocity difference of 0.15 km/s. For a total velocity range of 0–1.2 km/s or nine Sections, the increase in line profile is 0.3 km/s. The shifted profiles are shown on the right along with the final integrated line profile at the bottom in green. The final integrated line shows that even with increased contribution of red-shifted profiles in our LOS, the final line profile does not show significant line broadening – not enough to explain the increase in linewidths from quarter to full Moon.

4.1.2. Modeled Linewidth and Center with a Particle Transport Model of Atoms

A complementary way to assess the effect of viewing geometry (Section 4.1.1) is to use a model of exospheric particle transport. Here the sodium transport model of Sarantos et al. (2010) was used to simulate velocity distributions of sodium atoms and to

illustrate trends as a function of the lunar phase angle. The version of the model used here accounts for the evolution of the velocity distribution of exospheric ejecta with altitude and the effects of gravity based on the distance of the neutrals from the Moon (Hartle, 1971) but does not account for radiation pressure and should only be considered as an initial step toward an interpretation. The goal of utilizing this model is to probe the kinematics of our observational data and determine whether the increase in linewidth towards full Moon is due to a physical process. This model assumes a sticking coefficient of 1, that is, sodium atoms efficiently lose their energy upon contact with the surface and come to a full stop after one bounce. Initial model runs consisted of a symmetric atmosphere with the source function centered at the subsolar point and having a cosine dependence with SZA. The velocity distribution functions of atoms leaving the surface were assumed to be Maxwellians, with different source temperatures (1500, 3000, 5000, and 10,000 K). For each source, the distribution of LOS velocities as a function of velocity toward the Sun-Moon direction, which controls the g value (emission per atom per second) (Killen et al., 2009), was computed for different look directions of an Earth observer (lunar phase angles) by backtracking particles within three lunar radii of the tangent point, which was considered to lie at an altitude of 100 km.

The modeled linewidth as obtained from the model velocity distribution function, shown in Figure 4.5, indicates that the measured linewidth for the same source process should increase from quarter Moon (subsolar points) to full Moon (terminator side) since only the hottest particles with the largest ballistic range can travel from subsolar latitudes to the terminator/limb. This explains the increase in linewidths we see as we move to smaller phase angles. The increase in linewidth is expected to be fractional at small

temperatures (~25% for an initial distribution of T = 3000 K from the lunar surface), but the linewidth almost doubles for T = 10,000 K (a proxy for sputtering).

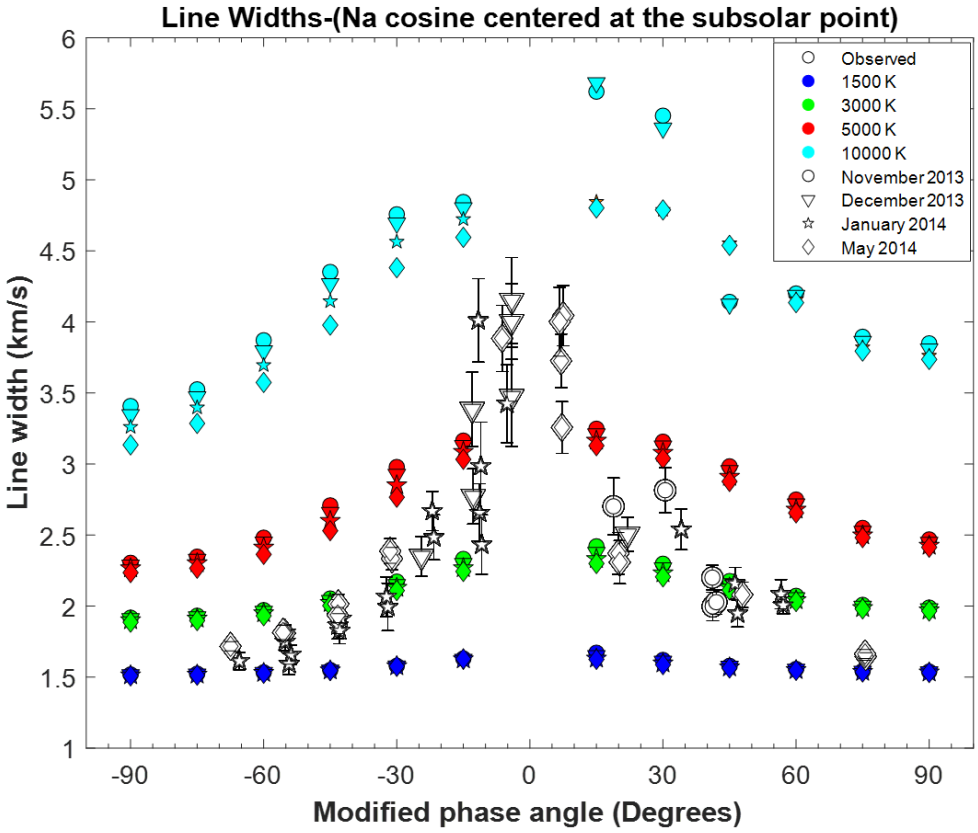

Figure 4.5: Sample symmetric exosphere model runs for a source with T = 1500, 3000, 5000, and 10000 K to assess geometric effects, for linewidth as a function of modified phase angle (Kuruppuaratchi et al. 2018). No simulations were performed for lunar phases < 10°

For hot source temperatures, the measurements should retrieve different widths for different months, particularly in waning phases, due to increased light scattering values of particles moving toward the Sun as the Moon-Sun velocity changes, an effect which was quantified using Jet Propulsion Laboratory ephemeris data for November, December, and May 2014. This effect is negligible for lower source velocities because an insignificant difference between particles that head toward and away from the Sun is found if escape

rates are small. Linewidths on the order of 3 km/s are expected when a source with an impact-like temperature (5000 K) is considered or more if sputtering is considered. The increase in linewidth for a 3000 K and 5000 K source is approximately 0.5 and 0.8 km/s, respectively (Figure 4.5) and is larger than the ≤ 0.3 km/s increase in linewidth estimated from the possible velocity dispersion along the LOS in Section 4.1.1 (Figure 4.4). These two different approaches indicate that the observed increase in linewidth at decreasing phase angle is not only due to changes in viewing geometry but rather signifies changing relative importance of the considered source processes during a lunation.

The Doppler velocities provide an important and previously unavailable constraint on velocity distribution functions, and the asymmetry in the Doppler shift between waxing (dusk) and waning (dawn) phases might indicate a nonuniform source distribution. For instance, a density asymmetry between dusk and dawn was measured by Kaguya data and indicated that sodium and potassium peak ion fluxes showed a 10° shift toward dawn (Yokota et al., 2014).

The same transport model used to estimate the increase in linewidth going from near quarter phases to small phase angles is used here in the interpretation of the LOS velocity data. Model Doppler shifts (Figure 4.6) approximately reproduce our at-limb velocity data (see Figure 4.5) when sources with Maxwellian ejection speed distributions with temperatures up to 5000 K are used, whereas sputtering by itself (10, 000 K) would produce excessive motion toward the observer. These simulations suggest that sodium atoms from a combination of PSD, impact vaporization, and sputtering sources are consistent with the trends reported in our measurements. The qualitative agreement

between this initial model and our data provides additional confidence in our data acquisition and reduction methods.

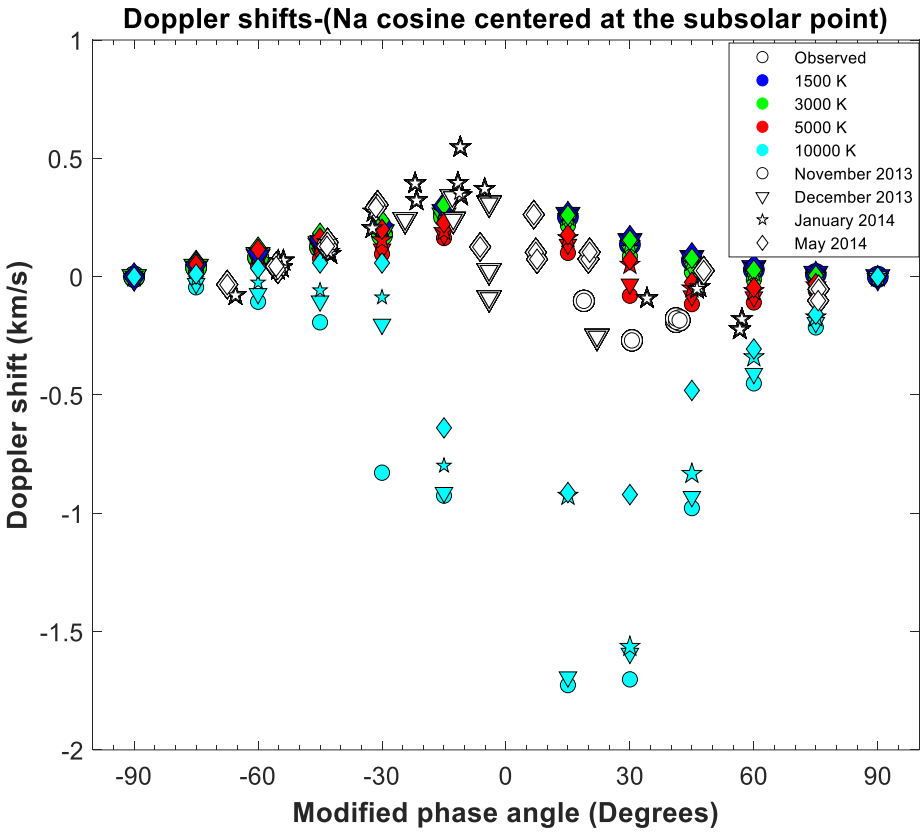

Figure 4.6: symmetric exosphere model runs for Doppler shifts as a function of modified phase angle (Kuruppuaratchi et al. 2018). No simulations were performed for lunar phases <10°.

4.1.3. A Comparison of Sodium Exospheric Temperatures: Linewidth Derived Effective Temperatures and Previous Ground-Based Scale Height Derived Temperatures.

To gain a better understanding of the data presented in Figures 4.1, 4.2, and Table 4.1 it is important to compare this dataset with earlier lunar sodium exospheric work. I first

compare: (1) linewidth derived effective temperatures from our observing campaign, as shown in Mierkiewicz et al. (2014), and (2) scale height derived temperature results from other ground-based observations.

The earlier work of Mierkiewicz et al. (2014) compared their temperature results of Potter et al. (2000) where both studies showed temperatures increasing going from large phase angles (greater than ~ 40^{o}) towards full Moon (small phase angles). Linewidth derived temperatures by Mierkiewicz et al. (2014) ranged from 3260 ± 190 K near full Moon to 1000 ± 140 K at a phase angle of 42° and Potter et al. (2000) derived a temperature of 2900 K near full phase (4.3°), decreasing to 1400 K at phase angles of 50°–76°. In comparison, the linewidth derived temperatures presented here range from 2500 to 9000 K during magnetotail passage. Figure 4.7 compares the range of temperatures derived from our equatorial data (including uncertainties) plotted in gray along with the smoothing spline, to the scale height derived temperature data compiled by Sarantos et al. (2010), the linewidth derived temperature data of Mierkiewicz et al. (2014), and the scale height derived temperature data of Sprague et al. (2012). Overall, the upper range of the linewidth derived temperatures at small phase angles are higher than those of Mierkiewicz et al. (2014) as well as the scale height derived temperatures (e.g., by about a factor of 2–3 during magnetotail passages). The waxing and waning phase scale height derived temperatures of Potter et al. (2000) and the waning phase linewidth derived temperatures of Mierkiewicz et al. (2014) agree with the lower range of our data set. Note that the trend of increasing temperatures toward full Moon (small phase angles) is seen clearly in the data from Potter et al. (2000) and Mierkiewicz et al. (2014) but to a lesser extent in data from Sprague et al. (2012).

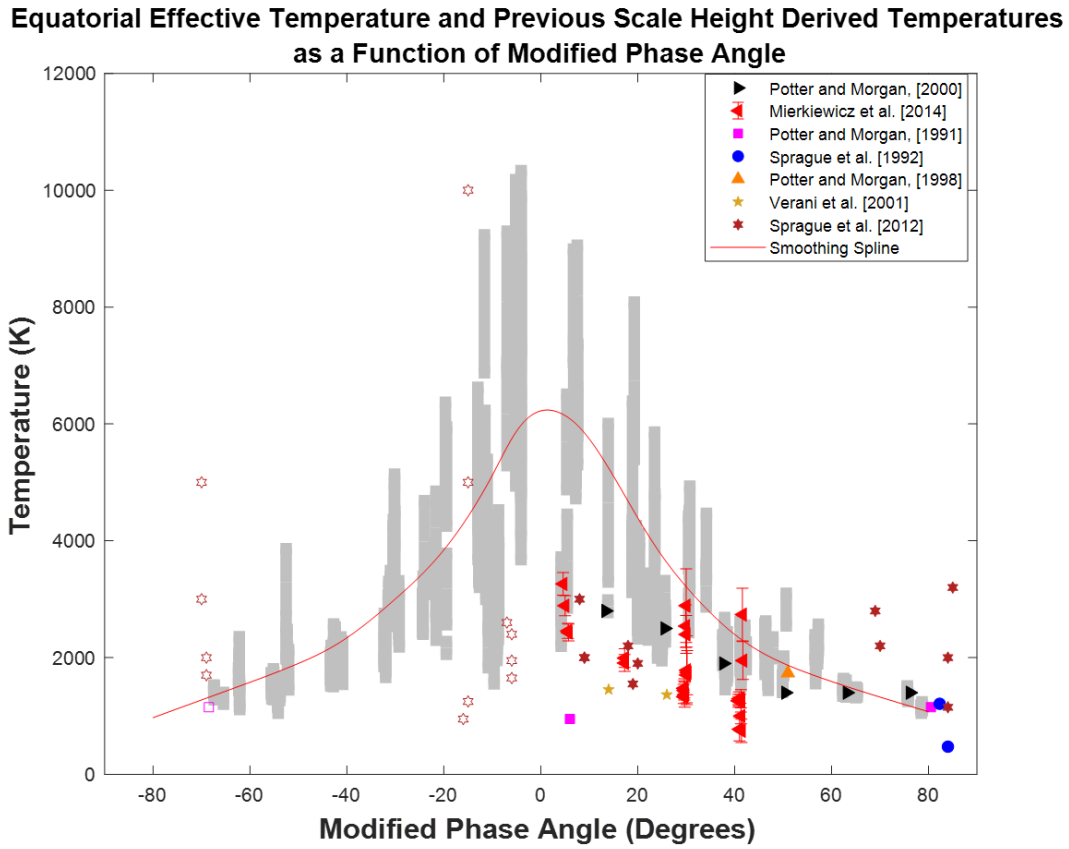

Figure 4.7: Scale height derived temperature data compiled by Sarantos et al. (2010); data from Sprague et al. (2012) and the linewidth derived temperature data of Mierkiewicz et al. (2014) are also included (Kuruppuaratchi et al. 2018). The data range (including error bars) for our equatorial data is plotted in gray along with the smoothing spline of Figure 4.2. Waxing and waning phase derived temperatures of Potter et al. (2000) and the waning phase temperatures of Mierkiewicz et al. (2014) agree with the lower range of our data set.

An addition to this previous ground-based studies shown here is the coronograph data of Killen et al. (2019); (2020) where sodium scale heights on the waxing and waning limbs as a function of lunar latitude were discussed. From these two studies, the temperature ranges are between 2255 – 6765 K (Killen et al., 2019) and 3600 – 8100 K (Killen et al., 2020), both in agreement with the linewidth derived effective temperatures shown as grey error bars in Figure 4.7. Note that some of the studies are not representative

of strictly equatorial data, such as Sprague et al., (1992);(2012), Killen et al., (2019); (2020) but their overall range of temperatures are useful for comparison with our linewidth derived effective temperatures.

A possible explanation for the difference in exospheric temperatures between our linewidth derived effective temperatures and scale height derived temperatures especially during magnetotail passage, is the difference in the two observing methodologies itself. Recall from Section 1.2.2 that linewidth measurements differ from observed altitude (scale height) distributions by offering a direct probe of the bulk radial kinematics (velocities) of the observed exospheric column at specific altitudes. In that regard, I expand on Section 1.2.2. on what the classical definition of the temperature of an exosphere encapsulates and the assumptions that go into it.

The theory of exospheres described here is adapted from Chapter seven in Chamberlain and Hunten (1987) and should be consulted by the reader for an in-depth explanation. An exosphere is the uppermost fringes of a neutral planetary atmosphere and the exobase, or the base of an exosphere, is defined as the height where the overhead integrated density accounts for one mean free path for a fast atom (Chamberlain and Hunten, 1987). For a classical exosphere, the exobase is located at the radius of the planetary center since the scale height, H is constant. The classic exosphere is one that has a Maxwellian distribution of velocities at and below the exobase and with no collisions above that level (Chamberlain and Hunten, 1987).

The initial assumption is that there are negligible collisions above the exobase and below the exobase collisions maintain a complete Maxwellian distribution of velocities. In the tenuous regions where the atomic collisions are rare, the spatial and momentum

distribution of particles is governed by Liouville's equation. The solution to Liouville's equation for a classical exosphere is therefore the same form as the solution to an atmosphere in hydrostatic equilibrium – that is the barometric law. The solution, which is the generalized form of the barometric law from Liouville's equation, depends upon the assumption that the Maxwellian distribution holds even in collision-free regions, provided that the momenta extend over all possible values (Chamberlain and Hunten, 1987). If, however, the entire range of molecular momenta is not present, which is the case at large distances above the exobase, the barometric law does not apply. In reality, the pressures at large distances are directional and the mean kinetic energy per atom decreases, ergo the barometric law breaks down. Since in an SBE the particles are constantly being replenished and lost and not at the same rate, the exosphere is not strictly in hydrostatic equilibrium. To treat the density distribution accurately, the individual orbits of particles in the exosphere need to be investigated separately. As such, for a collisionless system still with a Maxwellian distribution, the particle orbits are separated into three categories: ballistic, satellite, and escaping. Chamberlain and Hunten (1987) developed the model for quasi-collisionless exospheres that can be numerically integrated along a given LOS to obtain surface densities of the gas, the scale height derived temperature.

For an SBE, like the Moon, the exobase is set by a solid surface instead of an atmospheric layer. All the classical theories of exospheres assume that the lower boundary of the exosphere is the atmosphere – like Earth's exosphere. When the exospheric base is set with a solid surface, certain problems arise since particles interact with a solid surface differently than when they interact with an atmospheric layer. On an SBE, when particles hit the surface, they can interact with the surface immediately and stick or bounce, they can

release other particles, they can react chemically. If the particles do not stick and are reemitted to the exosphere, there is no reason to assume that they will do so with a Maxwellian distribution. It is entirely possible that when a particle interacts with the surface, there could be chemical reactions (for elements such as Hydrogen, Sodium, and Oxygen) (Killen and Ip, 1999) or due to momentum transfer to a lattice structure (Killen and Ip, 1999), thereby not guaranteeing thermal equilibrium to be reached.

While the collisionless system was considered by Chamberlain and Hunten (1987), no exosphere is completely collisionless. However, since collisions are still rare in an exosphere, the source atoms maintain characteristic distributions functions dependent on factors such as radiation pressure (photon-atom collisions and momentum transfer), momentum transfer upon collision to the lattice structure in the surface, loss processes (e.g., escape, ionization, photodissociation, sticking to the surface), the mass of the individual particle, and nature of the source process (including energy and distribution) (Killen and Ip, 1999). Note than in a complete Maxwellian distribution, these collisions that alter the momentum coordinates from one state to another are exactly balanced by inverse collisions that alter momentum in from the latter state to the starting state – such is the assumption of thermodynamic equilibrium. In this case, however, compensating collisions do not occur and the question to ask becomes what the new "equilibrium" state is. Trajectories in a collisionless exosphere are classified into three orbits and the distribution function can then be strictly Maxwellian only if all three orbit classes are fully represented, and if the escaping particles are fully replaced by incoming source particles (Sprague et al., 1992). However, on the SBE, this is not true as the three classes of particles on different orbits are not fully represented – for instance, the short atmospheric lifetime for alkali metals, such

as sodium and potassium, means that the population of particles on satellite orbits are essentially absent (Sprague et al., 1992).

Assumptions on the distribution of the exosphere in terms of how much of the three categories of particles are present can be made using the methods described in Chamberlain and Hunten (1987) through the use of partition functions for each category. Sprague et al. (1992) used the partition functions for the satellite and escaping particles and estimated a relation between the real temperature and the apparent scale height. The apparent scale height was the scale height obtained by fitting a line of best fit to a semilog plot of intensity as a function of altitude. This equation is shown in A (2) of Sprague et al. (1992) and in Section 4.14. I discuss the use of this equation to our lunar sodium data. Note that this method of reporting temperatures is different than the Chamberlain temperatures or "apparent" temperatures (obtained by using the scale height, $H = kT/mg$) which assumes that particle populations on all three orbit types are fully represented. This is an important distinction to keep in mind in Chapter 6 where I compare the latitudinal dependence of our linewidth derived effective temperatures to the coronograph results of (Killen et al., 2019; 2020).

A solution to departures from a Maxwellian distribution near the exobase has been proposed (refer to Chapter 7.2.3. in Chamberlain and Hunten, 1987) with the analytical approach being the use of the Boltzmann equation as an extension to Liouville's equation to include effects of collisions. While it is possible to obtain a first-order solution to this analytical equation, it is not adequate, especially if departures from a Maxwellian are large. To obtain a more accurate solution, the popular Monte Carlo method is employed where

each particle trajectory can be modeled independently with various conditions applied, such as effects of radiation pressure and gravity.

Many observational studies for the lunar exosphere report temperatures from fitting intensity derived line of sight abundances based on the Chamberlain model for collisionless atmospheres. Their temperatures are scale height derived or Chamberlain temperatures which are reasonable for the cold component of atoms in the exosphere. However, for the hot component (expected at high altitudes), departures from a Maxwellian might be large enough that this temperature might not be accurate. In such cases, the Monte Carlo method is best. As shown in Section 4.1.2., our results are indeed interpreted with the use of a Monte Carlo model. In Section 5.1, I discuss the use of the same Monte Carlo model but with solar radiation pressure effects added alongside gravitational effects, for our potassium results.

4.1.4. Empirical Scale Height Derived Temperatures

Considering what was discussed previously (Section 4.3.1.1), here I discuss the scale height derived temperatures in Figure 4.7 along with new scale height derived temperatures from the coronograph study (Section 3.2.1.1). This should provide the reader with a better understanding of the meaning of a temperature for an exosphere, and what this means in terms of our effective temperatures. Additionally, I also discuss our empirically determined scale height derived temperatures, by fitting an exponential to our relative intensity measurements. The trends in our relative intensity measurements are later discussed in Section 4.4.

Sprague et al. (1992) use the Chamberlain quasi-collisionless theory for exospheres where they also and estimated what the LOS abundances should be using the partition

functions for ballistic and satellite populations. The same assumption is used in their later work (Sprague et al., 2012) Potter and Morgan (2000) used a similar approach but used the partition functions for ballistic and escape populations while ignoring the satellite population. A summary of the assumptions used to obtain exospheric temperatures for the studies in Figure 4.7 along with newer results from a coronograph method (Killen et al., 2019;2020) are summarized in Table 4.2.

Table 4.2: *Summary of data analysis methods used in previous studies to obtain temperatures, shown in Figure 5.7.*

Study	Assumption for obtaining temperatures	Radial distance of observations from lunar surface (km)	Scale height (km)	Scale height derived temperature (K)
Sprague et al. (1992)	Integrate over a LOS to obtain densities, based on Chamberlain theory. Some assumptions were made for a few of the integrals where the barometric density was multiplied by the partition functions for the ballistic and escaping components.	100 to 450	119 - 1112	476 - 6878
Sprague et al. (2012)	a) Obtain scale heights from fitting a line to plot of logarithmic intensities vs geopotential height. This is based on Chamberlain theory. b) Numerically determine LOS abundances using Chamberlain model for various temperatures in steps of 50 K. Same mathematical procedure as their previous work (Sprague et al., 1992).	Up to 1800	212 – 5580	950 – 25,000 **

** Temperatures as large as 25,000 K were not included in Figure 4.7

Potter and Morgan (1991)	Fit altitude distribution of intensity with a simple two parameter model. The LOS intensity was estimated for a range of temperatures, including Jean's escape and the temperature that best fit the observational data was chosen. Based on Chamberlain model.	50 to 1500		
Potter and Morgan (1998)	Fit line of best fit to semilog plot of intensity as a function of altitude.	Up to 1200	44 (10) - 510 (19)	218 - 1638
Potter and Morgan (2000)	Numerically integrate over a LOS to determine surface abundances and temperature using theChamberlain model (same as Sprague et al., 1992) but included ballistic and satellite orbits. More accurate than Sprague et al., 1992 results.	100 to 4000	200 - 700	1200 – 2900
Verani et al. (2001)	Intensity extrapolated to the lunar surface and temperature calculated using H = kT/mg.	50 - 600	284 (34) – 345 (54)	1289 (171) – 1572 (249)
Mierkiewicz et al. (2014)	Direct velocity resolved measurements – linewidth derived effective temperatures.	Up to 1100	N/A	1000 (135) – 3260 (190) ***
Killen et al. (2019)	Intensity extrapolated to the lunar surface and temperature calculated using H = kT/mg. Scale height, H, obtained through a simple exponential fit to the log of the intensity vs altitude.	143 - 1738	500 - 500	2255 - 6765
Killen et al. (2020)	Intensity extrapolated to the lunar surface and temperature calculated using H = kT/mg. Scale height obtained the same way as Killen et al. (2019).	143 - 1738	800 - 1800	3600 - 8100

*** Effective temperature

Based on the methodology of the studies shown in Table 4.2, we have used our relative intensities as a function of tangent altitude with an exponential fit (Figure 4.8.), to estimate the LOS scale height and their corresponding apparent temperatures. From previous Sections, we know that our linewidth derived effective temperature is on average hotter than scale height derived temperatures. The purpose is to see if there is a difference between our linewidth derived temperatures and our empirically determined scale heights derived temperatures.

Relative intensity as a function of altitude for three data sets with good altitude coverage on 13 May 2014 off the Cleomedes Limb, 15 May 2014 off the Langrenus Limb, and 20 April 2014 off the Aristarchus Limb are shown in Figures 4.8a–4.8c, respectively. Good altitude coverage consists of observations made at least to over a 1000 km. These data sets were used to calculate an apparent scale height using the methodology found in Sprague et al. (1992, equation A2) which is based on the Chamberlain and Hunten (1987) model. The apparent scale heights, corresponding Chamberlain temperatures, and the average linewidth derived temperature for a data set, are given in Table 4.3.

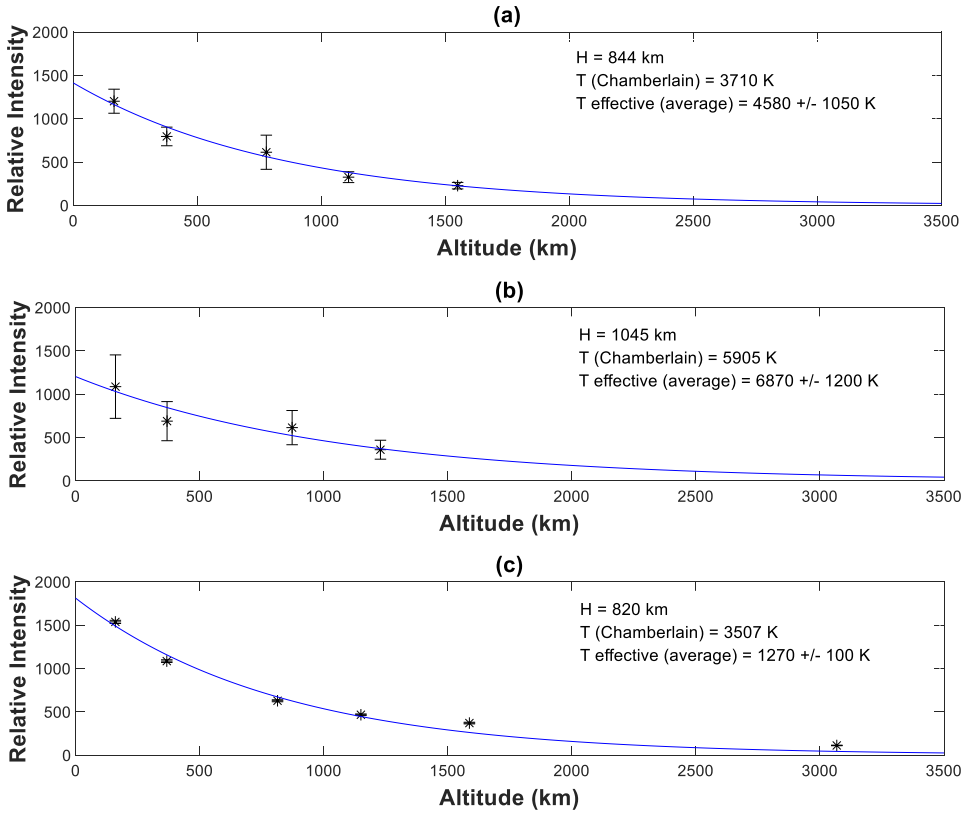

Figure 4.8: Relative intensity as a function of altitude for observations taken off the (a) Cleomedes limb on 13 May 2014 (phase ~ 18°), (b) Langrenus limb on 15 May 2014 (phase ~ 7°), and (c) Aristarchus limb on 20 April 2014 (phase ~ 65°) (Kuruppuaratchi et al. 2018). These data sets contain altitudes not included in the temperature analysis presented in this dataset, to effectively obtain scale height. The three nights used here sample latitudes from approximately 9°N to 24°N as the field of view is moved away from the Moon. The method in Sprague et al. (1992) was used to calculate the apparent scale height and scale height derived temperature. Note that the form of the exponential fit in blue is $y = a\exp(bx)$, where a and b are the coefficients, and the scale height is found by taking the reciprocal of b.

Table 4.3: A*pparent scale heights, corresponding chamberlain temperatures, and linewidth derived temperatures (Kuruppuaratchi et al. 2018)*

Figure	Date	Limb	Phase (degrees)	Apparent scale height (km)	Chamberlain temperature (K)	Linewidth derived temperature (K)
11a	13 May	Cleomedes	18	844	3710	4580 ± 1050
11b	15 May	Langrenus	7	1,045	5905	6870 ± 1200
11c	20 April	Aristarchus	65	820	3507	1270 ± 100

Our empirically determined scale height temperatures vary by a factor of 1.2 (Figures 4.8a and 4.8b) to 3 (Figure 4.8c) from the average linewidth derived temperature. The differences between our scale height derived temperatures and linewidth derived effective temperatures indicate that methodology may play a role in explaining the difference between our data and previous scale height measurements. Our measurements are a direct probe of the LOS velocity of the gas at a given altitude while a scale height obtains a single temperature obtained from various altitudes along a slit. Previous ground-based measurements produced scale heights on the order of ~120 km for sodium (Potter & Morgan, 1988a; Sprague et al., 2012) on the lower end, ~ 600 km (Sprague et al., 2012; Killen et al., 2019) on the mid-range, and 1500 km on the higher end (Sprague et al., 1992; Killen et al., 2019). A two-component model was used by both Potter and Morgan (1988a) and Sprague et al. (2012) to explain the hot and cold components of the lunar exosphere. Our observations sample sodium atoms with varying velocity distributions (Section 4.1.2) but are more sensitive to the nonthermal or hot component due to our large FOV. These

hot component velocity distributions could be due to sputtering, a nonthermal PSD population, or impact vaporization.

4.2. Solar Cycle Effects

Here I discuss our temperatures as a function of solar flux in order to determine solar cycle effects as it is possible that this plays a role in explaining the difference in our linewidth derived effective temperatures compared to earlier work. To explore the cause of the difference between data sets, all data in Figure 4.7 were plotted alongside the solar $F_{10.7}$ flux to indicate where in the solar cycle each data set was collected (see Figure 4.9a). $F_{10.7}$ data were obtained from the OMNI database (https://omniweb.gsfc.nasa.gov) and the Natural Resources of Canada database (http://www.spaceweather.gc.ca). Figure 4.4b shows the detrended temperature data presented here along with $F_{10.7}$ flux.

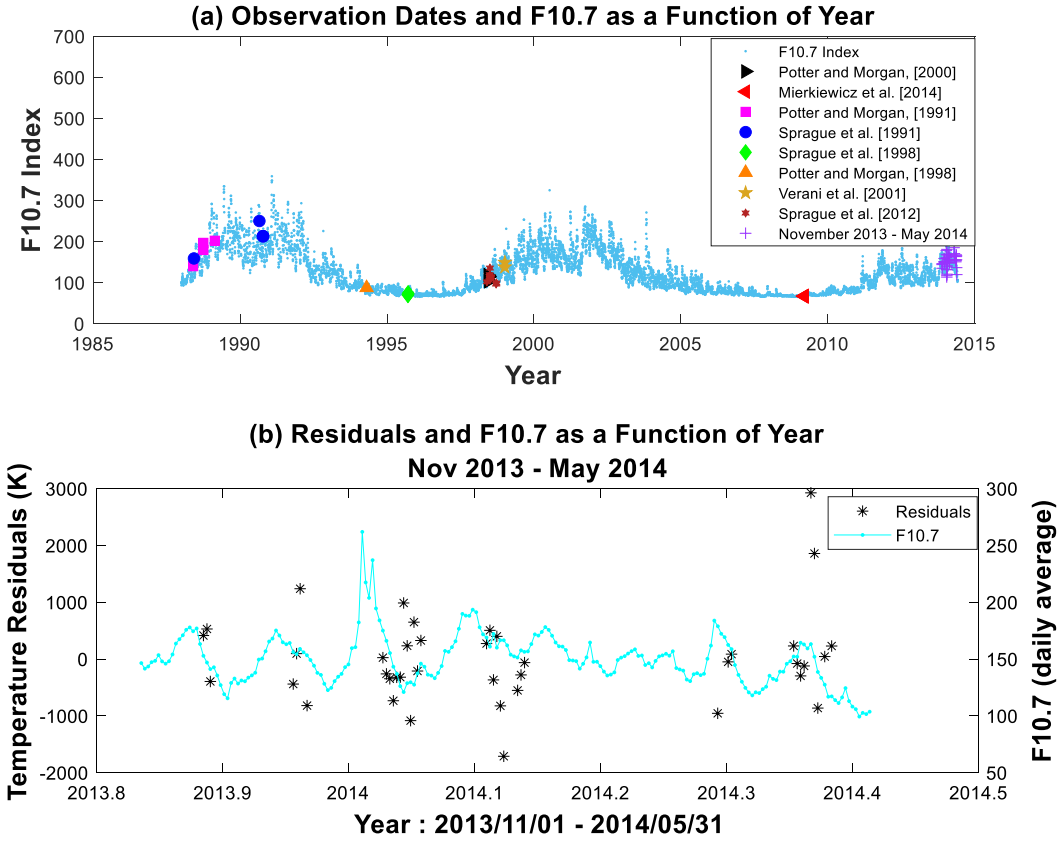

Figure 4.9: (a)Data of Figure 4.3 and solar cycle as indicated by $F_{10.7}$ flux (Kuruppuaratchi et al. 2018). (b) Temperature residuals as a function of $F_{10.7}$ daily averages. Residuals were obtained from subtracting a smoothing spline from temperature data averaged by day.

As seen in Figure 4.9a, the data of Potter and Morgan (1991) and Sprague et al. (1992) were collected close to solar maximum (cycle 22), whereas that of Sprague et al. (1998) and Potter and Morgan (1998) were collected close to solar minimum (also cycle 22). Data from Verani et al. (2001), Potter et al. (2000), and Sprague et al. (2012) were collected early in solar cycle 23, with the solar maximum in 2001. Using the same FPS instrument, the data from Mierkiewicz et al. (2014) were collected during solar minimum (cycle 24) while the data presented here were collected during solar maximum (cycle 24).

We investigated the correlation to the solar $F_{10.7}$ flux by detrending our 2013–2014 data and plotting the residuals alongside $F_{10.7}$ flux daily averages (see Figure 4.9b). The detrending was done by binning data by day then fitting a smoothing spline to obtain residuals. We do not find an obvious correlation to small variations in solar output within this November 2013 to May 2014 period, although correlations to larger variations over a solar cycle remain possible. There is not enough data in 2009 (from Mierkiewicz et al., 2014) to determine a proper trend for the residual correlation with $F_{10.7}$ flux. Since data were limited in 2009, we combined 2009 data with the 2013–2014 data and repeated the detrending procedure, but no correlation was found. Additionally, a more involved long-term correlation was performed using Acceleration, Reconnection, Turbulence and Electrodynamics of the Moon's Interaction with the Sun (ARTEMIS) proton and alpha/proton data but that study remains inconclusive too.

4.3. Effect of FOV size on Linewidth

The main trends here are reported through measurements made from our 3 arcmin FOV. During this period of 6 months, a small subset of data was collected with a 1 and 2 arcmin FOV (~112 and 224 km, respectively). The smaller FOV measurements are shown along with the error bars of the 3 arcmin data in Figure 4.10. While these data are within the range of 3 arcmin results, most 2 arcmin datapoints are systematically cooler. This is because the smaller FOV measures relatively more atoms closer to the surface than the larger FOV and thus potentially a cooler velocity distribution. Note that while there is a minor difference at some phases between the different sized FOV, they still fall within the overall range of temperatures and are not distinct. Later in Chapter 5, I combine 2 and 3

arcmin data for temperature results as the effect between the different FOV are not statistically significant enough to separate them.

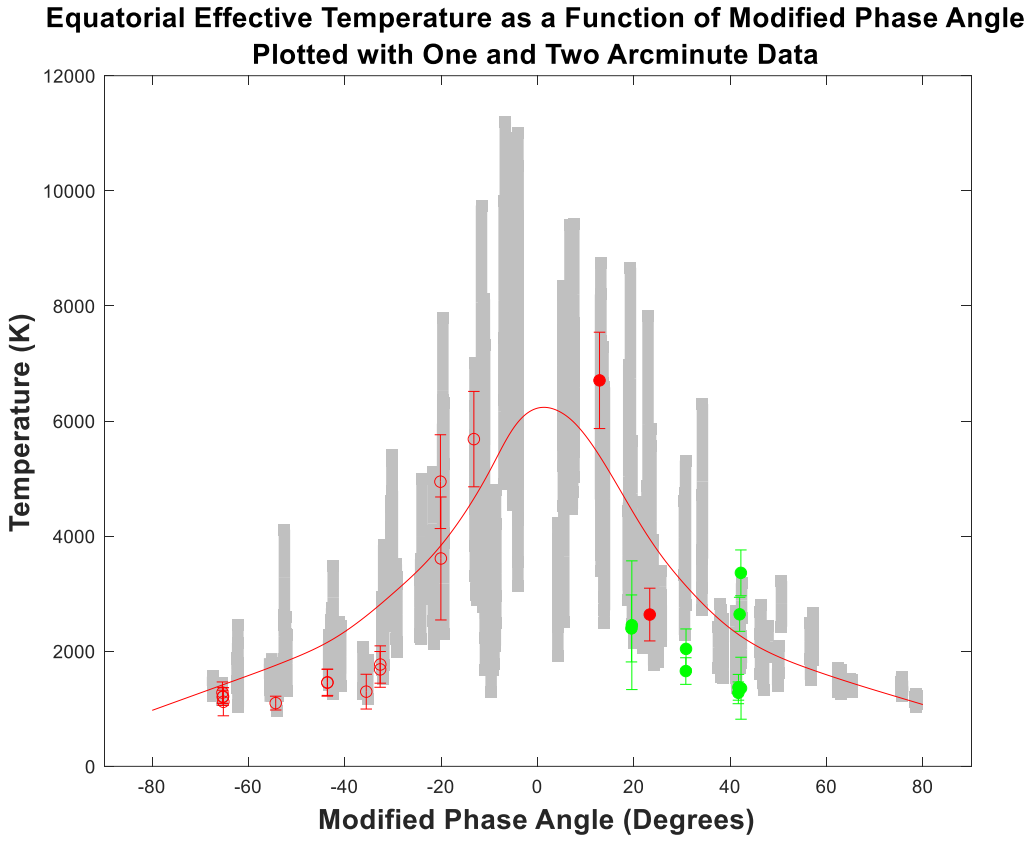

Figure 4.10: Gray error bars and the smoothing spline of Figure 4.2 plotted along with 1 (green) and 2 (red) arcmin field-of-view data points (Kuruppuaratchi et al. 2018). Open symbols represent waxing data, while filled symbols represent waning data.

4.4. Limb Relative Intensity Data and LADEE UVS Results

In this Section I discuss relative intensity as a function of phase for data taken at the limb while also comparing trends to LADEE UVS results. Relative intensities as a function of phase for all equatorial data (limb only) are shown in Figure 4.11. Our relative intensities have been corrected for Moon-Sun radial velocity shifts. Our relative intensities show large variability during magnetotail passage (0–30°) with a general trend of relative

intensities increasing from full Moon to near quarter phases. The spectral fit uncertainties for waning phase observations are smaller than those of the waxing phase due to a reduction in scattered light off the Selenographic West limb of the Moon (observations offset near Grimaldi and Aristarchus) which has a lower albedo due to the larger area of the surface covered by darker lunar maria.

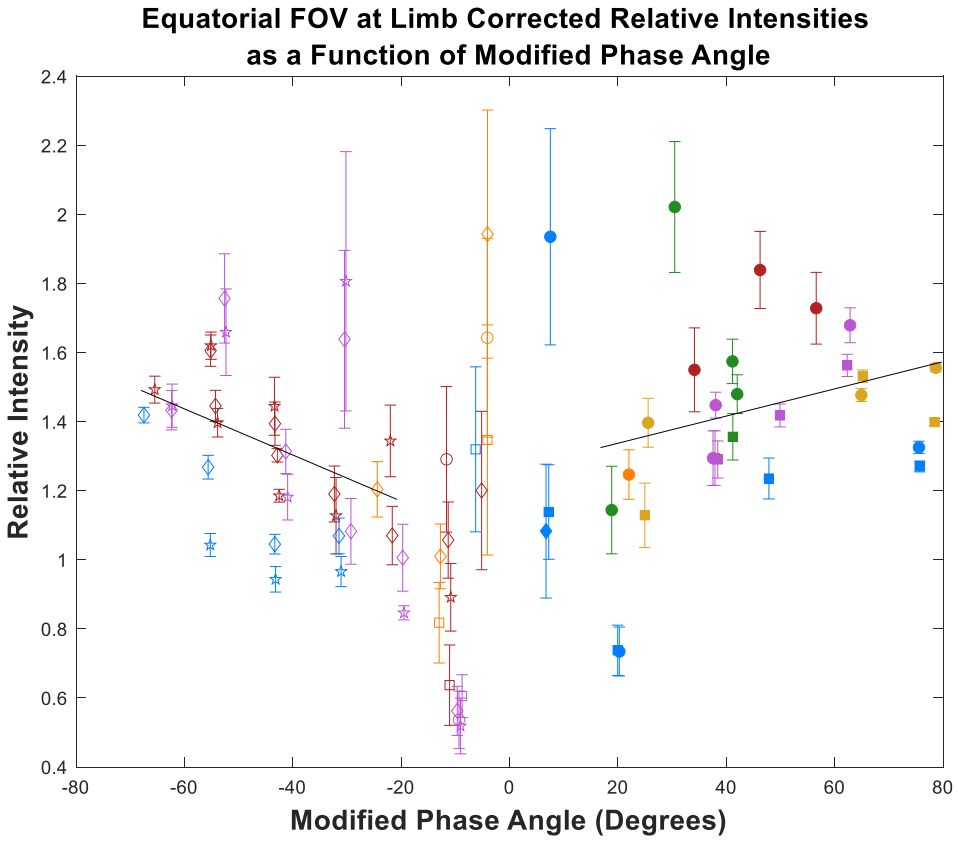

Figure 4.11: Relative intensity for limb equatorial data as a function of phase angle. Relative intensities have been divided by 1,000 (Kuruppuaratchi et al. 2018). The legend used in Figure 4.3 can be used here. Black lines highlighting the trends in intensity values between phase angles 20° and 80° for waxing and waning data are overplotted. While the month-to-month relative intensity remains around a value of 1.4, May 2014 is relatively flat compared to the other months. The overall consistent pattern is that the relative intensities increase from full Moon toward quarter phases, with waning phase intensities being about 10% higher than waxing phase intensities.

We know from prior discussions that during magnetotail passage the Moon usually resides in the cooler and more rarified plasma of the lobes but briefly encounters hotter and denser plasma during plasma-sheet crossings. These crossings may temporarily augment the exosphere via ion sputtering, electron-stimulated desorption, or other plasma impact effects (Wilson et al., 2006) and may explain the large variability in intensity and linewidth seen at small phase angles. Previous work by Potter et al. (2000) and Wurz et al. (2007) suggested that ion sputtering is an inefficient source mechanism for maintaining the lunar sodium exosphere, but the indirect effects of ions such as ion-enhanced diffusion might enhance the sodium reservoir and influence the exosphere. Therefore, depending on which region the Moon encounters, sodium exospheric abundances may vary. Sarantos et al. (2010) suggested that the plasma sheet ions may enhance the efficiency of PSD up to 2 times more than solar wind ions. The higher-energy plasma sheet ions can also penetrate further and potentially liberate sodium atoms that are buried deeper in the lunar soil. Due to observation geometries from Earth, sodium intensities from a time-invariant exosphere are expected to peak at quarter phases (Mendillo et al., 1997; Sarantos et al., 2010). This is because at quarter phases, limb observations probe subsolar points, where sodium abundances are presumed to peak (Mendillo et al., 1993; Potter & Morgan, 1998; Sprague et al., 1992). Our relative intensities increase going toward subsolar points from full Moon, with waning phase intensities being ~10% higher than waxing phase intensities.

LADEE measurements, however, indicated a sodium cycle during each lunation. LADEE UVS demonstrated a minimum sodium content a little after the new Moon and a more complex trend around full Moon. That is, as the Moon passes into Earth's magnetotail the sodium column densities first slightly decreased and then increased significantly (i.e.,

by about a factor of 2) through full Moon reaching a maximum at ~30° phase angle, after which it begins to decrease again (Colaprete et al., 2016). Our observations probe different local times for different lunar phases and hence likely convolve spatial and temporal variations in sodium rate, whereas the LADEE UVS results of Colaprete et al. (2016) were made at around local noon and are a consistent representation of the temporal variability of the total content of the lunar exosphere.

Both our brightness trend and LADEE UVS observations can partly be explained by the lack of sputtering by the solar wind during magnetotail passage, although a higher sodium content on the lunar nearside (Athiray et al., 2014) can also explain these trends. Colaprete et al. (2016) noted that the absence of sputtering in the magnetotail should allow for sodium surface reservoirs to increase if ion-enhanced diffusion is an insignificant source of sodium. Once the Moon exits the magnetotail, solar wind sputtering resumes expelling adsorbed particles, and thus the exospheric sodium decreases. In this interpretation, the solar wind is mainly a sink for exospheric adsorbates, unlike the suggestions of Potter et al. (2000) and Sarantos et al. (2010), and the monthly cycle evidenced by LADEE (and also surmised by Sarantos et al., 2010 and Sprague et al., 2012) must be attributed to nonuniform surficial sodium content.

Our lunar limb (relative) intensity data (Figure 4.12) show that overall relative intensities increase from full Moon toward quarter phases with some of the highest intensities recorded in December 2013, and May 2014 during magnetotail passage.

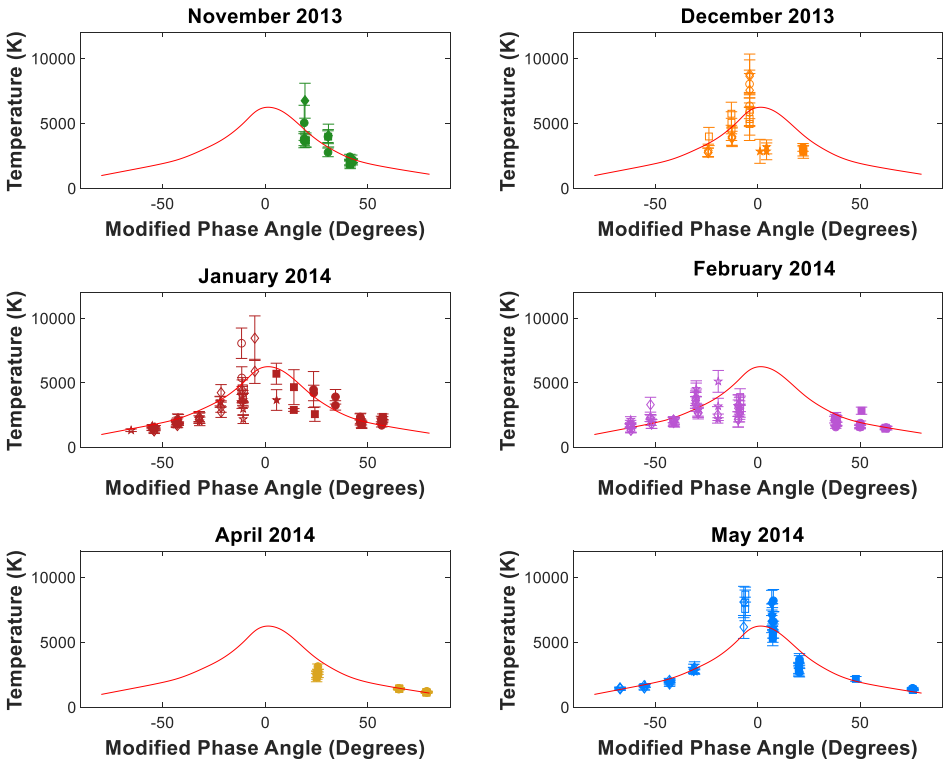

Figure 4.12: Equatorial temperature as a function of phase for each month (Kuruppuaratchi et al. 2018). The largest magnetotail passage temperatures are seen in December, January, and May. The legend used in Figure 4.2 can be used for Figure 4.11.

Intensity values from Table 1 of Sarantos et al. (2010) show a general trend toward reduced exospheric sodium intensity going from a pure solar wind environment (region of high ion flux) to the magnetosphere (region of low ion flux). Our relative intensity data follow a similar trend, with intensities decreasing, going from phase angle 70° toward phase angle 0°. Our data, however, show a large variation in relative intensity within the magnetosphere region (phase angles less than 30°) including a few of the brightest intensity data. Hence, our data indicate that various plasma environments may influence the evolution of the exosphere.

4.5. Summary and Conclusions

This unique data set provides additional insight into the spatial and temporal variation of the lunar sodium exosphere, especially with future work into possible correlations with Earth's magnetospheric plasma environment and solar wind conditions. Our relative intensity data show large variations when the Moon resides in the magnetosphere region (phase angles <30°) and indicate that the various plasma regions the Moon encounters can influence the sodium exosphere.

Our linewidth and the associated derived temperatures show a systematic increase from quarter Moon to full Moon. While temperatures at phase angles >40° and larger are slightly hotter than a pure PSD source (~1700 K), temperatures in the range of 2500 – 9000 K were routinely measured near Full Moon (0^o – 30°). The upper range of our temperatures is overall higher than those of previous studies by about a factor of 2 – 3 near full Moon.

This systematic trend indicates a transition from a PSD-dominated atmosphere to a mix of sources when we look near the terminator. The dominant cause of the upper range of our temperatures during magnetotail passage is not due to geometrical effects as we have shown that the bulk of the measured increase in linewidth from near quarter phase to small phase angles exceeds the geometrical effects of looking down the tail. Particle simulations confirm that linewidth from a single source increases when phase angles decrease as low energy atoms map along with subsolar points during quarter phases and high-energy atoms map along terminator lines during full Moon. However, no source could reproduce temperature results for all phases. Linewidths of ~3 km/s are expected when an impact source of 5000 K is considered and higher if sputtering is an important source. From these two lines of evidence, impact vaporization, sputtering, and/or a non- thermal distribution

for PSD likely combine to produce the trends shown here. In conclusion, although the systematic trend can be explained, the magnitude of linewidth increase near full Moon could be a result of transient ion events or meteor activity and requires additional modeling (see Sarantos et al., 2017) to extract the speed distribution with which sodium atoms are ejected from the surface.

As to the cause of the observed short and long-term temperature deviations from this systematic trend, possible reasons include a solar cycle variation, meteor showers, and solar wind variations. No correlation between F10.7 and this data set was found. Data collected with the same instrument during March 2009 by Mierkiewicz et al. (2014; solar minimum) show similar trends with lunar phase but lower temperatures by about a factor of 2 – 3 near full Moon than the upper range of data presented here, which were collected during solar maximum. Long-term solar cycle effects will, however, be addressed in a future work in which data obtained between 2011 and 2017 will be analyzed. Some other possibilities that could generate large temperatures like those seen in our data include a nonthermal PSD population, micrometeoroid impact vaporizations, and sputtering sources. The only major meteor shower that had its peak coincide with our observations were the Geminids (13/14 December), but we do not see any distinct responses in the sodium exosphere in terms of increased temperatures for that event, although we only obtained measurements 1 day after the peak of the Geminids. Sputtering by charged particles from different plasma environments (e.g., plasma sheet vs. lobes, variability in the magnetosheath, and solar wind) can produce variable temperatures depending on the energy and flux of particles in each environment, which affect the sputtering contributions to the exosphere relative to the other sources. Analysis of the in-situ plasma environment

measurements obtained by the Acceleration, Reconnection, Turbulence and Electrodynamics of the Moon's Interaction with the Sun (ARTEMIS) mission will help further detangle the roles played by these suggested source mechanisms.

In Chapter 5, I discuss our lunar exospheric measurements over multiple years (2013 – 2017) and expand on the results presented in this Chapter. As a companion study, I also discuss the phase angle dependence of the exosphere in terms of our potassium observations. Both sodium and potassium observations discussed in Chapter 5 will be compared to the published work of Kuruppuaratchi et al. (2018) (sodium), and to the published works of Rosborough et al. (2019) (potassium).

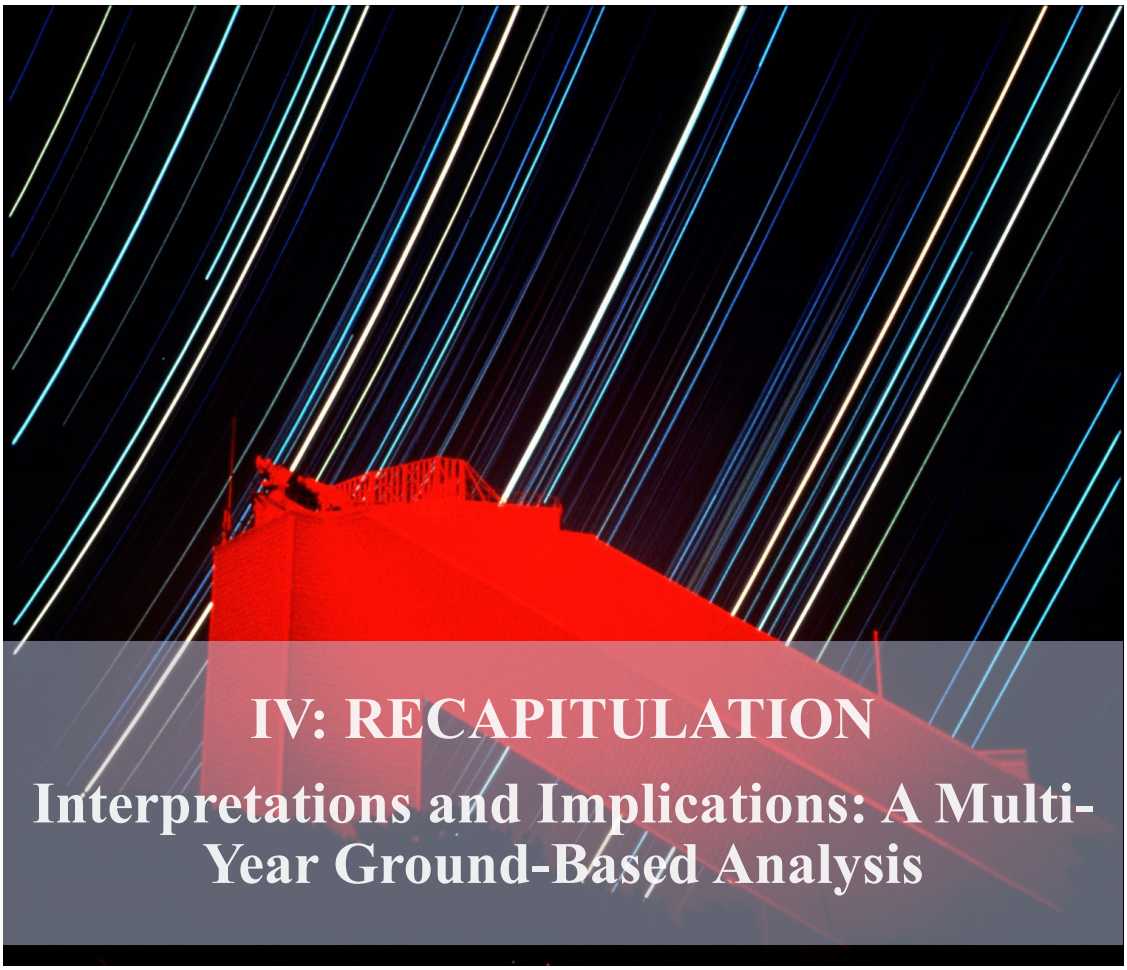

IV: RECAPITULATION

Interpretations and Implications: A Multi-Year Ground-Based Analysis

Photo Credit: NOAO/AURA/NSF

CHAPTER 5. MULTIYEAR ANALYSIS OF SODIUM AND POTASSIUM: A TALE OF TWO SPECIES

Key Points:

- Sodium equatorial observations confirm that PSD is the major contributor to the exosphere at subsolar points, with important contributions from micrometeoroid impact vaporization and charged particle sputtering, specifically charged particles found inside the Earth's magnetotail, close to the terminators.

- Sodium relative intensities over a year show a gradual and smooth response to meteor showers indicating that sodium atoms have a long lifetime.

- Potassium linewidth data describes an exosphere that has dawn-dusk asymmetry, with the waxing limb observations being hotter and following a combination of PSD and micrometeorite impact vaporization (MIV) while the cooler waning limb observations follow a PSD source.

- The extent of the dawn-dusk asymmetry seen in potassium data is possibly linked to meteor shower activity

- Potassium temperatures and intensities shows short lived responses to meteor shower activity and tracks very closely with surface abundance in the KREEP regions.

- The response in potassium linewidths, specifically the dawn-dusk asymmetry, indicates that meteor showers are more important for the exosphere than the sporadic background meteors.

In this Chapter, I expand on the phase angle dependence of the exosphere that was discussed in Chapter 4 by contrasting sodium and potassium observations. A two species approach is useful in setting additional constraints on the surface-atmosphere dynamics of the lunar exosphere as each species can respond differently to a given source. For example, LADEE UVS measurements (Colaprete et al. 2016) showed that sodium had an annual response to meteor showers while potassium showed short but strong responses and tracked closely with lunar surface abundance. Sodium column abundances showed a long-term and smooth cycle which increased from October 2013 to a peak in December 2013 and then a gradual decline from January till April 2014 – this was a cumulative response to meteor shower occurrences that reach peak activity from Fall to Winter then decrease from Spring to Summer. Potassium on the other hand, showed a regular variation across a lunation that correlates strongly with the increased abundance of potassium in the KREEP regions. Additionally, potassium also showed a strong but short-lived response to the Geminids meteor stream compared to sodium. The long term response to meteor showers for sodium versus the short response of potassium provides constraints on the surface residence times for the two species, with potassium having a lifetime significantly less than a lunation (Szalay et al., 2016) and sodium having substantial lifetimes of about 45-90 days which allows atoms to migrate towards the poles (Colaprete et al., 2016). Note that a lifetime is referred to as the time an atom spends in orbit or time between subsequent hops, once released from the surface.

A multiyear analysis will allow for comparisons between sodium and potassium under various conditions. To reiterate the goal of the dissertation as stated in Chapter 1:

The focus of this dissertation is the investigation of the lunar exosphere, using direct velocity-resolved measurements of sodium D2 (5889.9509 Å) and a smaller companion investigation of potassium D1 (7698.9646 Å) velocity-resolved measurements taken over multiple years– providing a unique and complementary way of investigating the morphology and dynamics of the lunar SBE.

Keeping this in mind, I expand on our earlier results and their implications (Chapter 4) and discuss sodium and potassium side-by-side. While sodium is the star of this work, the potassium analysis allows for a comparison which can shed light on the species-specific major source and sink mechanisms. While I have collected, processed, and analyzed the bulk of the sodium data, I have been an integral part of making the potassium observations (Specifically observations included in Rosborough et al. (2019)) and the analysis of a subset of this data (Section 5.1).

5.1. Phase Angle dependence of Sodium and Potassium: A Comparison Study

In this Section, I discuss sodium and potassium data taken during, but not limited to, the LADEE mission instrument testing and science phase (October 2013 – April 2014). All the data presented here encompasses data in Kuruppuaratchi et al. (2018) and Rosborough et al. (2019) along with new results from 2013 – 2017 presented here for the first time. Data from Kuruppuaratchi et al. (2018) and Rosborough et al. (2019) were taken between November 2013 – November 2014 (not continuous). For sodium, this larger dataset is limited to FOV at the limb and field lens edge while potassium observations are limited to FOV at the limb. For a 2 arcmin FOV, FOV at the limb and field lens edge correspond to ~ 168 km and 500 km, respectively. For a 3 arcmin FOV, FOV at the limb

and field lens edge correspond to ~ 112 km and 370 km, respectively. For a more accurate distance, the value in km is multiplied by the cos(δ) (Section 2.4.2). For sodium, FOV at limb and field lens are combined because these two offsets are statistically similar. Furthermore, 2 and 3 arcmin data will be combined in temperature results but presented separately for relative intensity results. To directly compare results, the new dataset has been limited to the same craters used in Kuruppuaratchi et al. (2018) and Rosborogh et al. (2019). Figure 5.1 shows the amount of data in Kuruppuaratchi et al. (2018) in comparison to the additional data and Figure 5.2 shows the amount of data in Rosborough et al. (2019) in comparison to the additional potassium data. Note that while Kuruppuaratchi et al. (2018) had only equatorial data, Rosborough et al. (2019) had both equatorial and high latitude data.

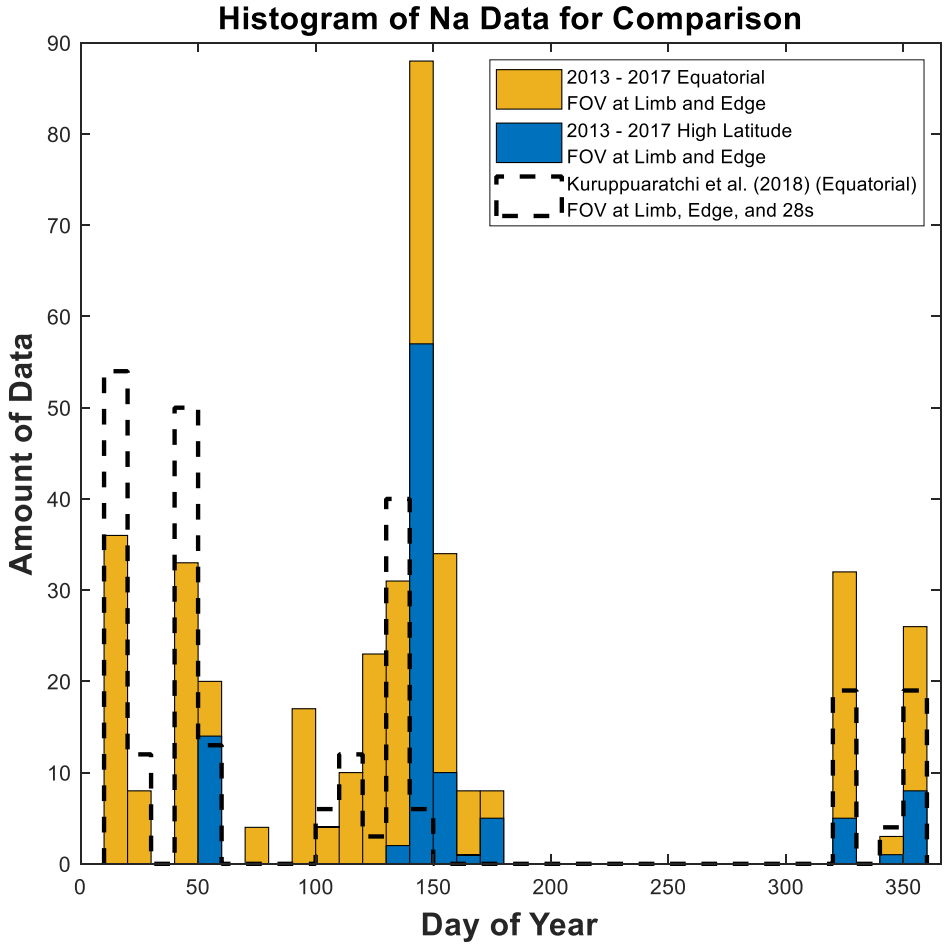

Figure 5.1: Equatorial data from Kuruppuaratchi et al. (2018) contrasted with the additional data from 2013-2017, limited to FOV at limb and field lens edge, and to the four reference craters used in the Kuruppuaratchi et al. (2018) study – Langrenus, Cleomedes, Aristarchus, Grimaldi. The two main high latitude reference craters have also been added – Plato and Tycho. Note that data in Kuruppuaratchi et al. (2018) contains 3 offsets – Limb, Edge, and 28 seconds of time (RA). The new data includes only Limb and Edge offsets. The marigold bars represent equatorial data, and the blue bars represent high latitude data. The dotted line represents data strictly in Kuruppuaratchi et al. (2018).

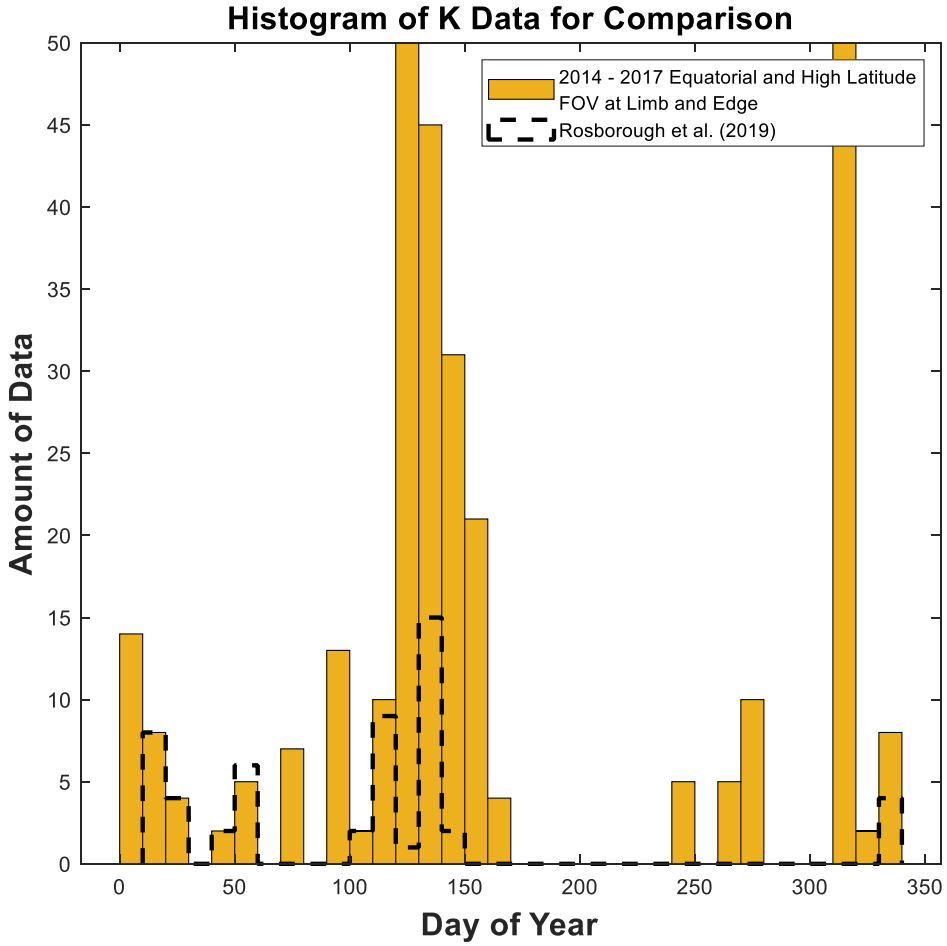

Figure 5.2: Data from Rosborough et al. (2019) contrasted with the additional data from 2013-2017, limited to FOV at Limb , and the reference craters used in Rosborough et al. (2019) – Langrenus, Cleomedes, Petavius, Aristarchus, Grimaldi, Tycho, Plato. Note that high latitude data has been added to the full potassium dataset, instead of having it separate, in order to match Rosborough et al. (2019).

5.1. Sodium and Potassium Linewidth (Effective Temperature) as a Function of Phase

I first discuss the sodium linewidth (and derived effective temperatures) as a function of phase and compare results to Kuruppuaratchi et al. (2018). The phase angle dependence of new data is shown on top of the grey backdrop of sodium data in Kuruppuaratchi et al. (2018), in Figure 5.3. Table 5.1 shows temperatures for the new data

calculated similarly to Table 4.1 (Section 4.1). The black smoothing spline describes the overall trend from all FOV at limb and edge data from 2013 – 2017. The smoothing spline is fit to the data excluding outliers, where an outlier is defined as a data point that is more than 3 scaled mean absolute deviations (MAD) away from the median. From the smoothing spline and the grey backdrop of data in Kuruppuaratchi et al. (2018), we can see that the trend between Kuruppuaratchi et al. (2018) and the new dataset (black spline) follow the same pattern with phase. Note that the black smoothing spline represents data that has much more phase coverage past quarter phase, compared to data in Kuruppuaratchi et al. (2018). Effective temperatures by reference crater for pre, post, and during magnetotail passage agree with reported temperatures in Kuruppuaratchi et al. (2018), as seen in Table 5.1. Note that in Kuruppuaratchi et al. (2018) the mean was used to calculate temperatures, here I use the median.

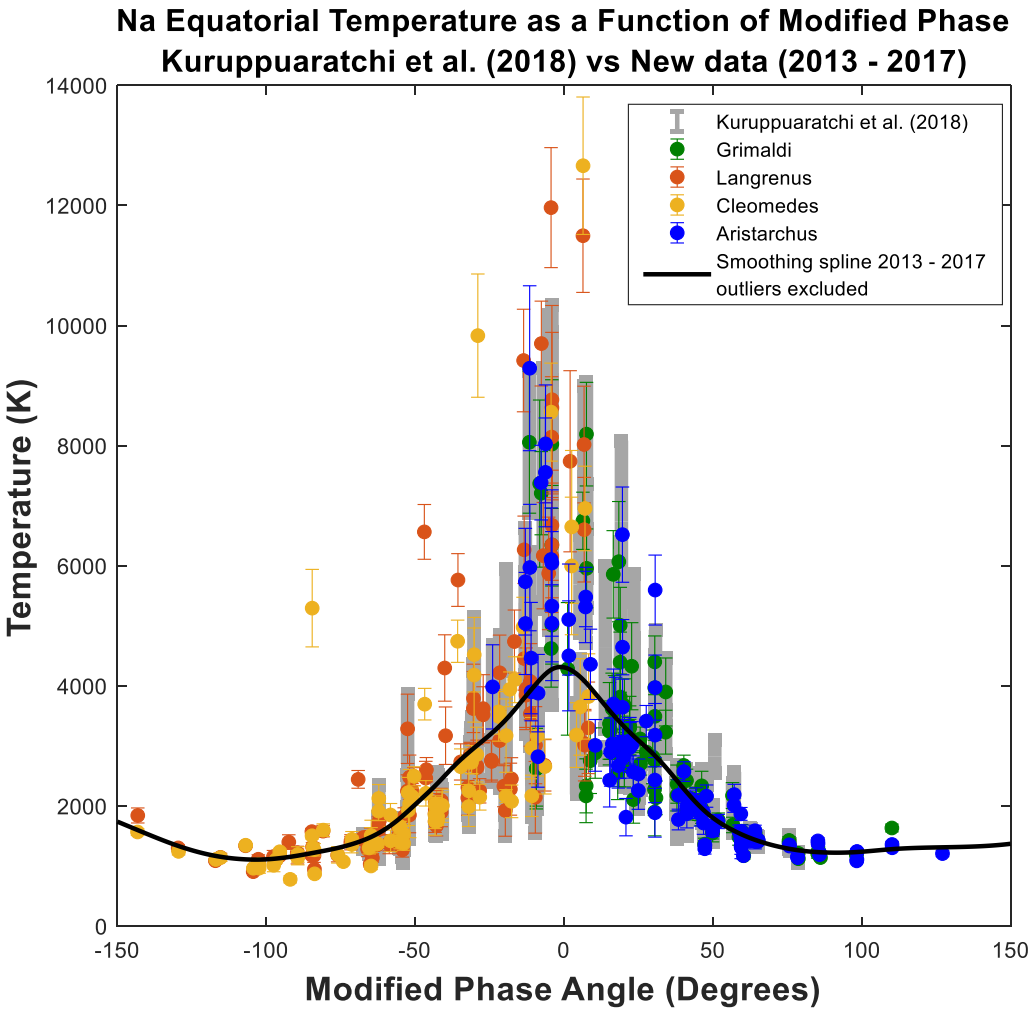

Figure 5.3: Equatorial sodium effective temperature as a function of modified phase angle. The four main craters represent the craters used in Kuruppuaratchi et al. (2018). The black smoothing spline describes the temperature trend for data taken during 2013 – 2017, limited to FOV at limb and Edge. The trend for sodium is consistent with Kuruppuaratchi et al. (2018).

Figure 5.4 shows sodium high latitude observations limited to data taken off the two main high latitude reference craters – Tycho and Plato. The equatorial data in Figure 5.3 is shown as a grey backdrop for comparison. A smoothing spline in blue has been added for comparison to the equatorial data (black smoothing spline). In general, sodium is consistently symmetric about full Moon (~ 0^{o} phase angle) for both high latitude and

equatorial data and the trend of temperatures increasing towards small phase angle holds. From Figure 5.4 and the values in Table 5.1, the difference in temperature from near quarter phases to full Moon phases is not as pronounced for high latitude data. This can be seen from the smoothing spline for the high latitude data in Figure 5.4, where the general trend with temperature falls off towards quarter phases remains but the fall-off is not as steep as for equatorial data. This can be explained in terms of proximity of FOV to the source location for a process dependent on SZA. While our FOV is right at the source for our equatorial data for observation made close to quarter phases, our FOV at high latitudes is at an angle from the source. This could in effect reduce the range of temperatures seen by high ballistic particles moving from right near the source to locations away from the source (terminator sides) because we are always seeing a high energy population of atoms. While the magnetotail temperatures of both equatorial and high latitude data are similar, the waxing and waning data indicate that high latitude data are overall hotter than equatorial data – this could be due to higher energy atoms travelling from the source location and a combination of other processes taking precedence. While the overall trend of our high latitude data is overall flatter than the equatorial data, there is a noticeable trend with phase, especially with high temperature data points during magnetotail passage, and since PSD is less efficient at high latitudes this puts emphasis on micrometeoroid impact vaporization (MIV) and transient ion events.

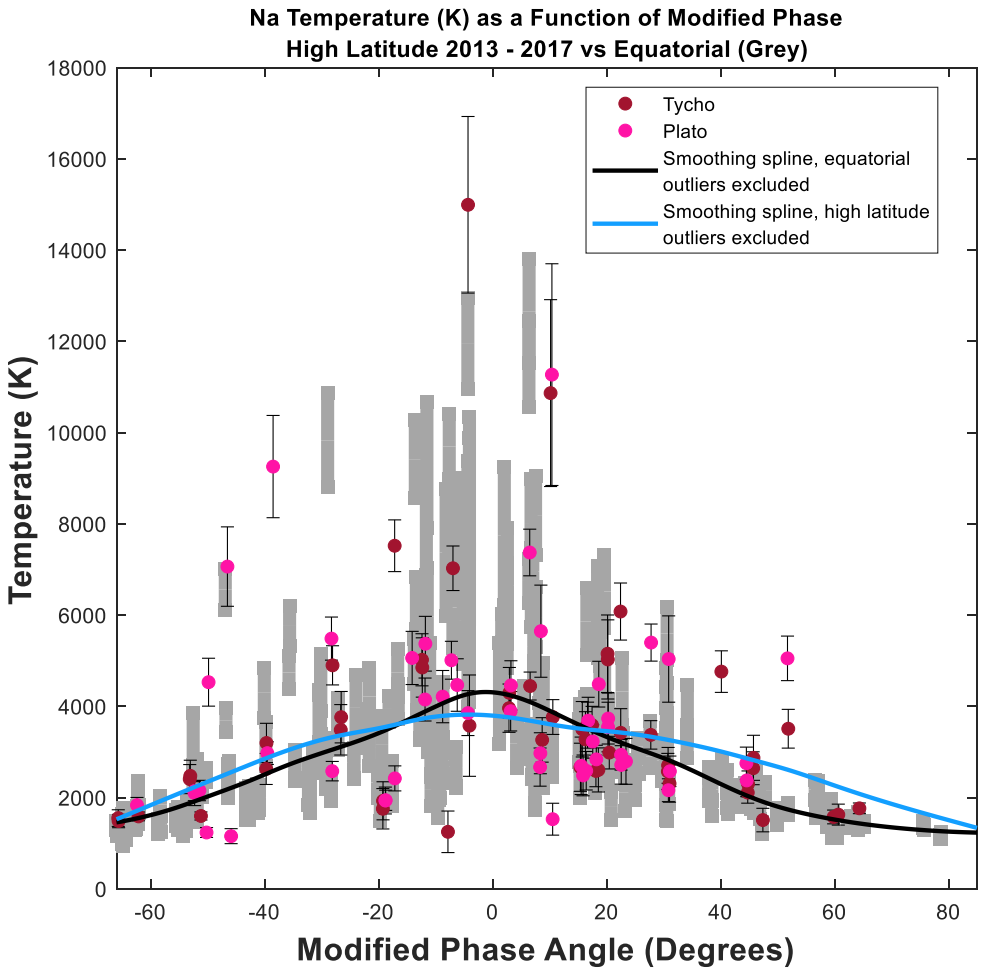

Figure 5.4: High latitude sodium effective temperatures as a function of phase angle, limited to Tycho and Plato, for the years 2013 – 2017 against the grey backdrop of the equatorial data in Figure 5.3. Tycho and Plato, were chosen to match the high latitude data of Rosborough et al. (2019). The equatorial smoothing splines for 2013 – 2017 data in Figure 5.3 (black) are shown alongside the smoothing spline of the high latitude data (blue) for comparison. The data follows the general trend of temperatures falling towards large phase angles, but high latitude data falls off at a less steep rate then equatorial data.

Table 5.1: *Sodium median temperatures for data taken pre magnetotail passage, during magnetotail passage, and post magnetotail passage.*

Limb (Reference Crater)	**Modified phase angle < -30° effective temperature (K)**	**Phase angle <30° effective temperature (K)**	**Modified phase angle > -30° effective temperature (K)**
Aristarchus	N/A	3893 ± 582	1541 ± 108
Grimaldi	N/A	3486 ± 543	1837 ± 156
Langrenus	1554 ± 124	3954 ± 596	N/A
Cleomedes	1585 ± 133	3568 ± 510	N/A
Tycho	2151 ± 236	3591 ± 529	2579 ± 353
Plato	2004 ± 250	3689 ± 471	2307 ± 322
All Craters Equatorial	**1573 ± 130**	**3655 ± 567**	**1586 ± 118**
All Craters High Latitude	**2151 ± 236**	**3640 ± 497**	**2379 ± 353**

I now discuss the potassium observations in a similar fashion to sodium, but with the use of linewidths (instead of temperature) as a function of phase to facilitate direct comparisons to Rosborough et al. (2019). The potassium linewidths as a function of phase are shown in Figure 5.5 along with the model runs from Rosborough et al. (2019). Table 5.2. shows the average waxing and waning temperatures for potassium along with the factor difference between the two limbs. FOV at limb data have the best signal to noise ratio for potassium and are easier to fit, so all potassium data shown in this work has only FOV at limb data. A stark difference between the potassium and sodium observations is that potassium is hard to detect when the Moon is inside Earth's magnetotail (≤30 ° phase). This might be due to a combination of two reasons: (1) potassium is less bright than sodium

and is harder to observe during full Moon time when the scattered light background is higher, (2) the heavier atomic mass, potassium atoms do not travel on large ballistic trajectories from the subsolar point, making potassium less abundant at high latitudes and at the limb/terminator. A combination of these two reasons contributes to a low signal to noise for potassium taken near full Moon. For comparison, in Chapter 3, a sodium spectrum and image taken during full Moon phase (Section 3.2) shows how difficult it can be for the emission to stand out from the scattered light background. Even for sodium, the fitting becomes increasingly difficult when getting closer to full Moon and many more fits are considered 'bad' compared to data taken at larger phase angles (phases outside of magnetotail passage) – an issue that is comparatively worse for potassium for the two reasons mentioned above.

Sodium temperatures on the waxing and waning limbs, do not show any noticeable difference about full Moon. Potassium on the other hand shows asymmetry in temperature between waxing and waning limbs. Figure 5.5 depicts the overall asymmetry in our new potassium data along with the original data from Rosborough et al. (2019). Note that the asymmetry between waxing and waning limbs is greater for the data in Rosborough et al. (2019), with a factor of two difference (Table 5.2). This factor of two difference in temperature was attributed to impacts by meteoroids in Rosborough et al. (2019). Rosborough et al. (2019) utilized a Monte Carlo model (Collier et al. (2014); Bennett et al. (2016)) modified to include the effect of radiation pressure to simulate the trajectories of potassium atoms. They used Maxwell-Boltzmann flux distributions with T = 1200 K and T = 5000 K for the initial speeds of a PSD and impact vaporization source, respectively.

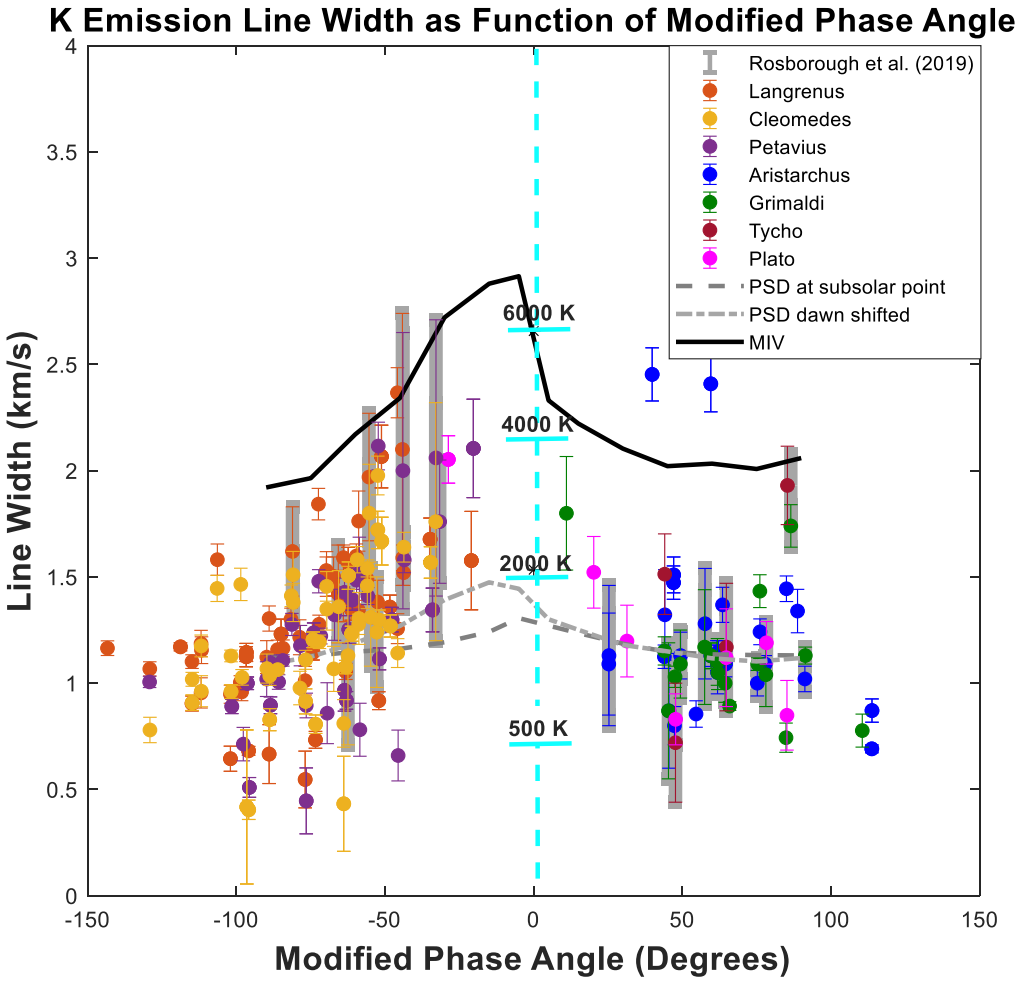

Figure 5.5: Potassium linewidths as a function of modified phase angle. There is an asymmetry between the waxing and waning phase linewidths, with waxing phases being larger. New data include only the craters used in Rosborough et al. (2019) and there is overlap between their data and data shown here. The grey error bars show Rosborough et al. (2019) data. Model runs are shown in black and grey lines and are taken from the model used in Rosborough et al. (2019), previously validated in Collier et al. (2014) and Bennett et al. (2016). The black line is simulated potassium linewidths for micrometeoroid impact vaporization (MIV). The dark grey dashed line is centered at the subsolar point with a source rate reducing as the cosine of the SZA whereas the light grey dash and dot line is offset by 20º longitude towards dawn.

The results of Rosborough et al. (2019) suggested that both a centered (centered at subsolar point) and a dawn-shifted PSD model (T = 1200 K) fit the waning phase observations with the waxing phase temperatures being more suited to a combination of

PSD and meteoroid impact sources. The difference in linewidths between waxing and waning phases were attributed to dawn-dusk asymmetry assumed in the impact vaporization rates (Pokornỳ et al., 2019). This assumption for a dawn-dusk asymmetry in the impact vaporization produces an increase in linewidths because when we probe the dusk exosphere (waxing phases) we are measuring a larger fraction of high speed, long ballistic range particles traveling from dawn. The highest concentration of mass production rates is expected at dawn/apex terminator (03 – 06 hr, Local Time (LT)) owing to the dominant ejecta yield from high-velocity apex meteoroids (impactor velocity~ 55 km/s) (Pokornỳ et al., 2019). Additionally, this remains true for any day of the year. This means that during waxing phases, where we look duskward from the subsolar point we are looking in a direction farther away from the source (i.e., the dawn terminator) and are thus observing very high energy potassium atoms that can travel far enough (duskward). This is the same idea that was discussed earlier for the increase in sodium linewidths from quarter phases to full Moon. During quarter phases we observe atoms that are close to or at the source (subsolar point) and during full Moon we observe atoms with the highest velocities that have made it from the subsolar point to the limb/terminator side. Interestingly, the lack of a noticeable distinction between waxing and waning temperatures for sodium means that these two species respond to meteor impacts differently. This agrees with the conclusion reported by Colaprete et al. (2016) based on the response to the Geminids, that potassium has a stronger but short-lived response compared to sodium.

The data shown in Figure 5.5 is replotted by year in Figure 5.6 with the trend lines for waxing and waning limbs showing asymmetry. An interesting observation is that the 2014 data in Rosborough et al. (2019) is the dataset that shows the most dawn-dusk

asymmetry. Recall that micrometeoroid impact vaporization has two sources – showers and sporadic. The sporadic background meteor model was used to explain the asymmetry in Rosborough et al. (2019) with the apex of the source situated on the dawn terminator. However, since the sporadic background meteors do not change too much over a year, this points to the likely influence of meteor shower streams that were present during our observations. Due to the nature of our observing program, no given year has the same coverage. The exception is during May and June where we tend to have the most observations per run due to the favorable weather at Kitt Peak and availability of student observers.

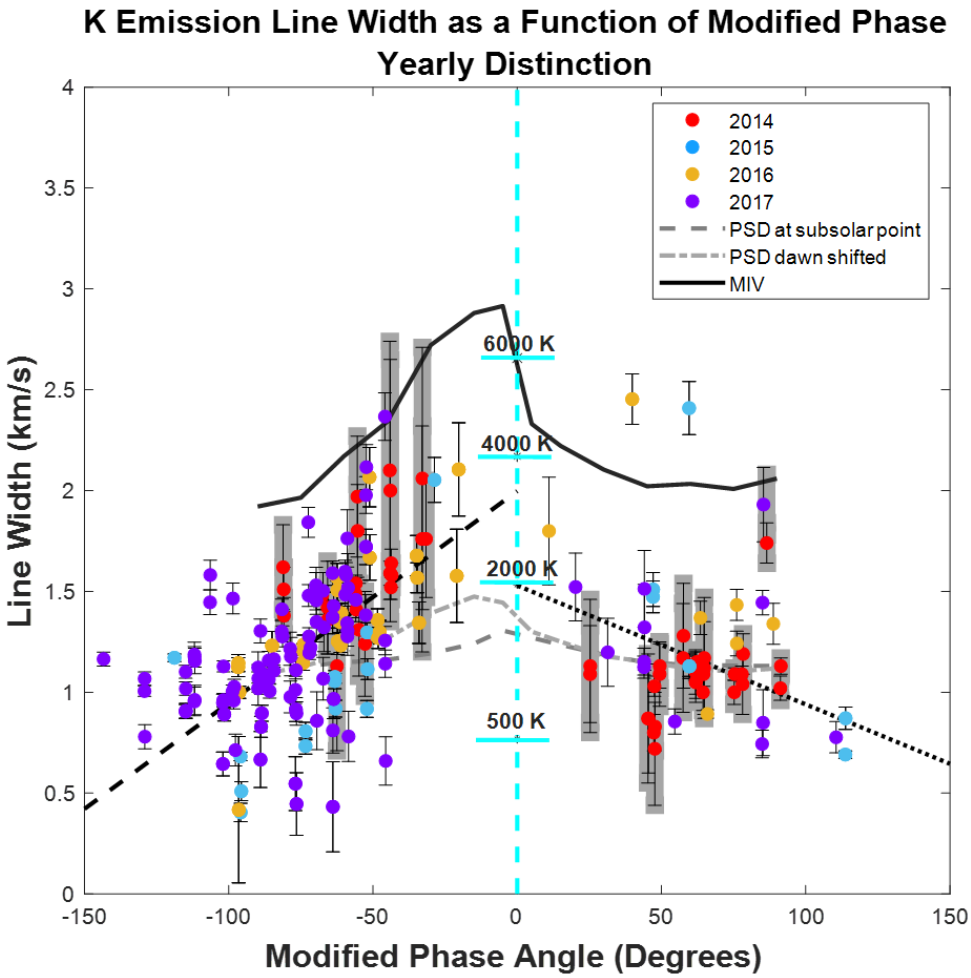

Figure 5.6: Potassium linewidths as a function of modified phase angle, in the same layout as Figure 5.5. Colors denote the year. Datapoints that are outliers (more than 3 MAD away from median) have not been used to calculate the dashed best-fit lines for the waxing and waning limbs.

To fully understand how the signatures of meteor showers manifest themselves in our data, I have made use of the information in Table 5.2 as provided by Stubbs et al. (2014) and Figure 5.7 (Tim Stubbs, private communication). The meteor showers that have a noticeable effect on the lunar exosphere are the ones that have a zenith hourly rate (ZHR) above the approximate sporadic rate of ~ 9.5 meteors/hr (Stubbs et al., 2014).

Table 5.2: *A summary of the 18 annual meteoroid streams that are anticipated to encounter the Moon during the LADEE mission (6 October 2013 to 25 March 2014, or perhaps later). ZHR is the Zenith Hourly Rate at the peak. Lat $_{SSE}$ and LT $_{SSE}$ are the latitude (degrees) and local time (HH:MM) of the stream normal in SSE coordinates.*

Date	Time	Name	Code	ZHR	Lat $_{SSE}$[1]	LT SSE
09-Oct-2013	12:52	October Draconids	DRA	1.0	+78.98	17:05
21-Oct-2013	20:21	Orionids	ORI	25.0	-7.28	04:29
22-Oct-2013	22:52	Leonis Minorids	LMI	1.9	+25.63	07:56
06-Nov-2013	06:10	SouthernSouthern Taurids	STA	7.3	-4.80	00:38
06-Nov-2013	06:10	Northern Taurids	NTA	4.0	+1.36	00:54
13-Nov-2013	05:30	Andromedids	AND	1.0	+29.06	22:55
17-Nov-2013	07:14	Leonids	LEO	13.0	+9.81	06:09
21-Nov-2013	11:07	alpha Monocerotids	AMO	4.0	-19.90	04:02
27-Nov-2013	02:19	November Orionids	NOO	5.0	-7.83	01:43
12-Dec-2013	18:32	December Monocerotids	MON	2.0	-14.58	01:29
13-Dec-2013	22:22	Geminids	GEM	92.0	+10.21	01:56
17-Dec-2013	07:04	sigma Hydrids	HYD	2.5	-16.82	03:20
22-Dec-2013	16:37	Ursids	URS	12.0	+72.62	02:58
25-Dec-2013	15:15	December Comae Berenicids	COM	5.0	+18.58	04:53
03-Jan-2014	17:51	Quadrantids	QUA	130.0	+64.82	06:23
08-Feb-2014	06:14	alpha Centaurids	ACE	7.3	-42.19	06:06
05-Apr-2014	13:44	kappa Serpentids	KSE	4.0	+34.45	01:43
22-Apr-2014	14:50	April Lyrids	LYR	12.8	+57.38	04:17

[1] While the Moon's orbital plane is tilted by ~ 5° with the ecliptic, the Moon's equator is always at an angle of 1.5° to the plane of the ecliptic. This means that the ecliptic latitude is almost interchangeable with the Selenographic latitude (Pokorny et al., 2019).

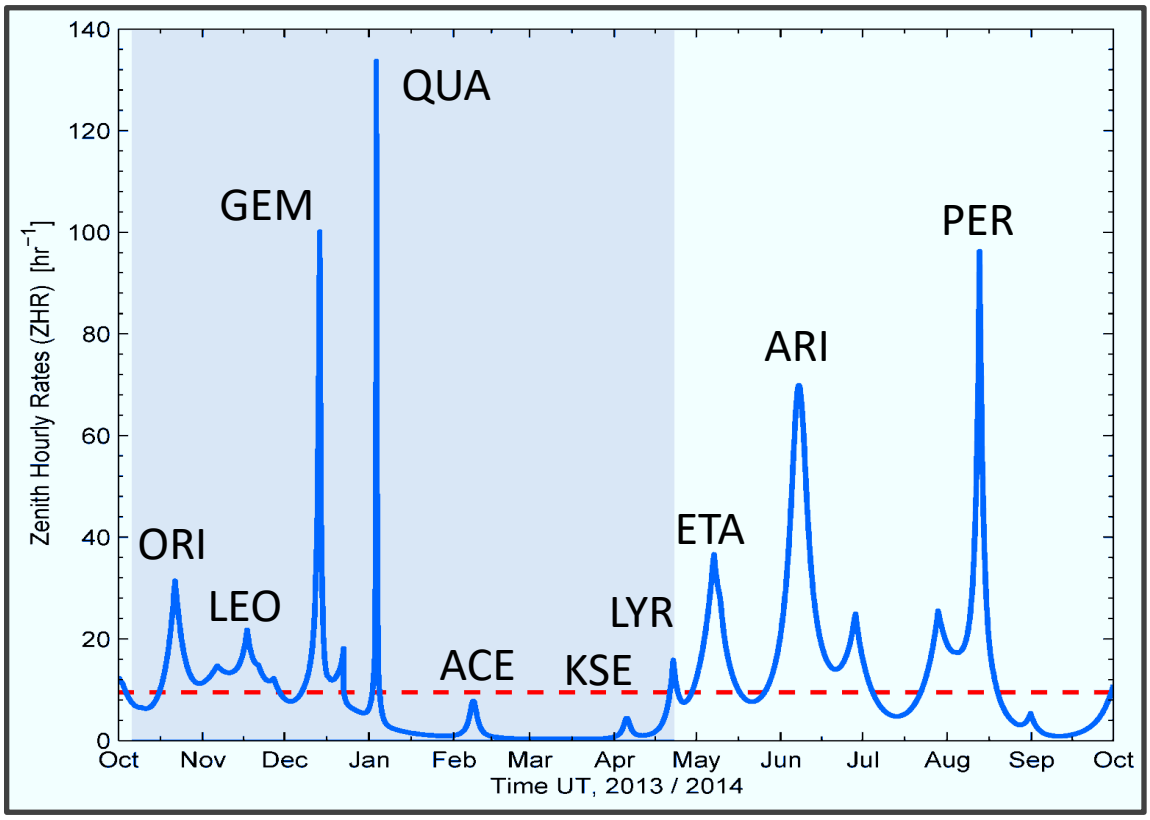

Figure 5.7: Zenith hourly rate of the 18 meteor streams expected to be encountered by the LADEE mission (Stubbs et al., 2014).

Our observations are not continuous and observing runs do not encompass the same range of days in each month. Due to this sampling issue, it is difficult to make direct comparisons between months. Nevertheless, I have checked our data as it relates to major meteor showers and here, I show the datasets that showcase the clearest trends. I have picked the observing runs that have approximately the same date range in a month. For this dataset, those observing runs are May 2014 and 2016, and January 2014 and 2017. The other observing runs were too different from each other or did not have enough data on both waxing and waning limbs to show a complete picture. We know that, overall, potassium linewidths (and derived temperatures) show a dawn-dusk asymmetry and that the cause for higher waxing phase linewidths is a combination of PSD and MIV. What we

do not know yet, is, what affects the degree of this dawn-dusk asymmetry in the next few paragraphs, I attempt to answer this question. The May observing runs in 2014 and May 2015 are shown in Figure 5.8. The solid grey line indicates the approximate peak of the May Eta Aquarids meteor shower, with the dashed grey lines showing the ± 3 days from the peak date. The dashed cyan blue line shows the full Moon date for the observing run.

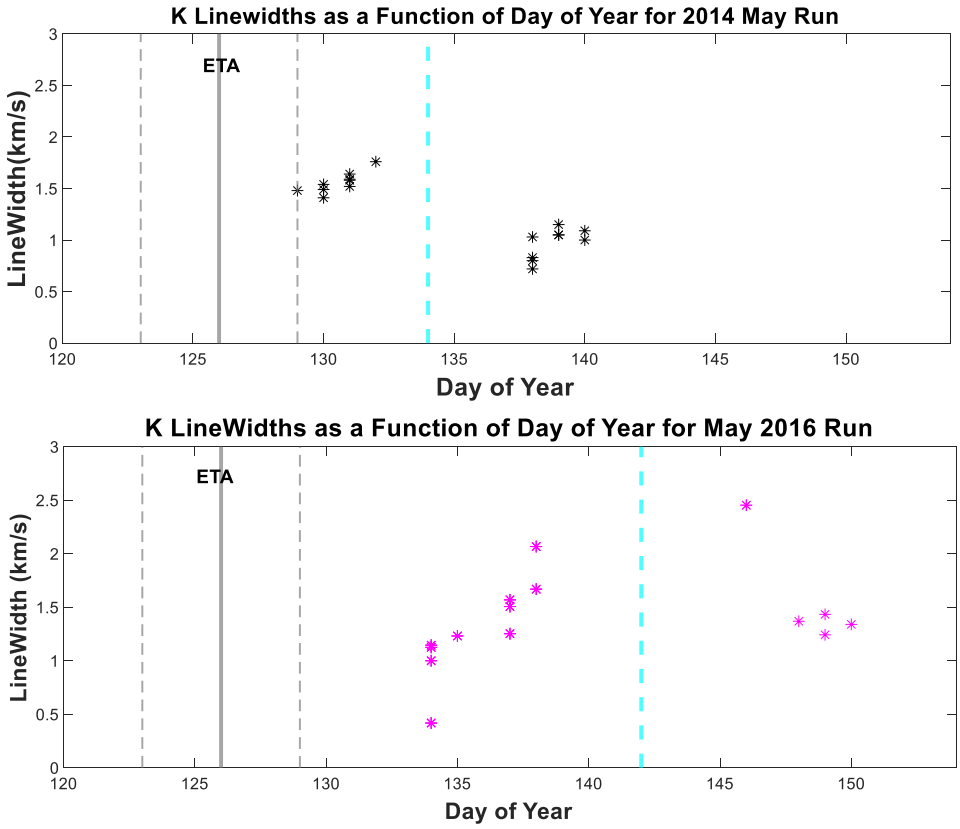

Figure 5.8: Potassium linewidths as a function of day of year for the 2014 and 2016 observing runs. The solid grey line indicates the approximate peak of the May Eta Aquarids meteor shower, with the dashed grey lines showing the ± 3 days from the peak date. The dashed cyan blue line shows the full Moon date for the observing run. The May 2014 observing run starts with waxing phase observations made 3 days from the peak date of the Eta Aquarids, and the May 2016 run starts with waxing phase observations made about 8 days from the peak date of the Eta Aquarids. There is a larger dawn-dusk asymmetry in the 2014 May data than the 2016 May data.

As seen from Figure 5.8, May 2014 data shows more dawn-dusk asymmetry than May 2016 data. The median temperature for waxing and waning phase data in May 2014 is 2016 ± 155 K and 902 ± 122 K while the median temperature for waxing and waning phase data in May 2016 is 1311 ± 156 K and 1699 ± 212 K, respectively. I have checked the solar wind environment during these times, and found no major solar event (i.e. CME) – the proton fluxes from ARTEMIS data are within the nominal flux for the solar wind (~ 10^{8} cm^{-2} s^{-1}). This means that, for the most part, the parameters that are different for the two runs are phase angle, and meteor shower activity, and latitude of observations. A review of the dataset revealed that the only latitudinal difference between the two datasets involved a small percent of the 2014 data (12%) in May containing high latitude observations. The two observing runs encompass approximately the same phase range which points us in the proximity of observations to the major meteor shower in May, the Eta Aquarids.

Using the explanation from previous discussions for potassium linewidths, the large linewidths on the waxing side are due to the contribution of high energy atoms released from MIV on the dawn side. Since a lot of meteor showers also hit the Moon on the dawn side, just like the sporadic background meteors, the strong dawn-dusk asymmetry in May 2014 is likely associated with how close the observations are to the peak of the Eta Aquarids. In May 2016, however, too many days have passed since the peak of the meteor shower, meaning that it is too late to see the high energy atoms released from MIV coming from the dawn side to the waxing limb. The difference between these two similar datasets points to the time sensitivity of potassium to meteor shower activity – an observation that was also made by LADEE data. If potassium has lifetimes significantly less than a lunation

(Szalay et al., 2016) then that would explain why the proximity of observations to the peak of a meteor shower seems to have affect.

Figure 5.9 shows January 2014 and January 2017 data in a similar fashion to Figure 5.8. As was the case for May data, there is no indication of a higher than normal solar wind proton flux. Both January 2014 and 2017 observations have equatorial data, meaning that there is no big latitudinal difference. The January Quadrantids is a very strong, short-lived (peak of less than a day), high latitude shower. As such, the contributions from high latitude showers in the production of vapor in equatorial latitudes should be reduced. Although, we can expect the transport of exospheric neutrals to be more of a global process (Szalay et al., 2016) and depending on the strength of the shower in terms of ZHR, the latitude of the meteor shower might not be an issue.

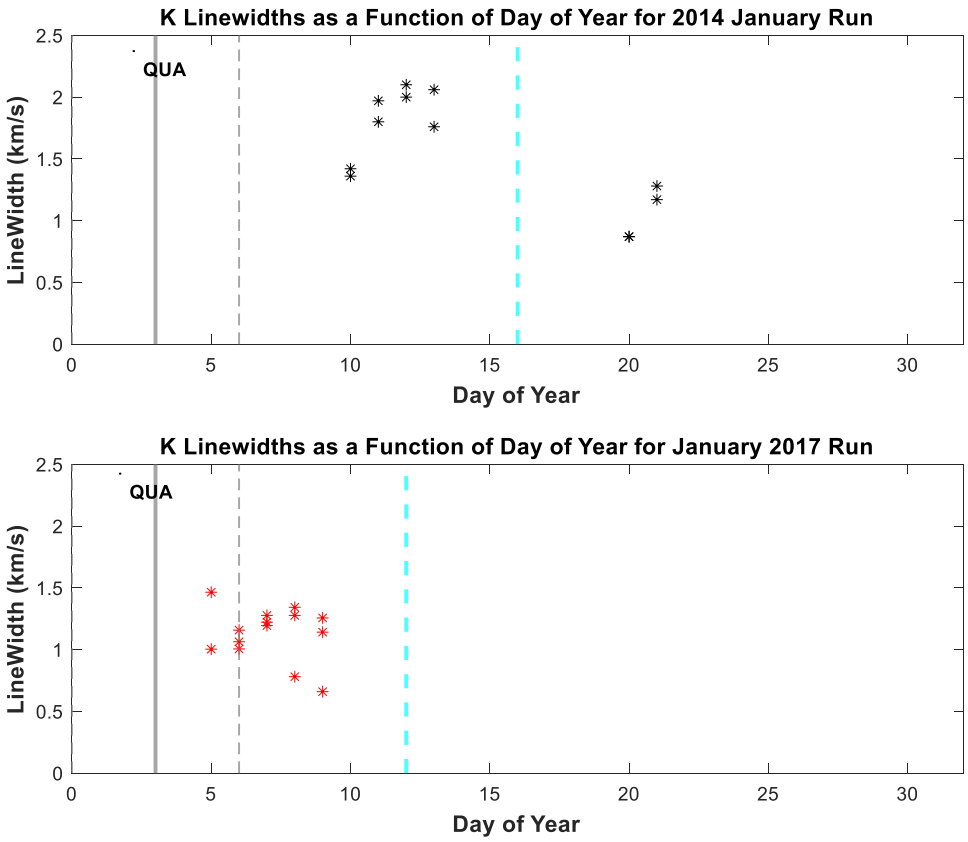

Figure 5.9: Potassium linewidths as a function of day of year for the 2014 and 2017 observing runs in January. The solid grey line indicates the approximate peak of the January Quadrantids meteor shower, with the dashed grey lines showing the ± 3 days from the peak date. The dashed cyan blue line shows the full Moon date for the observing run. Dawn-dusk asymmetry is seen in January 2014 data while waxing limb observations between January 2014 and 2017 indicate that January 2014 waxing observations are hotter.

January 2014 data shows the large dawn-dusk asymmetry and was taken about 6 days past the peak of the Quadrantids. The lack of waning phase data in the January 2017 makes it hard to comment on any asymmetry in the data, but what it is interesting is that January 2017 waxing observations have lower linewidths than January 2014 waxing observations. From Table 5.2, the Quadrantids impacted the Moon in 2014 at 06:23 AM LT. For purposes of this study, I assume the time is the same for 2017 as well and I also assume that the ZHR is the same. January 2014 observations started at around 1:40 PM LT

which means that about 7 hours had passed since the meteor shower peak impacted the lunar dawnside. In comparison, the January 2017 data observations started at around 11:24 AM LT, which means that about 5 hours had passed since the approximate peak impact time. It is possible that January 2014 waxing linewidths are larger because we are seeing a population of atoms with the highest energies, that have managed to travel far compared to 2017 waxing phase observations. In comparison, the May data in Figure 5.8 seems to indicate that the strength of the meteor shower in terms of ZHR might also be an important factor. If we use the same argument for May data as the January data, then one would expect the May 2016 waxing linewidths to be larger than the May 2014 waxing linewidths. However, this is not the case and can be explained by the fact that the Eta Aquarids are about 3 times weaker than the Quadrantids, so after a certain amount of time, we just do not see the atoms released from that shower. Since the Quadrantids are much stronger in comparison, the vapor cloud likely produced is substantial allowing atoms to be present in the exosphere even after a long time. It is also possible that the impactor speeds and ZHR in the 2017 Quadrantids were different, although this is a more in-depth topic that is beyond the scope of the discussions here.

The asymmetry seen between waxing and waning observations in 2014 is likely due to that dataset containing May and January 2014 observations, which were made close to meteor showers. In other years, we do not have observations that coincide with strong meteor showers and the major contribution is from the sporadic background meteors. Since the largest dawn-dusk asymmetry is seen at times close to major meteor showers, it is likely that the sporadic background meteors only produce a small response in our linewidths. LADEE LDEX data also found a weak correlation between the sporadic meteor influx and

the exospheric density as measured by LADEE UVS (Szalay et al., 2016). During times where only sporadic background meteors are present, the potassium exosphere seems to follow the PSD model.

Based on the results from Figure 5.8 and Figure 5.9, a few conclusions can be reached. (1) In order to see a strong dawn-dusk asymmetry, waxing observations in a run should have been made right after or at the peak of a meteor shower. (2) Depending on the strength of the shower, the time elapsed since the peak of the shower impacted the lunar surface can affect the magnitude of the waxing phase linewidths of an observing run. The second conclusion is not a comparison between waxing and waning observations in a run, but rather a comparison between waxing observations for an observing run taken around the same date range in a month. (3) potassium released due to impacts is time sensitive and is likely to have a short lifetime. (4) The sporadic meteors do not appear to produce a large response in the exosphere like the meteor showers do.

I have performed the same analysis for sodium to determine any meteor effects. Figure 5.10 shows our sodium data as a function of phase categorized by year and Table 5.3 shows waxing and waning temperatures denoted by year. Table 5.3 uses the same phase boundaries as Table 5.1, for pre magnetotail (waxing) and post magnetotail (waning) data.

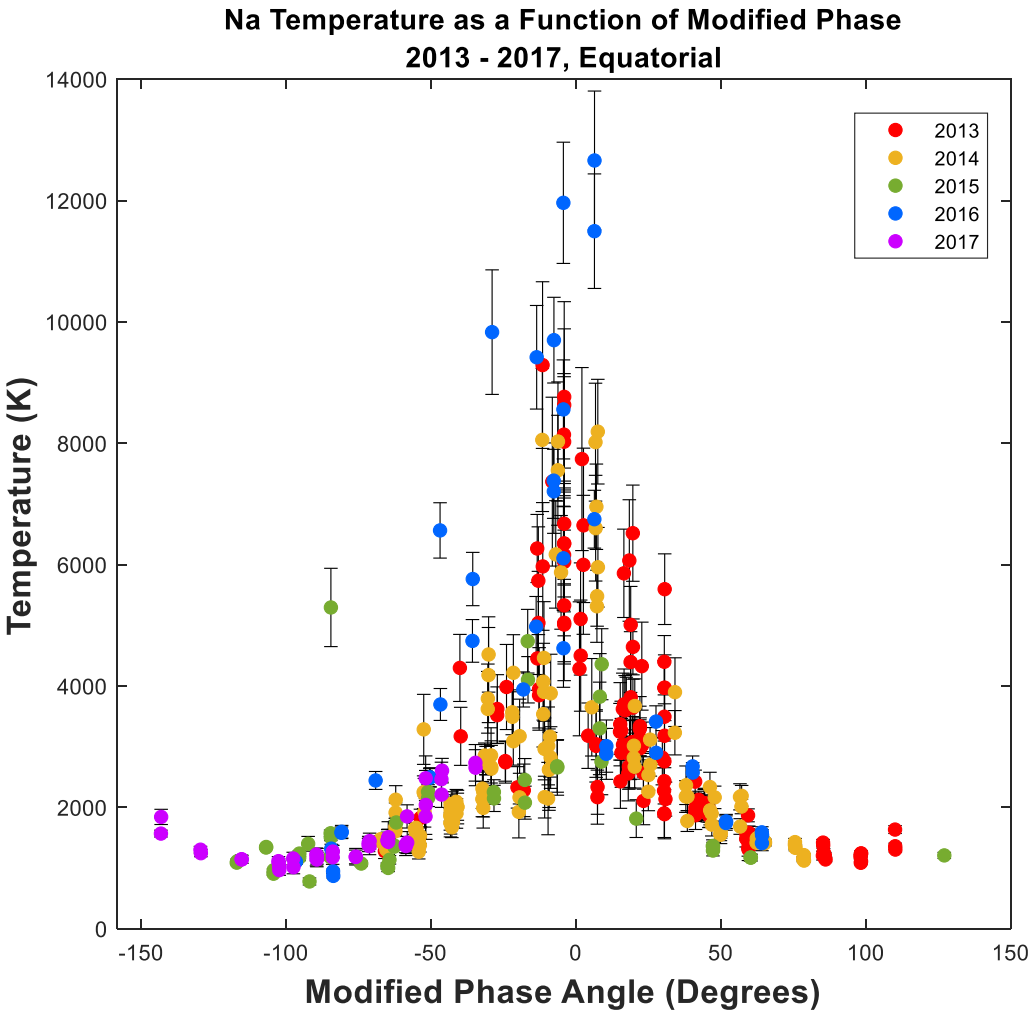

Figure 5.10: Sodium equatorial temperatures for 2013 – 2017 as a function of modified phase angle and color coded by year.

Table 5.3: *Summary table of median equatorial sodium temperatures for waxing and waning data, per year.*

Year	Wax/Wan	# Observations	Median Effective Temperature (k)	Median Effective Temperature error (km/s)
2013	Waning	5	1827	145
2013	Waxing	55	1871	153
2014	Waning	51	1917	178
2014	Waxing	35	1555	105
2015	Waning	6	1250	66
2015	Waxing	23	1241	53
2016	Waning	7	1744	118
2016	Waxing	15	1600	105
2017	Waxing	40	1373	127

While potassium data showed asymmetry between waxing and waning limbs, especially in 2014, equatorial sodium is more symmetrical and none of the years show a statistically significant hotter waxing limb. Figure 5.10 and Table 5.4 show high latitude sodium data. Note that 2017 data processed so far did not have any data taken off Tycho and Plato as seen from Table 5.4, the 2016 waxing and waning high latitude data are 2-3 times the values in other years. We only have a few observations made off Tycho and Plato in 2016 and these observations did not coincide with any major meteor shower. Additionally, the median temperatures for 2016 high latitude data are on average too high to be from a meteor source. 2016 also seems to be overall hotter for high latitude data than other years. For these reasons, the asymmetry in high latitude data for 2016 could be due to transient ion events. Although I have performed a simple correlation with ARTEMIS proton flux data for multiple years, the study remains inconclusive as no clear correlation with proton fluxes could be found.

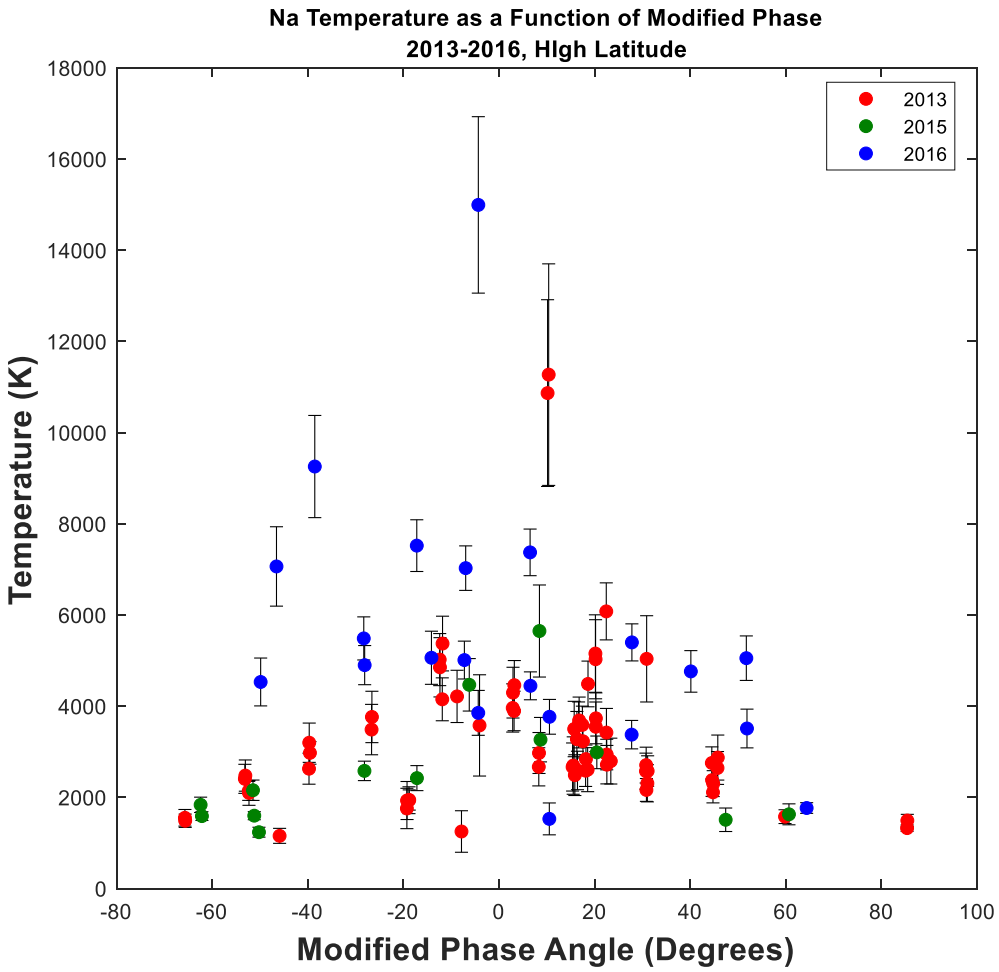

Figure 5.11: Sodium high latitude linewidth derived temperatures for 2013 – 2016 with color denoted by year.

Table 5.4: *Summary table of median high latitude sodium temperatures for waxing and waning data, per year.*

Year	Wax/Wan	# Observations	Median Effective Temperature (k)	Median Effective Temperature error (km/s)
2013	Waning	15	2379	353
2013	Waxing	10	2276	261
2015	Waning	2	1570	244
2015	Waxing	5	1600	109
2016	Waning	4	4138	440
2016	Waxing	3	7066	870

To help see the response to meteor showers between the two species better, I have chosen the months of January and May in 2014 and May in 2016 to show our sodium and potassium temperature data, and limited our waxing and waning sodium temperatures to phases that are outside of the magnetotail (greater than 30 degrees phase). Limiting the sodium data to the phases outside of magnetotail passage, allows for sodium and potassium data to be plotted together for a direct comparison. Figure 5.12 shows sodium and potassium for May 2014 (top) and May 2016 (bottom).

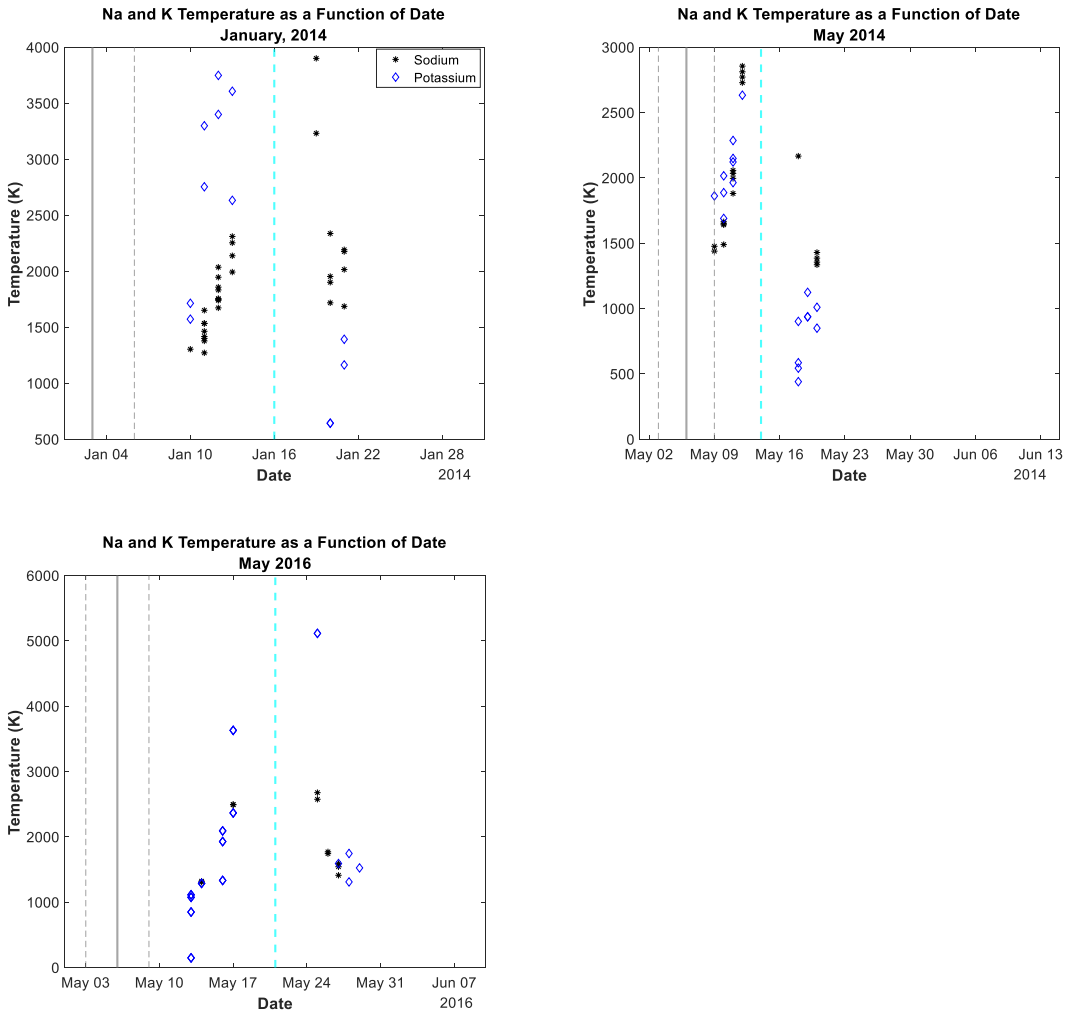

Figure 5.12: Sodium and potassium temperatures for months that had the most complementary set of observations with top left being January 2014, top right being May 2014, and bottom left being May 2016. Sodium data is shown as black asterisks and potassium data is shown as blue diamonds. Sodium temperatures do not contain magnetotail data to facilitate a direct comparison to potassium. The dawn-dusk asymmetry in potassium data for 2014 is very evident, compared to sodium. The dawn-dusk asymmetry in potassium data for May 2016 is not as apparent as May 2014.

From Figure 5.12, potassium data show greater asymmetry than sodium data if observations are made close to a meteor shower. This reinforces the conclusions reached earlier that potassium has a strong response to the same meteor shower. This is likely due to potassium having a substantially shorter lifetime than sodium and likely related to

surface abundance. Since most of the incoming meteor stream impacts the dawn terminator (when we probe the waning limb), just like the sporadic background meteors do, then due to the abundance of potassium in the KREEP region on that limb of the Moon, we might be seeing a larger population of potassium atoms that were available to be released through impacts. If on the other hand, the impacts occur on an area where there is less potassium abundance, then there will be fewer atoms available to be released through impact vaporization and our FOV is populated with atoms released mainly through other source mechanisms. Since impact vaporization has a higher temperature distribution and they turn the surface material into a molten state, they can probably penetrate deeper into the lunar regolith to access atoms that PSD cannot release. The sodium content on the lunar surface is not well known, so it is hard to constrain the effect of meteors. If the abundance of sodium on the lunar surface is more spread out than potassium, and if most meteors (showers and sporadic background meteors) hit on the dawn side, then this can explain the lack of dawn-dusk asymmetry in sodium data. A specific combination of the right time and the right location of the Moon is needed for this asymmetry to be seen. Additionally, since sodium has a long lifetime, compared to potassium, an asymmetry in temperature will be hard to spot. The spatial dependence of the exosphere should also show up in our relative intensity data, discussed in the next Section.

5.2. Sodium and Potassium Relative Intensity as a Function of Phase

Similar to the previous Section, here I discuss and contrast our relative intensities for both sodium and potassium, with 2 and 3 arcmin data presented separately. The reference craters are still limited to those used in Kuruppuaratchi et al. (2018) and

Rosborough et al. (2019). Our sodium 3 arcmin relative intensities are shown in Figure 5.13 with overlap from data in Kuruppuaratchi et al. (2018). Between 1st and 3rd quarter phases, the new data follows the same trend. Relative intensities show a general decrease towards full Moon from near subsolar points (quarter phases) with a lot of variation within the magnetotail region where some very bright measurements are made. If based on Section 5.1, sodium does not seem to be affected by meteors, then the pattern of intensity decreasing towards full Moon is plausible. Considering that the temperature away from full Moon (towards large phase angles) is closer to a PSD source, then at quarter phases (subsolar points) the intensity should be a maximum due to more photons available to release the sodium atoms. Moving away from quarter phases (local noon), intensity should decrease as the total flux of solar photons decrease since we are now moving away from the subsolar point where the PSD source is located. This effect is seen in Figure 5.13 and 5.14 where away from local noon, the intensity decreases going towards full Moon and new Moon. The peaks and troughs in the intensity data is a result of our FOV moving towards and away from the solar photon source. Our 2 arcmin sodium relative intensities in Figure 5.14 shows a similar trend between going to and away from the quarter phases. Note that for phases between 30^{o} and 50^{o}, the waning phase data is about 9% brighter than the waxing phase data, repeating the trend seen by Kuruppuaratchi et al. (2018) where waxing phase intensities were brighter than waning phase intensities. LADEE UVS data showed that sodium column abundances were seen to decrease then increase through full Moon, reaching a maximum at about 30^{o} phase after which it started to decrease again (Colaprete et al., 2016). Colaprete et al. (2016) attributed this enhancement partly, to the absence of sputtering inside the magnetotail, which means the sodium surface reservoir

had time to increase. By the time the Moon comes out of the magnetotail, solar wind sputtering causes release of adsorbed particle and the density decreases. In this interpretation, sputtering by the solar wind is considered a sink mechanism. This is in contrast to Killen et al. (2020) where the highest column abundances were observed after periods of increased ion flux (CME), implying that sputtering has an important role in refilling the exosphere. Note that the highest intensities are found during magnetotail passage in both 3 and 2 arcmin sodium data. The variation in relative intensity within the magnetotail, points to the exosphere responding to charged particle sputtering, not by solar wind ions but by plasma sheet ions.

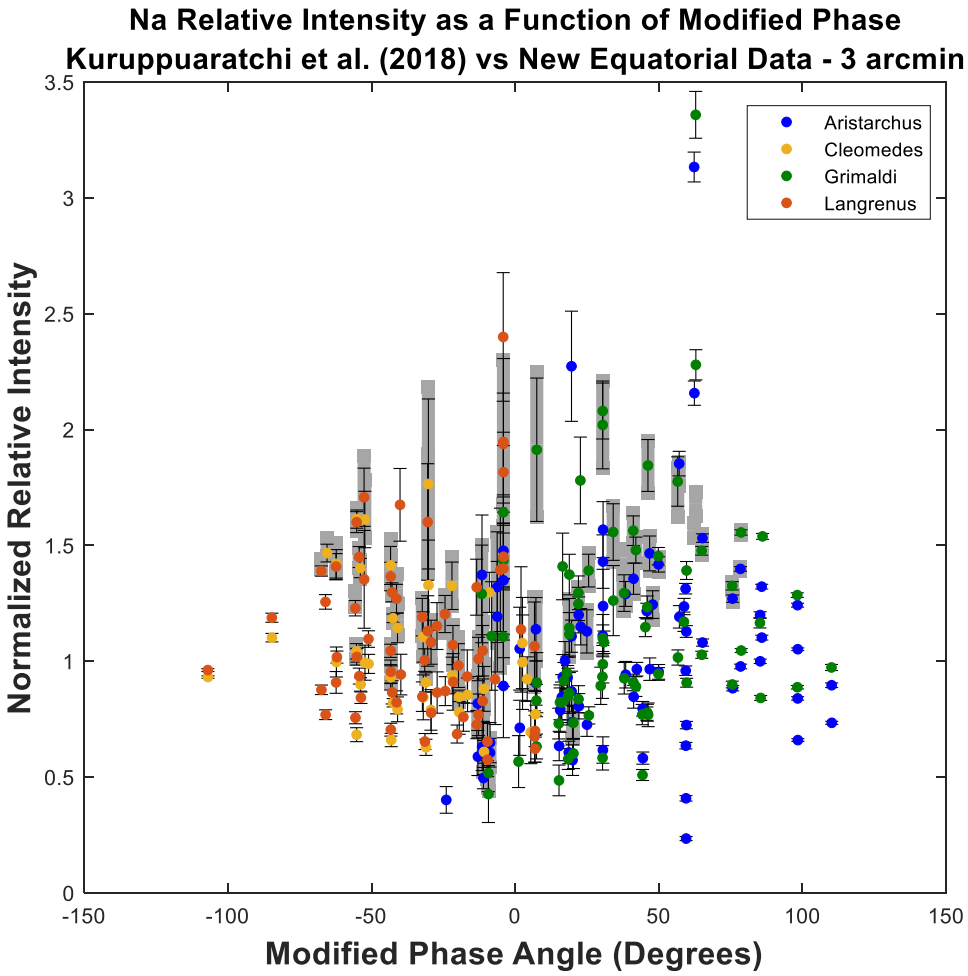

Figure 5.13: Sodium 3 arcmin equatorial relative intensities normalized by dividing values by 1000, to match the relative intensity plot of Kuruppuaratchi et al. (2018). Relative intensities in Kuruppuaratchi et al. (2018) show an increase from full Moon towards quarter phases, as so the data from 2013 – 2017. Data that goes past quarter phases show a decrease towards large phase angles going towards new Moon.

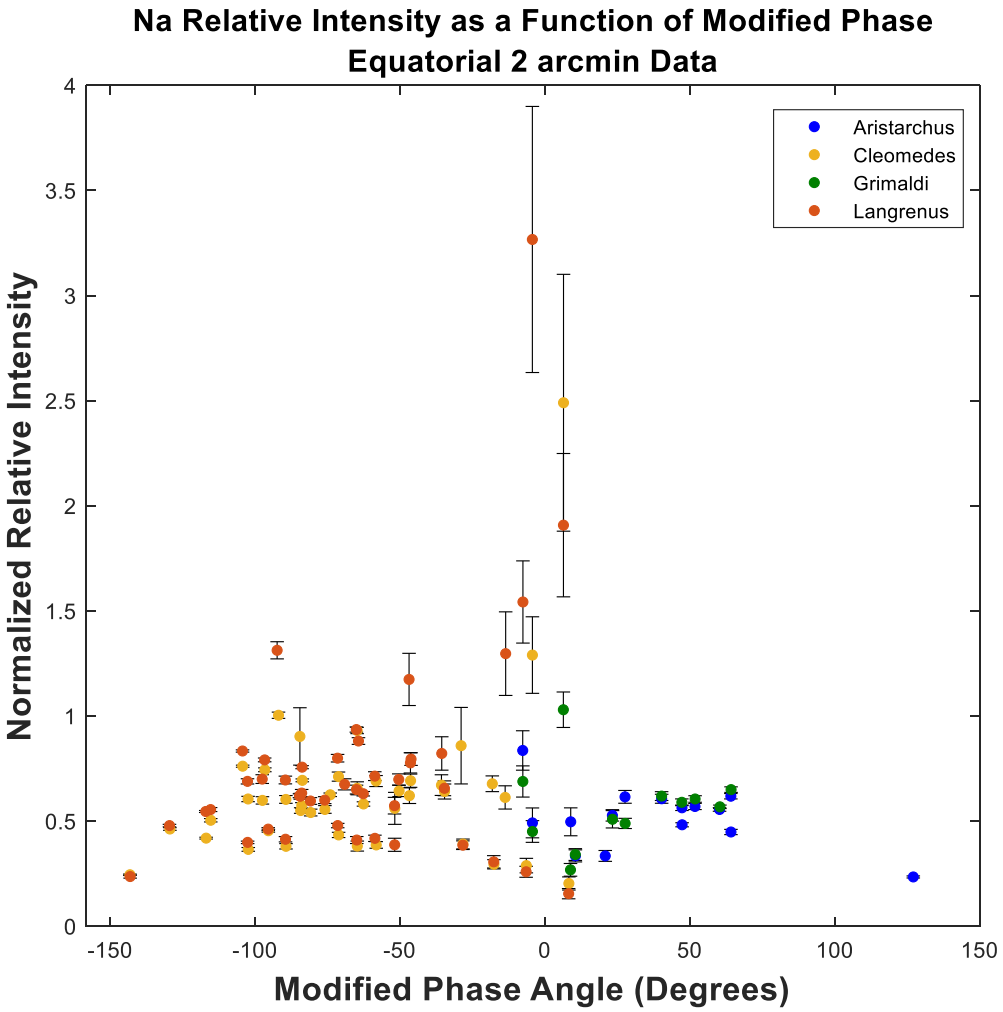

Figure 5.14: 2 arcmin sodium equatorial relative intensities that have been normalized by dividing values by a 1000 to match the equatorial data. The 2 arcmin data shows a similar pattern as the 3 arcmin data, ignoring the magnetotail values, with intensities increasing towards quarter phases from full Moon and falling off from quarter phases towards new Moon.

High latitude sodium 3 and 2 arcmin relative intensities are shown in Figure 5.15 and Figure 5.16, respectively. Both 3 and 2 arcmin relative intensities decrease from full Moon phases towards large phase angles – a trend that is opposite to the sodium equatorial intensities. As mentioned earlier, PSD is inefficient at high latitudes which means that it is expected for the exosphere to be dimmer closer to the poles. It is possible that because PSD is diminished at high latitudes, contributions by source processes with no SZA dependence

(e.g., MIV, charged particle sputtering from ions in the magnetotail) become important closer to the poles.

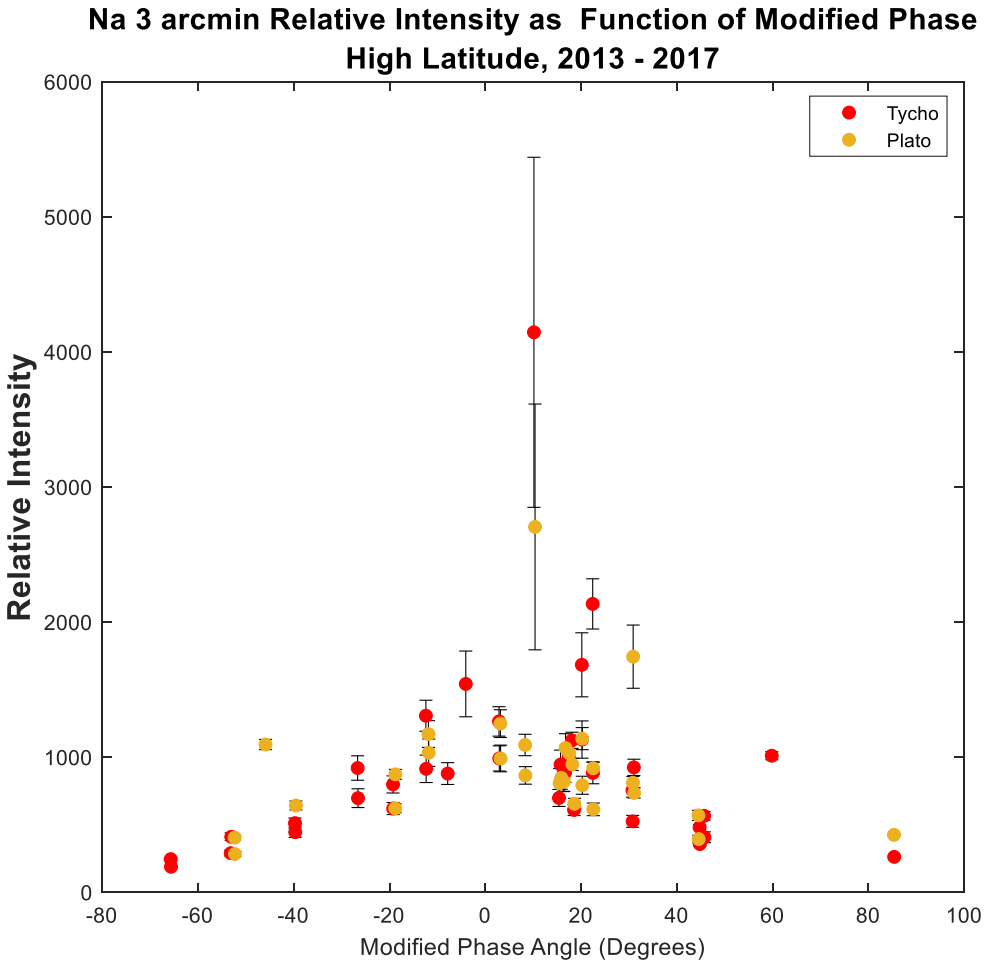

Figure 5.15: 3 arcmin high latitude sodium relative intensities for 2013 – 2017. The overall trend shows a decrease towards quarter phases full Moon, showing an opposite trend to the equatorial data.

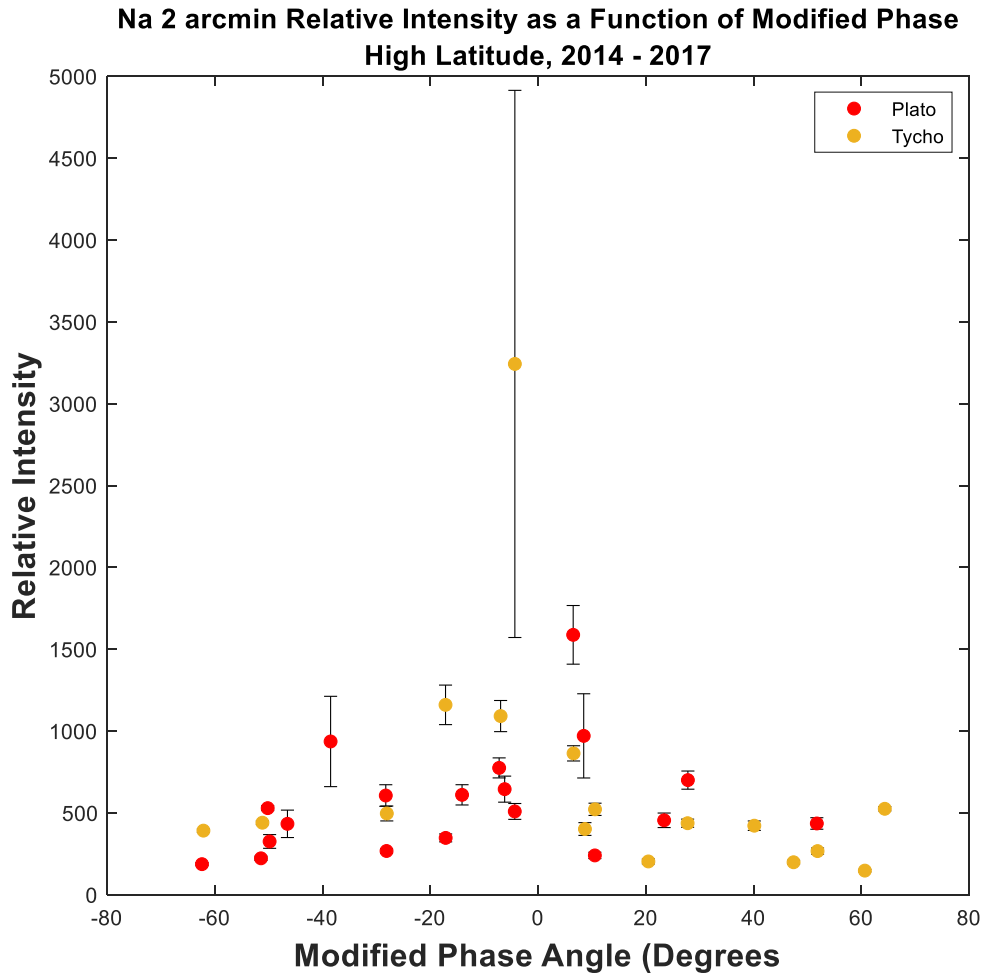

Figure 5.16: 2 arcmin high latitude sodium relative intensities for 2014 – 2017. The overall trend is relatively flat with a slight decrease towards quarter phases full Moon, showing an opposite trend to the equatorial data.

From the meteor correlation in Section 5,1, we know that sodium does not seem to respond to meteor streams as readily as potassium, nor did we catch any major streams during our high latitude observations for the dataset in this Chapter. We also know from previous discussions that once released through impacts, sodium migrates to the poles due to its long lifetime and so we can expect the high latitude exosphere to be populated by atoms released from micrometeoroid impacts. Table 5.5 shows median relative intensities for 2 and 3 arcmin sodium data, separated by equatorial and high latitude, based on where

the Moon is in its orbit. The opposing trend between equatorial and high latitude data we see visually from the plots is quantified in the table.

Table 5.5: *Summary of median sodium 2 and 3 arcmin relative intensities for equatorial and high latitude regions, denoted by position of Moon in its orbit.*

FOV (Arcmin)	Region	Modified phase angle < -30° relative intensity	Phase angle <30° relative intensity	Modified phase angle > -30° relative intensity
2	Equatorial	622 ± 16	497 ± 37	570 ± 13
	High latitude	413 ± 15	607 ± 48	345 ± 16
3	Equatorial	1027 ± 41	907 ± 94	1107 ± 33
	High latitude	408 ± 25	932 ± 82	566 ± 40

High latitude data is dimmer when the Moon is outside of the magnetotail compared to equatorial data but is brighter during magnetotail passage. If at high latitudes, we can expect an exosphere dominated by atoms that have migrated to the poles after being released by impacts, then ideally the exosphere should remain at a similar brightness. The increase in brightness during magnetotail passage then must be due to charged particle sputtering from plasma sheet ions inside the magnetotail. For equatorial data, PSD is always present and efficient, especially during times when we probe right at the source (noon). However, for high latitude data, PSD is inefficient allowing other processes to take precedence. The contradictory patterns in the high latitude relative intensity data and equatorial data is consistent with one source(s) taking precedence over the other source (s). The high latitude exosphere is created mainly through the response to meteors and charged particle sputtering. An in-depth discussion of the exosphere as a function of latitude at important regions of the Moon's orbit is presented in Chapter 6.

Relative intensity data for potassium is shown in Figure 5.17 and 5.18, for 3 and 2 arcmin data, respectively. The 3 arcmin potassium data contains all the data in Rosborough et al. (2019). Hints of the dawn-dusk asymmetry discussed for the potassium linewidths is seen here in relative intensity data, where the lines of best fit are added to guide the eye and shows waxing phases as having a steeper slope towards full Moon. Rosborough et al. (2019) reported that potassium relative intensities follow a source model centered at the subsolar point and reducing as a cosine (SZA) (T = 1200 K) for waning phase data, while waxing phase data implies a source that falls off more rapidly with SZA. In comparison, sodium relative intensities discussed earlier do not show any specific dawn-dusk asymmetry except that there is a lot of variability within the magnetospheric region (phase angles less than 30^{o}). Kuruppuaratchi et al. (2018) suggested that it is possible that the various plasma regions the Moon encounters over a lunation might explain some of the variations, especially inside the magnetospheric region. We cannot comment on this for potassium due to the lack of full Moon period data.

Waxing phase intensities that fall off faster than a cosine (SZA) is also seen in Figure 5.17, for the 2 arcmin potassium relative intensities. As for potassium, the waning phase trend was suggested to be a result of an integrated source rate that is higher at the dawn quadrant that at dusk. Rosborough et al. (2019) suggested that higher contributions by meteoroid impacts to the measured intensity are expected during the waxing phase because at that time the potassium-rich KREEP soils line up with the apex source of meteoroids. Rosborough et al. (2019) found that data taken at high latitudes are lower in intensity than data taken at low to mid latitudes, this trend was attributed to PSD being less efficient at high latitudes.

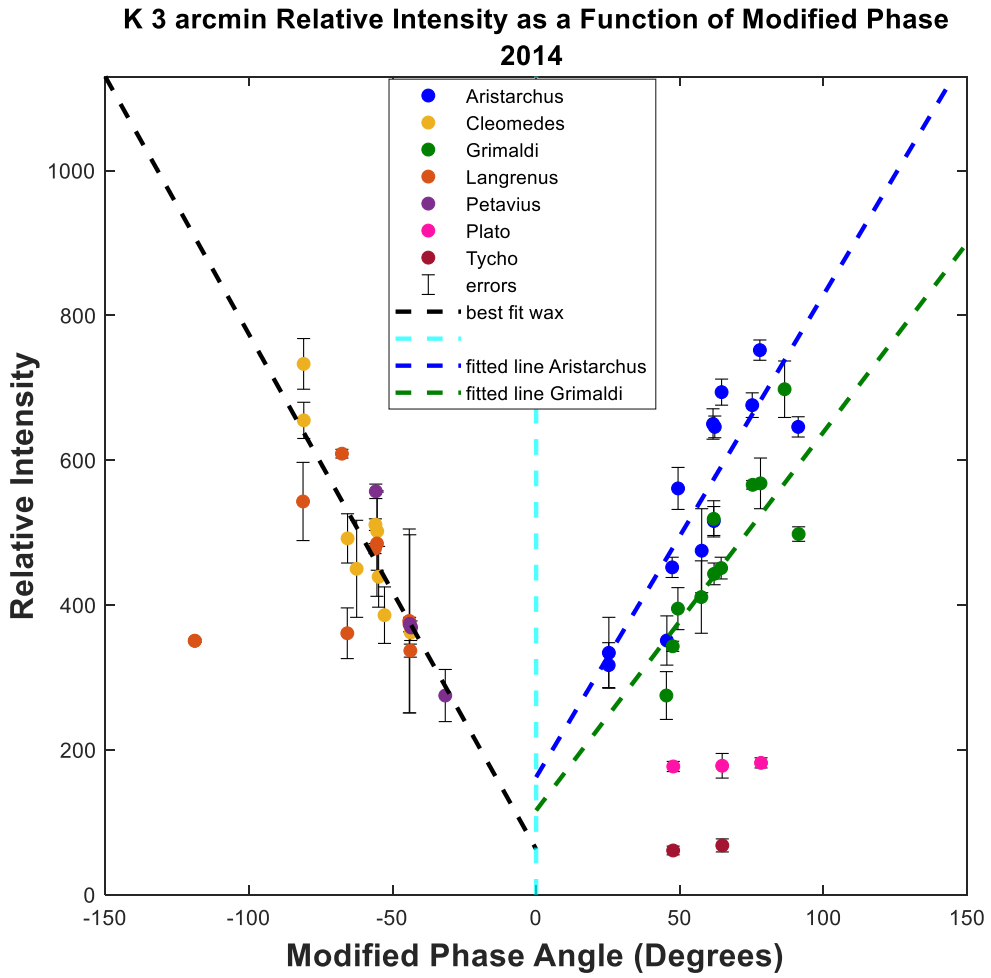

Figure 5.17: 3 arcmin potassium relative intensities with colors denoting the reference craters to match the same plot as shown in Rosborough et al. (2019). The trend lines are added to show the rate at which potassium falls off towards full Moon from subsolar points. The waxing phase data falls off faster than waning phase data indicating a source that falls off more rapidly with SZA. Aristarchus data is consistently brighter than Grimaldi data. Tycho and Plato are overall lower in intensity than equatorial craters. Plato intensities are also brighter than Tycho intensities, showing correlation with the KREEP regions.

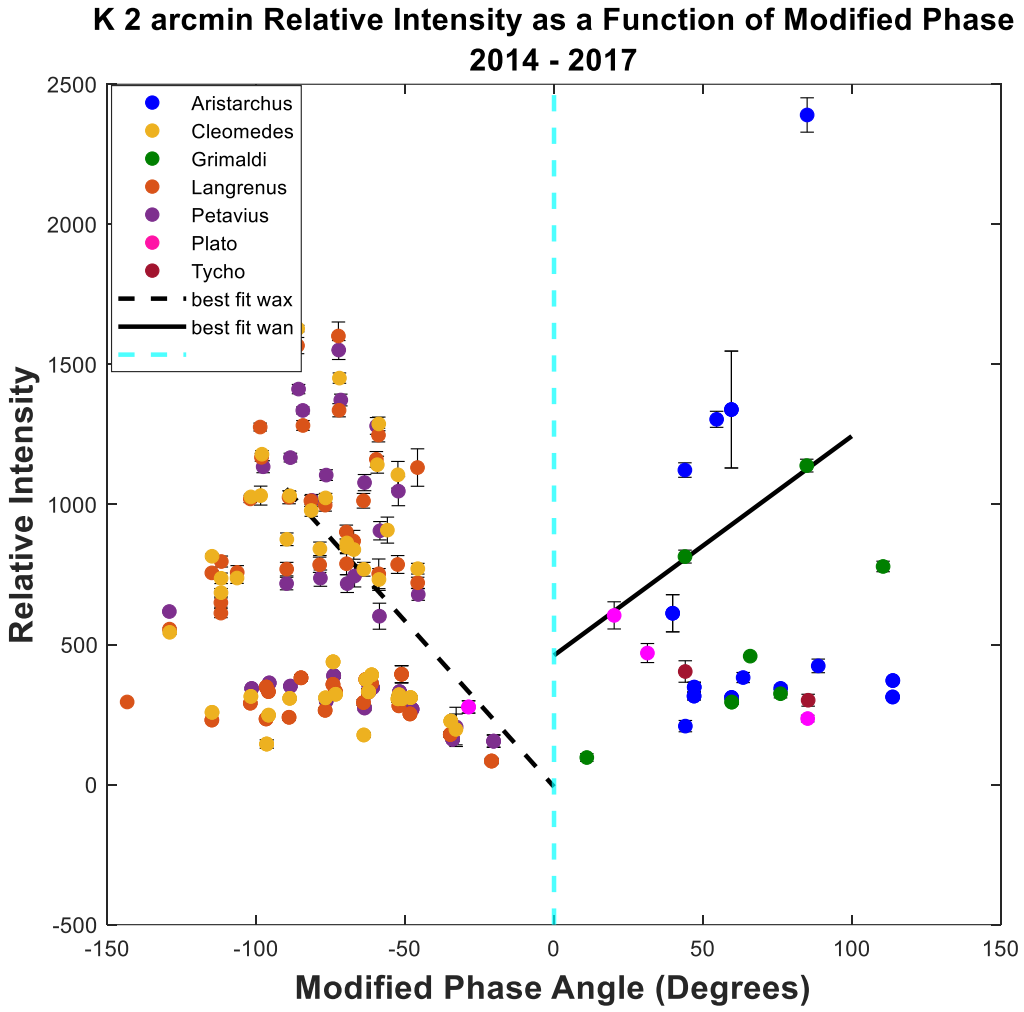

Figure 5.18: 2 arcmin potassium relative intensities with colors denoting the reference craters. The trend lines are added to show the rate at which potassium falls off towards full Moon from subsolar points. The waxing phase data falls off faster than waning phase data indicating a source that falls off more rapidly with SZA.

Rosborough et al. (2019) reported that intensities taken during waning phases, specifically off the KREEP areas, suggests that there is a strong dependence of the exosphere on surface composition. Data taken in regions that have high potassium concentrations (e.g. Aristarchus and Plato) than at other waning limb locations (e.g. Grimaldi and Tycho) have higher relative intensities. Note that intensities taken off the Plato and Tycho limbs are dimmer than equatorial data because PSD is inefficient at high

latitudes. The results of Rosborough et al. (2019) agree with LADEE results (Colaprete et al., 2016) that showed an asymmetrical potassium exosphere that is dependent on the KREEP regions. As such, Rosborough et al. (2019) concluded that the potassium exosphere exhibits both a North-South asymmetry (Plato vs Tycho) and a dawn-dusk asymmetry. Our 3 arcmin waning median relative intensities for potassium are shown in Figure 5.19 and shows that data taken off the Aristarchus and Plato limb are indeed brighter than the Grimaldi and Tycho limb, respectively. Our 2 arcmin waning phase median intensities in Figure 5.20 also shows that data taken off the Aristarchus limb is consistently brighter than Grimaldi limb and data taken off the Plato limb is brighter than the Tycho limb. The waning intensity data trends show that potassium tracks tightly with the surface abundance on the Moon.

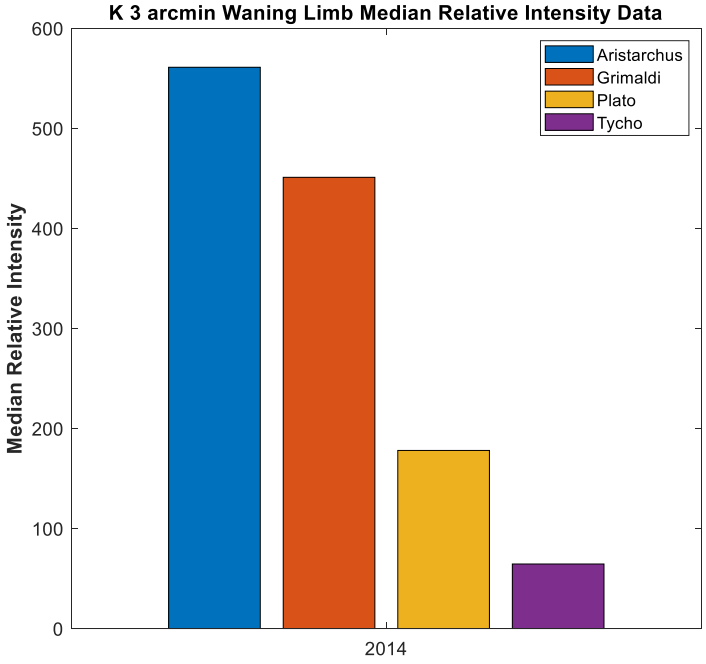

Figure 5.19: Bar chart showing 3 arcmin waning limb potassium median relative intensities with colors representing the reference crater data was taken off. Aristarchus median relative intensity is higher than Grimaldi, and Plato median intensity is higher than Tycho – both Aristarchus and Plato are located in the KREEP regions.

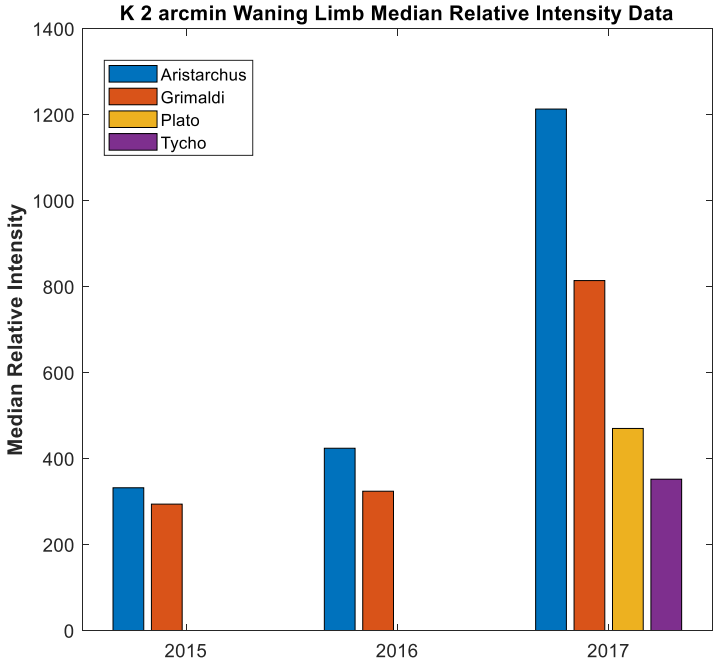

Figure 5.20: Bar chart showing 3 arcmin waning limb potassium median relative intensities with colors representing the reference crater data was taken off, grouped by year. Aristarchus median relative intensities are higher than Grimaldi for all 3 years, and Plato median intensities are higher than Tycho – both of which are in the KREEP regions.

To truly see the importance surface abundance plays, a dataset that has almost simultaneous observations of sodium and potassium is needed. LADEE UVS made simultaneous observations of sodium and potassium over 6 lunations, which makes it easier to compare. While it is not possible to observe sodium and potassium simultaneously with our instrument, there are some nights where we have made observations at the same locations and same offsets. For example, our 2014 January – May data have a lot of sodium data taken in a night where a complementary potassium offsets were made. Figure 5.21 shows our January – May 2014 3 arcmin relative intensity data as a function of day of year.

The meteor stream of interest is marked in grey as before. Note that high latitude data were removed from the potassium 3 arcmin dataset to facilitate the most direct comparison to sodium. I have also omitted sodium data taken inside the magnetotail to match the potassium population. The red curve on the plots were made to fit through the median relative intensity value per each run/Month shown on the plot. From Figure 5.21, sodium shows a gradually decrease from January towards May. Given that sodium has a cumulative response to meteor streams (Colaprete et al., 2016), this result is expected since meteor shower activity declines from Winter through Summer. Potassium shows an increase in Spring and decreases from April to May. This means that potassium is modulated more by the same process, compared to sodium. Since potassium waning data is likely to always be brighter than waxing data, due to the KREEP regions, then the overall trend as a function of time of year should also be looked at separately. In Figure 5.21, the black trendline passes through the median of the waxing phase data per run, while the marigold trendline passes through the waning phase data per run. Sodium waxing phase data follows the overall median trend very well, while waning phase data shows slight deviations from it. Overall, sodium has a smooth, gradual trend that shows a decline from Winter to Summer. Potassium on the other hand, shows that waxing phase data decline steadily from Winter to Summer, while waning phase data tracks the overall median trend closely. This means that the overall trend of potassium is heavily influence by the waning phase data – where the KREEP regions are.

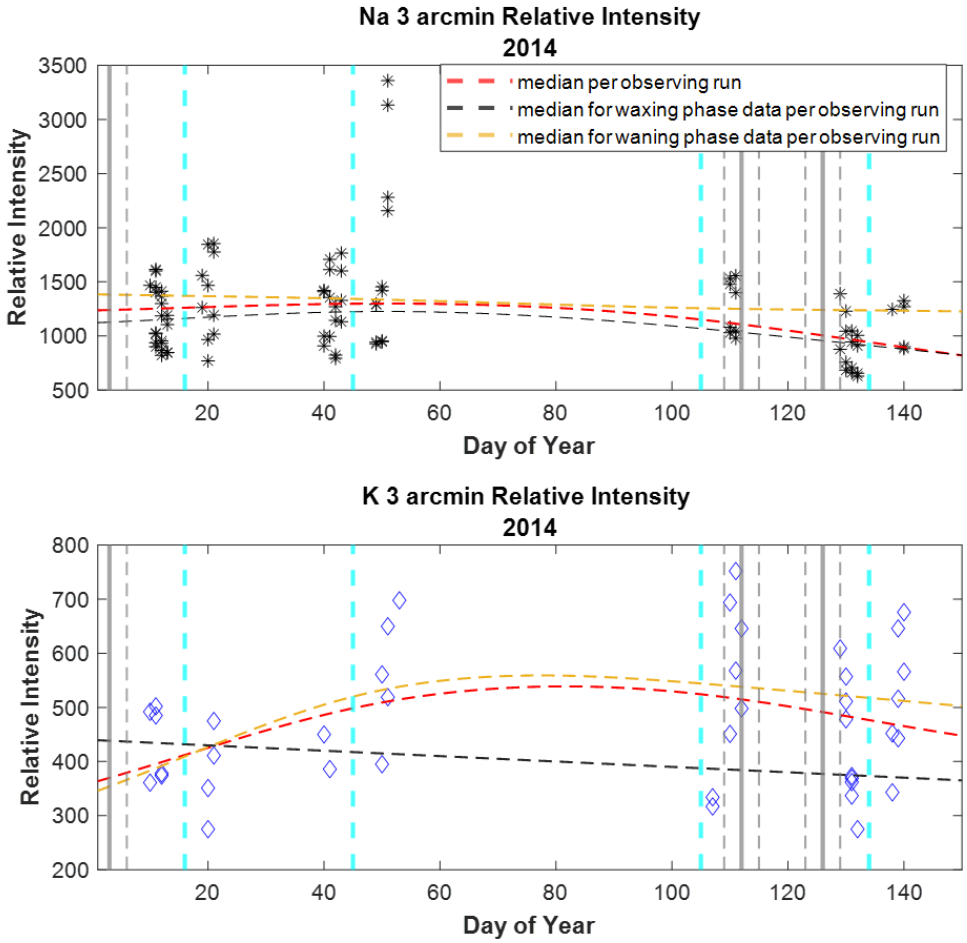

Figure 5.21: 3 arcmin sodium and potassium relative intensities in 2014. Magnetotail data in sodium has been omitted to facilitate a better comparison to potassium data. High latitude data (Tycho and Plato) have also been omitted from potassium data since the sodium data shown is only equatorial. The red curve goes through the median value for each run. The black curve goes through the median waxing data in each run. The marigold curve goes through the median values of the waning data in each run. The curves are shown as dashed lines because our data is not continuous and should only be used to show an overall trend. Sodium shows a very gradual decrease in intensity from Winter towards Summer. Potassium waxing phase data shows a steep decrease from Winter to Summer, while waning phase data shows an increase from Spring towards Summer. The waning phase potassium data, containing observations made from the KREEP regions, indicate that potassium is possibly responding to a source (meteors) more than sodium.

From the analysis of sodium and potassium discussed here, sodium and potassium behave differently as a function of phase angle, and to micrometeoroid impact vaporization. Additionally, there are differences within the same species as well that point to characteristics of source processes. For instance, sodium high latitude temperatures do not fall off towards large phase angles as steeply as sodium equatorial temperatures do. This is because PSD is not efficient at high latitudes since the source is located at subsolar points. The difference in temperature trends as a function of phase between equatorial sodium data and high latitude data further confirms the conclusions of Kuruppuaratchi et al. (2018) that, overall, PSD is the major source mechanism for the equatorial lunar exosphere at subsolar points, with contributions from other processes becoming more important towards the waning and waxing terminators.

While PSD also plays a role in the generation of the potassium exosphere, it appears that potassium tracks better with meteor showers than sodium. The lack of a significant dawn-dusk asymmetry in sodium data implies that unlike potassium, it has a long lifetime. This is apparent in both the symmetrical temperature data around full Moon, and the smooth change in relative intensities as a function of Month. Potassium, on the other hand, has shown signs of responding to strong meteor showers and the extent of the dawn-dusk asymmetry depends on how soon after the peak of the meteor shower observations had started. This implies that potassium can have pronounced but short-lived responses to meteor showers. Additionally, the effects of meteor streams are much more pronounced than just the sporadic background. The effects of the KREEP region (refer to Figure 1.5 in Chapter 1, Section 1.2.2) shows up in our potassium waning phase intensities, where Aristarchus is consistently brighter than Grimaldi, and Plato is consistently brighter than

Tycho. Furthermore, the waning phase potassium data shows more variation throughout the months, than the waxing phase data. This implies that potassium tracks closely with the surface abundance on the Moon. Sodium data does not point to any concentrations of abundances in the regolith, which implies that sodium might just be more spread out on the lunar surface than potassium.

5.3. Summary and Conclusions

In this Chapter I have analyzed data collected from 2013 – 2017, limited to equatorial and high latitude craters offsets. Furthermore, the bulk of the analysis was done as a function of phase angle. The key findings from sodium and potassium data in terms of temperature and relative intensity are summarized in Table 5.6 and Table 5.7. The tables have been structured to follow the Sections in this Chapter and offer a side-by-side interspecies comparison summary. The main constraints provided by the analysis in this Chapter is that the sodium exosphere is dominated by PSD at subsolar points in equatorial regions with contributions by MIV and sputtering at high latitudes and terminator/limb sides becoming more important. Furthermore, sodium does not show a response to meteor shower activity as readily as potassium and shows a smooth annual trend instead. This indicates that sodium atoms have long lifetimes. Sodium data at all latitudes indicate that passage through the magnetotail region is of importance and points to the importance of charged particle sputtering. The constraints for potassium include a high correlation with surface abundance and time sensitivity in the exosphere's response to meteor activity. These two factors are not independent but are likely to interact with each other. These key findings indicate that latitude, plasma region, surface abundance, and time are factors that

are likely not independent but interact with each other to form the response of the exosphere in terms of temperature and relative intensity.

In the next Chapter, I discuss our sodium and potassium data over the same years, but not limited to the main craters. Furthermore, I perform the analysis as a function of latitude and based on the plasma region the Moon is in. Breaking down this vast dataset according as many variables as possible hold the key to disentangling source processes and providing further constraints on them. Chapter 6 is a collection of studies aimed at bringing together all the key pieces that will not only strengthen arguments presented in Chapter 4 and 5 but help fill in gaps in the understanding of the evolution of the lunar exosphere itself.

Table 5.6: *Summary of key points in linewidth/linewidth derived temperature for sodium and potassium observations.*

Sodium	Potassium
• Equatorial temperatures increase from near quarter phases towards full Moon. This trend is attributed to viewing high energy, long ballistic range atoms travelling from subsolar points to limb/terminator sides and agrees with the study in Kuruppuaratchi et al. (2018). • High latitude data show the same overall trend as the equatorial data, with the difference being that high latitude data show a smaller increase from near subsolar points towards full Moon. • Both equatorial and high latitude temperatures indicate that charged particle sputtering from ions in the plasma regions of the magnetotail (i.e. plasma sheet) may be important. • Temperatures show no strong correlation to meteor shower activity.	• Potassium linewidths (and derived temperatures) show dawn-dusk asymmetry attributed to a combination of PSD and MIV. Waxing limb temperatures are overall higher than waning limb temperatures. This result agrees with the linewidth results of Rosborough et al. (2019). • Data that showed the largest dawn-dusk asymmetry consisted of observations made close to major meteor showers. • The sporadic background meteors are likely to have a weak correlation to the response of the exosphere because the most distinct responses are seen at times when observations were made close or at the peak of major showers. • Time sensitive responses from meteor shower activity indicate that potassium has a short lifetime.

Table 5.7: *Summary of key points in relative intensities for sodium and potassium observations.*

Sodium	Potassium
• Equatorial 2 and 3 arcmin relative intensities show an increase towards subsolar points from New Moon to quarter phases and from Full Moon to quarter phases. • High latitude 2 and 3 arcmin relative intensities show the opposite trend to equatorial data, with intensities falling off towards quarter phases from full Moon indicating that the role of PSD is diminished at these regions, with other source processes taking precedence. • Both equatorial and high latitude relative intensities indicate that passage through the magnetotail affect in the response of the exosphere. • Data in 2014 show that sodium has a smooth and gradual response to meteor shower activity that with relative intensities decreasing from Winter towards Summer a trend that follows annual meteor shower activity. The gradual response to meteor activity indicates that sodium atoms have long lifetimes.	• 2 and 3 arcmin relative intensities show both dawn-dusk asymmetry and North – South asymmetry. Asymmetry is linked to observations made off the KREEP regions. • Waxing phase data for both 2 and 3 arcmin relative intensities fall off faster than waning phase data, supporting the result of Rosborough et al. (2019) that waxing phase data fall off faster with SZA. • 2014 data show that waxing limb data follow a decrease in relative intensities from Winter to Summer, similar to sodium. Waning phase intensities, however, show signs of influence by meteor showers. The waning limb is also where the KREEP regions are, implying that the exosphere tightly follows the abundances on the surface. • Potassium relative intensities show an exosphere that responds to meteor showers on short timescales and is dependent on the surface abundance.

CHAPTER 6: TRACKING THE SPATIAL AND TEMPORAL DEPENDENCE OF THE LUNAR EXOSPHERE: A TALE OF TWO SPECIES

Key Points:

- Depending on the Moon's near plasma environment, the contributions from PSD, MIV, and charged particle sputtering vary.

- Sodium temperatures indicate that time spent in the plasma sheet is of importance as there is a possible positive correlation in sodium temperatures and relative intensities with time spent in the plasma sheet.

- Differences between sodium and potassium temperature and relative intensity trends as a function of plasma region indicates that potassium appears to respond more to a process that has no SZA dependence (MIV).

- Sodium temperatures increase from low to high latitudes.
- Sodium relative intensities peak on low-mid North and South latitudes.
- Potassium tracks closely with the KREEP regions.
- The sodium exosphere appears to cool down as a function of altitude.

In this Chapter, I build on the work of Chapter 4 and 5 and discuss the latitudinal and radial dependence of the exosphere. Additionally, while Chapter 4 and 5 discussed results in terms of simply moving in and out of the magnetotail region, here I discuss sodium and potassium data taken at all latitudes, as a function of the 3 main plasma regions the Moon encounters: solar wind, magnetosheath, and the magnetotail. Chapter 5 built on the results of Chapter 4 but only contained a limited dataset with observations matching the main reference craters used in Kuruppuaratchi et al. (2018) and Rosborough et al.

(2019). In this Chapter, I include FOV at Limb and Edge data taken off all the reference craters we have used (refer to Appendix B).

From discussions presented in Chapters 4 and 5, we know that PSD dominates the source mechanisms for the lunar sodium exosphere at subsolar points, with processes such as sputtering and micrometeoroids becoming more important towards the dawn and dusk terminators/limb. We also know that thermal desorption and PSD have a SZA dependence while charged particle sputtering follows a cosine dependence of the angle between the surface and the solar wind vector. Processes that follow SZA dependence are less efficient at high latitudes, as seen from results in Chapter 5, Section 5.1. We also saw that for sodium, the effect of meteors did not appear to be localized but had more of a global effect on the exosphere. From the trends seen in potassium it appears that a high latitude shower could affect the exosphere at equatorial latitudes. This is because impact vaporization due to meteor sources (both sporadic and showers) have a broad latitudinal distribution and so the entire lunar surface can be exposed to impacts. Some of these impacts can have velocities as high as 30 km/s, with near ecliptic directions producing impacts with velocities up to 72 km/s (Pokorny et al., 2019). While PSD is important for potassium, due to the KREEP regions and a much smaller lifetime on the surface than sodium, the effect of micrometeoroids on the lunar potassium exosphere is much more localized and significant than for sodium. Sodium has a cumulative response to micrometeoroids and only shows a smooth pattern related to meteor shower activity, indicating that sodium abundance on the lunar surface might be more spread out than potassium and that sodium atoms have much longer lifetimes. Potassium also showed dawn - dusk asymmetry in

addition to a North - South asymmetry. All this point to a spatial dependence of the lunar exosphere.

Additionally, it can be expected that exospheric atoms released from these source processes make up the near-surface exosphere and the extended corona, depending on their velocity distribution. Lower energy processes (PSD and thermal desorption) can be disentangled from higher energy processes (sputtering and impacts), by studying the dependence of the exosphere radially outward from the surface. Our FPS observing campaign was initially designed to make measurements of the lunar exosphere extending radially outward from the surface. Later, we adjusted this to include observations spanning a larger latitudinal range with measurements made closer to the surface. Spatial dependence can therefore be divided into latitudinal coverage and radial coverage. This temporal variation includes both short term (magnetospheric passage, CME's, meteor showers) and long term (solar cycle activity). In the next Section, I introduce the various plasma regions the Moon encounters and why it is important to study our observations as a function of latitude.

The Moon's interaction with the various plasma regions encountered during a lunation can provide us with important clues about source processes themselves. In Sections 6.2 – 6.5, I break up our sodium and potassium observations by plasma region and discuss how the exosphere responds to these various regions as a function of latitude. For the magnetotail region, I offer an in-depth analysis for determining the time spent inside the plasma sheet. I then discuss our data in terms of latitude by chosen nights to serve as a comparison to a coronograph study by Killen et al. (2019,2020) in Section 6.6. Finally, I discuss the radial dependence of the sodium exosphere in Section 6.7 to offer a

complete spatial study. The analysis of data by plasma region and latitude, in addition to the results of previous Chapters, aims to satisfy the goal of this dissertation.

6.1. The Moon in various plasma environments: An Introduction

As we know, the Moon lacks a global magnetic field and only has a tenuous atmosphere, thereby having most of its surface directly exposed to the near-space plasma environment. The interaction of the lunar surface with the ambient plasma results in physical processes that are spanning scales from a few meters above the lunar surface to the radius of the Moon (Kallio et al. 2015). There are regions on the Moon where the surface is strongly magnetized, called lunar magnetic (swirls) anomalies; these areas on the lunar surface are shielded from plasma due to their 'mini-magnetospheres'. This topic is, however, beyond the scope of this dissertation.

A variety of lunar surface – plasma interactions occur depending on the type of plasma in various regions over which the Moon is exposed during a lunation. During its orbit around Earth, the Moon spends most of its time in the supersonic solar wind but also encounters the terrestrial magnetosheath and the magnetotail for a quarter of the time (Kallio et al., 2015; Harada and Halekas, 2016). There are longitudinal and latitudinal effects to the way the plasma interacts with the lunar surface depending on the specific plasma environment characteristics. For instance, the optical properties of walls of lunar craters showed dawn-dusk asymmetry which was attributed to the systematic change of properties of plasma when the Moon is inside the Earth's magnetosphere (Sim et al., 2017). We also know that because of the angle between the lunar surface and the solar wind vector,

that in the undisturbed solar wind the solar wind particles act like PSD – having a SZA dependence. This results in the decrease in intensity of these precipitating solar wind particles with increasing latitude. A study by Kallio et al. (2015) found that the highest cumulative solar wind proton addition on the lunar surface is located on the farside, while the most energetic protons precipitate on the nearside.

The solar wind is a supersonic magnetized plasma from the Sun that fills the Solar System (Richardson 2013) with typical speeds of about 300-800 km/s (Borovsky et al., 2018). Without the solar wind the Earth's magnetosphere would be just that of a symmetric magnetic dipole, but due to the solar wind it is compressed on the sunward side and elongated into a long tail on the anti-sunward side (Borovsky et al., 2018). As the Earth's magnetosphere responds to the solar wind it is highly dynamic. Charged particle sputtering due to particles with higher energies than the undisturbed solar wind is encountered every lunation by the Moon, as it passes through Earth's magnetosphere region. The magnetosphere is driven by the solar wind and contains different populations of particles in various regions. The main regions that are of concern to this work are the magnetosheath and magnetotail (specifically the plasma sheet that resides in the magnetotail). The terrestrial magnetosheath plasma is typically supersonic at the lunar orbit and magnetotail plasma exhibits subsonic flows (Harada and Halekas, 2016). There are two sources of plasma in the magnetosphere, the first being plasma of solar wind origin entering the magnetosphere via the magnetopause. The solar wind origin plasma has particles characteristic of the solar wind itself and is comprised of protons (H^{+}) and alphas/ionized helium (He^{++}) (Borovsky et al., 2018) and trace amounts of heavy ions that can be highly ionized (Kivelson and Bagenal, 2007). The second source is the Earth's ionosphere, where

a small fraction of high energy ionospheric plasma can escape up magnetic field lines and into the magnetosphere (Kivelson and Bagenal, 2007). Ionospheric plasma composition is characteristic of the host planet's atmosphere – for Earth this is O^+, He^+, and H^+ (Kivelson and Bagenal, 2007; Borvsky et al., 2018).

Figure 6.1 shows the various plasma regions the Moon can encounter. The solar wind is 'shocked' at the bow shock where the solar wind plasma is heated, compressed, and deflected around the magnetosphere in a region called the magnetosheath. This deflection becomes important for charged particle sputtering discussed in Section 6.2 onward. The magnetosheath lies between the bowshock and the magnetopause. The next region of interest is the magnetotail on the nightside of Earth, which extends up to a couple of 100 R_E (Earth Radii). Once the Moon interacts with the magnetotail, it spends time in the extremely tenuous 'quiet' lobe regions and the high energy ion population in the plasma sheet. For purposes of this study, the tail lobes are of little importance since the particle density in the lobes are extremely low (see Table 6.1). The ion plasma sheet is a hot, low-density plasma, typically of solar wind origin, but becoming rich in O^+ when magnetospheric activity is high (Borvsky et al. 2018). The plasma sheet is a highly dynamic region and changes position through flapping and twisting motions. This motion is of importance to us because it determines the amount of time the Moon spends inside the plasma sheet per lunation.

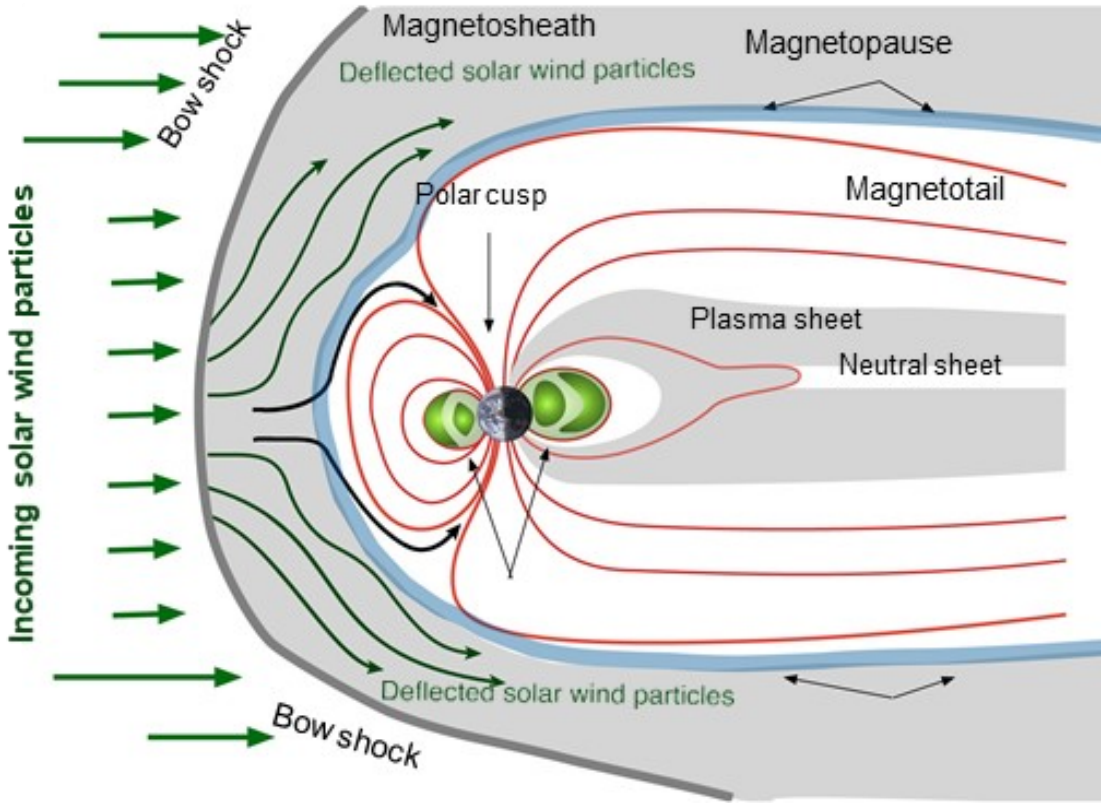

Figure 6.1: Cartoon depicting various regions in Earth's magnetosphere and the direction of the deflected solar wind particles (Luis Conde, 2018).

A summary of the different plasma regions of interest to us and a description of their particle populations are presented in Table 6.1 Note that there are more regions in the magnetosphere than what is described in Table 6.1; for a detailed discussion refer to Borovsky et al. (2018). The ion temperature ranges in Table 6.1 are adopted from Lue (2015), Harada and Helakas (2016) Table 18.1, Figure 2 from Borovsky et al. (2018), and Denton et al. (2017) for a typical order of magnitude ranges of plasma parameters in the near lunar environment. The values in Table 6.1 are approximate and during times of transient ion events such as CMEs or flares, these ion temperatures and fluxes can extend out to much larger values into the MeV range.

Table 6.1: *Typical order of magnitude plasma parameters in the near Lunar environment (Lue, 2015;Harada and Halekas, 2016; Denton et al., 2017; Borovsky et al., (2018).*

Region	Description	Ion population	Density (cm^{-3})	Ion temperature (eV)
Undisturbed solar wind	Supersonic plasma consisting mostly of ionized hydrogen – protons (H^+) and electrons and alpha particles (He^{2+}) with trace amounts of heavy atomic nuclei. It is responsible for forming the interplanetary magnetic field (IMF).	H^+ (~) 96%, He^{++} (~4%), very small amounts of ionized Carbon, Oxygen, and Neon.	~ 1 - 10	~ 1000 - 2000
Magnetosheath	Shocked solar wind plasma that lies between the bow shock and the magnetopause. The magnetosheath plasma is typically supersonic at the lunar orbit.	Heated and compressed, solar wind ions. Solar wind thermal distribution changes from a Maxwellian distribution to a distribution with significant tails towards higher thermal velocities (kappa distribution).	~ 2- 50	Comparable to solar wind ions but can have a broader energy distribution extending to higher ranges (Jasper Halekas, private communication).
Tail Lobes	Very low density, "vacuum" like region.	Plasma of magnetosheath and plasma sheet origin.	~0.01 - 1	~10 - 100
Plasma sheet	Hot, high energy but low-density plasma that lies close to the magnetic equatorial plane	H^+ (mainly), O^+, He^+	~0.1 - 1	~100 – 10,000

Now that we know the basics about the Earth's magnetosphere, I will discuss the importance of each of these regions in terms of our lunar sodium and potassium data. For purposes of this study, the approximate regions of the solar wind – magnetosheath – magnetotail boundaries will be taken to be at greater than 70 degrees lunar phase, between 70 and 30 lunar phase, and less than 30 degrees lunar phase. These cut-offs are approximate boundaries based on the works of Sarantos et al. (2010), Kallio et al. (2019), and my estimations based on ARTEMIS proton flux data provided by Jasper Halekas (private communication). The proton flux jumps up during magnetosheath passage and drops to very small amounts during magnetotail passage. As mentioned earlier, in the undisturbed solar wind we can expect solar wind ions to impact the lunar surface in straight lines - just like PSD. In the solar wind, we can expect all source processes to be at work with PSD dominating. In the magnetosheath, something interesting happens to the path taken by the shocked solar wind ions. As seen in Figure 6.2, the straight lines that the solar wind ions travel before the bow shock are 'curved' around - like water going around a rock in a stream. This means that the disturbed solar wind ions are now hitting the lunar surface at some angle instead of straight lines. Since solar wind ions have a cosine dependence with the angle of the surface element with respect to the solar wind normal (Killen et al. (2019), they can precipitate onto the lunar surface with a broader latitudinal distribution rather than a cosine of latitude function centered at the subsolar point.

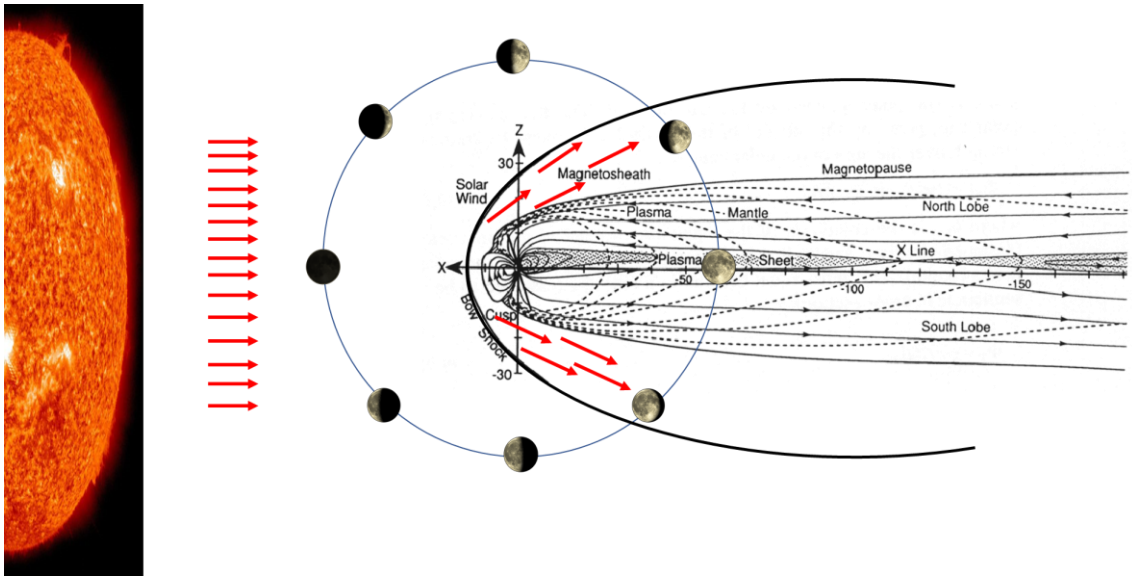

Figure 6.2: Cartoon depicting the location of the Moon in its orbit around Earth and the various plasma regions it encounters. The various angles at which solar wind particles (red arrows) impact the Moon are shown. The diagram was made using the magnetosphere cartoon from Hughes (1995). The Moon is at about 60 R_E from Earth. This cartoon is not to scale.

In the magnetotail we have the plasma sheet between the North and South lobe regions. The plasma sheet is a very dynamic region that is constantly in motion, meaning that the Moon encounters the plasma sheet multiple times during a lunation. The location and shape of the plasma sheet are of importance to us as it determines the amount of time the Moon spends inside this region, which may have implications for the exosphere. The drivers of the plasma sheet geometry include a mixture of effects involving interplanetary magnetic and plasma conditions, internal magnetospheric processes, and season and diurnal motion of the Earth's dipole tilt, (the angle between the Earth's geomagnetic dipole axis and the geocentric solar magnetospheric (GSM) Z-axis) (Dayeh et al., 2015). In a study designed to determine the shape of the plasma sheet, Dayeh et al. (2015) concluded that the plasma sheet is a complex structure that undergoes these 3 types of deformation:

a) Flapping: caused by the changing interplanetary flows due to deviations in the solar wind flow vector.

b) Twisting: caused by changes in the transverse component of the IMF and depends on the IMF magnitude and orientation.

c) Warping/hinging: Caused by variation of the dipole tilt due to the combined seasonal and daily variations – a process that moves the plasma sheet above and below the equatorial plane resulting in an oscillatory motion along the vertical Z direction that extends back in the tail.

Illustrations for the above 3 processes are shown in Figure 6.3 and we can see just how dynamic the plasma sheet is and how it can change over a day and a year. The angle between the dipole axis and the GSM axis, shown as the dipole tilt with Ψ in Figure 6.3c and Figure 6.4, varies as a function of the season due to the angle between the Earth's equatorial plane and the ecliptic plane (~23.5°) and as a function of time due to the angle between the Earth's rotation axis and the dipole axis (~ 10°) (Ingrid et al.,2012; Dayeh et al., 2015). During the Spring and Fall equinoxes, the Ψ is 0. During the Summer solstice in June, $\Psi > 0$,the plasma sheet is above the equatorial plane and during the Winter solstice $\Psi < 0$ which means that the plasma sheet is below the equatorial plane (Ingrid et al., 2012). The warping of the plasma sheet due to diurnal motion is always present throughout the year and is superimposed on top of the seasonal variation. A depiction of the plasma sheet during various seasons is shown in Figure 6.4 which shows model runs for the 1989c Tsyganenko global magnetic field model. As seen from Figure 6.3c the varying location of the plasma sheet due to seasonal and diurnal motion creates a 'hinge' whereby the near-Earth plasma sheet is at an angle to the ecliptic, but the distant plasma sheet is aligned

parallel to the ecliptic (in the solar wind direction). Here, we are only interested in the distant tail because the Moon is at about 60 R_E. The distant tail is a certain distance above the ecliptic with some oscillation due to diurnal motion.

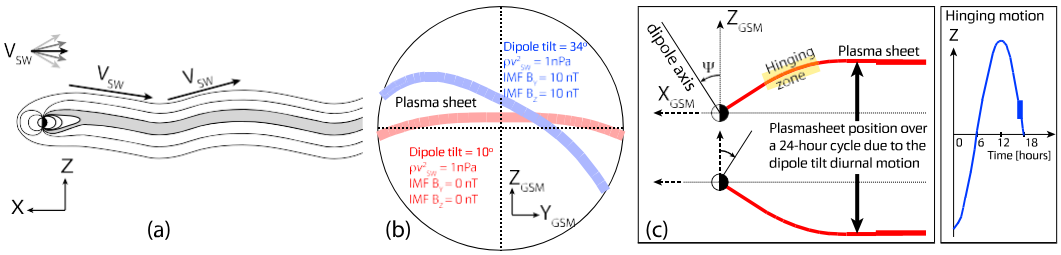

Figure 6.3: Illustration as shown in Dayeh et al. (2015) with (a) flapping,(b) twisting of the plasma sheet about the *X*-axis during two different IMF conditions and dipole tilt values and (c) warping of the plasma sheet; (c) the hinging motion during a 24 h period comprising midnight-dawn-noon-dusk. These illustrations were made by Dayeh et al. (2015) through adaptations of work by Bowling and Russell (1976) and plasma sheet models by Tsyganenko and Fairfield (2004).

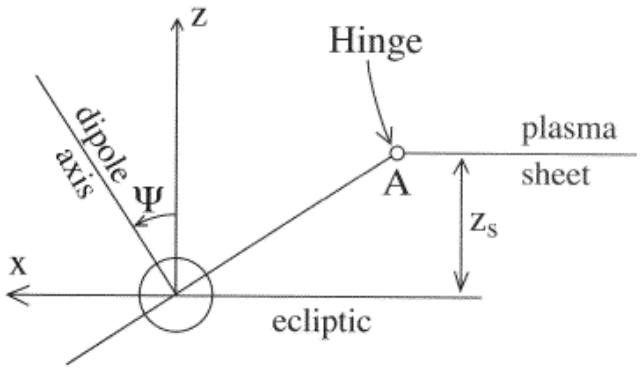

Figure 6.4: Diagram depicting the near-Earth plasma sheet and the distant plasma sheet beyond the hinge location. The deformation of the plasma sheet and the hinging occurs due to the varying dipole tilt angle (Stern, 2006).

In addition to the variation of the plasma sheet shape due to the seasonal and diurnal motion of Earth, there is another important factor that needs to be considered – lunar precession. The precession of the lunar orbital nodes around the ecliptic, with a period of

18.6 years, is responsible for the drift of solar and lunar eclipses and most importantly, the ecliptic latitude where the Moon crosses the magnetotail which in turn controls the duration and number of crossings the Moon makes with the plasma sheet (Hapgood, 2007). To determine the number and length of Moon – plasma sheet encounters, the following 2 factors need to be taken into consideration:

1) Moon's height above the ecliptic: The Moon is inclined by ~ 5^{o} to the ecliptic and depending on where it is in its orbit, this determines how high above the plane of the ecliptic the moon lies. On average, this vertical distance is about 5.5 R_E (Hapgood,2007).

2) The location of the plasma sheet above the ecliptic: As discussed above, the plasma sheet experiences warping and acts as if it is attached to a hinge at near-Earth distances with the distant tail aligning itself in the plane of the ecliptic at a certain height. The hinge distance is about 10 R_E and on average the vertical distance of the plasma sheet about the ecliptic is ~ 4 R_E (Hapgood, 2007).

The intersection between the Moon and plasma sheet locations is determined by the phase of the above 2 cycles. The lunar precession cycle minimum occurs when the ascending node of the Moon's orbit is close to RA of 0°. In this scenario, the Moon will have its Northerly and Southerly tail crossings in December and June, respectively (Hapgood, 2007). In this scenario, the Moon is out of phase with the location of the plasma sheet during the year. For this reason, the Moon will only occasionally encounter the plasma sheet during the cycle minimum. About 9 years later during the cycle maximum, the scenario is opposite and now the Moon has its most Northerly and Southerly tail

crossings are in phase with the location of the plasma sheet resulting in frequent encounters with the plasma sheet. Hapgood (2007) modeled the plasma sheet encounters of the Moon, considering the seasonal and diurnal motion of the plasma sheet and presented results for the amount of time the Moon spends inside the plasma sheet for each lunation from 1960 to 2030. These results will be used in conjunction with our magnetotail passage data to determine the effects of plasma sheet ions on the lunar exosphere in Section 6.2

6.2. Sodium effective temperature as a function of latitude in various plasma regions

In this Section, I present sodium and potassium data by plasma region in both temperature and relative intensity. Following the same methodology in Section 5.2, the sodium and potassium relative intensities will be broken up into 2 and 3 arcmin data. All data includes offsets for FOV at the limb and FOV at the field lens edge. Figure 6.5 (top) and (bottom) shows sodium and potassium effective temperature as a function of modified phase angle. At first glance, we can see that the most variation in temperature occurs within magnetotail passage (for sodium). The magnetosheath region for both species also shows some variation and temperatures that are in the magnetotail range. The solar wind data for both species show the coolest temperatures with the least number of variation/outliers.

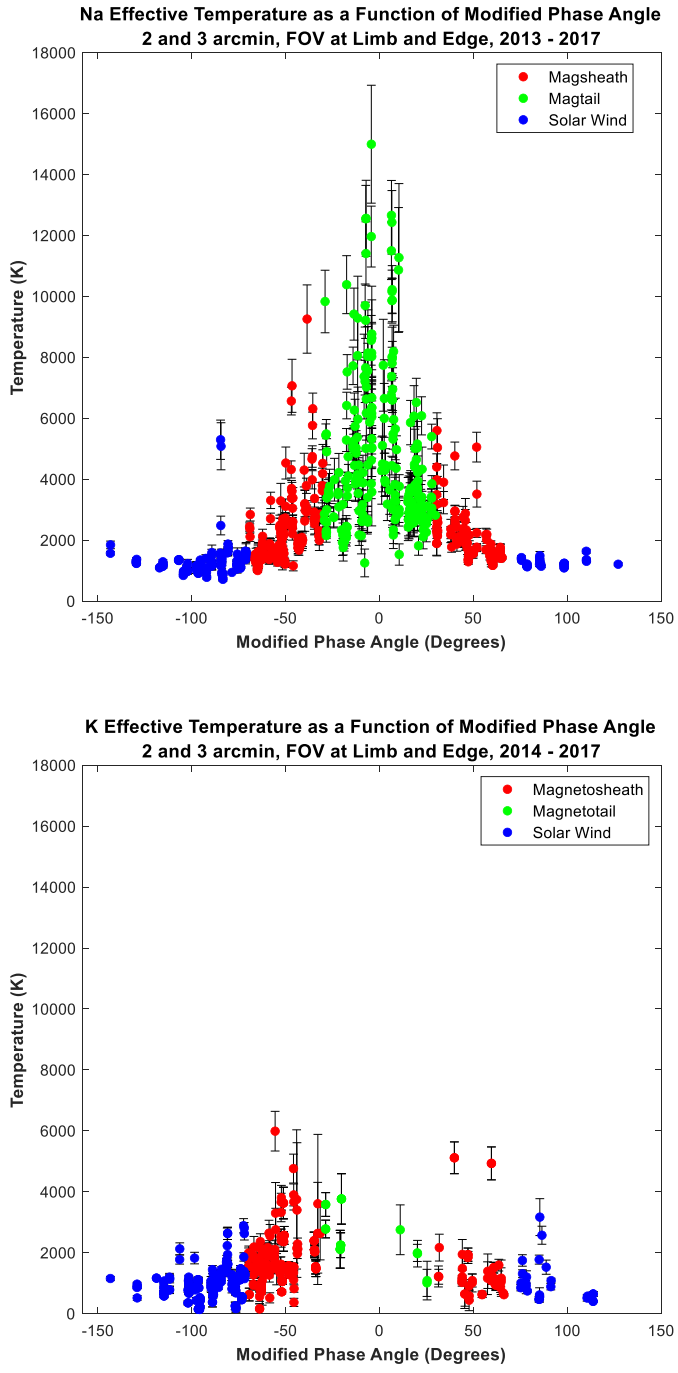

Figure 6.5: Sodium and Potassium effective temperatures as a function of modified phase angle, color-coded by the plasma region the observations belong to. Data contains all latitudes and limited to FOV at limb and edge. Most of our low temperatures reside in the pure solar wind regions. It is hard to observe potassium during magnetotail passage, but we have managed to make a few potassium observations during this time. This is possible only due to the background subtraction we perform for the potassium data analysis.

Sodium temperatures as a function of lunar latitude are shown in Figure 6.6; Table 6.2 lists the mean, median, and slope values for waxing and waning limbs for each region. In the solar wind, the median temperature is close to that of a PSD source (~ 1200 K) with the overall temperature being 'flat' or with low variance as a function of latitude. The most likely source process in this region is PSD with the outlier temperatures being more representative of impact vaporization. Sputtering due to solar wind ions is present but the temperature distribution seen in Figure 6.6a is not representative of a sputtering source (T > 5,000 K). This can be explained using the concept of 'source' atoms and 'ambient' atoms as described by Smyth and Marconi (1995). Source atoms are released from the regolith from a high energy process such as impact vaporization or charged particle sputtering because these processes have enough energy to release sodium atoms held together in the lunar regolith by chemical bonds (Gamborino et al., 2018). Note that PSD is capable of releasing atoms as long as the photon energy is greater than 4 eV (Yakshiniksy and Madey, 1999). Once released, these atoms are either lost from the exosphere or settle back down to the surface upon impacting the surface a couple of times, after which they are ready to be released by a lower energy process such as PSD or thermal desorption – these atoms then form the ambient particle population (Gamborino et al., 2018). This follows the results of Sarantos et al. (2010) in which they concluded that the prime role of solar wind ion sputtering is to enhance PSD efficiency. Thermal desorption is less efficient on the Moon than other SBE hosts like Mercury, leaving us with an ambient population of atoms released through PSD. In the undisturbed solar wind, it is safe to assume that solar wind ions travel to the lunar surface in the same direction as solar photons. Impact vaporization

is still present in this region and can be assumed to precipitate onto the surface from all directions – which is yet another process that can provide atoms for PSD to release.

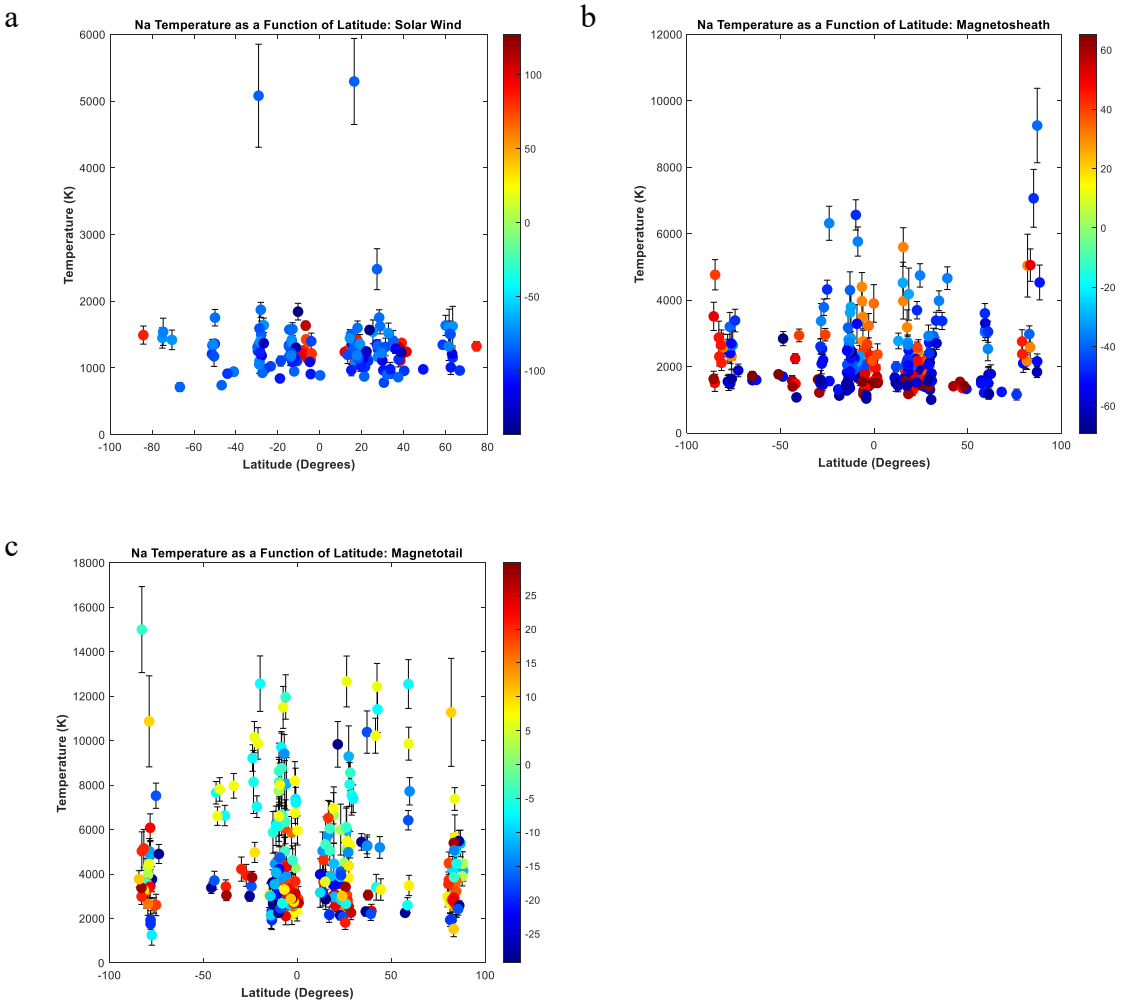

Figure 6.6: Effective temperature as a function of latitude with the color bar showing phase. Blueward colors are waxing while redward colors are waning. Temperatures in the undisturbed solar wind (a) lie between 1000 – 2000 K and are close to a PSD source. Magnetosheath (b) temperatures lie between 2000 – 4000 K and are representative of deviated, and heated solar wind ions that impact the lunar surface at a range of latitudes. Magnetotail temperatures (c) show a large variation, especially within 0° – 10° phase.

Table 6.2: *Table of mean and median sodium temperatures, and slopes for waxing and waning limbs in each plasma region.*

Region	Waxing/Waning	mean T (K)	median T (K)	Slope (K/ °): Equator - North	slope(K/°): Equator-South
Solar Wind	Waxing	1322	1233	1.65	0.532
	Waning	1234	1239	0.5	2.80
Magnetosheath	Waxing	2320	2002	2.29	3.45
	Waning	2149	1943	15.6	4.1
Magnetotail	Waxing	5035	4338	-7.79	-16.3
	Waning	4379	3550	-4.2	-1.5

A point to keep in mind, as put forth by Colaprete et al. (2016), is that we do not know if PSD is mainly responsible for re-releasing atoms released initially due to impacts or sputtering or if it acts as a primary source in releasing atoms from silicates and minerals. Therefore, in the undisturbed solar wind region, we can assume the temperature distribution is representative of (1) atoms that were previously released by MIV and charged particle sputtering by solar wind ions, that have fallen back to the surface and are now re-excited by PSD, and (2) atoms that are released from PSD on its own. Based on discussions in Chapter 5 we can assume MIV is more of a "global" distribution and does not have an SZA dependency. An important factor to consider is that due to the SZA dependence of PSD and sputtering by solar wind ions, the ambient exosphere is expected to be prominent around equatorial latitudes. This emphasizes the high energy processes such as impacts at latitudes away from the equator. For example, a few high temperatures

(> 2000 K) in Figure 6.6a have a temperature characteristic of impacts and since impacts can occur over a multitude of latitudes, this source process is the likely candidate for these outliers. Additionally, according to Pokorny et al. (2019), the velocity of impactors decreases with ecliptic latitude of meteoroids – meaning that the highest velocity impactors hit the lunar surface at near ecliptic latitudes. Note that while the Moon' orbital plane is tilted by ~ 5^{o} with the ecliptic, the Moon's equator is always at an angle of 1.5^{o} to the plane of the ecliptic. This means that the ecliptic latitude is almost interchangeable with the Selenographic latitude, with only small corrections due to the small (1.5^{o}) axial tilt of the Moon with respect to the ecliptic (Pokorny et al., 2019). Therefore, the outliers with temperatures on the higher end of the range for impacts (~ 5000 K) occurring at low-mid latitudes further strengthens the likelihood of these data points are candidates for atoms being released through high-velocity impactors.

In the magnetosheath, Figure 6.6b, the temperatures are about a factor of 2 higher than those in the solar wind. There are indications of asymmetry going from low latitudes to high latitudes on both waxing and waning limbs, with temperatures increasing going towards the poles. This trend was also seen by Killen et al. (2019) who found scale heights to increase going from low to high latitudes. Note that the temperature in this region is not that of a sputtering source (> 5, 000 K), rather what we might be seeing are atoms that have been released through sputtering or impacts (source atoms) that have fallen back to the surface to be rereleased by PSD (ambient atoms). Because solar wind ions can now travel towards all latitudes with greater ease in the magnetosheath, PSD can produce an ambient exosphere that is broader in distribution.

Additionally, in the magnetosheath region we are looking at points around the lunar limb that are farther away from the subsolar point than data taken close to quarter phases (undisturbed solar wind region). This means that we are starting to see some of the high ballistic range PSD atoms traveling from subsolar points towards the limb side. The median and mean temperatures are representative of an energetic PSD population while temperatures in the 3000 K – 5000 K range are representative of impacts. Furthermore, although the magnetosheath ions are comparable in energy to the solar wind ions, they do have a broader energy spectrum (Jasper Halekas, private communication) and can reach energies shown in Table 6.1. The density of precipitating ions also increases from the solar wind to the magnetosheath (Borovsky et al., 2018; Kallio et al. 2019). A combination of increased energy and flux along with a change in the path taken by solar wind protons going from the undisturbed solar wind to the magnetosheath might explain some high temperatures (> 5000 K), especially closer to the poles where PSD is less efficient. Recall that our effective temperature is a measure of the bulk movement of the gas in the line of sight of our FOV so very high temperatures could be representative of a column of gas that had a high proportion of atoms released from an energetic source process such as impacts or sputtering. In the magnetosheath, we are seeing a high energy tail population of PSD mixed with impacts and sputtering. Temperatures in the 3000 – 5000 K range can be attributed to impacts as they occur over a range of latitudes. Since the highest energy impactors hit near ecliptic latitudes and the temperature of the data points at the Northern pole are larger than what is expected of a meteor source, sputtering by shocked solar wind ions is a likely candidate for these outliers.

In the magnetotail (Figure 6.6c) the temperatures are highest with ~ factor of 2 from magnetosheath and ~ factor of 4 from solar wind temperatures, respectively. In the magnetotail region, the lunar surface should be shielded from solar wind ions – leaving us with only impacts and plasma sheet ions that can provide source atoms or ambient atoms for PSD to re-excite. While the mean and median temperatures in the magnetotail are more representative of the velocity distribution of impacts, some data points that are higher than 10,000 K can be attributed to the extremely high energy plasma sheet ions. In this region, we can expect a combination of a high-energy PSD population (population from the tail of the velocity distribution), impacts, and sputtering from plasma sheet ions – as concluded by Kuruppuaratchi et al. (2018). Note that data taken in the magnetotail are even farther away from the subsolar point than data taken during magnetosheath passage, meaning that we are now seeing only a fraction of the atoms released at the PSD source – those being the atoms released by PSD with the highest ballistic range and energy. The slopes are not easy to interpret in this region due to the high variability of data points. We know from previous discussions that the plasma sheet is highly dynamic and thus the plasma sheet ions can precipitate onto the lunar surface from all directions – like micrometeoroid impacts.

Figure 6.7 depicts an alternate way of presenting data as a function of latitude and modified phase angle, with log(temperature) as the color. Figure 6.7a shows the uniformity of the temperature in the undisturbed solar wind. Figure 6.7b points out the broader temperature range across all latitudes and even shows hints of asymmetry between data taken very close to 50 degrees during waxing and waning phases. Not only does the magnetosheath data have North-South asymmetry, but there are also waxing and waning asymmetry. This could be an effect of the varying proton parameters (flux, thermal

pressure, velocity) during the entry magnetosheath and the exit magnetosheath. For example, Kallio et al. (2019) investigated properties of impacting protons and found that during entry into the magnetosheath, the proton density increased and during exit from the magnetosheath into the solar wind (waning limb) the proton density decreased. This is an interesting phenomenon and requires an in-depth investigation of proton parameters (fluxes, thermal pressure, velocity) over multiple lunations.

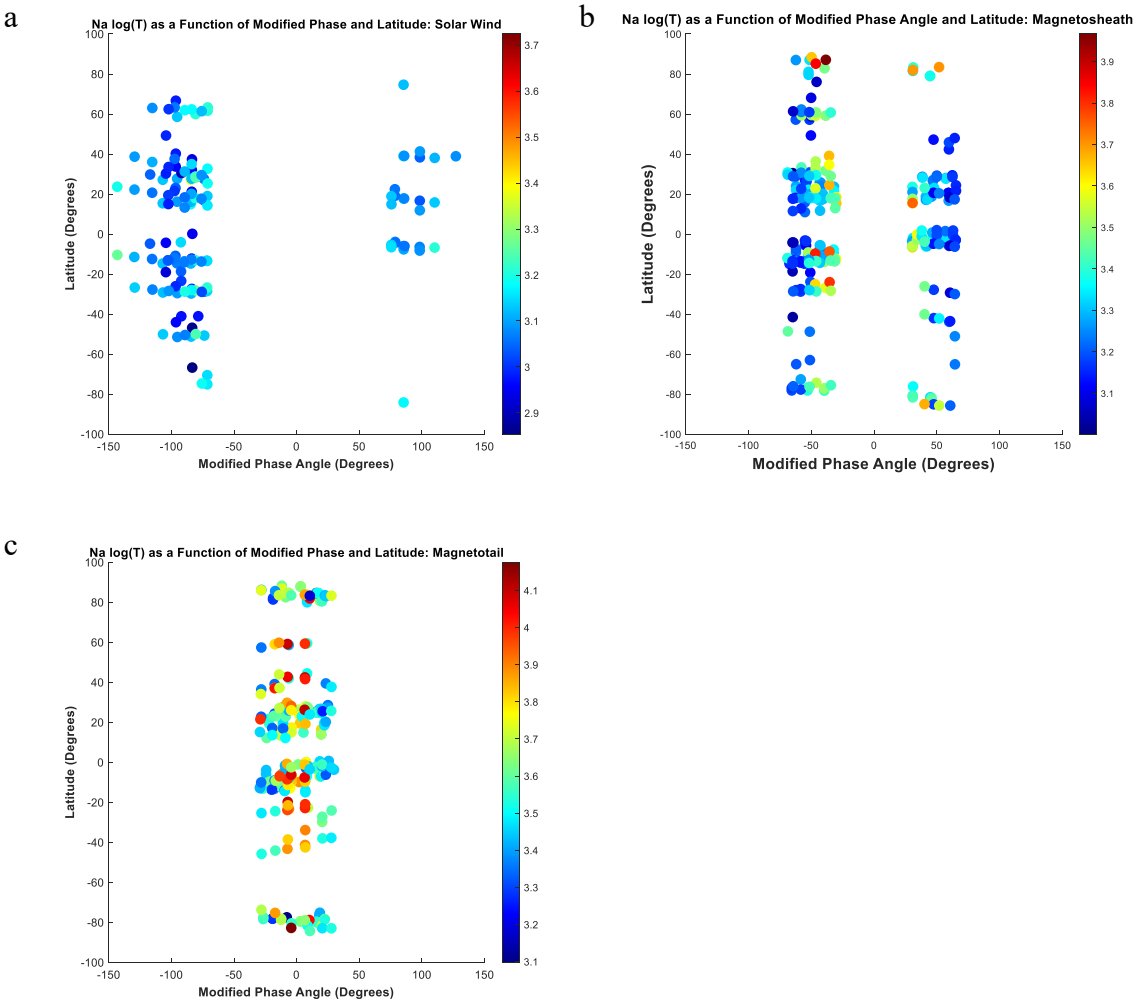

Figure 6.7: Sodium logarithmic temperatures as a function of modified phase and latitude. a) shows that the exosphere is cool and uniform in the undisturbed solar wind, while b) shows there are North-South asymmetry and dawn - dusk asymmetry during magnetosheath passage. c) temperatures closest to full Moon during magnetotail passage show an exosphere that is hot across all latitudes.

We also know from earlier on in Section 6.1 the importance of the position of the plasma sheet relative to the position of the Moon in its orbit. In Figure 6.8 the total number of hours the Moon spends inside the plasma sheet from 1960 to 2030 as modeled by Hapgood (2007) is shown.

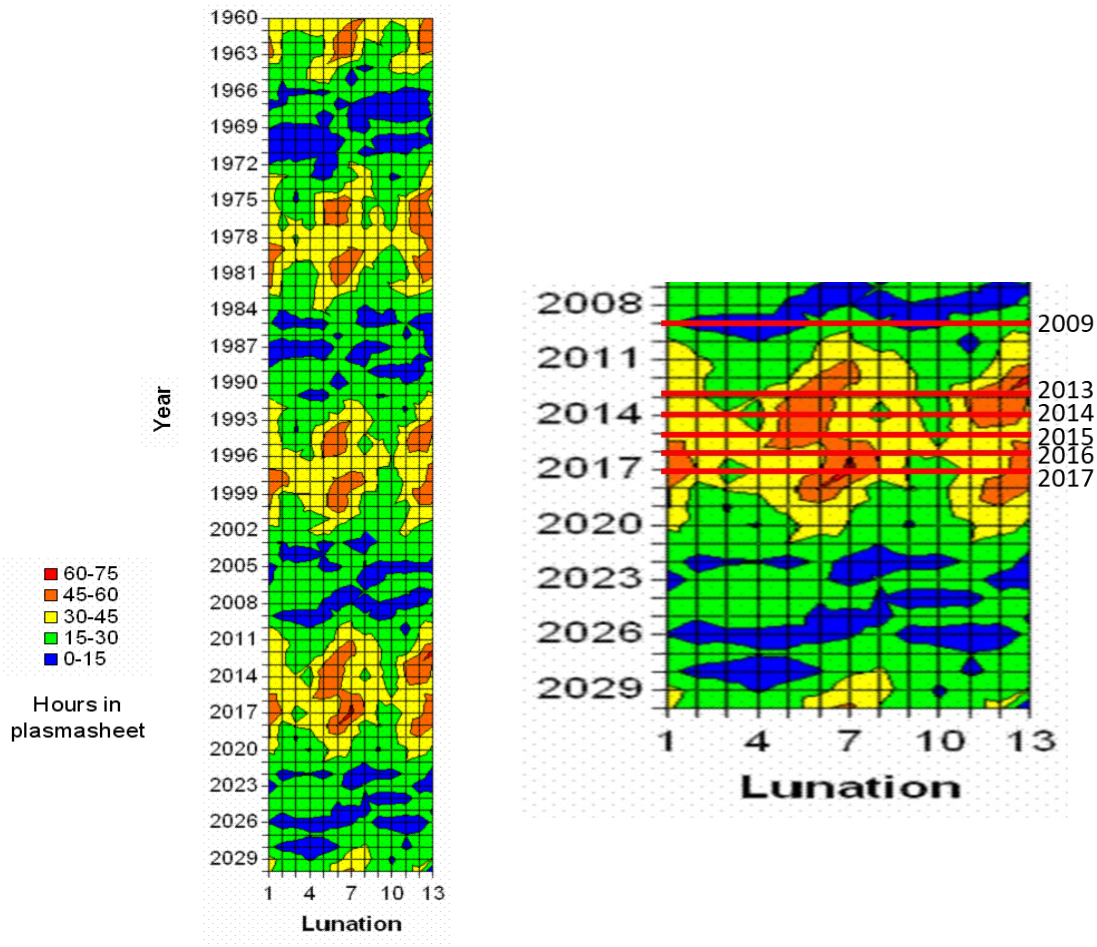

Figure 6.8: Seasonal variations in lunar exposure to the plasma sheet as shown in Figure 6 of Hapgood (2007). Blue and green regions correspond to the minimums of the 18.6-year lunar precession cycle with yellow and orange regions correspond to the maximums. The right image shows a zoomed in version to better delineate the years we have data. To look at a year, the reader must look at the boxes right below the line that denotes the year of interest.

The dataset presented by Kuruppuaratchi et al. (2018) and the new data presented here were taken during 2013 – 2017 coincides with the maximum of the 18.6-year lunar precession cycle. Recall that the Moon spends the most time encountering the plasma sheet during the maximum of this cycle – this is shown as orange, yellow, and red colors. Figure 6.9 shows the magnetotail data in Figure 6.6c but color-coded by the amount of time spent inside the plasma sheet. The categories for the time ranges spent inside the plasma sheet

are as follows: category 1 (0 – 15 hours), category 2 (15 – 30 hours), category 3 (30 – 45 hours), category 4 (45 – 60 hours), category 5 (60 – 75 hours). Note that some of the cells in Figure 6.8 have 2 colors inside and it is not easy to determine the exact time range in such cases. In Figure 6.9 the 'ambiguous' data points have been assigned one category based on the decision that if a cell from Figure 6.8 had two colors, the color that was more than 50 % of that cell would be the default category. As seen in Figure 6.9 (top), the sodium exospheric temperatures for categories 3 and 4 are not statistically different. This might be expected as all these data were taken during the maximum of the lunar precession cycle. For comparison, a subset of sodium data taken in March of 2009 as presented in Mierkiewicz et al. (2014) is shown superimposed on top of data from other years in Figure 6.9 (bottom).

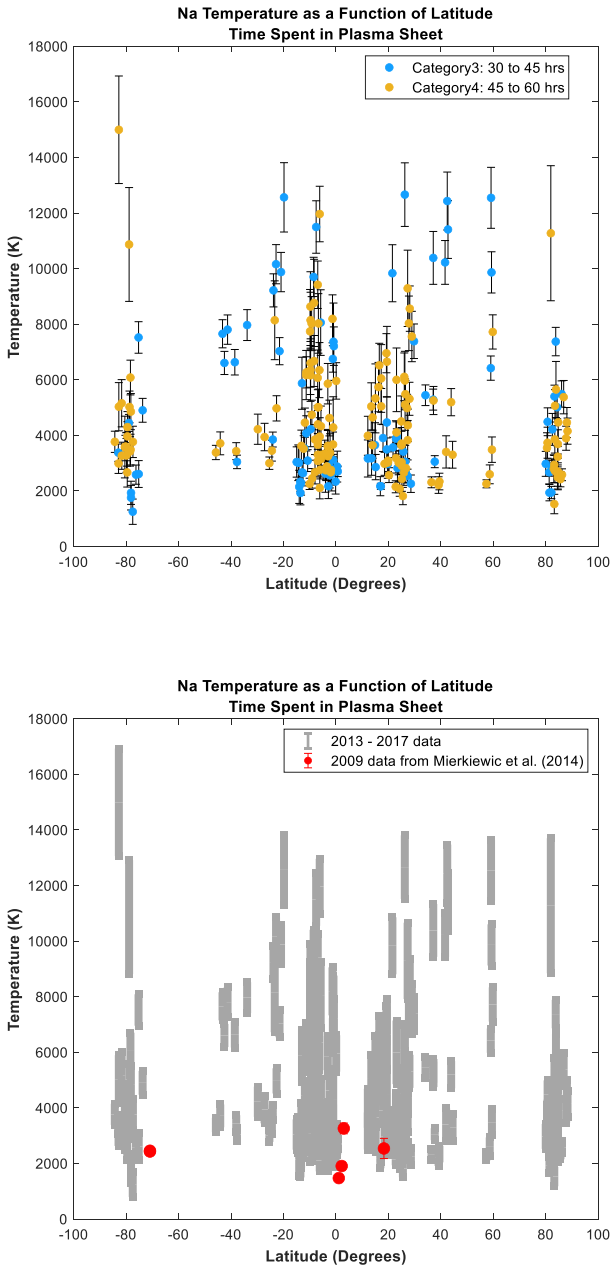

Figure 6.9: (top) Sodium temperatures color-coded by the amount of time spent in the plasma sheet. 2013 – 2017 data were taken during the maximum of the lunar precession cycle. No statistically significant difference is seen between the two different times spent inside the plasma sheet. (bottom) Sodium temperatures contrasted with a subset of the data of Mierkiewicz et al. (2014) taken during the minimum of the lunar precession cycle (March 2009). The temperatures for observations made during lunar minimum is consistently cooler than the temperatures for observations made during lunar maximum.

The 2009 data shown in Figure 6.9 were selected to match the FOV at the limb and edge of field lens offsets. Note that from Figure 6.8, March 2009 data were collected during the lunar precession cycle minimum and corresponds to the smallest amount of time spent inside the plasma sheet. While the data taken during the maximum of the lunar precession cycle show no difference between category 3 and 4, data taken during the minimum belonging to category 1 are consistently cooler by about a factor of 2. For comparison, the mean temperature for category 3 and 4 data is 4974 K and 4533 K while the mean temperature for category 1 data is 2345 K. This might indicate that perhaps it is not sufficient to simply spend time in the plasma sheet, but that the amount of time spent is crucial. Since the plasma sheet can sweep across the Moon multiple times during one lunation, during the maximum of the lunar precession cycle the likelihood of the plasma sheet sweeps over the lunar surface increases, thereby maximizing the impact probability between surface and plasma sheet ions despite the low density. It is likely that temperatures above ~ 5000 K are representative of the energy distribution of the high energy plasma sheet ions. Since we can ignore the effects of solar wind ion sputtering inside the magnetotail, the source atoms now come from MIV and plasma sheet ions. This might explain the difference in slopes going from equatorial latitudes towards high latitudes compared to magnetosheath data. Due to the low flux of plasma sheet ions, their contribution to the overall signature of the exosphere during magnetotail passage would be small compared to the larger contributions by the high-energy PSD population and MIV. Additionally, between MIV and PSD, at phases close to full Moon, it is likely that MIV is more dominant since it is omnipresent while only a fraction of atoms from the PSD source make up the high-energy tail distribution that make it to the terminator/limb sides.

6.2.1. Determination of Time Spent in Plasma Sheet: A Closer Look

The previous results indicate that while there is not an apparent effect between data taken during lunar cycle maximum, there is a difference in sodium effective temperatures between data taken during lunar cycle minimum and maximum. In this Section, I describe a method used to zone in on the specific plasma regions the Moon encounters during a lunation – thereby allowing us to determine the time spent in the plasma sheet with greater cadence than the 15 hour time periods shown in Hapgood et al. (2007).

Previously I mentioned that some cells in Figure 6.8 contained two categories (two colors) and if a cell had more than half of one category, it would default to that one. For this study, I make use of the two-probe Acceleration, Reconnection, Turbulence and Electrodynamics of the Moon's Interaction with the Sun (ARTEMIS) mission daily summary plots to determine when the Moon is in the solar wind, magnetosheath, tail lobes, and plasma sheet regions. The ARTEMIS mission, which was repurposed from The Time History of Events and Macroscale Interactions during Substorms (THEMIS) missions, is designed to understand the lunar plasma environments and comprises two twin probes, P1 and P2. For this study, I analyze measurements taken from instruments aboard the P1 probe as it lies directly on the Sun-Earth line (see Figure 2 in Sibeck et al.2011). The Electrostatic Analyzer (ESA) (measures ions from 0.006 - 20keV/q) and Solid State Telescopes (SST) (measures ions from 35keV – 6MeV) instruments on the ARTEMIS probes measure the energy and direction of pickup ion particle distributions, while the Electric Field Instruments (EFI) and Fluxgate Magnetometers (FGM) instruments measure the ambient electric and magnetic fields (Sibeck et al. 2011; Wang et al., 2012). Figure 6.10 shows the

key for the daily summary plots with data from the various instruments onboard the ARTEMIS probes. I focus on analyzing the magnetic field strength and orientation along with ion and electron energy spectra to determine when the Moon is in the Solar wind, magnetosheath, tail lobes, and plasma sheet regions, as these instruments are the most useful in determining these regions.

In the solar wind, ions are supersonic and have a very narrow energy distribution with relatively weak, highly variable magnetic field directions. In the magnetosheath, the ion energy distribution becomes broader but does not yet reach extremely high energies. Ion fluxes and magnetic field strength become larger in the magnetosheath since the bulk flow of ions gets compressed across the bow shock (Jasper Halekas, personal communication). In the lobe regions, the ion flux is significantly low, and the magnetic field is dominant in the positive or negative x-direction. In the plasma sheet, the ions reach very high energies with significant fluxes extending up into the SST instrument energy range (Jasper Halekas, personal communication). Additionally, during the ingress of the Moon from the solar wind into the magnetosheath the ion density, thermal pressure, and the total magnetic field are increased while the proton bulk velocity is decreased (Kallio et al., (2019)). According to Kallio et al. (2019), the Moon passes through the smallest plasma densities, bulk velocities, and magnetic fields along with the highest temperatures and thermal pressure of ions, along the Moon's orbit near the center of the tail. Using the information from Kallio et al. (2019) and advice from Jasper Halekas from the ARTEMIS team, I have only included a few ARTEMIS daily summary plots out of the full analysis to show the reader how I have separated the various regions. These example plots are shown

in Figure 6.11 where I have only utilized the 3 panels of importance highlighted in Figure 6.10.

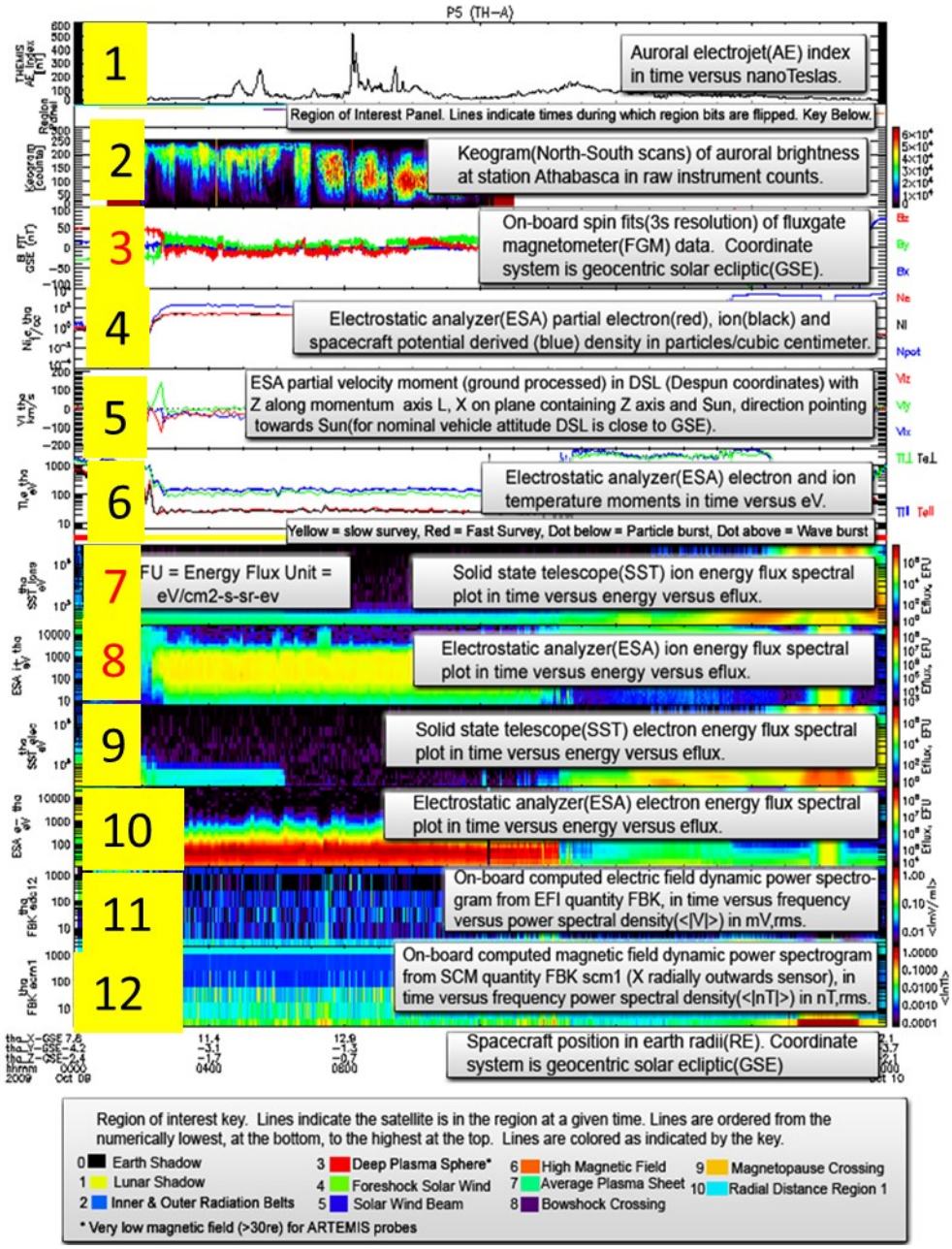

Figure 6.10: ARTEMIS daily summary plot key as taken from (Artemis mission website). The key features to use, numbered in red, are the ESA ion energy flux, SST ion energy flux, and the magnetic field data.

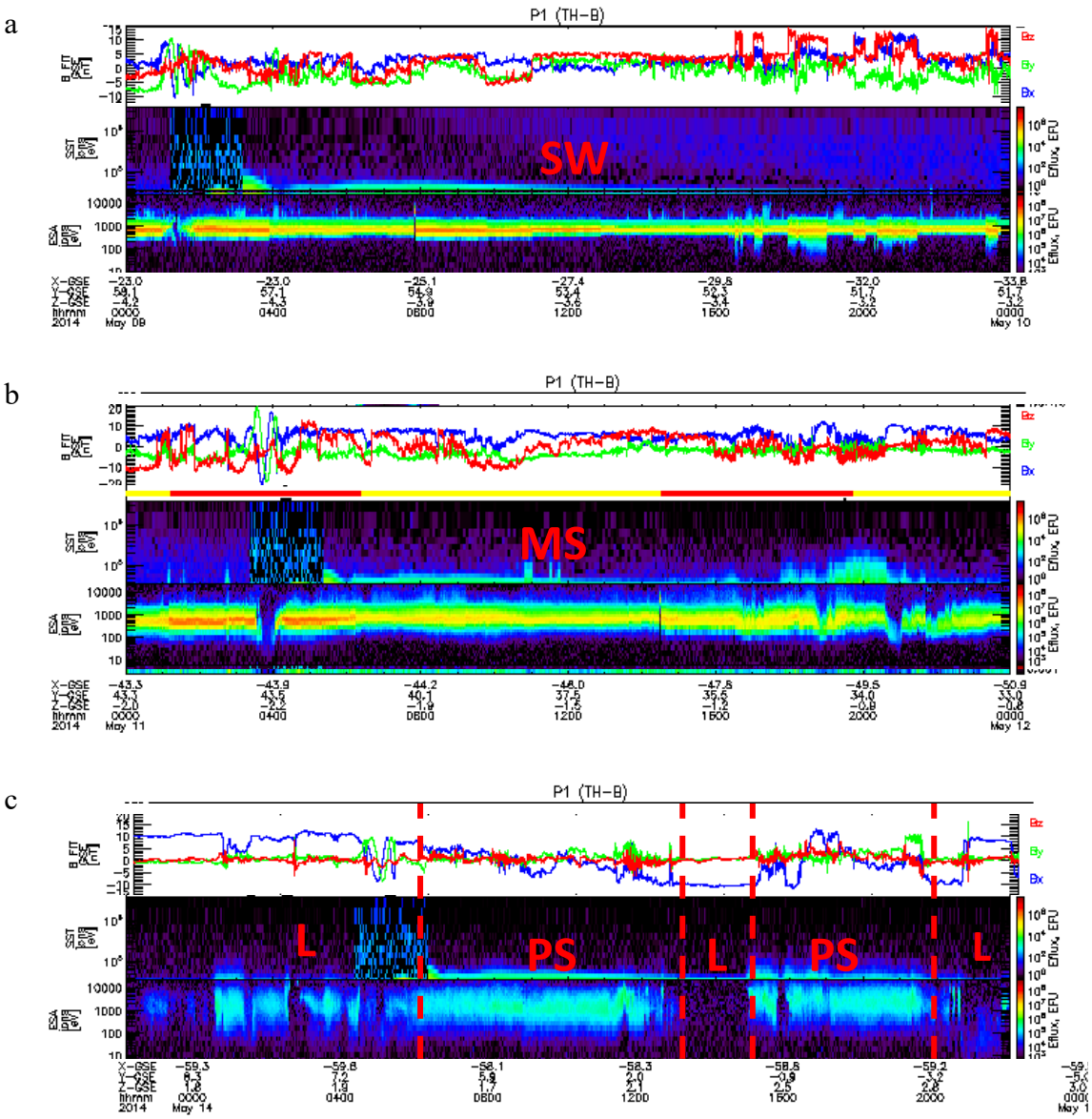

Figure 6.11: Sample ARTEMIS daily summary plots in May 2014 are shown with a) the Moon interacting with the undisturbed solar wind (SW), b) the Moon interacting with the Magnetosheath (MS), and c) the Moon passing the through the Lobes (L) and Plasma Sheet (PS). Notice how in the solar wind the ESA ion energy (panel 8) is concentrated around 1keV while the magnetic field (panel 3) is highly variable in each direction. In the Magnetosheath (b), the ion energies are now broader than the solar wind but still in the keV range while the magnetic field strength (panel 3) is larger than in the solar wind. In the magnetotail (c), the lobe region is almost empty (looks like gaps in the data in panels 7 -8) although the available ions can extend up into the SST range and the magnetic field is predominantly in the x-directions. In the plasma sheet, fluxes of ions extend well into the SST range.

In the case study presented in Figure 6.11, we can see that the Moon encounters the plasma sheet multiple times during one lunation. For this lunation, the total time the Moon has spent inside the plasma sheet is about 48 hours (orange). This is useful for instances where there are ambiguous regions in Figure 6.8 or if we simply want a more accurate answer. Additionally, a study like this is important if we want to find a correlation between our observations and the various plasma regions when the Moon is inside the magnetotail. I have performed an additional analysis for February 2014 where the total amount of time spent inside the plasma sheet was 33 hours (yellow). Interestingly, the median temperature during magnetotail passage for May 2014 is 6065 ± 680 K while the median temperature during magnetotail passage for February 2014 is 2668 ± 596 K. The factor of two difference in temperature between data taken at 33 hours in plasma sheet and 48 hours in plasma sheet indicates that to see a real effect of time spent in the plasma sheet, a finer study like I've shown here needs to be performed. Nevertheless, from the results here it can be seen that the time spent in the plasma sheet does have an effect on our temperatures but only if the data is analyzed on a smaller scale grid. Additionally, note that from results in Chapter 4, 5, and here, within the magnetotail there is a lot of variation in our data with magnetotail passage temperatures having both very high data points and low data points. This could be due to the Moon passing through the lobes (low data points) and the plasma sheet (high data points) and needs further investigation.

6.3. Sodium relative intensity as a function of latitude in various plasma regions

Sodium relative intensities as a function of latitude with the color denoting phase for the various plasma regions are shown in Figure 6.12. complementing the phase and

latitude information with log (relative intensity) as the color shown in Figure 6.13. As presented earlier for relative intensity data, data taken at 2 arcmin FOV are shown separately from data taken at 3 arcmin FOV. For solar wind region data shown in Figure 6.12a and b, relative intensities are highest at equatorial latitudes with a steep fall-off towards high latitudes. For data taken during solar wind passage, Figure 6.12 a and d, a source process that has an SZA dependence (e.g. PSD), and solar wind sputtering can be expected to produce this sort of pattern since they are all centered at the subsolar point. For reasons mentioned earlier, we can ignore thermal desorption. For atoms released by PSD, we can expect a 'double' release of sodium at the subsolar point – one from PSD acting as the source, and another from PSD re-exciting material released from charged particle sputtering by solar wind ions.

The waxing phase data in Table 6.3 indicates that the slope from the equator to Southern high latitudes is larger compared to the slope from the equator to Northern high latitudes – indicating that there is a bias in relative intensity towards the Southern hemisphere. The preference for low to mid-Southern latitudes as seen in Figure 6.13a. We do not have enough waning phase 2 arcmin data during the solar wind region to calculate the slope. The 3 arcmin data shown in Figure 6.13d and Table 6.4 indicate that intensities peak slightly to the North during waxing phases and slightly to the South during waning phases.

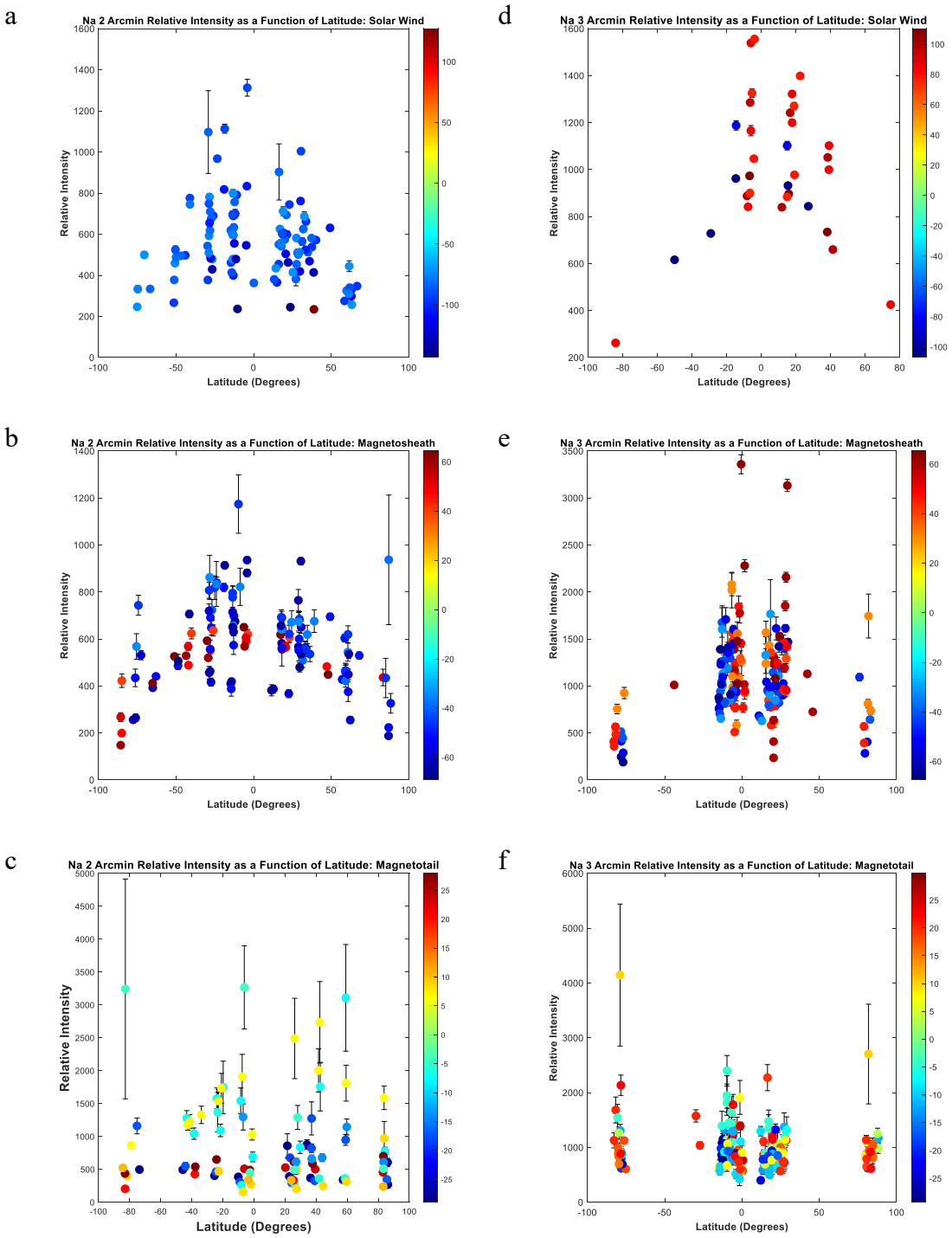

Figure 6.12: Two (left) and three (right) arcmin sodium relative intensity data as a function of latitude. Blueward colors are waxing and redward colors are waning phases. In the solar wind (a,d) relative intensities are highest at equatorial latitudes with a steep fall-off towards high latitudes. In the magnetosheath region (b,e) the intensities fall off towards high latitudes slower than in the solar wind. In the magnetotail (c,f) intensities are highly variable very close to full Moon.

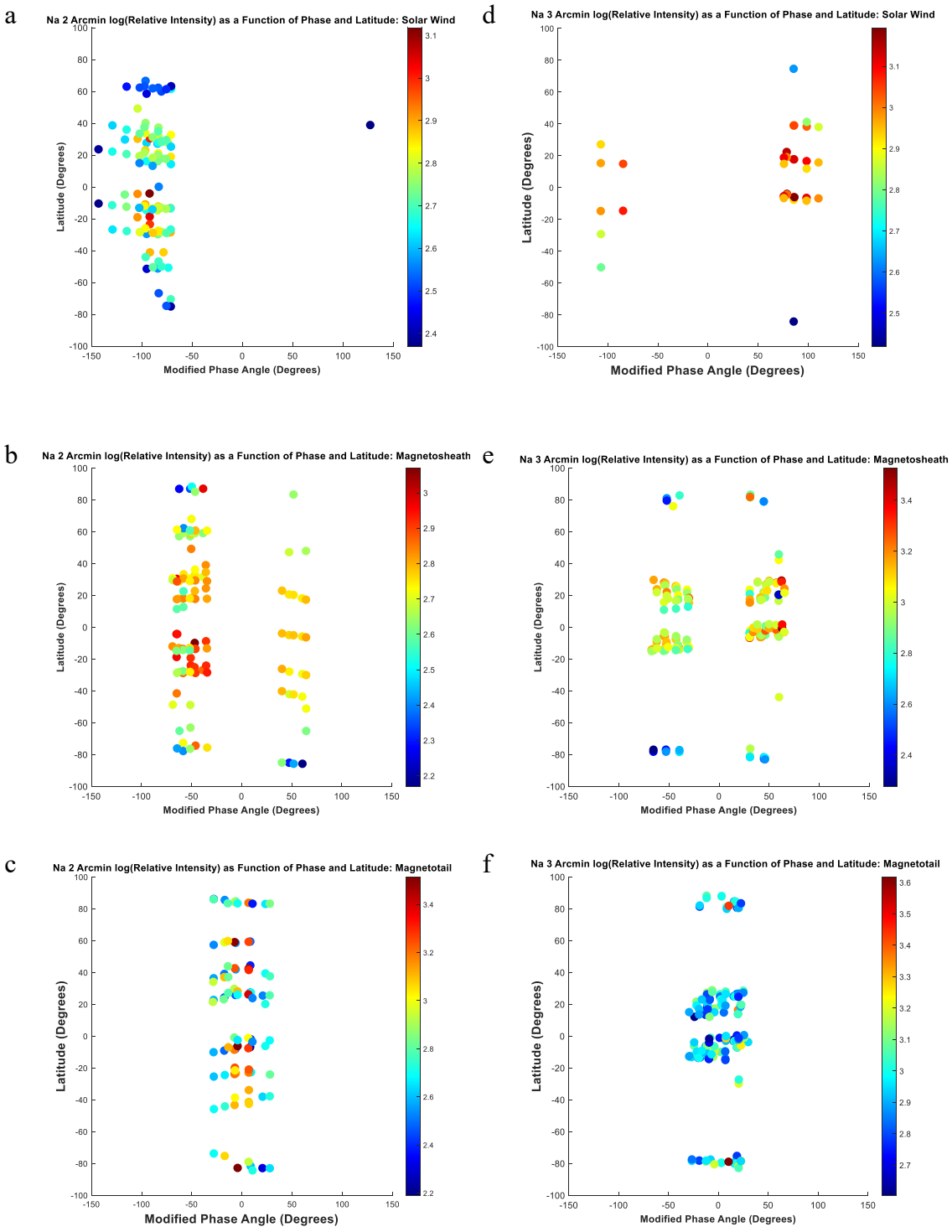

Figure 6.13: Sodium two (left) and three (right) arcmin log (relative intensity) data as a function of modified phase and latitude. Sodium intensities sometimes peak at low-mid North and Southern latitudes. In the 2 arcmin magnetosheath data, there is dawn-dusk asymmetry. Our 2 arcmin magnetotail data (c) shows that the exosphere is globally bright right at full Moon. This effect is not apparent in our 3 arcmin data (f).

Table 6.3: *Table of mean and median sodium relative intensities, and slopes for waxing and waning limbs in each plasma region for 2 arcmin sodium data.*

Region	Waxing/Waning	Mean Relative Intensity	Median Relative Intensity	Slope (Intensity/^{o}): Equator - North	Slope (Intensity/^{o}): Equator-South
Solar Wind	Waxing	555	531	-4.21	-5.125
	Waning	234	234	N/A	N/A
Magnetosheath	Waxing	591	574	-3.41	-3.54
	Waning	511	556	-2.46	-3.91
Magnetotail	Waxing	895	658	-3.64	-3.83
	Waning	834	523	1.35	1.89

Table 6.4: *Table of mean and median sodium relative intensities, and slopes for waxing and waning limbs in each plasma region for 3 arcmin sodium data.*

Region	Waxing/Waning	Mean Relative Intensity	Median Relative Intensity	Slope: Equator - North	Slope: Equator-South
Solar Wind	Waxing	910	932	-18.6	-15.83
	Waning	1030	1023	-9.51	-12.1
Magnetosheath	Waxing	1016	997	-8.07	-12.1
	Waning	1142	1028	-5.12	-9.24
Magnetotail	Waxing	1016	917	1.30	0.811
	Waning	1031	917	-1.32	1.95

For magnetosheath passage data, relative intensities do not fall off as fast from equatorial latitudes to high latitudes as data taken in the solar wind, as seen from Figure 6.12a and d and Figure 6.13a and d. The slopes in Table 6.3 and Table 6.4 show that going from the solar wind to the magnetosheath, the magnitude of the slope from equatorial to high latitude is smaller on both waxing and waning limbs. This is probably due to the direction of solar wind ion impact changing from directly head on to a more 'curved' path as described earlier. Magnetosheath ions along with impacts prime the lunar surface resulting in an intensity pattern that is more spread out in latitude. As was the case for the temperature equivalent of these relative intensity results, intensities that are outliers can be attributed to impacts and sputtering. In their study, Pokorny et al. (2019) conclude that impacts, not sputtering, is likely the key player in releasing original sodium atoms from minerals and rocks. The distribution of intensities during the magnetosheath interaction is likely a mix of impacts releasing original sodium atoms from the surface and sputtering re-releasing those original atoms. From the 2 arcmin data in Figure 6.12b and Table 6.3 we can see that the intensities are biased slightly towards low to mid Southern latitudes with the waning side showing a larger bias. For 3 arcmin data in Figure 6.13e and Table 6.4, intensities show a slight bias towards low to mid-Southern latitudes as well. From Figure 6.13b and e, the waxing phase 2 arcmin intensities are brighter than the waning phase intensities, especially around phase angle ~ 50. Interestingly, the 3 arcmin relative intensity data does not show this asymmetry. As mentioned for the temperature data, this asymmetry can be attributed to the conditions in the magnetosheath itself, where ingress into the magnetosheath can have increased proton flux compared to the egress. Most of our 3

arcmin data were taken in 2013 and 2014, while our 2 arcmin data were taken from 2015 onward. If there is an effect due to magnetosheath ingress and egress, and if the proton fluxes during these two points change monthly, and yearly, this might explain the difference between our 2 and 3 arcmin data. However, this needs a thorough investigation before anything further can be said.

In the magnetotail, the 2 arcmin intensities are overall 'flat' if data taken within 0 – 10° are ignored and counted as outliers. Much of the variation comes from these data points. As seen from Figure 6.12 and Table 6.3 a slight bias towards low to mid-Southern latitudes is seen in the 2 arcmin data. For 3 arcmin data as shown in Figure 5.13f. intensities look overall 'flat' with some variation in data points taken close to full Moon. From Figure 6.13f and Table 6.3. we can see that the 3 arcmin data shows a slight bias towards low to mid-Northern latitudes on the waxing side with the waning side showing a slight bias towards low to mid-Southern latitudes. As for effective temperatures, relative intensities that show large variation can be attributed to impacts or sputtering by plasma sheet ions. However, due to the low flux of plasma sheet ions it is unlikely that the largest intensities are solely due to plasma sheet ion sputtering. What we may be seeing is a combination of impacts and sputtering with sputtering contributing to intensities having temperatures larger than ~ 5000 K. From Figure 6.13c and f, our 2 arcmin data show that the exosphere is brighter overall closest to full Moon (close to 0^{o}) while our 3 arcmin data does not show this effect. The 3 arcmin data shows some bright observations during full Moon, but it is not global like for the 2 arcmin data.

Relative intensity data as a function of time spent in the plasma sheet, using Figure 6.8 to categorize data, are shown in Figure 6.14 for 2 and 3 arcmin.

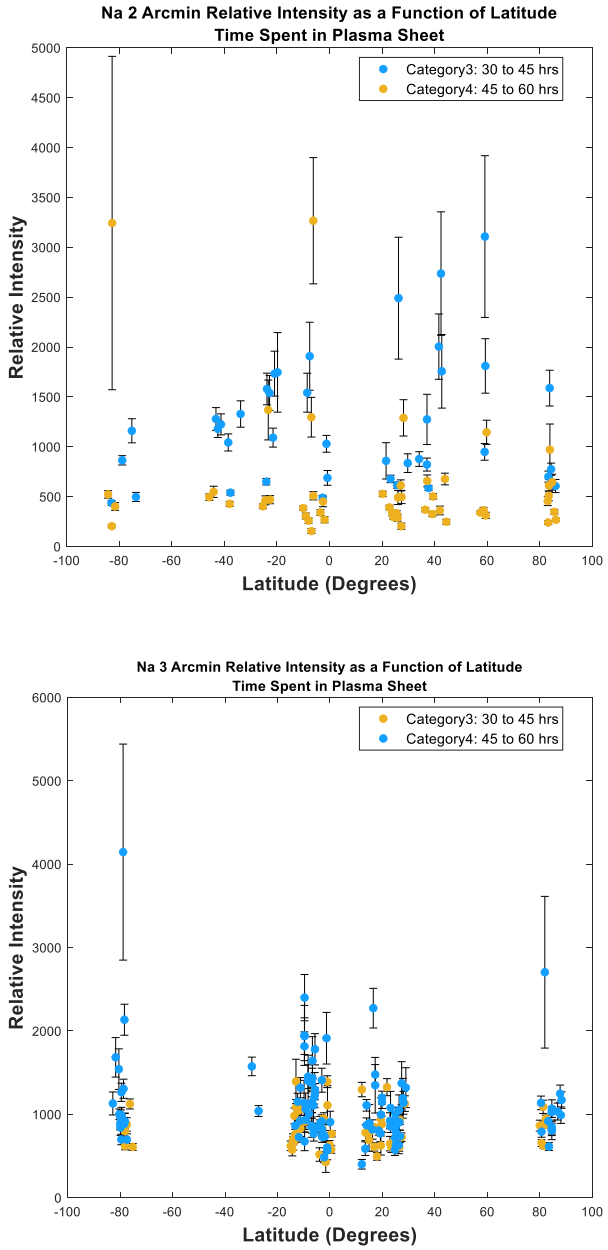

Figure 6.14: (top) Sodium 2 arcmin relative intensities color-coded by the amount of time spent in the plasma sheet. 2013 – 2017 data were taken during the maximum of the lunar precession cycle showing a negative correlation with time spent in the plasma sheet. (bottom) Sodium 3 arcmin relative taken during the same period show little overall variation between the two categories.

For the 2 arcmin data (Figure 6.14, top) the mean and median value for category 3 intensities is 1216 ± 170 and 1068 ± 94, while the mean and median value for category 4 intensities is 596 ± 97 and 427 ± 32. For the 3arcmin data (Figure 5.14, bottom) the mean and median value for category 3 intensities are 838 ± 81 and 794 ± 72, while the mean and median value for category 4 intensities are 1114 ± 142 and 993 ± 99. The different intensities related to category could be a result of the exact amount of time spent within the plasma sheet, spatial contributions, or a result of another process and needs to be investigated further. For now, the effect of plasma sheet ions on our relative intensity results can be studied by performing the same finer cadence study as in Section 6.2.1. For the same dataset used in Section 6.2.1, May 2014 (48 hours in plasma sheet) 3 arcmin data has a median relative intensity of 907 ±120 while the median relative intensity for February 2014 (33 hours spent in plasma sheet) is 778 ± 87. From this we can see that the time spent in the plasma sheet does affect the brightness of the exosphere, but to a smaller extent than the temperature. Recall that the temperature difference was a factor of two for these 2 months in our temperature data (Section 6.2.1) but the relative intensity only shows a slight difference. This adds further weight to the argument that despite plasma sheet ions being extremely high energy, their flux is too low to release a substantial amount of sodium into the exosphere. This points us in the direction of impacts for being most effective in releasing sodium atoms into the exosphere with some contribution from sputtering. While the effective temperature signature of plasma sheet ions can be detected over the sum of atoms on our FOV, not enough atoms are released by these high energy plasma sheet ions to increase the overall brightness of the gas in our FOV. In fact, for sputtering to be more effective than impacts and PSD in generating the lunar sodium exosphere, it might require

a high energy and high flux event such as a CME. Such an observation was observed by Killen et al. (2020) where the highest column abundances in the lunar sodium exosphere were measured during times of increased ion flux to the surface.

An interesting latitudinal dependence is that our relative intensities tend to peak from low to mid-latitudes on the Southern limb of the Moon for both waxing and waning data. The coronograph data of Killen et al. (2019) also showed intensities that are slightly skewed to the Southern hemisphere. An interesting observation is that Killen et al. (2019) reported the skewness of their intensities towards the South for waning side data while some of their waxing phase data peaked at low-mid Northern latitudes. Our data are skewed to the South on both waxing and waning sides and there is some indication of the exosphere peaking towards mid-Northern latitudes for waxing phase 3 arcmin data taken during solar wind passage. This may very well be an effect of sampling in both our observations and the coronograph observations, as Killen et al. (2019) only presented data for a handful of nights whereas the data here covers multiple years and lunations from which only nights with good latitudinal coverage were chosen. Nevertheless, there is enough evidence to claim that the sodium exosphere is skewed in intensity towards mid-Southern latitudes – hinting at a possible compositional effect. Surface composition measurements from the Chandraayan-1 X-ray Spectrometer (C1XS) showed sodium abundances of 2-3 percent by weight at mid-Southern latitudes (Athiray et al., 2014) – although such a small abundance on the surface is not likely to produce a strong enough signal for us to detect. Nevertheless, the peak in relative intensities at low-mid latitudes is an interesting observation and could provide a previously unavailable constraint on the surface abundance of sodium. Note that the surface abundance of sodium could also affect the intensity results for the time spent in

the plasma sheet. While the flux is still important, how the yield of sodium atoms is affected by surface abundance is not yet understood. It could be that there was only a slight increase in relative intensity from 33 hours in the plasma sheet to 48 hours because there was no surface enhancement of sodium in the areas probed during these two case studies.

6.3.1. Special Case: Total Lunar Eclipse of the Heart

Each of the 3 plasma regions provided insights into the role of source processes and surface composition. This brings us to a special case that falls under magnetotail passage, where PSD only plays a minor role. Our extensive dataset also contains data taken during the total lunar eclipse that occurred on April 15, 2014. Figure 6.15 below shows linewidths for data taken during various parts of the lunar eclipse. Note that the effects of PSD decrease going from the penumbral phase towards the total eclipse phase, providing us with a unique opportunity to observe the lunar exosphere as it responds solely to impacts and plasma sheet ion sputtering. This means that we should start seeing less to none of the high ballistic range PSD released sodium atoms. Linewidths between 04:00 to 05:00 UT are representative of the high ballistic PSD population and impacts. Linewidths in the penumbral region from 05:00 to 06:00 UT are higher than ~ 5000 K which is the upper range of temperatures characteristic of impacts meaning that the effects of plasma sheet ions on the lunar surface are now emphasized. During the partial eclipse period from 06:00 – 07:00 UT, the linewidths correspond to about 3000 K and since PSD should be minimal to none during this time, this population of atoms most likely represent purely impacts. The same goes for the partial eclipse period from 08:00 to 10:00 UT coming out of total eclipse. The one data point during the penumbral eclipse from around 10:00 – 11:00 UT is also

representative of an impact source. Note that during the eclipse, solar radiation pressure becomes more diminished as we near totality. Even with reduced or minimal solar radiation pressure, our linewidths imply hot temperatures characteristic of ranges we see during full Moon even for non-eclipse data. This case study could provide a way to further assess the effects of solar radiation pressure, or the lack thereof, on our linewidths.

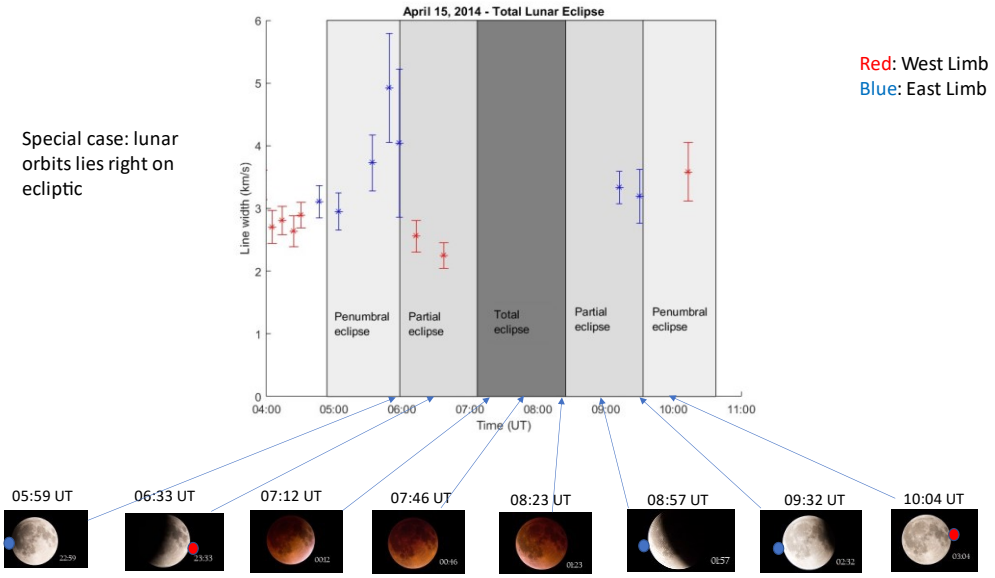

Figure 6.15: Linewidths as a function of time (UT) during a total lunar eclipse in April 2014. With the absence of PSD, the role of MIV and charged particle sputtering by plasma sheet ions are amplified.

Relative intensity data for the sodium emission in Figure 6.16 are brightest right before the start of the eclipse during 04:00 – 05:00 UT indicating that PSD has an important role to play in the brightness of the exosphere. In the penumbral period between 05:00 – 06:00 UT, and partial eclipse periods from 06:00 to 07:00 UT and 08:00 – 09:00 UT the intensities are overall low indicating that without sunlight we start to see a dimmed down exosphere. The one data point in the penumbral eclipse after 10:00 UT is brighter than the

penumbral and partial periods before total eclipse indicating the role plasma sheet ions have to play in priming the lunar surface. If during this time some PSD effects come into play, then the primed lunar surface should respond with a brighter exosphere. However, there is not enough data to make a definitive conclusion. Nevertheless, this total lunar eclipse data provides a unique way of investigating the response of the exosphere with minimal PSD effects.

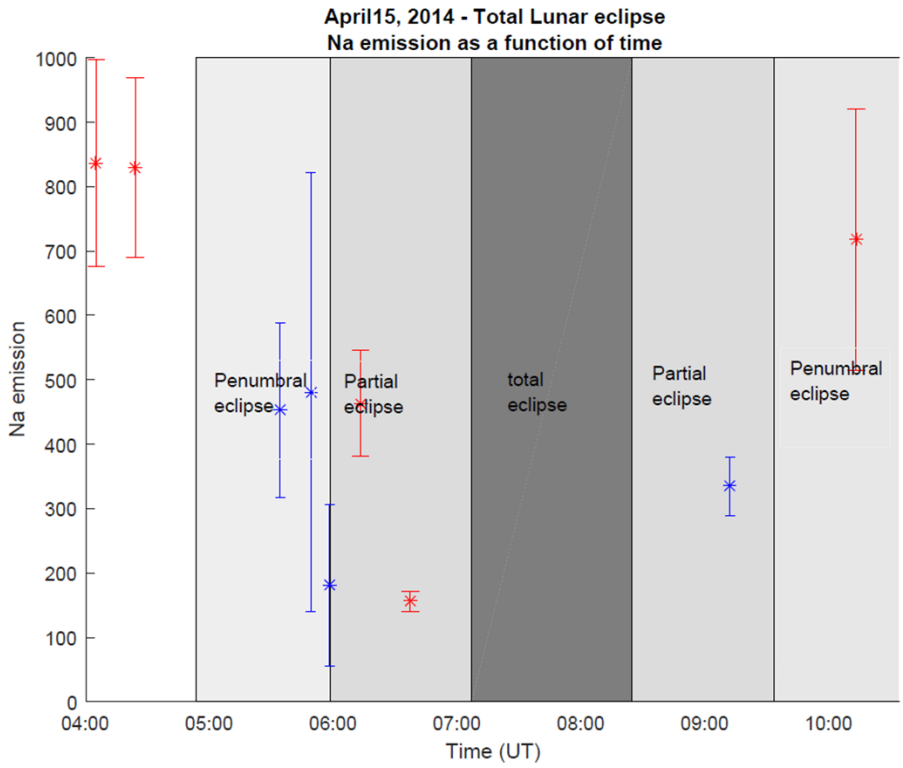

Figure 6.16: Relative intensity for linewidth data in Figure 5.15 as a function of time (UT) during a total lunar eclipse in April 2014. The highest intensities are observed during times PSD is fully present – indicating that PSD is very efficient in releasing sodium atoms into the exosphere.

6.4. Potassium effective temperature as a function of latitude in various plasma regions

A complementary study to Section 6.2 is presented here. Potassium effective temperature results are shown in Figure 6.17, Figure 6.18, and Table 6.4. In the solar wind, potassium temperatures are close to that of a PSD source overall, except for a few outliers with temperatures characteristic of impacts. Compared to sodium solar wind region temperatures, the potassium temperatures show more scatter at all latitudes with a bias towards waxing phases and are not overall 'flat' as we saw for the sodium equivalent. Waxing phase temperatures show large North - South asymmetry with temperatures increasing towards Northern high latitudes and temperatures decreasing towards Southern high latitudes. Waning phase temperatures show North - South asymmetry with temperatures decreasing towards high latitudes. Waxing phase temperatures are comparable to waning phase temperatures, in contrast to the factor of 2 difference in temperature reported by Rosborough et al. (2019). It appears that while sodium predominantly showed a 'flat' temperature distribution characteristic of PSD (source and ambient atoms) with some contribution from impacts, potassium follows a more spread out pattern.

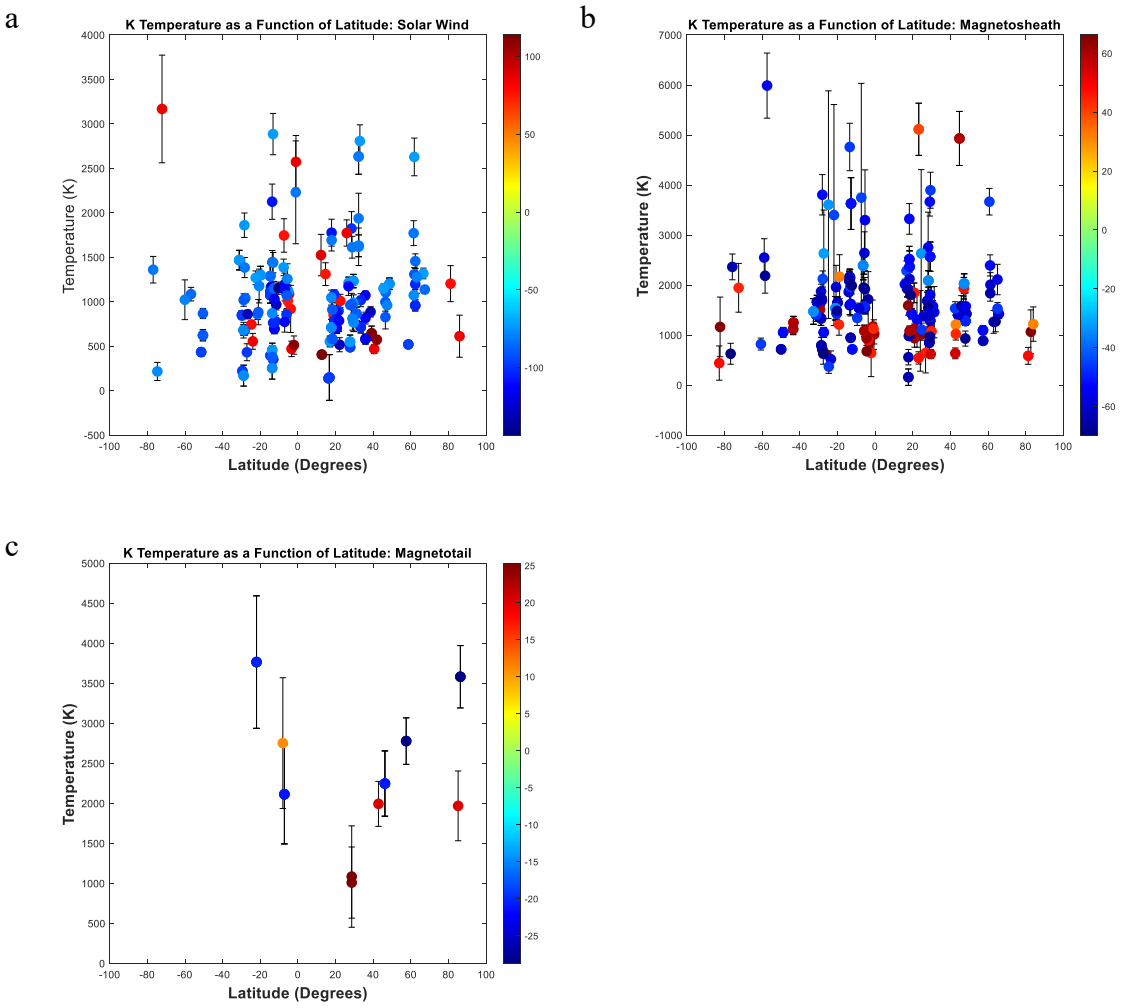

Figure 6.17: Potassium 2 and 3 arcmin, FOV at limb temperatures as a function of latitude. Temperatures in the solar wind (a) show North-South asymmetry for both waxing (blue colors) and waning (red colors) limbs and show a lot of variation compared to sodium temperatures in the solar wind. In the magnetosheath (b), the North-South asymmetry is not as pronounced as in the solar wind. As opposed to sodium, potassium temperatures in the solar wind do not increase towards high latitudes. In the magnetotail (c) temperatures increase towards high latitudes for both waxing and waning data.

Inside the magnetosheath, the asymmetry between North -South temperatures is not as pronounced as in the solar wind for both waning and waxing phases. Waxing phase temperatures are higher than waning phase temperatures, although still not the factor of 2 difference seen in our 2014 potassium data. An interesting observation is that potassium temperatures do not increase going from low latitudes to high latitudes like what was seen for sodium temperatures. Instead, temperatures (without the large outlier temperatures) decrease from equatorial to high latitudes on both waxing and waning limbs. The explanation for sodium was that shocked solar wind ions that are diverted around the Earth have better access to high lunar latitudes than in the solar wind. This opposing trend would suggest that solar wind ions may not be as important for the temperature distribution in the potassium exosphere. In the magnetotail, potassium waxing phase temperatures are about a factor of 2 higher than waning phase temperatures, as reported by Rosborough et al. (2019). Temperatures increase from equatorial towards high latitudes for both waxing and waning limbs.

The logarithmic temperature plots in Figure 6.18 highlight the dawn-dusk asymmetry in the potassium data, especially in the solar wind. In the magnetosheath, (Figure 6.18b potassium temperatures are on average higher around 50° during waxing phase compared to waning phase. This is the same result we had for sodium in Section 6.2 implying that the entry magnetosheath seemed to have more of an effect than the exit magnetosheath.

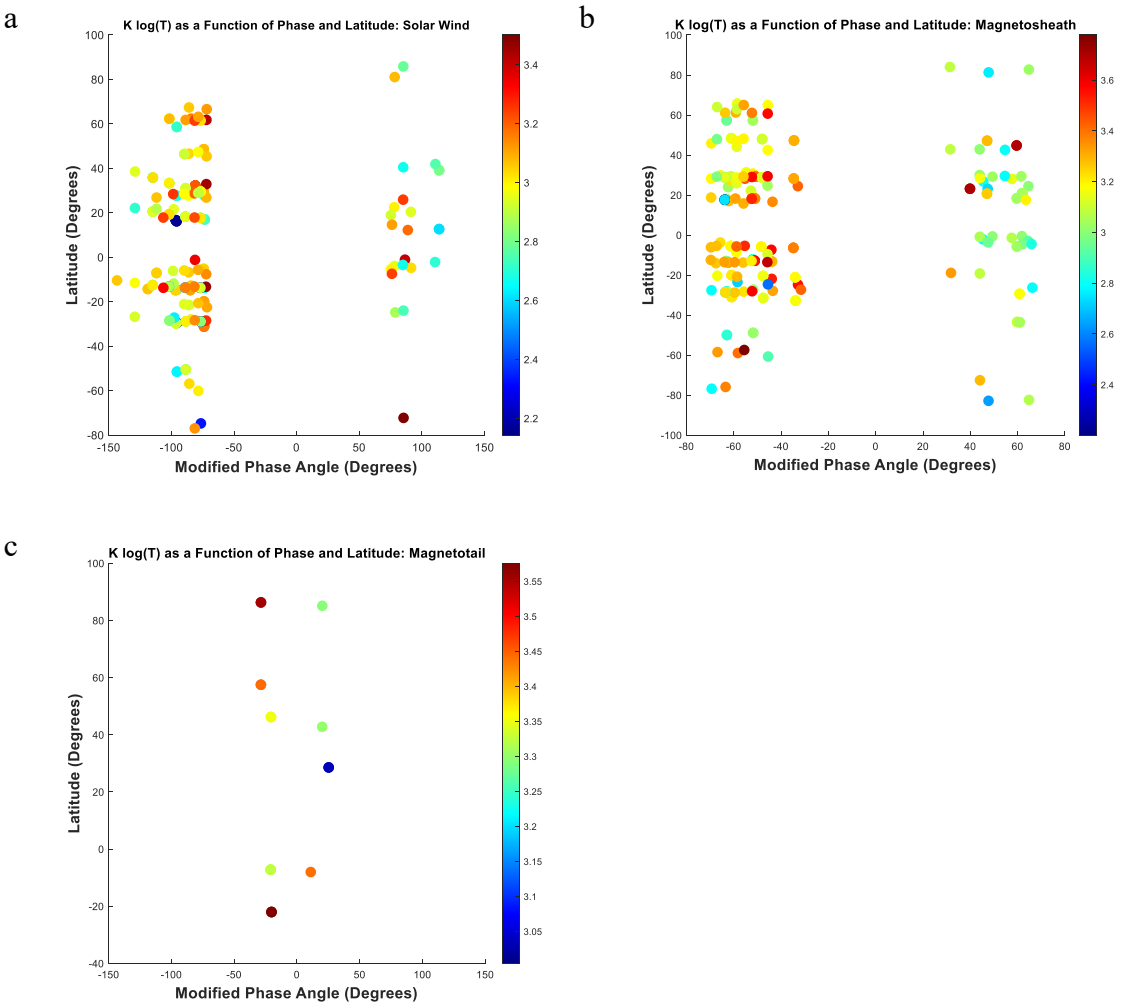

Figure 6.18: Potassium log(temperatures) as a function of modified phase angle. The color bar is the log (temperature). In all 3 regions, the potassium waxing phase temperatures are hotter compared to waning temperatures – showing a clear dawn-dusk asymmetry.

Table 6.5: *Table of mean and median sodium temperatures, and slopes for waxing and waning limbs in each plasma region.*

Region	Waxing/Waning	Mean T (K)	Median T (K)	Slope: Equator - North	Slope: Equator-South
Solar Wind	Waxing	993	965	11.1	-6.65
	Waning	1046	867	-2.24	-8.3
Magnetosheath	Waxing	1853	1570	-3.27	-7.23
	Waning	1451	1120	-4.6	-2.7
Magnetotail	Waxing	4456	3674	15	120
	Waning	1762	1969	15	N/A

6.5. Potassium relative intensity as a function of latitude in various plasma regions

A complementary potassium analysis for Section 6.3 is shown here. In the solar wind, potassium 2 and 3 arcmin relative intensities in Figure 6.19 a and b, follow a similar pattern to sodium with intensities falling off from equatorial latitudes towards high latitudes. Potassium 2 arcmin intensities show a slight bias towards Northern high latitudes (Table 6.6) which agrees with the result of Rosborough et al. (2019) that saw a slight bias towards data taken off the Northern limb (Plato) compared to data taken off the Southern limb (Tycho). The highest intensity for 2 arcmin data is found at waning phase latitude at around 20° North which is where we observe the limb off Aristarchus crater – a location found in the KREEP region. For the 3 arcmin data (Figure 6.19d and Figure 6.20d) waning phase intensities show a peak around the same latitude as Aristarchus as well. An

interesting observation is that 3 arcmin data show the largest intensities on the waxing side at similar latitudes however this is not on the KREEP region. Compared to sodium, potassium intensities show a more spread out form in the solar wind indicating that it is responding more to a process that does not have SZA dependence.

In the magnetosheath, the 2 arcmin data (Figure 6.19b) shows an opposite trend to the 3 arcmin data (Figure 6.20b). The 2 arcmin waning intensity data show a large North - South asymmetry while the 3 arcmin data show both limbs decreasing in intensity towards the poles. In contrast, sodium relative intensities in the magnetosheath showed a decrease going from equatorial to high latitude on both limbs for both 2 and 3 arcmin data. Potassium relative intensities for both 2 and 3 arcmin waning phase data show a peak at latitudes near Aristarchus (Figure 6.20b and e). The magnetosheath data also indicate that observations around 50° on the waxing side is overall brighter than observations around 50^{o} on the waning side. This is seen in sodium intensities as well, pointing to asymmetries in the magnetosheath itself.

In the magnetotail, potassium 2 arcmin data show North -South asymmetry on the waxing side, although there is not enough latitudinal coverage to make a definite conclusion. There is not enough 3 arcmin data in this plasma region for further comment. Waning phase relative intensities are larger than waxing phase, possibly due to KREEP enhancements.

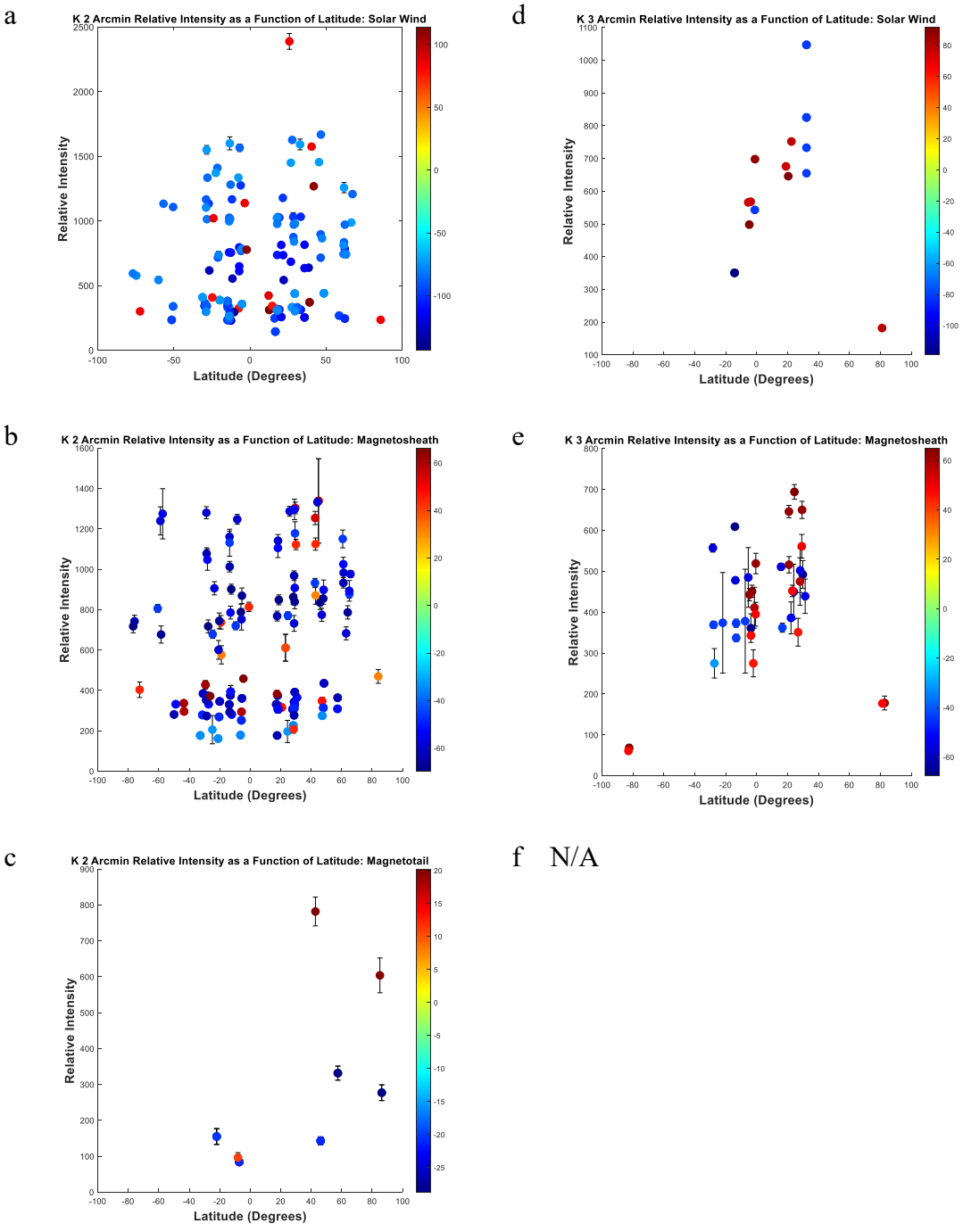

Figure 6.19: Potassium 2 (left) and 3 (right) arcmin relative intensity data as a function of latitude. The color bar denotes the modified phase angle (waxing phases are blueward while waning phases are redward). In the solar wind (a,d) relative intensities fall off from Equatorial latitudes towards high latitudes. In the magnetosheath, the 2 arcmin data (b) show North-South asymmetry, while the 3 arcmin data (e) show a decrease in intensity toward high latitudes for both waxing and waning limbs. In the magnetotail, there are signs of North-South asymmetry but there is not enough data.

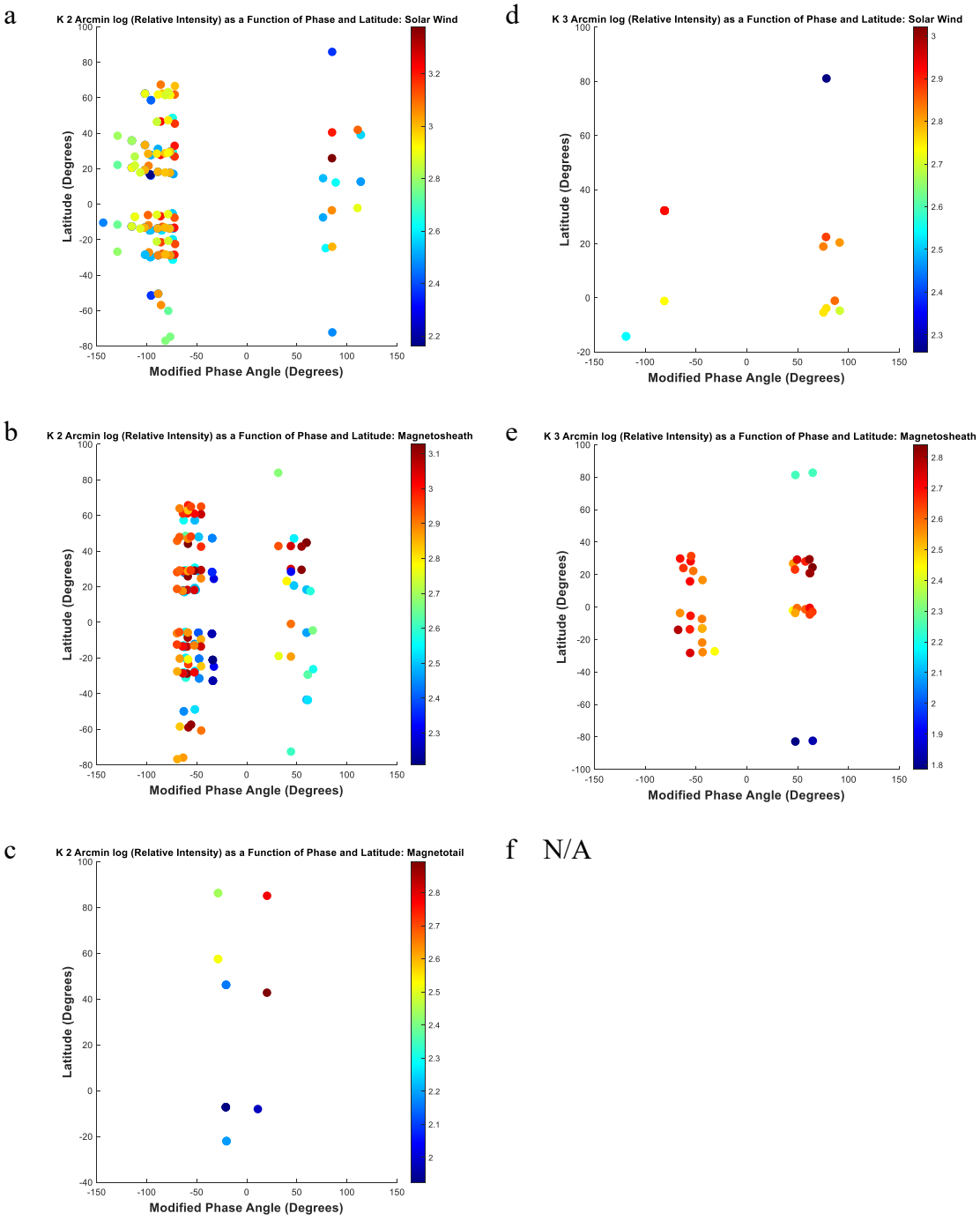

Figure 6.20: Potassium log (relative intensity) for 2(left) and 3 (right) arcmin data as a function of latitude and modified phase angle. The color bar denotes the log (relative intensity) values. The peaks in intensity on the waning limbs (positive phase angles) occur around the latitudes where the KREEP regions are found.

Table 6.6: *Table of mean and median relative intensities, and slopes for waxing and waning limbs in each plasma region for 2 arcmin potassium data.*

Region	Waxing/Waning	Mean Relative Intensity	Median Relative Intensity	slope: Equator - North	slope: Equator-South
Solar Wind	Waxing	626	410	5.9	-1.34
	Waning	724	390		
Magnetosheath	Waxing	541	361	4.23	3.66
	Waning	583	416	6.56	-3.12
Magnetotail	Waxing	277	246	-1.1	12.9
	Waning	494	604	-4	N/A

Table 6.7: *Table of mean and median relative intensities, and slopes for waxing and waning limbs in each plasma region for 3 arcmin potassium data.*

Region	Waxing/Waning	Mean Relative Intensity	Median Relative Intensity	Slope: Equator - North	Slope: Equator-South
Solar Wind	Waxing	709	733	14.3	-9.15
	Waning	573	607		20.4
Magnetosheath	Waxing	430	413	2.72	4.12
	Waning	404	443	-0.018	-5.17
Magnetotail	Waxing	N/A	N/A	N/A	N/A
	Waning	325	325	N/A	N/A

6.6. Phase binned exospheric temperatures

In this Section, I compare our sodium data to the coronograph study showing the latitudinal dependence of sodium scale heights and intensities as presented in Killen et al. (2019). The coronograph method takes measurements along a slit in 10° latitude cuts going out radially. Our method involves making offsets from a reference crater, and on certain nights we would have marched all along the limb of the Moon to obtain data from various latitudes. I have chosen a few nights that had the best latitudinal coverage from the dataset presented in this dissertation. Good latitudinal coverage must have included latitudes ranging from the equator to at least 50° North and South. Additionally, the coronograph data does not contain near full Moon data (from 5° – 9°), therefore, I have omitted any nights that fall within this range. Note that Killen et al. (2019) presents scale heights and calibrated intensities while our data is presented as an effective temperature and relative intensity. Nevertheless, the overall trends are of importance and can be discussed regarding the coronograph data. In order to match the coronograph data best, I present data separated by waxing and waning limb. For simplification and ease of comparison, I also have limited data to the closest in offset – FOV at the limb and as usual, the temperature is shown combined for 2 and 3 arcmin while relative intensity will be separated.

Our waxing and waning limb temperature data with the best latitudinal coverage are shown in Figure 6.21. On most nights, both the waxing and waning temperatures increase from low to high latitudes except for of May24, 2013 (phase 13°), May 22,2013 (phase 40°), and May 29, 2015 (phase 51°).

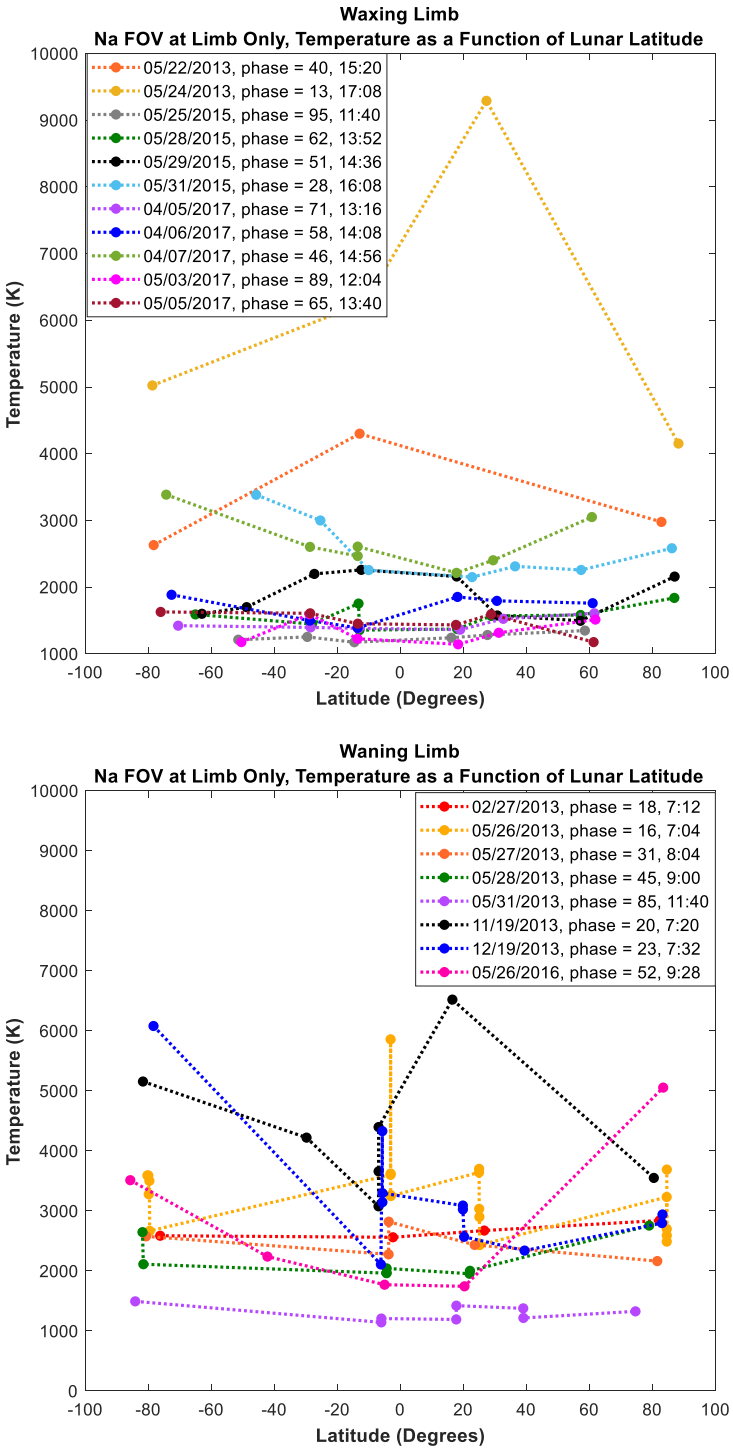

Figure 6.21: Waxing (top) and waning (bottom) limb temperatures for sodium data taken at the Limb only. Local time and phase are provided for each of the nights. On most nights, the temperature increases from low to high latitudes. Waning phase temperatures also show this trend but shows more North -South asymmetry, overall, compared to waxing phase data.

The increase in temperature with latitude agrees with the scale height results of Killen et al. (2019) shown in Figures 6.22, and Killen et al. (2020). While the data in Killen et al. (2019) is shown as a continuous line, due to the simultaneous latitudinal coverage of the coronograph method, our data is not continuous in time and therefore, the data points are only joined by a dotted line to show the general trend. Killen et al. (2019) reported that their waning phase scale heights decreased from dawn to noon with no monotonic change in their waxing phase scale heights, whereas our results show this decrease on both waxing and waning limbs. Figure 6.23 shows the median waxing (top) and waning (bottom) temperatures by date along with the approximate range of local times on the Moon added.

The results of Killen et al. (2020) showed that both waxing and waning scale heights are at least around noon (90^{o}) and increase towards the morning and evening terminators – a result that agrees with our temperature results. This uptick in temperature as a function of phase is also seen in Section 5.1. The reason for the discrepancy between the waxing phase scale height trend in Killen et al. (2019) and the waxing phase scale height trend in Killen et al. (2020) and the waxing temperature here could be a sampling issue.

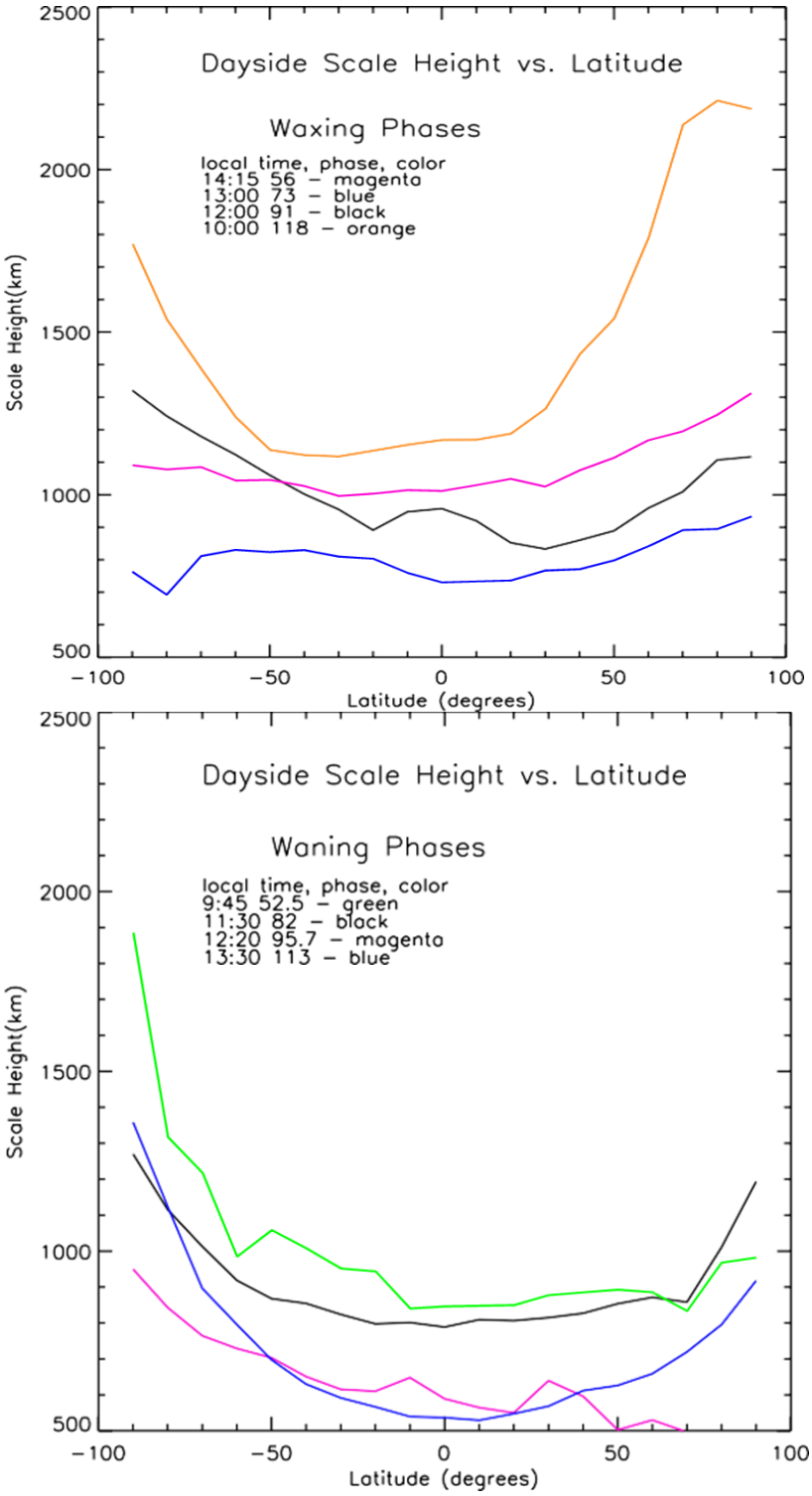

Figure 6.22: Scale heights are shown for waxing (top) phases and waning (bottom) phases 53°, 82°, 96°, 113°, 118°. Most of the scale heights cluster between 500 and 1500 km increasing at higher latitudes. Scale heights appear to decrease from dawn to noon (Killen et al., 2019).

An interesting observation is that our waning phase temperatures show large North-South asymmetry compared to our waxing phase temperatures, with some nights showing a factor of 2 difference between North and South limbs. Considering this is the dawn limb, the only process that this points to is meteor activity or charged particle sputtering. The nights of November 19, 2013 and December 19, 2013 show large asymmetry and while meteor effects were not apparent in the analysis in Sections 5.1 and 5.2 and considering that some datapoints on these nights are too high to be from a meteor source (larger than ~ 5000 K), this points to charged particle sputtering. This is further reinforced by the fact that both these nights are within the magnetotail. The night of May 26, 2016 is out of the magnetotail and there are no datapoints that exceed the maximum temperature of a meteor source, this may be due to meteor activity.

The relative intensity for 2 and 3 arcmin data for waxing and waning limbs are shown in Figures 6.24 and 6.25. The asterisks show a cosine of latitude function multiplied by the median relative intensity by night. The latitudes ranged from -100 to 100, in steps of 10° to produce the asterisk curves. This shows that the relative intensity does not follow a cosine of the latitude function also shown by Killen et al. (2019), nor does it follow any form of cosine (not shown here) as expected from previous results (Sarantos et al., 2010; Potter and Morgan, 1991). This also shows that the intensities are not symmetric about the equator and peaks at low-mid latitudes on both North and South limbs. The one night of data with good latitudinal coverage for the 2 arcmin waning limb data also shows the relative intensity peaking at low-mid latitudes. Our 3 arcmin waxing limb data follow this trend too.

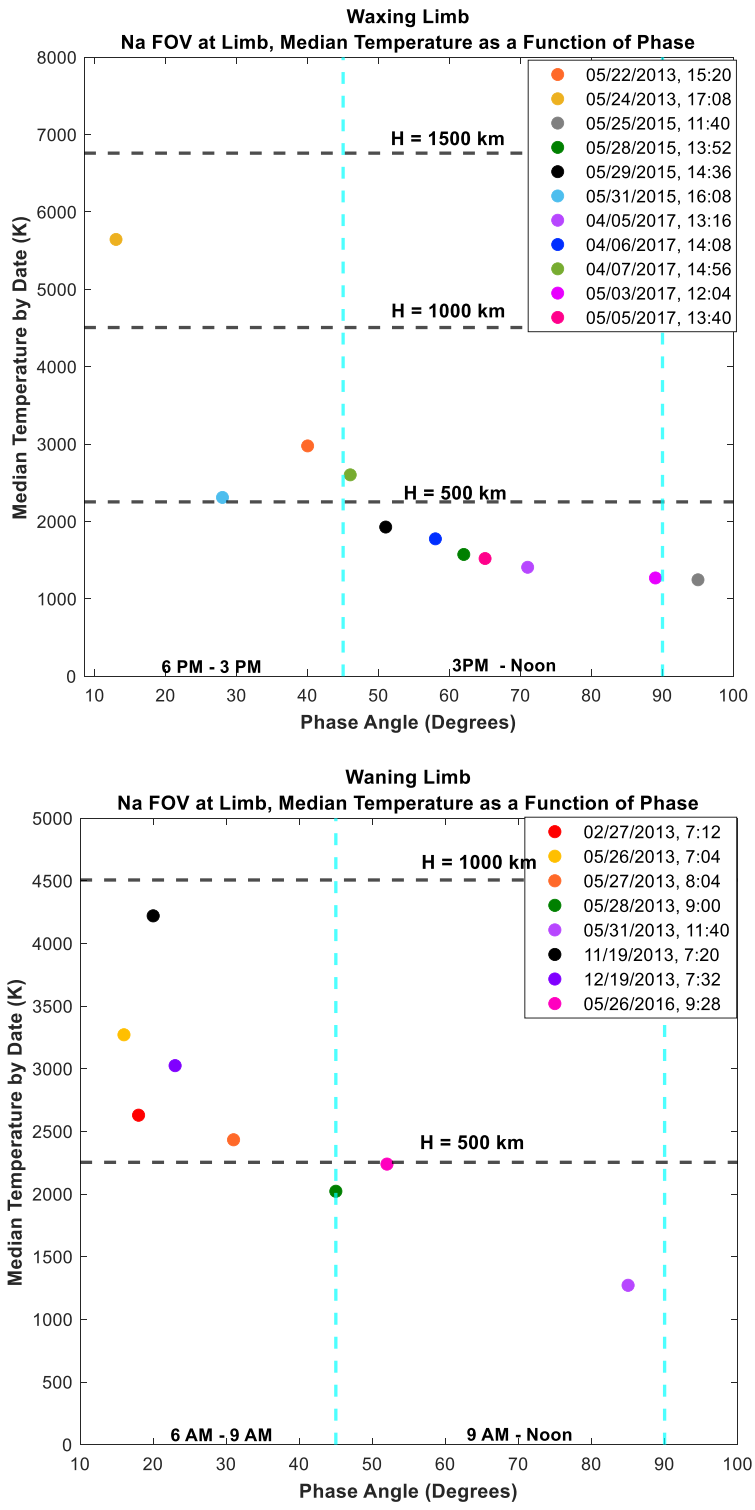

Figure 6.23: Median FOV at limb sodium temperatures per night for waxing (top) and waning (bottom) limbs. Waxing temperatures decrease from the evening/afternoon towards the morning. Waning temperatures decrease from dawn till noon. An approximate scale height is shown in 500 km intervals at the temperature equivalent obtained from using H = kT/mg.

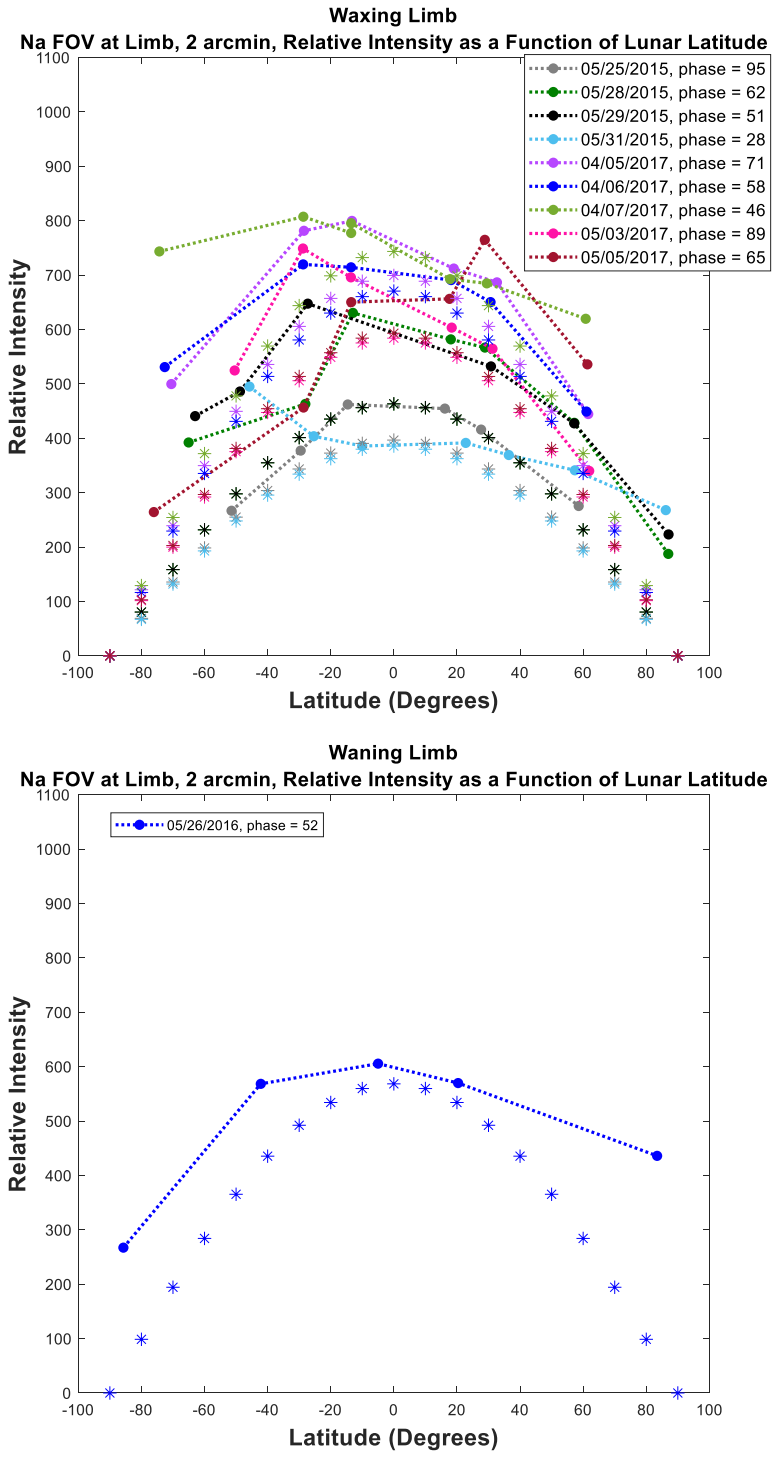

Figure 6.24: Sodium at limb 2 arcmin relative intensities as a function of latitude for waxing (top) and waning (bottom) limbs. The observations by night are shown as dots connected by a dashed line (not continuous data) and the asterisks of the same color show a cosine of the latitude function multiplied by the median relative intensity of that night. Relative intensities on both waxing and waning limbs do not follow any cosine of latitude form and does not peak at the equator.

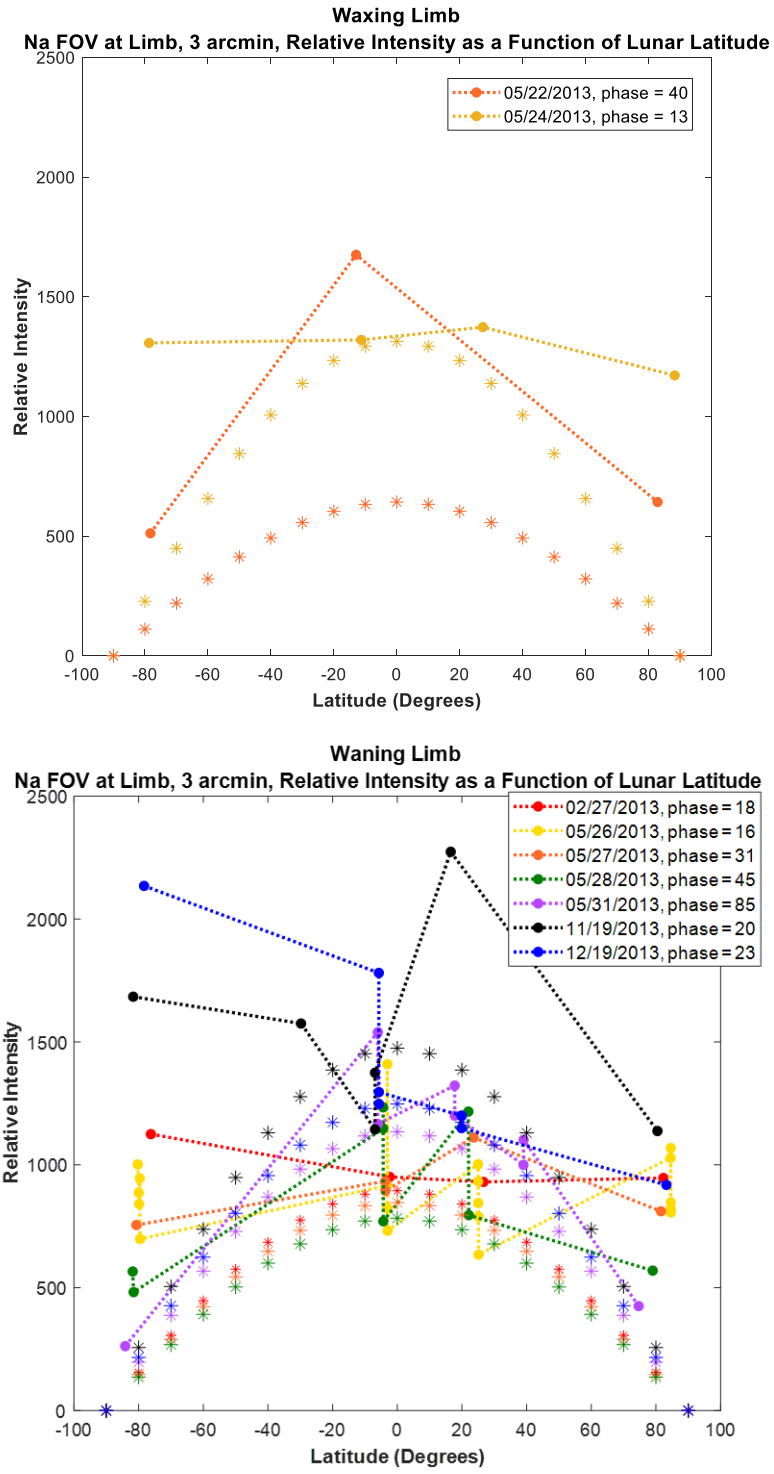

Figure 6.25: Sodium 3 arcmin relative intensities as a function of latitude for waxing (top) and waning (bottom) limbs. Relative intensities on both waxing and waning limbs do not follow any cosine of latitude form and does not peak at the equator. Some nights on the waning limb show large North-South asymmetry.

The intensity data of Killen et al. (2019) is shown in Figure 6.26 for waxing and waning phases. Their data also do not follow any cosine of latitude function nor is their data symmetric about the equator – in agreement with our relative intensity results. Their results also show that some of the waxing phase intensities peak at Northern mid-latitudes while many waning phase intensities peak at slightly Southern latitudes. Our waxing data, both 2 and 3 arcmin, peak at both low-mid Southern latitudes and Northern latitudes. Our waning phase data also peak at both North and South low-mid latitudes. The difference in peak intensity location between Killen et al. (2019) and our relative intensity data here, again, could be a sampling issue. Nevertheless, intensities peaking at low to mid-latitudes on both North and South limbs could be an indication of sodium surface abundance on the surface. Killen et al. (2019) also reported that they do not see an obvious relation of intensity derived column abundances with time of day, although in Killen et al. (2020) they report that waning phase column abundances are highest in the early morning and decrease throughout the day. Our 2 arcmin median waxing relative intensities as a function of phase and LT and our 3 arcmin waning relative intensities as a function of phase and LT are shown in Figure 6.27. I have not included the 2 arcmin waning median relative intensities and the 3 arcmin waxing relative intensities since there is not enough data to make a meaningful connection. Our 3 arcmin waning phase data show that in general intensities are brightest early morning and decrease throughout the day, except for, the one data point around noon which shows an increase. Our waxing phase intensities do not show any particular pattern with time of day.

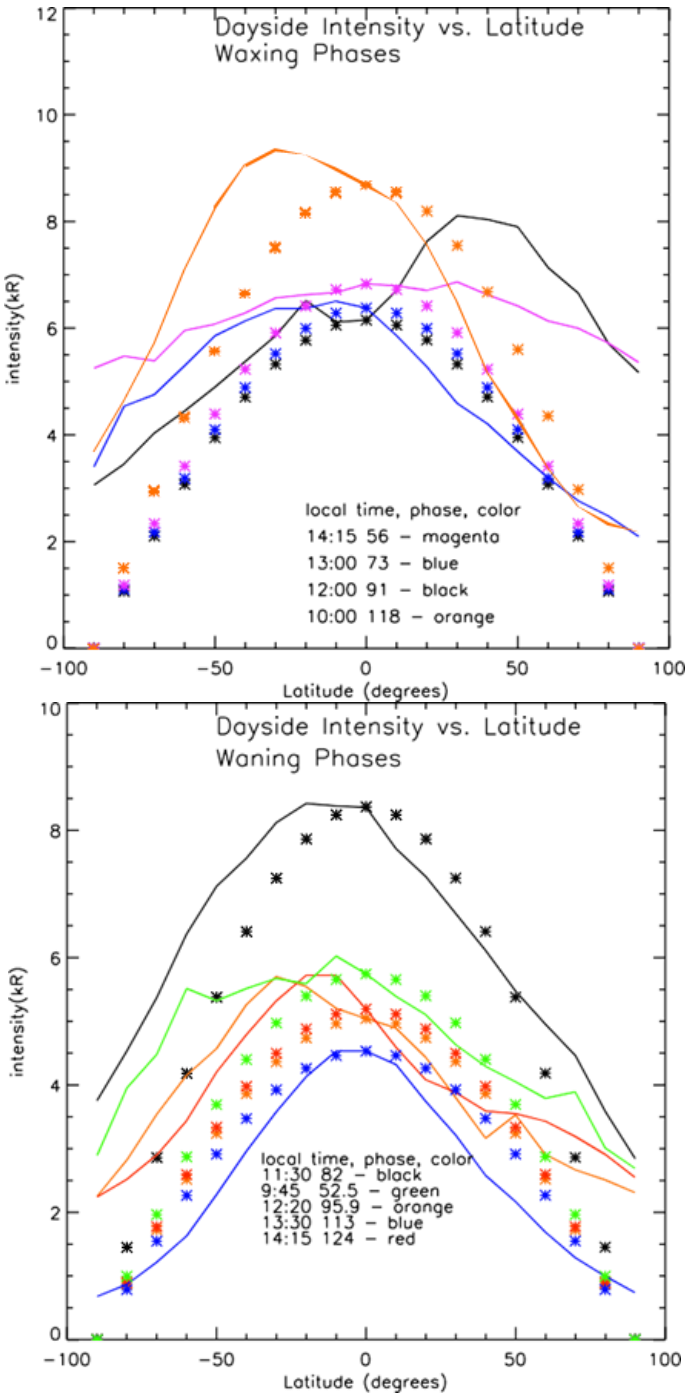

Figure 6.22: Intensities (kR) are shown for waxing (top) phases and waning (bottom) phases 53°, 82°, 96°, 113°, 118°. Intensities do not follow any form of cosine (latitude) function nor are they strictly symmetric about the equator (Killen et al., 2019).

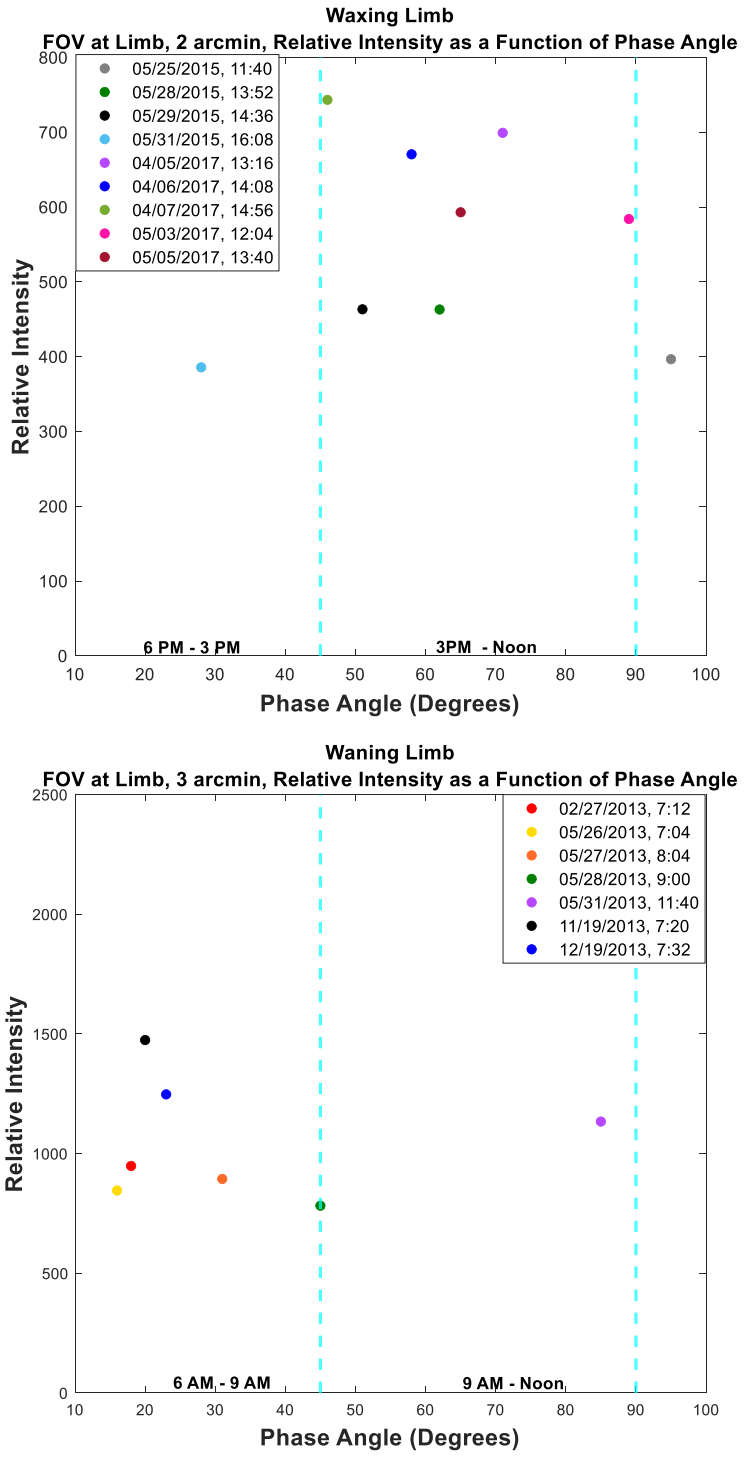

Figure 6.27: Median sodium relative intensities per night as a function of phase for waxing 2 arcmin data (top) and waning 3 arcmin data (bottom). 3 arcmin waning phase data show that in general intensities are brightest early morning and decrease throughout the day, except for the one data point around noon which shows an increase. Our waxing phase intensities do not show any particular pattern with time of day.

In summary, our waxing and waning temperatures increase from low to high latitudes and also increase from around noon towards the morning (dawn) and evening (dusk) terminators. This increase from subsolar points towards the terminator limb is in agreement with the conclusion of Kuruppuaratchi et al. (2018) that PSD dominates at subsolar points while processes such as impacts and sputtering take precedence towards the terminators. Our FOV is right at the morning and evening terminators during full Moon, and temperatures that are very high (more than 5000 K) could be indicative of the influence of plasma sheet ions on the exosphere. Killen et al. (2020) attributed the increase in scale height from noon towards the morning and evening terminators to radiation pressure. However, we have shown in Section 4.1.1, and Section 4.1.2. that it is unlikely that our high temperatures during full Moon are largely due to an effect of viewing geometry or looking down the lunar tail.

6.7. Radial Dependence of the Lunar Sodium Exosphere

In this Section, I discuss the radial dependence of the lunar sodium exosphere as an addition to the latitudinal study discussed in previous Sections. While the latitudinal study can shed light on the surface abundance and how source processes can switch depending on the plasma region the Moon is in, a radial study can shed light on source processes as a function of altitude. In theory, energetic source processes should be found at higher altitudes like the implications of the work from Schmidt et al. (2018) where the sodium line profile of the Hermean exosphere increased with altitude. It is also possible for the high energy tail distribution of a non-thermal process like PSD to be found at high altitudes.

Sodium linewidths as a function of altitude are shown in Figure 6.28 for waxing data (top) and waning data (bottom). Nights of observations where we made a decent number of offsets going out radially were picked for this study. While there is some variation in the linewidth per night, the overall trend for both waxing and waning limbs is that the linewidths decrease with altitude. It also appears that for data taken greater than 90° on the waxing limb, the linewidths appear almost constant. During this time the sunlit limb is in the morning (11:12 AM). All data taken less than 90° phase on the waxing side is in the afternoon. The waning limb data (Figure 6.28, bottom) show large decreases in linewidth as a function of altitude compared to the waxing limb data. Note that all the data taken on the waning side is in the morning. The overall trend of decreasing linewidths indicates that the exosphere is escaping. This means that the exosphere is losing more and more of the high energy atoms as the altitude increases, leaving the lower energy atoms. If we take the example of the non-thermal PSD population, moving away from subsolar points (quarter phase) we are seeing the high energy tail of the initial distribution released from the source. This high-energy tail is however not replenished and most of it is escaping, leaving the lower energy atoms. Our data is also in agreement with the altitude variation of linewidth shown in Mierkiewicz et al. (2014). This is an interesting observation and offers insight into the kinematics of atoms as we step out further from the lunar surface. It is possible that closer to the surface, there is a mix of all source processes, but as one steps out further the atoms that were released from high energy processes have escaped. We only go out to about 2 lunar radii in our observations and it is possible that the high energy atoms that have left the surface may be found at even higher altitudes or have completely escaped. This is an interesting trend and further investigation is necessary using the line center

positions of this data to determine the velocity of the atoms in the lunar reference frame (as shown in Section Chapter 4). Additionally, based on conclusions drawn from earlier Sections and Chapters, MIV appears to be a constant source in both sodium and potassium exospheres. MIV is thermal and likely has a global effect since it is very effective in releasing material to the exosphere (large vapor clouds). Additionally, for sodium, MIV is likely to produce a more uniform distribution since there is no strong correlation with surface abundance like with potassium. For potassium, the effects of MIV can be localized due to the dependence on KREEP regions. While the overall trend is a decrease in line width from low to high altitudes, closer to the Moon, there is some variation. On some nights, the overall decrease to about 1500 km is steeper compared to 1500 km and beyond. In fact, on nights where observations were made above ~ 1500 km, the line width almost settles out. This might be due to all the high energy atoms escaping, leaving the thermal MIV population and some contributions from high energy PSD atoms. One could also expect atoms released from charged particle sputtering to be present at altitudes greater than ~ 1000 km (Wurz et al., 2007), however, our temperatures beyond this limit are representative of MIV and not sputtering.

The decrease in line width as a function of altitude for all phases provides additional confidence that we do not look down the sodium tail. If that were true, we should be seeing increasing line widths as we step out radially from the Moon. Furthermore, this also shows that our data is a literal snapshot of the exosphere with each radial offset capturing a unique mix of source atoms. This could be the reason why in Section 4.1.4, when an exponential was fit to our relative intensity data, the scale height derived temperature did not always agree with the average of the effective temperatures over all the altitudes. Averaging the

temperature over all altitudes is probably incorrect because we are assuming the sources are well mixed. As seen from the line width variation with altitude, the exosphere appears to fluctuate in linewidth closer to the surface, and slowly decreases and almost 'settles' out at higher altitudes. Each FOV offset is unique with a temperature and relative intensity characteristic of the population of atoms within that FOV at that time. The exosphere, then, cannot be attributed to a single scale height or temperature, because the populations are not well mixed. Instead, the lunar exosphere should be studied in specific temporal and spatial slots. An interesting piece of information is that a similar trend was observed in Balmer α geocoronal observations where effective temperatures were found to decrease with increasing shadow altitudes in the Earth's exosphere (Mierkiewicz et al. 2012). While no firm conclusions can be drawn from the altitude variation shown here, it is an important result that could provide clues on the bulk movement of atoms.

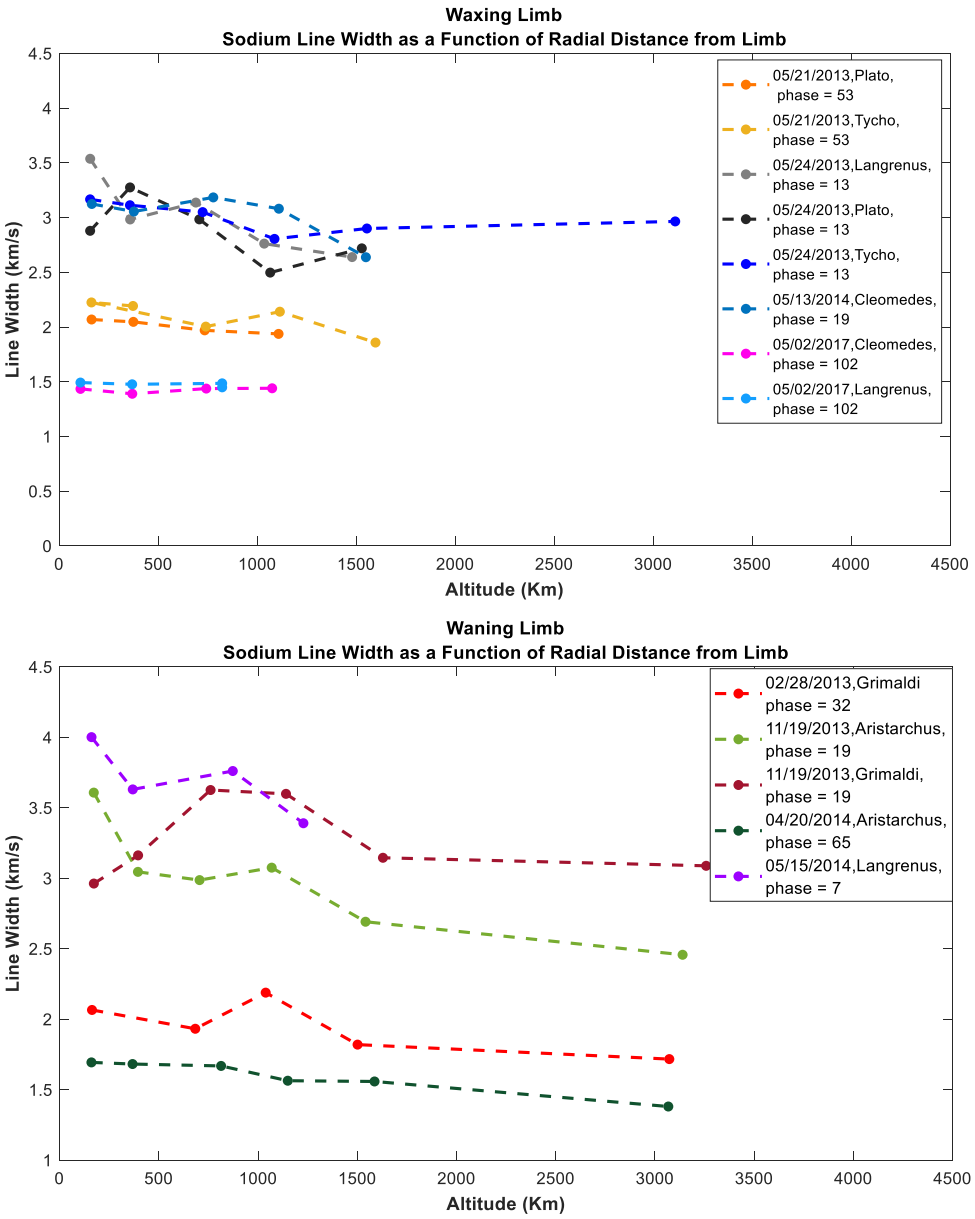

Figure 6.28: Linewidth as a function of altitude (km) for select nights on waxing (top) and waning (bottom) limbs. Overall, linewidths (and derived effective temperatures) fall off towards high altitudes.

6.8 Summary and Conclusions

In this Chapter, I analyzed 2 and 3 arcmin sodium and potassium FOV at the limb and edge data separated by the plasma region and as a function of latitude. The latitudinal

study indicated that during a lunation, the Moon shows signatures that arise due to the dynamics of source particles that can change with phase and the near lunar environment. The results from this Chapter also reinforced the conclusions from Chapters 4 and 5 while also providing some further insight in grasping how to better monitor the health of the lunar exosphere. The temperature and relative intensity results from Sections 6.1 – 6.5 of this Chapter are summarized for both sodium and potassium in Tables 6.8 and 6.9.

Table 6.8: *Summary of sodium temperature and relative intensity data as shown in Section 6.1 – 6.5*

Region	Temperature	Relative Intensity
Solar Wind	• Temperature distribution is overall flat and represents a PSD population. • PSD and solar wind ion sputtering both follow SZA dependence with a maximum near subsolar points. Temperature here describes an exosphere generated by PSD source atoms and PSD releasing atoms from a surface primed by solar wind ions. • Temperatures greater than a PSD source can be attributed to MIV.	• 2 and 3 arcmin data indicate that the exosphere is brightest at equatorial latitudes and become dimmer towards the poles. Source in the undisturbed solar wind region is one that follows a form that has SZA dependence. • Intensities peak at low – mid-latitudes indicating that while the major source might be SZA dependent, surface composition causes the source location itself to shift from being purely at the equator.

		• Since the fall-off is steep, PSD is the major source, with contributions from MIV and sputtering.
Source processes:	**Major source: PSD** **Contributions by: MIV**	
Magnetosheath	• Temperatures are hotter than in the solar wind and increase going towards high latitudes. Likely due to a mid-high energy population of PSD atoms that have more energy than atoms that are closer to the subsolar point – like in the solar wind. • Heated, compressed, and deflected solar wind ions in the magnetosheath, can now reach latitudes away from the equator easier than the in the solar wind. The ambient population released by PSD is not concentrated at the subsolar point. • Contributions from MIV are present. • Temperatures greater than ~ 5000 K can be attributed to magnetosheath	• Relative intensities fall off slower from the equator towards the poles, compared to the solar wind. This indicates that the source(s) is no longer mainly SZA dependent. • Magnetosheath ions create more ambient atoms for PSD to release, even at latitudes away from the equator. • There is an asymmetry between waxing data and waning data, with data around 50° phase on the waxing side being brighter than data around 50^{o} phase on the waning side. The higher flux during magnetosheath ingress compared to magnetosheath egress may provide more source and ambient atoms.

	ions. • PSD follows less of the SZA pattern like in the solar wind and becomes less important the farther away we get from the subsolar point.	
Source Processes:	**Major source process: MIV** **Contributions by: mid-high energy PSD population, charged particle sputtering by magnetosheath ions**	
Magnetotail	• Only the highest energy PSD atoms make it from the source location to the limb sides during full Moon. This also means that only a fraction of particles present at the source has the highest energies. This fraction is smaller than the fraction of atoms present during magnetosheath passage. • Overall, temperatures are representative of MIV. • Some very high temperatures can be	• Intensities are overall flat except for large variations very close to full Moon (0 – 10^{o} phases). • Flat intensities could be indicative of the global MIV population. From Chapter 5 we know that sodium responds very slowly to meteors, meaning that the brightness of the vapor cloud produced by MIV will be a uniform one with only small changes over time. • Varying brightness levels very close to full Moon could be

	attributed to the energetic plasma sheet ions.	due to the response of the exosphere as a result of interacting with the plasma sheet.
Source Processes:	**Major: MIV Contributions by: plasma sheet ions followed by high energy PSD population.**	
Special Cases:		
Interaction with Plasma Sheet	• Temperatures during longer plasma sheet interactions were about a factor of 2 higher than temperatures during shorter plasma sheet interactions.	• Intensities for corresponding temperatures only show a slight increase in brightness from short to longer plasma sheet interactions. • Points to other importance of flux or spatial dependence, or both.
Total Lunar Eclipse		
	• Temperatures right before eclipse are a mix of high energy PSD atoms and MIV. • Temperatures in the Penumbra are representative of MIV and charged particle sputtering by plasma sheet ions.	• Intensities are the brightest right before the eclipse began (when sunlight is still fully present). • PSD is important in both releasing atoms from the surface and re-exciting previously released atoms from other processes.

Table 6.9: *Summary of potassium temperature and relative intensity data as shown in Section 6.1 – 6.5*

Region	Temperature	Relative Intensity
Solar Wind	• Temperatures are not 'flat' like sodium and are more spread out latitudinally. Implies that potassium responds to a process that has no SZA dependence – like MIV. • Large North-South and dawn-dusk asymmetry. Result of meteors and surface composition.	• Overall, intensities are brightest near the equator and fall off towards high latitudes, but the fall-off is not as steep as for sodium. • On the waning side, intensities are the brightest at KREEP latitudes.
Source Processes:	**Major: MIV Contributions: from PSD**	
Magnetosheath	• Temperatures decrease towards high latitudes, opposite to the trend seen in sodium. This implies that potassium is not readily affected by charged particle sputtering as much as sodium, or surface abundance is overwhelming any underlying trend. • Temperatures can be explained by MIV.	• Intensities show an increase towards the poles at times, while sodium showed a constant decrease towards the poles. • Near KREEP regions show increased brightness. • Waxing phase angle intensities around 50^{o} phase angle are brighter than waning counterpart – similar to sodium. Might be due to

		magnetosheath ingress vs egress.
Source Processes:	**Major: MIV Contributions from: PSD, charged particle sputtering.**	
Magnetotail		
	• Temperatures are in the MIV range. • Temperatures increase from mid to high latitudes.	• Intensities are brighter near KREEP regions.
Source Processes:	**Major: MIV Contributions from: PSD with no comments on plasma sheet effects since we cannot observe potassium so close to the full Moon.**	
Additional Comments:	**MIV seems to be the most important source process for potassium along with important contributions from the surface composition.**	

The main conclusions from Sections 6.1 – 6.5 for sodium and potassium support the results of Chapters 4 and 5 and point to the importance of flux and surface composition in understanding the response of the exosphere. While high energy processes liberate atoms into the exosphere if their flux is low it might not be as important as a lower energy process with very high flux. Additionally, while charged particle sputtering from solar wind ions seem to mostly enhance PSD, the ions in the plasma sheet seem to affect the lunar sodium exosphere. Since the abundance of sodium on the lunar surface is not as well-known as potassium, it is hard to further constrain observations. However, results from Section 6.6 point to possible surface abundance interactions showing up in the lunar sodium exosphere.

Linewidth variation as a function of latitude from Section 6.7 indicate an exosphere that cools off with altitude while observations that are closer to the surface show variation.

This dissertation consists of an extensive body of work pertaining to the analysis of lunar sodium and potassium both temporally and spatially from observations made from 2013 - 2017. The results shown in this work along with their respective discussions are the most comprehensive analysis of velocity resolved lunar exospheric emissions made to date. While there have been lunar exospheric studies made from both ground-based and space observations, the analysis presented in this work has provided valuable insight into the processes that govern the lunar exosphere. This work has provided insight into:

- The way source processes contribute to the exosphere as a function of lunar phase.
- The importance of meteor impacts in maintaining the lunar exosphere and how sodium and potassium appear to respond differently to MIV.
- The way the exosphere responds to its near plasma environment.
- Surface – atmosphere interactions with results confirming the importance of the KREEP regions in modulating the response of the potassium exosphere.
- The influence of the plasma sheet on exospheric observations.
- The latitudinal dependence of the exosphere, providing both confirmations with other ground-based observations and providing further results for interpretation.
- The usefulness of velocity resolved observations as a complementary way to monitor the health of the exosphere through comparisons to scale height derived studies.

The goal of this dissertation was to investigate the lunar exosphere using sodium and a smaller potassium dataset, as a function of multiple variables. These

variables include latitude, near plasma region, meteor shower activity, phase, time (month, year, lunar cycle), altitude, and surface abundance. Together, these variables interact to form the response of the exosphere in terms of temperature, velocity, and relative intensity signals. This work has shown the importance of incorporating as many variables as possible in trying to disentangle source processes and has met the goal of providing a unique way of investigating the lunar exosphere. While there are more variables at play, this work lays a decent amount of ground-work for future studies and models to be tested and built upon.

Appendix A - Observing Runs

Month	Year	Run	Nights with Data	Full Moon Date
March	2009	03/11 - 03/14	4	11-Mar-2009
Total		**2009**	**4**	
March	2011	03/17 - 03/23	5	19-Mar-2011
June	2011	06/8 - 06/12	5	15-Jun-2011
September	2011	09/16 - 09/17	2	12-Sep-2011
December	2011	12/11 - 12/11	1	10-Dec-2011
Total		**2011**	**13**	
March	2012	03/05 - 03/11	5	8-Mar-2012
May - June	2012	05/30 - 06/10	12	4-Jun-2012
September - October	2012	09/26 - 10/07	11	30-Sep-2012
Total		**2012**	**28**	
February - March	2013	02/23 - 03/02	8	25-Feb-2013
May - June	2013	05/20 - 06/02	13	25-May-2013
November	2013	11/19 - 11/21	3	17-Nov-2013
December	2013	12/13 - 12/19	7	17-Dec-2013
Total	2013	**2013**	**31**	
January	2014	01/10 - 01/21	12	16-Jan-2014
February	2014	02/09 -02/20	12	14-Feb-2014
April	2014	04/14 – 04/22	7	15-Apr-2014
May	2014	05/09 – 05/20	10	14-May-2014
November - December	2014	11/30 - 12/07	5	6-Dec-2014
Total		**2014**	**46**	
January	2015	01/16 - 01/18	3	5-Jan-2015
May - June	2015	05/23 - 06/12	17	2-Jun-2015
November	2015	11/17 - 11/22	6	25-Nov-2015
Total		**2015**	**26**	
January	2016	01/01 - 01/03	3	25-Dec-2015
March	2016	03/13 - 3/18	6	23-Mar-2016
May	2016	05/13 - 05/29	16	21-May-2016
June	2016	06/12 - 06/21	10	20-Jun-2016

September	2016	09/11 - 09/16	6	16-Sep-2016
October	2016	10/08 - 10/12	5	16-Oct-2016
November	2016	11/09 - 11/20	11	14-Nov-2016
December	2016	12/18 - 12/20	2	14-Dec-2016
Total		**2016**	**59**	
January	2017	01/05 - 01/09	6	12-Jan-2017
March	2017	03/09 - 03/17	9	12-Mar-2017
April	2017	04/03 - 04/08	6	11-Apr-2017
April - May	2017	04/29 - 05/06	8	10-May-2017
May - June	2017	05/31 - 06/03	3	9-Jun-2017
June	2017	06/13 - 06/16	4	9-Jun-2017
August - September	2017	08/30 - 09/05	5	6-Sep-2017
September - October	2017	09/26 - 10/01	6	5-Oct-2017
November	2017	11/10 - 11/12	2	4-Nov-2017
December	2017	12/03 - 12/08	4	3-Dec-2017
December	2017	12/30 - 12/31	2	2-Jan-2018
Total		**2017**	**55**	
TOTAL		**2009 - 2017**	**262**	

Appendix B - Reference Feature (Offset)

Lunar Feature (Crater/Mare/Mons)	Longitude (East)	Latitude	Direction Offset
Albategnius	4.1	-11.2	Crater, W
Apollonius	61.1	4.5	W
Aristarchus	-47.4	23.7	E
Aristoteles	17.4	50.2	W
Atlas	44.4	46.7	W, N
Censorinus	32.7	0.4	Crater
Cleomedes	55.5	27.7	W
Copernicus	-20.1	9.6	Crater, E
Dionysius	17.3	2.8	Crater
Endymion	56.5	53.6	W
Furnerius	60.4	-36.3	W
Gambart	-15.2	0.9	Crater
Gassendi	-40.0	-17.6	E
Godin	10.2	1.8	Crater, W
Grimaldi	-68.8	-5.2	E
Janssen	40.8	-45.0	E
Kepler	-38.0	8.1	E
Kunowsky	-32.5	3.2	Crater
Langrenus	60.9	-8.9	W
Mare Cognitum	-23.1	-10.0	Mare
Mare Crisium	59.1	17.0	Mare, W
Mare Fecunditatis	51.3	-7.8	W
Mare Humorum	-38.6	-24.4	Mare
Mare Imbrium	-15.6	32.8	Mare, N
Mare Nectaris	35.5	-15.2	Mare
Mare Nubium	-16.6	-21.3	Mare
Mare Serenitatis	17.5	28.0	Mare
Mare Tranquillitatis	31.4	8.5	W
Mare Vaporum	3.6	13.3	Mare, E
Messala	60.0	39.3	W
Mons Gruithuisen	-40.7	36.6	E

Lunar Feature (Crater/Mare/Mons)	Longitude (East)	Latitude	Direction Offset
Mons Rumker	-58.4	40.8	E
Moon Central Highlands	-5.0	5.0	Crater, W, E, N, S
Moon Equator E	-68.8	-5.2	E
Moon Equator W	55.2	4.6	W
Moon NW	39.1	46.7	NW
Moon SE	54.2	-32.5	W
Mosting	-5.9	-0.9	Crater
Pallas	-1.6	-5.5	Crater
Petavius	60.4	-25.3	W
Plato	-9.3	51.6	N
Proclus	46.8	16.1	W
Ptolemaeus	-1.8	-9.2	Crater
Scheiner	-43.4	-60.5	E
Schickard	-54.1	-44.4	E
Sinus Iridium	-31.7	45.0	Mare, N
Stevinus	54.2	-32.5	W
Taruntius	46.5	5.6	W
Theophilus	26.4	-11.4	W
Tycho	-11.4	-43.3	S
Vieta	-56.3	-29.2	E

Appendix C – Observing Log

Lunar Sodium & Potassium Observations

NSO - McMath-Pierce Telescope Main at North Port
2016 May 28

L1	L2	L3	L4
f = 30"	f = 750 mm	f = 308 mm	f = 200 mm
d = 6"	d = 50.8 mm	d = 59 mm	f/4

Dual Etalon Fabry-Perot: Master (A) = 4 mm; Slave (B) = 1.76 mm

Observers: Oliversen, Gallant, Rosborough

Weather: T= 14 C, RH~25%, winds 10 mph NW, Clear

Moon illumination ~62%

North Port: Trm = 18.6 C, RH = 22.5%; Tgas = 58 F

Telescope focus = NA

#	Object	File	Time	HA	Expo	Filter	Pres_A	Pres_B	Comment #1
1	Na Lamp	na_01	0.214583333	0:00	10	Na D2 5890/4 A	1190	1098	Std Config - Lamp off ceiling card
2	Th-Ar HC Lamp	th_02	0.222916667	0:00	30	Na D2 5890/4 A	1190	991	Std Config - HC over Entr Aperture
3	Th-Ar HC Lamp	th_03	0.224305556	0:00	30	Na D2 5890/4 A	1070	871	Std Config - Reduced ring
4	Th-Ar HC Lamp	th_04	0.234027778	0:00	30	Th I 7647/5.5 A	880	862	Std Config - HC over Entr Aperture
5	K HC Lamp	k_05	0.247916667	0:00	30	K D1 7699/5 A	870	775	Std Config - Lamp off ceiling card
6	Tycho Limb	moon_06	0.339583333	-4:35	300	K D1 7699/5 A	870	775	FOV at limb (E)
7	Schickard Limb	moon_07	0.345138889	-04:27	300	K D1 7699/5 A	870	775	FOV at limb (S)
8	Vieta Limb	moon_08	0.351388889	-03:25	300	K D1 7699/5 A	870	775	FOV at limb (E)
9	Grimaldi Limb	moon_09	0.363194444	-03:09	300	K D1 7699/5 A	870	775	FOV at Aperture Edge (E)
10	Grimaldi Limb	moon_10	0.36875	-03:01	300	K D1 7699/5 A	870	775	FOV at Field Lens Edge (E)
11	Grimaldi Limb	moon_11	0.372916667	-02:55	300	K D1 7699/5 A	870	775	FOV at limb (E)
12	Aristarchus Limb	moon_12	0.377777778	-02:48	300	K D1 7699/5 A	870	775	FOV at limb (E)
13	Aristarchus Limb	moon_13	0.382638889	-02:42	300	K D1 7699/5 A	870	775	FOV at Aperture Edge (E)
14	Aristarchus Limb	moon_14	0.3875	-02:35	300	K D1 7699/5 A	870	775	FOV at Field Lens Edge (E)
25	Aristarchus Limb	moon_15	0.392361111	-02:27	300	K D1 7699/5 A	870	775	FOV at limb (N)
16	Aristarchus Limb	moon_16	0.397222222	-02:21	300	K D1 7699/5 A	870	775	FOV at Aperture Edge (N)
17	Aristarchus Limb	moon_17	0.402083333	-02:14	300	K D1 7699/5 A	870	775	FOV at Field Lens Edge (N)
18	Plato Limb	moon_18	0.406944444	-02:06	300	K D1 7699/5 A	870	775	FOV at limb (N)
19	Th-Ne HC lamp	th_19	0.414583333	0:00	30	Th I 7647/5.5 A	880	862	Std Config - HC over Entr Aperture
20	Plato Limb	moon_20	0.420833333	-01:47	300	Na D2 5890/4 A	1190	1098	FOV at limb (N)
21	Aristarchus Limb	moon_21	0.425694444	-01:41	300	Na D2 5890/4 A	1190	1098	FOV at limb (N)
22	Aristarchus Limb	moon_22	0.430555556	-01:35	300	Na D2 5890/4 A	1190	1098	FOV at limb (E)
23	Grimaldi Limb	moon_23	0.434722222	-01:28	300	Na D2 5890/4 A	1190	1098	FOV at limb (E)
24	Vieta Limb	moon_24	0.440277778	-01:17	300	Na D2 5890/4 A	1190	1098	FOV at limb (E)
25	Schickard Limb	moon_25	0.445138889	-01:10	300	Na D2 5890/4 A	1190	1098	FOV at limb (S)
26	Tycho Limb	moon_26	0.45	-01:04	300	Na D2 5890/4 A	1190	1098	FOV at limb (E)
27	Th-Ar HC Lamp	th_27	0.459722222	0:00	30	Na D2 5890/4 A	1190	991	Std Config - HC over Entr Aperture
28	Th-Ar HC Lamp	th_28	0.461111111	0:00	30	Na D2 5890/4 A	1070	871	Std Config - Reduced ring
29	Na Lamp	na_29	0.473611111	0:00	10	Na D2 5890/4 A	1190	1098	Std Config - Lamp off ceiling card

#	Type	Gain	FOV	Wavelength	Comment #2	CntrX	CntrY	<Xcntr>	<Ycntr>	Crater	Origin
1	comp	4	120	5889.9509	Focus at Infinity	267.3	274.9	267.2	275.0		
2	comp	4	120	5891.451		267.0	275.0	267.2	275.0		
3	comp	4	120	5891.451		267.2	275.2	267.2	275.0		
4	comp	4	120	7647.38	Focus at 3|0	265.7	263.0	265.7	262.9		
5	comp	4	120	7698.9647		265.8	262.9	265.7	262.9		
6	obj	4	120	7698.9647				265.7	262.9	Tycho	Limb E
7	obj	4	120	7698.9647				265.7	262.9	Schickard	Limb S
8	obj	4	120	7698.9647				265.7	262.9	Vieta	Limb E
9	obj	4	120	7698.9647				265.7	262.9	Grimaldi	Aper E
10	obj	4	120	7698.9647				265.7	262.9	Grimaldi	Edge E
11	obj	4	120	7698.9647				265.7	262.9	Grimaldi	Limb E
12	obj	4	120	7698.9647				265.7	262.9	Aristarchus	Limb E
13	obj	4	120	7698.9647				265.7	262.9	Aristarchus	Aper E
14	obj	4	120	7698.9647				265.7	262.9	Aristarchus	Edge E
15	obj	4	120	7698.9647				265.7	262.9	Aristarchus	Limb N
16	obj	4	120	7698.9647				265.7	262.9	Aristarchus	Aper N
17	obj	4	120	7698.9647				265.7	262.9	Aristarchus	Edge N
18	obj	4	120	7698.9647				265.7	262.9	Plato	Limb N
19	comp	4	120	7647.38	Trm = 18.9 C, RH = 21.7%	265.7	262.9	265.7	262.9		
20	obj	4	120	5889.9509	Focus at Infinity			273.5	259.2	Plato	Limb N
21	obj	4	120	5889.9509				273.5	259.2	Aristarchus	Limb N
22	obj	4	120	5889.9509				273.5	259.2	Aristarchus	Limb E
23	obj	4	120	5889.9509				273.5	259.2	Grimaldi	Limb E
24	obj	4	120	5889.9509				273.5	259.2	Vieta	Limb E
25	obj	4	120	5889.9509				273.5	259.2	Schickard	Limb S
26	obj	4	120	5889.9509				273.5	259.2	Tycho	Limb E
27	comp	4	120	5891.451	Trm = 18.8, RH = 21.8%	273.5	259.0	273.5	259.2		
28	comp	4	120	5891.451	T = 13.7 C, RH = 28.8%,	273.5	259.4	273.5	259.2		
29	comp	4	120	5889.9509	Winds ~10 mph NE	273.5	259.1	273.5	259.2		

#	Offset_EW	Offset_NS	Moon_Long	Moon_Lat	Alt	RA	DEC	Azimuth	Elevation	LST	AM
1											
2											
3											
4											
5											
6	0	0	-98.2404376	-54.4578948	110.2304	324.9692	-12.511	112.8767	11.7306	17.18046	4.781
7	0	0	-99.763282	-66.0507959	110.176	325.0315	-12.4981	114.0401	13.2508	17.31416	4.267
8	0	0	-96.8026174	-31.5041091	110.1178	325.1005	-12.4834	115.3808	14.9456	17.46457	3.811
9	0	0	-95.9021219	-7.79652444	165.0754	325.2279	-12.4553	118.0145	18.0972	17.74868	3.183
10	0	0	-95.9300944	-9.1076545	378.2825	325.2865	-12.4418	119.3043	19.5554	17.88238	2.959
11	0	0	-95.922726	-7.42246851	109.9104	325.3299	-12.4317	120.2947	20.6375	17.98265	2.813
12	0	0	-95.1508526	14.64685465	109.8649	325.38	-12.4197	121.4763	21.8868	18.09964	2.662
13	0	0	-95.2031748	13.47444098	164.8143	325.4295	-12.4076	122.6877	23.1209	18.21662	2.53
14	0	0	-95.3275837	9.645233423	377.7042	325.4785	-12.3954	123.9304	24.3389	18.33361	2.412
15	0	0	-93.544806	46.18846234	109.7439	325.5268	-12.3831	125.206	25.5398	18.4506	2.307
16	0	0	-93.4984536	46.89807663	164.6167	325.5746	-12.3706	126.516	26.7225	18.56758	2.213
17	0	0	-93.2676659	49.25983052	377.2937	325.6218	-12.358	127.8622	27.8858	18.68457	2.129
18	0	0	-78.2796404	82.70476464	109.6297	325.6685	-12.3453	129.2461	29.0285	18.80155	2.053
19											
20	0	0	-78.366905	82.72606296	109.5217	325.799	-12.3082	133.4225	32.1682	19.1358	1.872
21	0	0	-93.6867017	46.2289194	109.483	325.8438	-12.295	134.967	33.2189	19.25279	1.82
22	0	0	-95.3494995	14.51153342	109.4553	325.8881	-12.2816	136.5569	34.242	19.36977	1.772
23	0	0	-96.1296646	-7.49345363	109.4242	325.9258	-12.27	137.9568	35.0959	19.47005	1.735
24	0	0	-97.0408815	-31.6555978	109.3849	325.9755	-12.2544	139.8782	36.1993	19.60375	1.689
25	0	0	-99.9063341	-66.3011602	109.3623	326.0185	-12.2405	141.612	37.1299	19.72073	1.653
26	0	0	-98.4755662	-54.8515595	109.3335	326.0612	-12.2265	143.3958	38.0261	19.83772	1.62
27											
28											
29											

#	Mv	S_Brt	Illum	Ang_Dia	Obs_Long	Obs_Lat	S_Long	S_Lat	r	rdot	delta	deldot
1												
2												
3												
4												
5												
6	0.756	4.99	62.299	1889.068	354.1358	-2.04018	278.3341	-1.508	151,710,301	-0.62966	379,410	-0.39748
7	0.675	4.99	62.251	1890.012	354.1241	-2.03104	278.2663	-1.50798	151,709,999	-0.62999	379,221	-0.39251
8	0.603	4.99	62.198	1891.061	354.1101	-2.02123	278.1899	-1.50795	151,709,658	-0.63037	379,010	-0.38644
9	0.503	4.99	62.101	1892.998	354.081	-2.00406	278.0458	-1.50791	151,709,015	-0.63107	378,622	-0.37367
10	0.468	4.99	62.056	1893.887	354.0662	-1.9966	277.978	-1.50789	151,708,712	-0.63139	378,445	-0.36707
11	0.445	4.99	62.022	1894.544	354.0546	-1.99126	277.9271	-1.50787	151,708,485	-0.63164	378,313	-0.36188
12	0.421	4.99	61.984	1895.299	354.0406	-1.98531	277.8677	-1.50785	151,708,219	-0.63192	378,163	-0.35557
13	0.4	5.00	61.946	1896.04	354.0261	-1.97966	277.8084	-1.50783	151,707,954	-0.6322	378,015	-0.34899
14	0.381	5.00	61.908	1896.769	354.0111	-1.97432	277.749	-1.50781	151,707,688	-0.63249	377,870	-0.34215
15	0.365	5.00	61.871	1897.483	353.9956	-1.96928	277.6897	-1.5078	151,707,423	-0.63277	377,728	-0.33505
16	0.35	5.00	61.834	1898.182	353.9796	-1.96453	277.6303	-1.50778	151,707,157	-0.63305	377,588	-0.3277
17	0.337	5.00	61.798	1898.866	353.9632	-1.96009	277.571	-1.50776	151,706,891	-0.63333	377,452	-0.3201
18	0.325	5.00	61.762	1899.535	353.9464	-1.95594	277.5116	-1.50774	151,706,625	-0.63361	377,320	-0.31226
19												
20	0.296	5.00	61.661	1901.352	353.8959	-1.94569	277.342	-1.50768	151,705,864	-0.6344	376,959	-0.2886
21	0.288	5.00	61.626	1901.954	353.8775	-1.94266	277.2827	-1.50767	151,705,597	-0.63467	376,839	-0.2799
22	0.28	5.00	61.591	1902.538	353.8587	-1.93991	277.2233	-1.50765	151,705,331	-0.63494	376,724	-0.271
23	0.274	5.00	61.562	1903.024	353.8423	-1.93778	277.1725	-1.50763	151,705,102	-0.63518	376,628	-0.26321
24	0.267	5.00	61.523	1903.65	353.8201	-1.93525	277.1046	-1.50761	151,704,797	-0.63549	376,504	-0.25261
25	0.261	5.01	61.49	1904.176	353.8004	-1.93333	277.0453	-1.50759	151,704,530	-0.63576	376,400	-0.24314
26	0.256	5.01	61.456	1904.683	353.7803	-1.93168	276.9859	-1.50757	151,704,263	-0.63603	376,300	-0.2335
27												
28												
29												

#	S-O-T	L/T	Phase	Line_Depth	Local_Time	Fit_Quality	Weather	Comment #3
1								
2								
3						Good		
4								
5								
6	104.0991	/L	75.7619	0.194108521		Good		
7	104.0428	/L	75.8182	0.194113714		Good		
8	103.9805	/L	75.8806	0.194119532		Good		
9	103.8653	/L	75.9958	0.194130454				
10	103.8123	/L	76.0489	0.194135564				
11	103.7729	/L	76.0883	0.194139383		Good		
12	103.7275	/L	76.1337	0.194143824		Good		
13	103.6826	/L	76.1786	0.194148251				
14	103.6382	/L	76.223	0.194152662				
15	103.5943	/L	76.267	0.194157058		Good		
16	103.5509	/L	76.3104	0.194161439				
17	103.508	/L	76.3534	0.194165807				
18	103.4654	/L	76.3959	0.194170157		Good		
19								
20	103.3463	/L	76.5152	0.050559636		Good		
21	103.3053	/L	76.5561	0.050560092		Good		
22	103.2648	/L	76.5967	0.050560546		Good		
23	103.2303	/L	76.6312	0.050560934		Good		
24	103.1847	/L	76.6769	0.05056145		Good		
25	103.1451	/L	76.7165	0.050561899		Good		
26	103.1058	/L	76.7558	0.050562347		Good		
27								
28						Good		
29								

Object	Source
File	Fits file (unsigned 16 bit image)
Time	Start Time (UT: Universal Time))
HA	Hour Angle
Expo	Exposure time (seconds)
Filter	Blocking Filter
Pres_A	Pressure Etalon A (torr)
Pres_B	Pressure Etalon B (torr)
Comment #1	Typically FOV or setup information
Type	Category of observations (Comp, Zero, Dark, Obj, Bias)
Gain	Pre-Amp gain (e^{-s} /DN) Setting
FOV	Field of View (arcsec)
Wavelength	Emission Line (Angstroms)
Comment #2	Typically weather, room conditions, setup information
Cntr X	Fabry-Perot Ring Center (X)
Cntr Y	Fabry-Perot Ring Center (Y)
<Xcntr>	Fabry-Perot Ring Center (X) – Average value based on rings since last CCD focus change
<Ycntr>	Fabry-Perot Ring Center (Y) - Average value based on rings since last CCD focus change
Crater	Offset Reference Crater
Offset_EW	Distance from Origin (min, sec)
Offset_NS	Distance from Origin (arcmin, arcsec)
Origin	Reference point from which Moon_Long & Moon_Lat is calculated
Moon_Long	Selenographic longitude coordinate of FOV (degrees)
Moon_Lat	Selenographic latitude coordinate of FOV (degrees)
Alt	Altitude - Distance (FOV center) off lunar limb (km)
RA	Right Ascension of observation (α)
Dec	Declination of observation (δ)
Azimuth	Azimuth at moon center (N thru E) – North (0), East (90), South (180), West (270) - Degrees
Elevation	Elevation at moon center (angle from horizon) - Degrees
LST	Local Sidereal Time
AM	Air Mass
Mv	Apparent Integrated Visual Magnitude

S_Brt	**Surface Brightness (visual magnitude per square arcsec)**
Illum	**Lunar Illumination (%) as viewed from the Earth**
Ang_Dia	**Angular Diameter of moon (arcsec)**
Obs_Long	**Planetodetic Longitude of moon center as seen by Observer (degrees) – positive longitude is East**
Obs_Lat	**Planetodetic Latitude of moon center as seen by Observer (degrees)**
S_Long	**Sub-Solar Longitude of the sun (degrees)**
S_Lat	**Sub-Solar Latitude of the sun (degrees)**
r	**Radial Distance between Sun and Moon (km)**
rdot	**Radial Velocity between Sun and Moon (km/s)**
delta	**Distance between Earth and Moon (km)**
deldot	**Radial Velocity between Earth and Moon (km/s)**
S-O-T	**Angle between Sun – Observer – Moon (elongation angle)**
L/T	**Moon (L)eading/(T)railing the Sun; Leading = Waning phase, Trailing = Waxing phase**
Phase	**Angle between Sun – Moon - Observer**
Line_Depth	**Line Depth of Na D2 relative in the Sun – Moon frame of reference**
Local Time	**Difference in longitude between FOV & subsolar point**
Fit Quality	**Good (standard parameters), Fair (at least, one parameter 'constrained' relative to standard), Bad (failed fit)**
Weather	**Guide as to whether the weather affected the results ('fits')**
Comment #3	**Assessment of any issues especially the 'fit quality'**

Appendix D1 – Lunar Potassium Fits

Lunar Potassium Fits				Solar K D1 Fraunhofer (7698.9646 Å)						Lunar K Emission (R: 7698.9681 Å)					
Date (2017)	**Object**	**File**	**Mod phase**	**V1 Center**	**V1 DW**	**V1 Area**	**V1 Err**	**V1 DWerr**	**V1 A_err**	**V2 Center**	**V2 DW**	**V2 Area**	**V2 Err**	**V2 DWerr**	**V2 A_err**
Mar 05	Langrenus Limb (W)	moon_06	-98.70	54.18	7.45	5385	0.06	0.04	31	58.71	3.24	1276	0.02	0.10	14
Mar 05	Cleomedes Limb (W)	moon_07	-98.54	53.96	6.94	13719	0.04	0.03	65	58.52	4.73	1032	0.05	0.25	34
Mar 06	Langrenus Limb (W)	moon_10	-86.16	54.61	7.02	7994	0.08	0.09	126	58.87	3.74	1567	0.03	0.15	29
Mar 06	Cleomedes Limb (W)	moon_11	-86.10	54.21	7.17	4070	0.06	0.04	25	58.75	3.44	1628	0.01	0.06	12
Mar 06	Atlas Limb (W)	moon_12	-86.02	54.02	7.12	4420	0.05	0.04	23	58.62	3.68	1669	0.01	0.06	11
Mar 06	Atlas Limb (N)	moon_13	-85.96	54.25	6.82	3058	0.06	0.04	20	58.46	3.73	1209	0.01	0.07	10
Mar 06	Petavius Limb (W)	moon_14	-85.81	54.35	7.76	6398	0.06	0.05	38	58.84	3.25	1412	0.02	0.11	17
Mar 06	Janssen Limb (S)	moon_15	-85.68	54.81	7.51	5696	0.06	0.05	35	58.83	3.65	1134	0.02	0.13	17
Mar 07	Langrenus Limb (W)	moon_24	-72.21	53.50	6.88	10167	0.04	0.03	47	58.14	4.12	1336	0.03	0.14	23
Mar 07	Cleomedes Limb (W)	moon_26	-72.08	53.60	6.83	7389	0.04	0.03	37	58.02	3.86	1451	0.02	0.10	18
Mar 07	Atlas Limb (W)	moon_29	-71.90	53.70	6.63	4426	0.06	0.04	29	57.76	3.76	1456	0.02	0.08	15
Mar 07	Atlas Limb (N)	moon_31	-71.80	53.76	6.46	3282	0.05	0.04	22	57.39	4.02	989	0.02	0.09	12
Mar 07	Petavius Limb (W)	moon_33	-71.63	53.46	6.65	7136	0.05	0.03	41	57.81	3.95	1373	0.02	0.12	21
Mar 08	Langrenus Limb (W)	moon_23	-58.97	55.02	7.22	7783	0.05	0.04	47	59.18	4.34	1248	0.03	0.15	24
Mar 08	Cleomedes Limb (W)	moon_25	-58.88	54.66	7.38	7788	0.06	0.05	50	59.04	4.12	1288	0.03	0.15	24
Mar 08	Atlas Limb (W)	moon_27	-58.79	55.00	6.84	5980	0.05	0.04	35	58.79	4.14	1333	0.02	0.11	19
Mar 08	Atlas Limb (N)	moon_30	-58.60	54.76	6.72	5438	0.05	0.04	32	58.39	4.18	977	0.03	0.13	18

Observations are at the limb with FOV = 2’

- Center = (bins); DW = Doppler Width (bins); Area = Intensity (counts per 300 sec * bins)
- V3 = K S-resolved Blue component (7698.9586 Å); $\delta\lambda_B$ - $\delta\lambda_R$ = 1.200 bins; $DW_B = DW_R$; Area(B) = Area(R) * 0.6

Appendix D2 – Lunar Sodium Fits

Lunar Sodium Fits					Solar Na D2 Fraunhofer (5889.9509 Å)						Lunar Na Emission (R: 5889.9584 Å)					
#	Date (2016)	Object	File	Mod phase	V1 Center	V1 err	V1 DW	V1 DWerr	V1 Area	V1 A_err	V2 Center	V2 err	V2 DW	V2 DWerr	V2 Area	V2 A_err
0	15-Mar	Langrenus Limb	moon_24	-96.8	56.21	0.14	32.98	0.56	-880	11	55.28	0.01	4.79	0.09	623	6
1	15-Mar	Cleomedes Limb	moon_25	-96.7	56.17	0.14	31.31	0.59	-727	10	55.20	0.01	4.80	0.09	586	6
2	15-Mar	Petavius Limb	moon_26	-96.6	57.70	0.14	36.24	0.47	-1132	12	55.29	0.02	4.53	0.09	543	5
3	15-Mar	Messala Limb	moon_27	-96.6	59.61	0.18	39.30	0.53	-923	13	55.21	0.02	4.36	0.08	521	4
4	15-Mar	Atlas Limb	moon_28	-96.5	61.62	0.22	40.81	0.61	-957	16	55.15	0.02	4.46	0.10	450	4
5	15-Mar	Atlas Limb	moon_29	-96.4	64.16	0.26	45.48	0.76	-887	17	55.10	0.02	4.47	0.12	274	3
6	15-Mar	Janssen Limb	moon_30	-96.4	60.84	0.25	40.09	0.69	-954	18	55.38	0.03	4.36	0.13	392	5
7	15-Mar	Langrenus Limb	moon_31	-96.3	57.03	0.20	33.28	0.66	-525	9	55.34	0.02	4.58	0.13	309	4
8	15-Mar	Cleomedes Limb	moon_32	-96.2	56.90	0.21	33.27	0.70	-484	8	55.33	0.02	4.69	0.13	286	4
9	15-Mar	Cleomedes Limb	moon_33	-96.2	56.63	0.24	31.12	0.79	-314	7	55.37	0.03	4.79	0.19	165	3
10	16-Mar	Langrenus Limb	moon_27	-83.8	57.48	0.14	39.41	0.54	-1297	15	55.39	0.02	4.44	0.09	595	5
11	16-Mar	Cleomedes Limb	moon_28	-83.8	57.61	0.15	41.05	0.59	-1233	15	55.30	0.02	4.26	0.09	546	4
12	16-Mar	Petavius Limb	moon_29	-83.7	58.20	0.14	41.23	0.55	-1347	15	55.31	0.02	4.39	0.10	531	4
13	16-Mar	Messala Limb	moon_30	-83.7	59.17	0.19	43.48	0.62	-1329	18	55.23	0.02	4.34	0.10	492	4
14	16-Mar	Atlas Limb	moon_31	-83.6	60.15	0.17	44.76	0.63	-1360	17	55.17	0.02	4.24	0.10	457	4
16	16-Mar	Janssen Limb	moon_33	-83.4	59.76	0.17	42.42	0.57	-1202	15	55.14	0.02	3.93	0.12	389	4
17	16-Mar	Janssen Limb	moon_34	-83.4	58.61	0.17	43.52	0.59	-1204	15	55.06	0.03	3.86	0.17	263	3
18	16-Mar	Apollonius Limb	moon_35	-83.3	56.67	0.19	37.41	0.69	-695	10	55.30	0.02	4.30	0.14	285	4
19	16-Mar	Cleomedes Limb	moon_37	-83.2	56.25	0.18	35.25	0.71	-625	9	55.25	0.03	4.70	0.15	270	4

Appendix D2		Terrestrial H_2O (5889.637 Å)						Terrestrial H_2O (5890.227 Å)*		Terrestrial H_2O (5890.090 Å)+		Continuum			
#	Object	V4 Center	V4 err	V4 DW	V4 DWerr	V4 Area	V4 A_err	V5 Center	V5 err	V6 Center	V6 err	Cont	Cont err	Slope	Slope err
0	Langrenus Limb	111.52	0.22	14.64	0.70	-126.6	7.5	6.04	0.39	36.14	0.47	113.0	0.2	0.032	0.001
1	Cleomedes Limb	111.27	0.22	13.49	0.66	-109.8	6.1	6.19	0.36	36.49	0.45	97.5	0.2	0.048	0.001
2	Petavius Limb	109.27	0.15	15.80	0.42	-243.2	8.5	6.77	0.24	37.13	0.27	132.0	0.2	0.148	0.002
3	Messala Limb	109.51	0.17	20.73	0.49	-304.2	11.3	6.09	0.31	38.17	0.29	97.9	0.2	0.090	0.001
4	Atlas Limb	109.63	0.20	24.33	0.61	-419.1	17.7	6.00	0.39	38.68	0.35	88.1	0.3	0.116	0.002
5	Atlas Limb	110.60	0.23	27.05	0.71	-431.5	21.3	5.48	0.45	38.41	0.37	63.4	0.3	0.101	0.002
6	Janssen Limb	109.98	0.20	21.13	0.59	-356.6	15.8	7.31	0.36	38.05	0.36	96.7	0.3	0.120	0.002
7	Langrenus Limb	110.01	0.19	17.09	0.59	-140.1	6.8	7.57	0.34	35.68	0.41	69.9	0.2	-0.007	0.001
8	Cleomedes Limb	110.39	0.19	16.25	0.58	-126.0	6.2	7.25	0.33	35.58	0.40	62.8	0.2	0.012	0.001
9	Cleomedes Limb	111.32	0.21	15.57	0.68	-82.5	4.6	7.45	0.38	34.56	0.48	43.6	0.1	-0.024	0.001
10	Langrenus Limb	108.34	0.21	19.42	0.60	-253.9	11.3	3.85	0.50	37.95	0.40	148.3	0.3	0.046	0.002
11	Cleomedes Limb	108.71	0.21	19.33	0.60	-251.3	11.1	4.12	0.46	38.49	0.39	134.3	0.3	0.105	0.002
12	Petavius Limb	108.46	0.18	18.66	0.50	-290.3	10.8	5.67	0.33	38.63	0.32	147.7	0.3	0.126	0.002
13	Messala Limb	108.98	0.20	21.12	0.57	-352.7	15.4	6.64	0.38	39.28	0.33	129.7	0.3	0.138	0.002
14	Atlas Limb	109.13	0.19	22.48	0.52	-408.7	15.3	5.59	0.33	39.11	0.31	123.3	0.3	0.161	0.002
16	Janssen Limb	108.84	0.18	20.38	0.47	-346.3	12.0	6.63	0.28	38.73	0.29	125.4	0.3	0.156	0.002
17	Janssen Limb	109.30	0.17	16.88	0.48	-247.0	9.7	7.49	0.27	38.72	0.28	124.4	0.3	0.139	0.002
18	Apollonius Limb	109.78	0.21	16.46	0.60	-144.2	7.1	6.19	0.38	36.95	0.41	91.5	0.2	-0.024	0.001
19	Cleomedes Limb	110.04	0.21	15.67	0.61	-127.2	6.6	6.72	0.36	36.50	0.43	82.3	0.2	0.011	0.001

- Center = (bins); DW = Doppler Width (bins); Area = Intensity (counts per 300 sec * bins)
- V3 = Na S-resolved Blue component (5889.9386 Å); $\delta\lambda_B$ - $\delta\lambda_R$ = 3.255 bins; $DW_B = DW_R$; Area(B) = Area(R) * 0.6
- *V5 = Terrestrial H_2O absorption (5890.227 Å); $DW_{V5} = DW_{V2}$; Area(V5) = Area(V4) * 0.67
- +V6 = Terrestrial H_2O absorption (5890.090 Å); $DW_{V6} = DW_{V2}$; Area(V6) = Area(V4) * 0.67

APPENDIX E: Acronyms

APPENDIX E - ACRONYM LIST	
ADU	Analog to Digit Unit
Ar	Argon
ARTEMIS	Acceleration, Reconnection, Turbulance, and Electrodynamics of the Moon's Interaction with the Sun
AURA	Association of Universities for Research in Astronomy
CCD	Charge Coupled Device
CME	Coronal Mass Ejection
δ	Declination (Degrees)
DC	Direct Current
DW	Doppler Width
eV	Electron Volts
FOV	Field of View
FP	Fabry-Perot
FPS	Fabry-Perot Spectroscopy
FSR	Free Spectral Range
FWHM	Full-Width Half-Maximum
Ga	Billion Years
GSFC	Goddard Space Flight Center
GSM	Geocentric Solar Magnetospheric
H_2	Molecular Hydrogen
HA	Hour Angle
He	Helium
HC	Hollow Cathode
Hr	Hours
IDL	Interactive Data Language
IP	Instrument Profile
JPL	Jet Propulsion Lab
K	Potassium

km	Kilometer
KREEP	Potassium, Rare Earth Elements, and Phosphorus
LACE	Lunar Atmospheric Composition Experiment
LADEE	Lunar Atmosphere and Dust Environment Explorer
λ	Lambda (wavelength)
LOS	Line of Sight
LW	Lorentz Width
MATLAB	Matrix Lab
MMP	McMath-Pierce (Solar Telescope)
Na	Sodium
NASA	National Aeronautics and Space Administration
Ne	Neon
NOAO	National Optical Astronomy Observatory
NSF	National Science Foundation
NSO	National Solar Observatory
PSD	Photon-Stimulated Desorption
QC	Quality Control
R	Resolving Power (λ/δλ)
RA	Right Ascension (α)
R_E	Earth Radius (6378 km)
R_M	Moon Radius (1738 km)
Rn	Radon
SBE	Surface Boundary Exospheres
SELENE	SELonographic and ENgineering Explorer
SZA	Solar Zenith Angle
T_{eff}	Effective Temperature
Th	Thorium
UT	Universal Time
UVS	Ultraviolet and Visible Spectrometer
UW	University of Wisconsin
VF	Voigt Fit

REFERENCES

"Hyperfine Structure." *Encyclopædia Britannica*, Encyclopædia Britannica, Inc., 2015, www.britannica.com/science/hyperfine-structure.

Athiray P.S, S. Narendranath, P. Sreekumar, M. Grande, C1XS results—First measurement of enhanced sodium on the lunar surface, *Planetary and Space Science,* Volume 104, Part B, 2014, Pages 279-287, ISSN 0032-0633, https://doi.org/10.1016/j.pss.2014.10.010.

Athiray, P. S., S. Narendranath, P. Sreekumar, and M. Grande (2014), C1XS results—First measurement of enhanced sodium on the lunar surface. *Planetary and Space Science*, *104*, 279-287.

Bhardwaj, A., Dhanya, M.B., Alok, A. *et al.* A new view on the solar wind interaction with the Moon. *Geosci. Lett.* **2,** 10 (2015). https://doi.org/10.1186/s40562-015-0027-y

Borovsky, J.E., Valdivia, J.A. The Earth's Magnetosphere: A Systems Science Overview and Assessment. *Surv Geophys* **39,** 817–859 (2018). https://doi.org/10.1007/s10712-018-9487-x

C.A. Dukes and R.E. Johnson, Contribution of Surface Processes to the Lunar Exosphere: Laboratory Experiments, in Encyclopedia of Lunar Science, Springer International, ed. B. Cudnik, 1 - 7 (2017).

Cassidy, T.A. and R.E. Johnson (2005), Monte Carlo Model of Sputtering and Other Ejection Processes Within a Regolith. *Icarus*, 176, 499-507.

Cassidy, T.A., R.E. Johnson, P.E. Geissler, and F. LeBlanc (2008). Simulation of Na D Emission Near Europa During Eclipse. *J. Geophys. Res.*, 113.

Chamberlain, J.W. and D. M. Hunten (1987). Theory of Planetary Atmospheres. *Academic Press,* Orlando.

Chamberlain, Joseph W. & Hunten, Donald M. (1987). *Theory of planetary atmospheres : an introduction to their physics and chemistry*. Orlando : Academic Press

Coakley, M. M., F.L. Roesler, R. J. Reynolds, and S. Nossal (1996), Fabry-Perot CCD Annular-summing Spectroscopy: Study and Implementation for Aeronomy Applications. *Appl. Optics.*, 35, 6479-6493. doi: 10.1364/AO.35.006479.

Colaprete, A., M. Sarantos, D. H. Wooden, T. J. Stubbs, A. M. Cook, M. Shirley (2016), How Surface Composition and Meteoroid Impacts Mediate Sodium and Potassium in the Lunar Exosphere. *Science*, 351, 249-252. doi: 10.1126/science.aad2380.

Colaprete, A., M. Sarantos, D. H. Wooden, T. J. Stubbs, A. M. Cook, and M. Shirley (2016), How surface composition and meteoroid impacts mediate sodium and potassium in the lunar exosphere, Science, 351(6270), 249–252.

Dayeh, M. A., Fuselier, S. A., Funsten, H. O., McComas, D. J., Ogasawara, K., Petrinec, S. M., Schwadron, N. A., and Valek, P. (2015), Shape of the terrestrial plasma sheet in the near-Earth magnetospheric tail as imaged by the Interstellar Boundary Explorer. *Geophys. Res. Lett.*, 42, 2115– 2122. doi: 10.1002/2015GL063682.

Denton, M. H., Thomsen, M. F., Reeves, G. D., Larsen, B. A., Henderson, M. G., Jordanova, V. K., … Spence, H. A. (2017). The evolution of the plasma sheet ion composition: Storms and recoveries. *Journal of Geophysical Research: Space Physics*, 122, 12,040– 12,054. https://doi.org/10.1002/2017JA024475

Domingue, D.L., Patrick, L. K., R.M. Killen, A. L. Sprague, M. Sarantos, A. F. Cheng, E. T. Bradley, W. E. McClintock (2007), Mercury's Atmosphere: A Surface-Bounded Exosphere. *Space Sci Rev*., 131: 161–186. doi 10.1007/s11214-007-9260-9

Dukes, C., D. Hurley, *Science.*15 Jan 2016:Vol. 351, Issue 6270, pp. 230-231 DOI: 10.1126/science.aad8245

Dunbar, Brian. "Is There an Atmosphere on the Moon?" *NASA*, NASA, 2014, www.nasa.gov/mission_pages/LADEE/news/lunar-atmosphere.html.

Galilei, Galileo, 1564-1642. *Sidereus Nuncius:* Venice, 1610. Palo Alto, CA :Octavo, 1998.

Gamborino, D, P. Wurz, Velocity distribution function of Na released by photons from planetary surfaces, Planetary and Space Science, Volume 159, 2018, Pages 97-104, ISSN 0032-0633, https://doi.org/10.1016/j.pss.2018.04.021.

Gardner, S., Voelz, D., Sechrist, C., Segal, A. (1986). Lidar Studies of the Nighttime Sodium Layer over Urbana, Illinois 1. Seasonal and Nocturnal Variations. *Journal of Geophysical Research,* 91(13), 659 – 673.

Hapgood, M. "Modelling Long-Term Trends in Lunar Exposure to the Earth's Plasmasheet." *Annales Geophysicae*, Copernicus GmbH, 2 Oct. 2007, angeo.copernicus.org/articles/25/2037/2007/.

Hapke, B., 1986. Bidirectional reflectance spectroscopy. IV - The extinction coefficient and the opposition effect. Icarus 67, 264–280.

Harada, Y, and J.S. Halekas. "Upstream Waves and Particles at the Moon." *Low-Frequency Waves in Space Plasmas*, by Andreas Keiling et al., John Wiley & Sons, 2016, pp. 307–318.

Harald Hiesinger, Ralf Jaumann, Chapter 23 - The Moon, Encyclopedia of the Solar System (Third Edition), Elsevier, 2014, Pages 493-538, ISBN 9780124158450, https://doi.org/10.1016/B978-0-12-415845-0.00023-2.

Hartle, J.B, Phys. Rev. D **3**, 2938 – Published 15 June 1971

Hartle, R. E. (1971), Model for rotating and nonuniform planetary exospheres. *The Physics of Fluids*, 14(12), 2592-2598.

Helfenstein, P., Veverka, J., 1987. Photometric properties of lunar terrains derived from Hapke's equation. Icarus 72, 342−357.

Hernandez G. (1986). Fabry-Perot Interferometers: Cambridge Studies in Modern in Optics 3, *Cambridge University Press,* 343 pages.

Herwartz D., A. Pack, B. Friedrichs, A. Bischoff. Identification of the giant impactor Theia in lunar rocks. *Science.* 2014 Jun 6;344(6188):1146-50. doi: 10.1126/science.1251117. PMID: 24904162.

Horányi, M., J.R. Szalay, S. Kempf, J. Schmidt, E. Grün, R. Srama, and Z. Sternovsky (2015), A permanent, asymmetric dust cloud around the Moon. *Nature,* 522(7556), 324-326.

Hughes, A.R.W. VLF waves in the magnetosphere. *Astrophys Space Sci* **230,** 431–438 (1995). https://doi.org/10.1007/BF00658200

Hunten, D. M., T. H. Morgan, and D. E. Shemansky, The Mercury atmosphere, in Mercury, edited by F. Vilas, C. R. Chapman, and M. S. Matthews, pp. 562-612, Univ. of Ariz. Press, Tucson, 1988.

Hurley, D.M, *Lunar Polar Volatiles and Associated Processes***.** A white paper submitted to the Planetary Decadal Survey Inner Planets Panel September 15, 2009.

Ip, W.H. (1991), The Atomic Sodium Exosphere/ Coma of the Moon. *Geophys. Res. Lett.,* 18, 2093 -2096.

Janches, D., P. Pokorný, M. Sarantos, J.R. Szalay, M. Horányi, Nesvorný, D. (2018), Constraining the Ratio of Micrometeoroids From Short-and Long-Period Comets at 1 AU From LADEE Observations of the Lunar Dust Cloud. *Geophysical Research Letters*, *45*(4), 1713-1722.

Johnson R.E. (1990), Energetic Charged – Particle Interactions with Atmospheres and Surfaces. *Springer,* 19.*Journal of Geophysical Research,* 110 (D23).

Juncar, P., Pinard, J., Hamon, J., Chartier, A. (1981). Absolute Determination of the Wavelengths of the Sodium D_1 and D_2 Lines by Using a CW Tunable Dye Laser Stabilized on Iodine. *Metrologia,* 17(3).

Juncar, P., Pinard, J., Hamon, J., Chartier, A. (1981). Absolute Determination of the Wavelengths of the Sodium D_1 and D_2 Lines by Using a CW Tunable Dye Laser Stabilized on Iodine. *Metrologia,* 17(3).

Kagitani, M., M. Taguchi, A. Yamazaki, I.Yoshikawa, G. Murakami, K. Yoshioka, S. Kameda, S. Okano (2010), Variation in Lunar Sodium Exosphere Measured from Lunar

Orbiter SELENE (Kaguya). *Planet. Space Sci.*, 58(12), 1660-1664. doi: 10.1016/j.pss.2010.07.025.

Kallio, E, S. Dyadechkin, P. Wurz, M. Khodachenko, Space weathering on the Moon: Farside-nearside solar wind precipitation asymmetry, Planetary and Space Science,Volume 166, 2019, Pages 9-22, ISSN 0032-0633,https://doi.org/10.1016/j.pss.2018.07.013.

Esa Kallio, Gábor Facskó, Properties of plasma near the moon in the magnetotail, Planetary and Space Science, Volume 115, 2015, Pages 69-76, ISSN 0032-0633, https://doi.org/10.1016/j.pss.2014.11.007.

Killen, R. M., and Ip, W.-H. (1999), The surface-bounded atmospheres of Mercury and the Moon, *Rev. Geophys.*, 37(3), 361– 406, doi:10.1029/1999RG900001.

Killen, R., D. Shemansky, and N. Mouawad (2009), Expected emission from Mercury's exospheric species, and their ultraviolet-visible signatures. *The Astrophysical Journal Supplement Series*, *181*(2), 351.

Kivelson, M.G, F. Bagenal, in Encyclopedia of the Solar System (Second Edition), 2007

Kozlowski, R.W.H, A.L. Sprague, and D.M. Hunten (1990), Observations of Potassium in the tenuous lunar atmosphere. *J. Geophys Res.,* 17, 2253-2256.

Kuruppuaratchi, D. C. P., Mierkiewicz, E. J., Oliversen, R. J., Sarantos, M., Derr, N. J., Gallant, M. A., et al. (2018). High-resolution, ground-based observations of the lunar sodium exosphere during the Lunar Atmosphere and Dust Environment Explorer (LADEE) mission. *Journal of Geophysical Research: Planets*, 123, 2430– 2444. https://doi.org/10.1029/2018JE005717

Kuruppuaratchi, D.C.P. (2015), The Lunar Exosphere: Spatial and Temporal Variations of Sodium and Potassium Emissions from November 2013 to May 2014, M.S. thesis, Dep. of Phys. Sci., Embry-Riddle Aeronautical Univ., Daytona Beach, Florida, USA.

Line, M. R., Mierkiewicz, E. J., Oliversen, R. J., Wilson, J. K., Haffner, L. M., & Roesler, F. L. (2012). Sodium Atoms in the Lunar Exotail: Observed Velocity and Spatial Distributions. *Icarus, 219*(2). https://doi.org/10.1016/j.icarus.2012.04.001

Line, M.R., E.J., Mierkiewicz, R.J., Oliversen, J.K., Wilson, L.M., Haffner, F.L., Roesler (2012), Sodium atoms in the lunar exotail: Observed velocity and spatial distributions. *Icarus*, 219, 609-617.

Lue, c, (2015),Solar Wind Proton Interactions with Lunar Magnetic Anomalies and Regolith

Luis Conde (2018), An Introduction to Plasma Physics and Its Space Applications, Volume 1, Fundamentals and elementary processes, http://dx.doi.org/10.1088/2053-2571/aae132

Madey, T.E., B.V. Yakshinskiy, V.N. Ageev, and R.E. Johnson (1998), Desorption of alkali atoms and ions from oxide surfaces – Relevance to origins of NA and K in atmospheres of Mercury and the Moon. *J. Geophys, Res.,* 103, 5873-5887.

Marsh, R., Janches, D., Feng, W., Plane, J. (2013). A Global Model of Meteoritic Sodium. *Journal of Geophysical Research,* 118(11), 442-452.

McNutt, D.P., and J.E. Mack (1963), Telluric absorption, residual intensities, and shifts in the Fraunhofer D lines. *J. Geophys. Res.,* 68, 3419-3429.

Mendillo, M., B. Flynn, and J. Baumgardner (1993), Imaging Experiments to Detect an Extended Sodium Atmosphere on the Moon. *Adv. Space Res.*, 13(10), 313-319. doi:10.1016/0273-1177(93)90085-P.

Mendillo, M., J. Baumgardner, and B. Flynn, Imaging observations of the extended sodium atmosphere of the Moon, Geophys. Res. Lett., 18, 2097- 2100, 1991

Mendillo, M., J. Emery, and B. Flynn (1997), Modeling the Moon's extended sodium cloud as a tool for investigating sources of transient atmospheres. *Avd. Space. Res.,* 19(10), 1577-1586.

Mierkiewicz, E. J., Line, M., Roesler, F. L., and Oliversen, R. J. (2006), Radial velocity observations of the extended lunar sodium tail, *Geophys. Res. Lett.*, 33, L20106, doi:10.1029/2006GL027650.

Mierkiewicz, E. J., Roesler, F. L., and Nossal, S. M. (2012), Observed seasonal variations in exospheric effective temperatures, *J. Geophys. Res.*, 117, A06313, doi:10.1029/2011JA017123.

Mierkiewicz, J., R. J. Oliversen, F.L. Roesler, O. L. Lupie (2014), High-resolution Spectroscopy of the Lunar Sodium Exosphere. *J. Geophys. Res.*, 119, 4950-4956.

Morgan, T.H. and D.E. Shemansky (1991), Limits to the lunar atmosphere. *J. Geophys Res.,* 96, 1351-1367.

Mouawad, N., Burger, M.H., Killen, R.M., Potter, A.E., McClintock, W.E., Vervack, R.J.,Bradley, E.T., Benna, M., Naidu, S., 2011. Constraints on Mercury's Na exosphere:combined MESSENGER and ground-based data. Icarus 211, 21−36. https://doi.org/10.1016/j.icarus.2010.10.019.

National Research Council of the National Academies, 2007. The Scientific Context for Exploration of the Moon. National Academies Press, Washington, DC.

Oliversen, R. J., Doane, N. E., Scherb, F., Harris, W. M., and Morgenthaler, J. P.: 2002a, *Ap. J.* 581.

P. Matlovič, L. Kornoš, M. Kováčová, J. Tóth, J. Licandro, Apr Characterization of the June epsilon Ophiuchids meteoroid stream and the comet 300P/Catalina Astron. Astrophys., 636 (2020), p. A122

Pokorný, P., Janches, D., Sarantos, M., Szalay, J. R., Horányi, M., Nesvorný, D., & Kuchner, M. J. (2019). Meteoroids at the Moon: Orbital properties, surface vaporization, and impact ejecta production. *Journal of Geophysical Research: Planets*, 124, 752– 778. https://doi.org/10.1029/2018JE005912

Poppe, A. R., Halekas, J. S., Sarantos, M., and Delory, G. T. (2013), The self-sputtered contribution to the lunar exosphere, *J. Geophys. Res. Planets*, 118, 1934– 1944, doi:10.1002/jgre.20148.

Potter, A. E, and T.H. Morgan (1988a), Discovery of sodium and potassium vapor in the atmosphere of the Moon. *Science,* 241(4866), 675-680.

Potter, A. E, and T.H. Morgan (1988b), Extended Sodium Exosphere of the Moon. *Geophys. Res. Lett.,* 15(13), 1515-1518.

Potter, A. E, R. M. Killen, T.H. Morgan (2000), Variation of the Lunar Sodium During Passage of the Moon Through the Earth's Magnetotail. *J. Geophys. Res.*, 105, 15,073-15,084.

Potter, A. E, T.H. Morgan (1998), Coronagraphic observations of the lunar sodium exosphere near the lunar surface. *J. Geophys. Res.*, 103, 4, 8581-8586073-15,084. doi:10.1029/98JE00059

Potter, A.E, and T.H. Morgan (1988a), Discovery of Sodium and Potassium Vapor in the Atmosphere of the Moon, *Science*, 241*,* 675-680. doi: 10.1126/science.241.4866.675.

Potter, A.E, and T.H., Morgan (1985), Discovery of sodium in the atmosphere of mercury. *Science.* 1985 Aug 16;229(4714):651-3. doi: 10.1126/science.229.4714.651.

Potter, A.E, and T.H., Morgan (1986), Potassium in the atmosphere of Mercury, *Icarus*,Volume 67, Issue 2,Pages 336-340,ISSN 0019-1035, https://doi.org/10.1016/0019-1035(86)90113-2.

Potter, A.E., and T.H. Morgan (1991), Observations of the lunar sodium exosphere. *J. Geophys Res.,* 18, 2089-2092.

Potter, A.E., and T.H. Morgan (1994), Variation of lunar sodium emission intensity with phase angle. *J. Geophys Res.,* 21(21), 2263-2266.

Potter, A.E., W. Mendell, and T.H. Morgan (1984), Lunar luminescence and the filling-in of the Fraunhofer lines in moonlight. *J. Geophys Res.,* 89(S01), C240-C244.

Prettyman, T. H., Hagerty, J. J., Elphic, R. C., Feldman, W. C., Lawrence, D. J., McKinney, G. W., and Vaniman, D. T. (2006), Elemental composition of the lunar surface: Analysis of gamma ray spectroscopy data from Lunar Prospector, *J. Geophys. Res.*, 111, E12007, doi:10.1029/2005JE002656.

R. C. Elphic et al., The Lunar Atmosphere and Dust Environment Explorer Mission (LADEE), Cham, Switzerland:Springer, pp.4, 2015.

R. M., Killen, Thomas H. Morgan, Andrew E. Potter, Claude Plymate, Roy Tucker, Jamil D. Johnson Coronagraphic observations of the lunar sodium exosphere January - June, 2017, *Icarus* (2019), 10.1016/j.icarus.2019.02.027

R.M. Killen, T.H. Morgan, A.E. Potter, Giovanni Bacon, Irima Ajang, Andrew R. Poppe, Coronagraphic observations of the lunar sodium exosphere 2018–2019, *Icarus (2020)*, Volume 355, 2021,114155, ISSN 0019-1035,https://doi.org/10.1016/j.icarus.2020.114155.

Richardson, J.D, Voyager observations of the interaction of the heliosphere with the interstellar medium, Journal of Advanced Research, Volume 4, Issue 3, 2013, Pages 229-233, ISSN 2090-1232, https://doi.org/10.1016/j.jare.2012.09.002.

Righter, K. (2019) Volatile Element Depletion of the Moon–The Roles of Precursors, Post-impact Disk Dynamics, and Core Formation, *Science Advances,* v. 5(1), doi: 10.1126/sciadv.aau7658.

Roesler, F., (1974). Fabry-Perot Instruments of Astronomy. *Astrophysics. Part A: Optical and Infrared,* 531-569.

Rosborough, S. A., Oliversen, R. J., Mierkiewicz, E. J., Sarantos, M., Robertson, S. D., Kuruppuaratchi, D. C., et al. (2019). High-resolution potassium observations of the lunar exosphere. *Geophysical Research Letters*, 46, 6964– 6971. https://doi.org/10.1029/2019GL083022

Ryan K Hanley *et al* 2015 *J. Phys. B: At. Mol. Opt. Phys.* **48** 195004

Sarantos, M., D. C. P. Kuruppuaratchi, P. Pokorny, S. D. Robertson, E. Williams, R. J. Oliversen, E. J. Mierkiewicz, and D. Janches (2017), Improved velocity distributions for exospheric Na and K surrounding the Moon, *AGU Fall Meeting Abstracts*.

Sarantos, M., R. M. Killen, S.A. Surjalal, J. A. Slavin (2008), Influence of plasma ions on source rates for the lunar exosphere during passage through the Earth's magnetosphere. *Geophys. Res. Lett.,* 35, L04105, doi:10.1029/2007GL032310.

Sarantos, M., R. M. Killen, S.A. Surjalal, J. A. Slavin (2010), Sources of Sodium in the Lunar Exosphere: Modeling Using Ground-Based Observations of Sodium Emission and Spacecraft Data of the Plasma. *Icarus*, 205, 364-374. doi: 10.1016/j.icarus.2009.07.039.

Sarantos, M., Hartle, R. E., Killen, R. M., Saito, Y., Slavin, J. A., and Glocer, A. (2012), Flux estimates of ions from the lunar exosphere, *Geophys. Res. Lett.*, 39, L13101, doi:10.1029/2012GL052001.

Schmidt, C. A. (2013), Monte Carlo modeling of north-south asymmetries in Mercury's sodium exosphere, *J. Geophys. Res. Space Physics*, 118, 4564– 4571, doi:10.1002/jgra.50396.

Schmidt, C.A. (2013), Monte Carlo modeling of North-South asymmetries in Mercury's

Sibeck, D.G., Angelopoulos, V., Brain, D.A. *et al.* ARTEMIS Science Objectives. *Space Sci Rev* **165,** 59–91 (2011). https://doi.org/10.1007/s11214-011-9777-9

Sigmud, P., Theory of Sputtering. I. Sputtering Yield of Amorphous and Polycrystalline Targets, July 1969, *Physical Review* 184(2):383-& Follow journal DOI: 10.1103/PhysRev.187.768

Sim, C. K., Kim, S. S., Lucey, P. G., Garrick-Bethell, I., & Choi, Y.-J. (2017). Asymmetric space weathering on lunar crater walls. *Geophysical Research Letters*, 44, 11,273– 11,281. https://doi.org/10.1002/2017GL075338

Slanger, T., et al. (2005). Variability of the Mesospheric Nightglow Sodium D_2/D_1 Ratio.

Smith, S., J. Wilson, J. Baumgardner, M. Mendillo (1999), Discovery of the distant lunar sodium tail and its enhancement following the Leonid meteor shower of 1998. *Geophys. Res. Lett.,* 26(12), 1649-1652.

Smyth, W.H., M.L. Marconi (1995), Theoretical Overview and Modeling of the Sodium and Potassium Atmospheres of the Moon. *Astrophys. J.*, 443, 371-392. doi: 10.1086/175532.

sodium exosphere. *J. Geophys Res.,* 118, 4564–4571, doi:10.1002/jgra.50396, 2013

Sprague A.L., M. Sarantos, D.M. Hunten, R.E. Hill, and R.W.H. Kozlowski (2012), The lunar sodium atmosphere: April – May1998. *Can. J. Phys.,* 90, 725-732.

Sprague, A. L., R.W.H. Kozlowski, D.M. Hunten, W.K. Wells, and F.A. Grosse (1992), The Sodium and Potassium Atmosphere of the Moon and its Interaction with the Surface. *Icarus, 96*, 27-42. doi: 10.1016/0019-1035(92)90004-Q.

Sprague, A.L., D.M. Hunten, R.W.H. Kozlowski, F.A. Grosse, R.E. Hill, R.L. Morris (1998), Observations of sodium in the lunar atmosphere during international lunar atmosphere week, 1995. *Icarus*, 131(2), 372-381.

Stern, David P. "Systematic Identification of Preferred Orbits For." *Systematic Identification of Preferred Orbits for Magnetospheric Missions 1. Single Satellites.*, 2006, www.phy6.org/Education/JAS1.htm.

Stern, David P. "The Exploration of the Earth's Magnetosphere." *The Exploration of the Earth's Magnetosphere"*, 2003, www.phy6.org/Education/Intro.html.

Stern, S. A. (1999), The Lunar Atmosphere: History, Status, Current Problems, and Context. *Rev. Geophys.,* 37, 453-491.

Stubbs et al. (2014) LPSC (Lunar Planetary Science Conference), 45, 2705.

Szalay, J. R., Horányi, M., Colaprete, A., and Sarantos, M. (2016), Meteoritic influence on sodium and potassium abundance in the lunar exosphere measured by LADEE, *Geophys. Res. Lett.*, 43, 6096– 6102, doi:10.1002/2016GL069541.

Szalay, J.R., M. Horányi, A. Colaprete, and M. Sarantos (2016), Meteoritic influence on sodium and potassium abundance in the lunar exospheremeasured by LADEE. *Geophys. Res. Lett.,*6096-6102, 10.1002/2016GL069541.

Tenishev, V., M. Rubin, O. Tucker, R. Combi, M. Sarantos (2013), Kinetic modeling of sodium in the lunar exosphere. *Icarus*, 226, 1538-1549.

Tufte, S. (1997). The Wham Spectrometer: Design, Performance Characteristics, & First Results. Ph.D. Dissertation. University of Wisconsin-Madison.

Tyler, A. L., D.M. Hunten, and R. Kozlowski (1988), Observations of sodium in the tenuous lunar atmosphere. *Geophys. Res. Lett.,* 15, 1141-1144.

Verani, S., C. Barbieri, C. Benn, G. Cremonese (1998), Possible detection of meteor stream effects on the lunar sodium atmosphere. *Planet. Space Sci.*, 46(8), 1003-1006.

Verani, S., C. Barbieri, C.R. Benn, G. Cremonese, M. Mendillo (2001), The 1999 quadrantids and the lunar Na atmosphere. *Mon. Not. R. Astron. Soc.,* 327(1), 244-248.

Wilson, J.K., M. Mendillo, H.E. Spence (2006), Magnetospheric influence on the Moon's exosphere. *J. Geophys. Res.,* 111.

Wurz, P., U. Rohner, J.A. Whitby, C. Kolb, H. Lammer, P. Dobnikar, J.A. Martin-Fernändez (2007), The lunar exosphere: The sputtering contribution. *Icarus*, 191(2), 486-496.

Yakshinskiy, B.V., T.E. Madey (1999), Photon-stimulated desorption as a substantial source of sodium in the lunar atmosphere. *Nature,* 400(6745), 642-644.

Yokota, S., et al. (2014), Structure of the ionized lunar sodium and potassium exosphere: Dawn-dusk asymmetry, *J. Geophys. Res. Planets*, *119*, 798–809, doi:10.1002/2013JE004529.